Complex Oscillations in IBR-Dominated Networks: Detection, Localization and Mitigation

PhD Thesis

Taimur Zaman

Dynamic Power System Laboratory

Department of Electronic and Electrical Engineering

University of Strathclyde, Glasgow

September 10, 2025

Signed:

Date:

Abstract

This thesis addresses the critical challenges of identifying and localizing the source of complex oscillations in power network. These mainly originate as a consequence of the abundant proliferation of networks with inverter-based resources (IBRs) and their evolving topologies. This significant emphasis on the IBRs and their participation in modern power grids have significantly changed grid dynamics, making the observability and localization of critical disturbances such as complex oscillations, more challenging. Standard Phasor Measurement Units (PMUs) and Wide Area Monitoring Systems (WAMS) adopted for grid observability face significant limitations in detecting these complex oscillations. This becomes more concerning when the localization of such disturbances depends on devices that are barely able to detect closely spaced, time-varying frequency modes. These oscillations are often caused by control interactions in inverter-based systems, such as Wind Turbine Generators (WTGs), and are amplified by disturbances, faults, and resonance phenomena.

To address these challenges, this thesis develops a systematic diagnostic approach for detecting and localizing complex Subsynchronous Control Interactions (SSCI) modes in real-time. A comprehensive review of the literature on oscillation detection methods is conducted, highlighting the need for improved observability and diagnostic tools. The thesis presents a detailed modeling of

WTGs, including the dynamics of control loops and their impact on system stability, and provides stability criteria for assessing and analyzing the SubSynchronous Oscillations (SSO) occurrences. A novel approach to overcoming observability constraints using sliding Discrete Fourier Transform (DFT) is explored, followed by the proposal of a new technique using Synchronized Waveform Measurement Units (SWMUs) for time-frequency analysis, enhancing the detection of complex SSCI modes.

The research also introduces an innovative methodology for deriving the admittance model at the point of connection (POI), which enables the identification and localization of oscillation sources based on their active/reactive power behavior. The proposed approach is validated through multiple case studies, including the use of synthetic signal testing, real-world data from the northwest China grid, and EMT models of the ERCOT south-region network. Finally, the thesis proposes a novel adaptive control approach for WTGs, integrating a Generalized Hebbian Learning algorithm to enhance damping and prevent oscillations in response to SSR or SSCI events. Simulation results demonstrate the effectiveness and applicability of the proposed methods in real-world scenarios, marking a significant step toward operational solutions that deliver improved grid stability and resilience.

Acknowledgment

First and foremost, I would like to express my deepest gratitude to my supervisor, Prof. Graeme Burt, for his exceptional technical support, patient guidance, insightful research suggestions, and unwavering supervision. His contributions have been instrumental in shaping my research journey.

I am also sincerely grateful to Dr. Mazheruddin Syed, Dr. Zhiwang Feng, and Dr. Yljon Saferi for their invaluable support, technical discussions, and insightful feedback. Their dedication in reviewing and supervising my work has played a crucial role in my progress, and I am fortunate to have had such knowledgeable and dedicated mentors throughout my PhD.

I would like to extend my appreciation to my colleagues at the Institute of Energy and Environment, particularly Richard Munro, Vassilieos Psaras, Abdulrahman Babagana, Issah Abdul Rashid, and Rafael Pena Alzola, as well as the many collaborators I have worked with globally. The research outcomes presented in this thesis would not have been possible without the collective efforts, support, and expertise of my supervisors, teammates, and collaborators.

My sincere thanks also go to the Energy Technology Partnership (ETP) and its associated partners (SORAYTEC) for the invaluable support provided throughout my research. Additionally, I am thankful to Dr. Aqib Javed, Dr. Abdul Razzaq, Dr. Awais Aziz Shah, and Mr. Asmatullah for their significant guidance

and assistance during my work.

Lastly, I extend my deepest gratitude to my family—especially my father and mother—for their unwavering love, sacrifice, and support throughout my PhD journey. Their strength, patience, and encouragement during the most challenging moments have been a constant source of inspiration. This thesis is dedicated to them and to my wife and future children.

Contents

List of Figures

List of Tables

List of Abbreviations

AIFST	Adaptive Instantaneous Frequency based Synchro Transform
BESS	Battery Energy Storage System
CSDC	Conventional Sub-Synchronous Damping Control
CSCs	Current Source Converters
DFIG	Dual-fed Induction Generator
DFT	Discrete Fourier Transform
DTA	Damping Torque Analysis
DVIC	Dynamic Virtual Impedance Control
EMT	Electromagnetic Transient
FACTs	Flexible AC Transmissions
FT	Fourier Transform
GSC	Grid Side Converter
HVDC	High Voltage Direct Current
IBRs	Inverter Based Resources
IGE	Induction Generator Effect
IF	Instantaneous Frequency

List of Abbreviations

MMCs	Modular Multilevel Converters
MSR	Multi Mode Synchronous Resonance
PDC	Phasor Data Concentrators
PLL	Phase Loop Lock
PMUs	Phasor Measurement Units
PoC	Point of Connection
POW	Point on Wave
PSS	Power System Stabilizer
RES	Renewable Energy Sources
RSC	Rotor Side Converter
SCR	Short Circuit Ratio
SCL	Short Circuit Level
SDFT	Sliding Discrete Fourier Transform
SSCI	Subsynchronous Control Interactions
SSR	SubSynchronous Resonance
SSO	SubSynchronous Oscillations
STFT	Short Time Fourier Transform
SupSR	SuperSynchronous Oscillations
SST	Synchro-Transform
SWMUs	Synchronized Waveform Measurement Units
TFA	Time Frequency Analysis

TFR	Time Frequency Representation
TFRs	Time Frequency Representations
VSCs	Voltage Source Converters
WAMS	Wide Area Monitoring Systems
WFs	Wind Farms
WPP	Wind Power Plant
WTGs	Wind Turbine Generators

List of Abbreviations

Chapter 1

Introduction

1.1 Research Context

The increasing adoption of Renewable Energy Sources (RES) in modern power systems has been largely facilitated by advancements in power converter technologies. These converters play a pivotal role in integrating intermittent energy sources like wind and solar by enhancing grid compatibility and stability. For instance, the voltage and current source converters (Voltage Source Converters (VSCs)/ Current Source Converters (CSCs)) equipped with passive network components offer enhanced flexibility and reliability of transmission networks in modern power networks. Likewise, VSCs and modular multilevel converters (Modular Multilevel Converters (MMCs)) are widely used in photovoltaic (PV) systems and high-voltage direct current (High Voltage Direct Current (HVDC)) applications penetrating the grid with modern power sources and sophisticated control mechanisms. Similarly, wind turbine generation (WTGs) based systems are equally equipped with power converters with specialized control mechanisms, tailored to meet the unique demands of modern power networks. However, integrating RES requires not only sophisticated power converters but also robust control methodologies to ensure secure operation despite diminishing inertia and system fault level currents. To improve the system inertia and strengthen the grids, battery energy storage systems (Battery Energy Storage System (BESS)) based solutions are encouraged through grid service methods, with tighter requirements on control mechanisms and performance to supply fast response to the grids for network disturbances. While this transition reduces dependence on conventional energy sources, the explicit reliance on Inverter Based Resources (IBRs) introduces significant challenges, particularly in maintaining power system stability. Among these challenges, power system oscillations have gained prominence, with a shift in focus from merely conventional subsynchronous oscillations (SSO) to complex sub and super-synchronous (SuperSynchronous Oscillations (SupSR) and SupSR) oscillations, exacerbated by the widespread use of power converters and control mechanisms reported globally.

The huge proliferation of IBRs in present grids and greater emphasis on decentralized energy generation have significantly evolved the dynamics of power networks from the simplest form to the one characterized by increasing complexity. These changes are reshaping the operation of grids, making it imperative to observe and monitor network behavior more comprehensively and vigilantly. Therefore, comprehensive observation by measurement and analysis of key parameters of the grid is now a cornerstone of effective grid management for socially acceptable levels of reliability and stability. Enhanced observability helps grid operators to predict, detect, and mitigate potential instabilities, such as complex oscillations, which are amplified by the integration of renewable energy sources and varying control mechanisms. As grid dynamics grow more complex, sophisticated tools like PMUs, WAMS, and advanced analytics will become essential to ensuring reliable and resilient grid operations, through more comprehensive observability. Complex disturbances can thus be managed without causing system wide outages.

Phasors and PMU-based WAMS are extensively used to monitor and control the wider network. However, as grid dynamics change, the transition from conventional torsional oscillations to subSynchronous oscillations (SSO) and further to complex SSCI based oscillations accelerates. PMU based WAMS will therefore be faced with significant challenges to their contribution to observability [3]. Diagnosing such complex oscillations depends on accurate estimation and detailed information regarding their characteristics. The majority of these oscillations are reported due to control interactions initiated by disturbances, low Short Circuit Ratio (SCR), faults, or resonance phenomena [4]. These interactions precipitate control instability in IBRs systems, particularly within WTG systems leading to the wide spread appearance of complex oscillations in the network [5]. The nature of these oscillations exhibits frequency modes that are closely spaced, exceed the limits of DFT-based approaches, and are explicitly time-varying, making detection using PMU-based WAMS highly challenging [6]. Therefore, this leads to an important need for a systematic diagnostic tool capable of identifying and localizing these complex modes in real-time so that preventive measures can be directed.

The mitigation strategy for complex oscillations is explicitly dependent on identification of their origin and so the solution pathway is twofold; primarily reliant on advanced control methodologies [7] or enhancing the grid dynamics [**?**]. Improvements to grid dynamics, such as increasing system inertia or short-circuit levels, are effective approaches but are considered expensive for the sole purpose of oscillation mitigation. Consequently, a huge interest in both academia and industry has shifted to control methodologies. Numerous strategies proposed in the literature leverage sophisticated control of VSCs and specifically for wind turbine generators (WTGs), but most remain at the level of academic research. Many methods rely on state models of WTGs [8–10] or computationally intensive approaches [11], limiting their industrial applicability. On the contrary, the industrially favored approaches often depend on prior knowledge of oscillation modes [12,13]. The Majority of these approaches use techniques tuned to specific frequencies to inject stabilizing signals or filter oscillation effects. However, such methods are only effective in networks with conventional and well-detected oscillations. Therefore, this gap highlights the need for innovative solutions to first acquire precise information on the modes involved in the complex oscillations and provide adequate control based solutions leading towards their mitigation and ensuring optimal system stability, reliability, and performance in the face of evolving challenges.

Despite technological advancements in measuring and estimating power system metrics—such as Point on Wave (POW) measurements and SWMUs —an online diagnostic tool capable of identifying and localizing complex SSCI in the network remains absent. The lack of such methods poses significant hurdles in developing effective control mechanisms for mitigating these oscillations. An independent approach, free from reliance on conventional diagnostic and mitigation techniques, is essential to overcome these challenges. Such innovations will not only address the pressing issues of system stability but also pave the way for a more resilient and adaptive power grid.

1.2 Research Motivation

In recent years, power network oscillations have become increasingly common due to the rapid integration of renewable energy sources into power grids. These events are reportedly evolving from conventional SubSynchronous Resonance (SSR) events to SSCI that leads to more complex oscillations. Interestingly, they are frequently reported in networks where IBRs based generation sources and specifically wind farms are connected via line compensator to the grid. This proliferation of grids connections are giving rise to new phenomena involving complex modes of oscillations, where a range of frequencies around the fundamental frequency are interpolated and oscillations with complex modes are introduced into the network. Detecting such events and localizing their source is crucial for maintaining stable system operation, as such oscillations can propagate to the wider network, potentially leading to the disconnection of generation sources and damage to power system assets. Therefore, it is extremely important to detect and identify the precise modes involved in complex SSCI and localize their origin in the network. However, the precise detection and identification of origin is constrained by limitations in observability and control mitigation approaches. The key factors are highlighted as:

- **System Observability Challenges:** Phasor Measurement Units (PMUs) are extensively utilized in power networks to provide synchronized phasor measurements of voltage and current in transmission and distribution systems. They play a critical role in applications such as WAMS, inertia control, and maintaining power network stability. The applications of PMUs have been widely reported for torsional or very low-frequency oscillations [14]. However, the rapid changes in power network topology have led to a corresponding evolution in network disturbances. Likewise, power network oscillations have grown more intricate, showing notable changes in their characteristics and frequency modes. Consequently, the complex SSCI displaying these modes exceeds the observability capabilities of the algorithms used in PMUs, making it particularly challenging to report within the network.

- **Accuracy and Fidelity of PMUs in Complex Oscillations :** PMUs are utilized to obtain synchrophasors and detect power network oscillations. Traditionally, they use DFT methods, employing advanced DFT algorithm variants to extract synchronized phasors. Recently, these algorithms have been applied to detect SSR oscillations, which typically occur below 25 Hz and are detectable with current PMU reporting rates. However, complex oscillations exhibit non-stationary frequency modes and inter-harmonic components, making detection more challenging. These oscillations have bandwidths ranging from 5 Hz to 100 Hz when modes are coupled, or up to several hundred Hertz when uncoupled. A method to estimate the super-synchrnonous mode coupled with subsynchrnous component has been reported in [15]. However, the performance of such methods significantly deteriorates Instantaneous Frequency (IF) the coupled modes are closely located and have inter-harmonic order. In such a case, the energy distribution of the frequency components is not uniform over the integral bins of discrete intervals and consequently leads to the picket fence effect. The picket fence effect can be mitigated for frequency components laying at integral bins by introducing different windowing functions, however this approach leads to several degradations in reporting the accurate amplitudes for the modes of interest. In addition, appropriate selection of windowing function leads to further complications for time-varying modes such as attenuation of signals, losing important information associated with signals at the terminals and computational complexities. Therefore, the accuracy and readiness of DFT and its variants are significantly affected by the complex SSCI and lead to erroneous estimation and reporting of modes. As a result, this opens up a new research opportunity to more transparently analyze the most advanced discrete Fourier transform (DFT) methods for time-varying oscillation modes and to outline their limitations, ultimately suggesting alternative approaches.

- **Time-Frequency Analysis and Constraints on Accuracy**:
  To alleviate the constraints associated with the optimal estimation and precise reporting of frequency components, the SWMUs have recently been reported meeting the criteria for high resolution and high bandwidth to cover a wide range of frequency components [16,17]. Consequently, this approach is considered as an alternative to DFT and its variants, and academic/research community significantly emphasize for its adoption for procuring complex information from the wide range of frequencies associated with power network disturbances [18,19].
  The Time Frequency Analysis (TFA) approach is a significant and systematic methodology to analyze the time-series data in the time-frequency domain. This method offers intrinsic insights into non-stationary complex signals by allowing the estimation of IF and its amplitude, all represented over time [20]. However, the conventional approaches adopted for TFA,

such as Short Time Fourier Transform (STFT) and continuous wavelet transforms, are constrained by the uncertainty principle, preventing them from accurately reconstructing signals in time and frequency simultaneously. Approaches such as reassignment methods where high-resolution Time Frequency Representations (TFRs) of the signals can be achieved by reassigning the coefficients of the signals, however, this lacks the ability to reconstruct the signal [21]. Consequently, an approach called Synchro-Transform (SST) is introduced [22] which enables the concentrated reconstruction of the signals with its coefficients. The application of this approach is reported for forced oscillations which have stationary and non-complex frequency components [23]. In the context of fast and time-varying signals, the reconstruction of the precise modes is constrained by the inability of SST to provide concentrated TFRs of the signals. This is due to the rapid dispersion of the signal's energy over TFRs, thus restricting the application of SST to signals with slowly varying IF. Consequently, this constraints the accuracy of revealing the time-varying modes in complex SSCI and affecting the post-process dependent on this modes. Therefore, in contrast to the well-presented methods in the literature for improving TFA to analyze the time-varying signals, no appropriate method has been reported considering the complex SSCI modes detection.

- **The Localization of Complex SSCI Origin in the Network:**
  The oscillation source localization has always been an interest to the research community. This is mainly steamed by the factors that the power network dynamics are rapidly changing and so the construction of these oscillations is evolving as well. Previously, rigorous methods have been re-

ported to localize the source of oscillations in the network, however, this has only been limited to the torsional or forced oscillations in the network [24, 25]. An initiative to indulge both academia and industry were organized by the NASPI in an effort to make a concrete consensus on the detection and localization approach, however, the test cases were only limited to the forced oscillations and didn't even consider the simplest SSCI cases. However, for the simplest cases, there have been rigorous challenges with the source localization as reported in [25, 26]. The main concern associated with precise localization of the source is regarded to the accurate estimation of the frequency modes involved in the oscillations. There are several approaches discussing this widely in literature where an immediate focus is emphasized on the precise detection of these modes [27] These modes are specifically then utilized to approach the source localization in the power network. However, the industrial realization of the reported methods is constrained by the assumptions, realistically not achievable with the synchrophasors [28]. In a nutshell, the localization of the oscillation source relies on two main factors: first, on the estimation of intact modes of complex SSCI, and second, an online method to reconstruct system dynamics based on these estimated or detected modes. An intriguing gap here is that the reconstructed system dynamics should reflect the varying operating conditions of the network as this is in alignment with the inherent intermittent nature of the IBRs-based generation sources. Therefore, in the interest of finding the solution for this, there is a significant research gap to first reconstruct the exact dynamic helping in localizing the source and secondly, the dynamic should be based on varying operating conditions of the network to peruse the source localization with accuracy.

- **The Mitigation Strategy**

  The mitigation of complex SSCI is very important and strategic for the reliable and stable operation of the power networks. Several considerations are to be catered to while mitigating the power network oscillations. These include the modification at both generator as well as network side to support the network with deficit dynamics caused by the integration of renewable energy sources. Employing and integrating the power electronics based system components to solely react for damping the oscillations at the network side is an expensive approach. Several methods are provided to damp these oscillations at the generator side as provided in [29], [30], [12], [31], however these are explicitly relying on prior information of the system dynamics. Most of these approaches employ different type of filters tuned at specific frequencies based on prior system dynamic studies and only provides performance for the specific range. However, the complex SSCI is explicitly related to system varying operating conditions and the frequency modes are changing for the same system with different operating conditions. Therefore, relying specifically on these approaches is potentially challenging for the stable operation of the network. This identifies a significant research opportunity to investigate the state of the art control method and provide an explicit cost-effective solution that is adaptive to all operating conditions of the network and provide independent performance regardless of changing system dynamics and complexity.

Motivated by addressing these challenges, significant efforts have been devoted in this thesis to develop a systematic and diagnostic approach for complex SSCI. The efforts are underpinned by several steps for identifying, assessing, and analyzing the core limitations of the state-of-the-art reported for detection, localization, and mitigation. Sequential limitations regarding the observability constraints are provided through detailed mathematical analysis followed by employing state-of-the-art methods for detection. A novel approach using SWMUs is provided removing the barriers of observability constraints. Significant research has contributed to the improvement in accuracy and efficacy of the method employed for the detection. A novel method for localizing the source is developed, employing for the first time the complex SSCI modes for online reconstruction of the system admittance at varying operating conditions. This led to the latest approach in literature providing a complex SSCI-based power flow in the network identifying the true source of disturbance in the network. Following the identification process, a novel control mechanism is developed providing more robust and adaptive performance with higher fidelity than the conventional one proposed in the literature.

1.3 Research Contributions

This thesis contributes the following aspects towards the existing body of knowledge:

- Complex SSCI are formulated by firstly providing an in-depth knowledge on the evolution of oscillations in the power network. A precise assessment of the quantification of oscillations and the emergence of complex SSCI is provided by comparing the state-of-the-art literature. A definite consensus on participant involvement and observability bandwidth is summarized through a comparative analysis of the literature. A comprehensive review is constructed on system analysis methods for oscillations detections following by a detailed analysis of detection methodologies and their applicability. In addition to that, through thorough analysis, an emphasize on an alternate approach is provided removing the barriers for constrained observability. Finally, a strong foundation is provided by reviewing explicit literature for the mitigation of oscillations in the network and open challenges for detection, localization and mitigation are provided. The more in-depth comprehension is provided in **Chapter 2.**

- A detailed modeling of the WTG is carried out by first deriving a full-order model of the WTG. The model is simplified to obtain a reduced order model of the grid-connected WTG and detailed mathematical analyses are carried out to reflect the effect of control dynamics. This mainly includes the effect of PLL, control loops with faster and slower dynamics corresponding to current and DC bus voltage dynamics, respectively. The respective mathematical models are used to establish the stability criteria and provide the necessary conditions for which the violation leads to the occurrence of the SSO. Finally, detailed analysis followed by mathematical derivations are provided explaining the dynamic effect of participants violating the stability conditions and leading to the complex SSCI based SSOs. Further details providing the foundational argument for the occurrence of complex SSCI is provided more elaborately in **Chapter 3.**
- Using the foundational arguments emphasizing that complex SSCI are a

consequence of the control interactions in the network, the observability constraints for their detection using synchrophasors are provided through mathematical derivations. Firstly, it is analytically derived that the synchrophasors based approach lacks the ability to estimate the correct modes of oscillations. Secondly, a state-of-the-art sliding DFT is employed to verify the observability constraints for complex SSCI modes detection. This is persued by a test case where SSCI is triggered by the resonance due to the line compensator leading to complex SSCI modes.

Based on the foundational research findings, an alternate approach using SWMUs is proposed where the detailed information of complex SSCI is presented in the time-frequency domain. However, the accuracy of such methods is constrained by several factors such as the inability to retrieve the accurate coefficients, reassignment issues leading to inaccuracy, and instantaneous frequency misalignment for digital implementation. Therefore, to make it robust and adaptive for precisely reporting the complex SSCI modes, firstly an adaptive windowing function is provided to enhance the resolution. Secondly, to facilitate the precise reconstruction, a novel instantaneous frequency based realignment methodology is developed to retrieve the coefficients.

Leveraging the coefficients of complex SSCI, a unique approach is developed using mathematical analysis to derive the admittance model at the Point of Connection (PoC). The model leverages the online coefficients obtained for varying operating conditions and is adopted to constitute a complex SSCI-based power flow. The unique approach identify the participant source of oscillations by its behavior for absorbing/injecting active/reactive power into the network. This behavior provides significant evidence of highlighting and localizing the active participant for oscillations in the network. The details methodology is derived in **Chapter 4.**

- To demonstrate the robustness and effectiveness of the proposed approach, the detection and localization method is validated through three main cases. First, to ensure the adaptivity and robustness of the proposed method against time-varying and noisy signals, mode detection is tested using synthetic signals. Second, it is crucial that the proposed method be applicable to real grid scenarios. Therefore, the mode detection approach is further validated using real-world data from the northwest China grid. Finally, the overall detection and localization mechanism is analyzed with a real-world dynamic system by developing Electromagnetic Transient (EMT) models of the ERCOT south-region network. The detailed analysis of the test cases and description of the studied systems is provided in **Chapter 5**.
- While numerous control methods have been proposed to tackle the power system oscillations, fictitious variation in damping using dq-based control of WTGs is seen as both cost-effective and dependable. Nevertheless, such methods are dependent on the prior knowledge of SSCI frequency modes and their effectiveness diminishes when the SSCI-oriented oscillations contain non-stationary and complex frequency modes. To enhance the WTGs control performance adaptive to diverse oscillation modes, this work proposes a single-layer feed-forward-based control approach, where the damping of WTG is fictitiously strengthened by the adaptive mechanism of Generalized Hebbian learning algorithm integrated into the dq vector control of WTG.

The proposed method dynamically reacts to any SSR or SSCI occurrence and adjusts the WTG impedance to forestall oscillation initiation within a finite time. Through simulations and diverse test cases, the effectiveness and feasibility of the proposed method are demonstrated, marking its potential for real-world applications for the first time. The detailed analysis of the proposed method and test cases highlighting its efficacy is further elaborated in **Chapter 6**.

1.4 Thesis Overview

This thesis focuses on the complex SSCI emerging as a consequence of changing dynamics in the grid and initiated by the SSR and power network disturbances. The thesis aims to provide a systematic and diagnostic approach for complex SSCI detection, localization, and its mitigation. The structure of the thesis including the literature, novel contributions and conclusions, is organized in seven chapters. The summary of the thesis is provided as:

- **CHAPTER 2** provides a brief introduction to the power network oscillations. By comparing the state-of-art literature, a precise assessment of the quantification of oscillations and the emergence of complex SSCI is provided. Through comparative analysis, a clear consensus on participant involvement and observability constraints is discussed for complex SSCI. This is followed by a comprehensive review constructed on state-of-the-art methodologies for analyzing power network oscillations using existing methodologies. Finally, an in depth comprehension on the mitigation approach and the associated open challenges is discussed.

- **CHAPTER 3** is based on the comprehensive mathematical modeling of the WTG connected through a series compensated lines to the grid. Firstly, a detailed model of the WTG is derived and simplified to obtain the reduced order model of grid-connected WTG. The control dynamics with both with faster and slower time scale are derived including the effect of Phase Loop Lock (PLL) control dynamics. Following the comprehensive mathematical derivation, further discussions are provided on the violation of stability criteria leading to the escalation of complex SSCI.

- **CHAPTER 4** provides a detailed analysis of the complex SSCI by firstly providing the mathematical derivations on the constraint measurements of DFT based reporting for complex SSCI. To justify the arguments, state-of-the-art sliding DFT is employed and analysed with complex SSCI modes in the simplest possible case to illustrate the limitations of DFT. Next, the proposed method, Adaptive Instantaneous Frequency-based Synchro-Transform (AIFST) is mathematically derived, discussing the constraints related to adaptivity to noise and time-varying modes. The concept of adaptive windowing is proposed, along with modes of reconstruction with enhanced accuracy through an instantaneous frequency realignment method. Finally, the chapter provides detailed mathematical analytics of the complex SSCI mode-based power flow, preceded by the online admittance model constructed for varying operating conditions, concluding the source localization.

- **CHAPTER 5** is comprised of a comprehensive analysis of the proposed method with both simulations and real-time grid data. First, the detection methodology is verified through synthetic data strictly illustrating the complex SSCI with time-varying modes coupled frequency modes, corrupted with significant noise to demonstrate applicability to the real grid data. Next, the accuracy and precision of the proposed method are compared against state of the art methods illustrating promising results. The validation is further assessed with real time grid data obtained from the North China grid demonstrating SSCI phenomena. Further to that, the EMT model of the ERCOT network is developed and modified with the control loops as discussed in the previous chapters. The test cases first replicate the SSCI event occurred in the ERCOT network and then network parameters are updated resulting in low SCR at POI to challenge the control algorithms. Consequently, the localization method is verified by identifying the SSCI participants using the complex SSCI based power flow.

- **CHAPTER 6** is based on a detailed control methodology aiming to provide a comprehensive solution for the complex SSCI. This chapter is comprised of the mathematical model of the WTG, reduced to the impedance model representation. The chapter discusses in details the candidate of instability in WTG-based system and provides a comprehensive mathematical analysis of the Conventional Sub-Synchronous Damping Control (CSDC) elucidating its limitations for complex SSCI with time varying modes. Next, an adaptive Dynamic Virtual Impedance Control (DVIC) is proposed and its performance is compared to the state of the art optimal control derived from the state space model of the WTG. Finally, the EMT model of the ERCOT network is adopted to test the efficacy of the proposed method for complex SSCI mitigation. The detailed test cases are specifically illustrated to align with the latest grid code requirements and ensure that the amendments in the control mechanism doesn't affect the performance under dynamic grid conditions.

1.5 List of Publications

The research work in this thesis contributed to the following research publications, published in journal/articles and conference papers.

1.5.1 Journal Articles

[1] **T. Zaman**, M. Syed, Z. Feng and G. Burt, "A Realigned Instantaneous Frequency Approach for SSCI Oscillation Localization in Power Networks," in IEEE Transactions on Power Systems, 2024, doi: 10.1109/TPWRS.2024.3474177.

[2] **T. Zaman**, Z. Feng, S. Mitra, M. Syed, S. Karanki, L. Villa, and G. M. Burt, "ANN Driven FOSMC Based Adaptive Droop Control for Enhanced DC Microgrid Resilience," in IEEE Transactions on Industry Applications, vol. 60, no. 2, pp. 2053-2064, March-April 2024, doi:10.1109/TIA.2023.3328577.

[3] A.Issah, **T. Zaman**, M. Syed, H. Yue, G. Burt and M. S. E. Moursi, "Linear Parameter varying model predictive control of a Wind Energy Conversion System" in IEEE Transaction on Sustainable Energy, 2024, doi: 10.1109/T-STE.2024.3512997

[4] **T.Zaman** et al., "A Finite Time Dynamic Virtual Impedance Control for

SSCI mitigation in IBRs Dominated Network." in IEEE Transaction on Energy Conversion, 2025 -*under review.*

1.5.2 Conference Papers

[5] **T. Zaman** et al., "Multimode synchronous resonance detection in converters dominated power system using synchro-waveforms." in 27th International Conference on Electricity Distribution (CIRED 2023), 2023, pp. 3620–3624

[6] **T. Zaman**, Z. Feng, M. Syed and G. Burt, "Mitigation of SSCI-Driven Complex Oscillations using Dynamic Virtual Impedance Based Control," 2024 IEEE Power & Energy Society General Meeting (PESGM), Seattle, WA, USA, 2024, pp. 1-5, doi: 10.1109/PESGM51994.2024.10689206.

[7] **T. Zaman** et al., "Endurance Driven Energy Management System for All-Electric Marine Autonomous Surface Vehicle," IECON 2022 – 48th Annual Conference of the IEEE Industrial Electronics Society, Brussels, Belgium, 2022, pp. 1-6, doi: 10.1109/IECON49645.2022.9968947.

[8] A. Babagana, **T. Zaman**, Y. Seferi, M. Syed and G. Burt, "Comparison of Non-Communication based DC Load Shedding Schemes," 2022 57th International Universities Power Engineering Conference (UPEC), Istanbul, Turkey, 2022, pp. 1-6, doi: 10.1109/UPEC55022.2022.9917898.

1.5.3 Contribution to Professional Working Groups and Projects:

- Member of the UK National Grid, Grid Forming Expert Committee.
- Member of the CIGRE Committee for Power Network Stability.
- **Research Project:** Endurance Driven Autonomous Ocean Drone Energy Management System.
- **Research Project:** Coordinate Control for enhanced Grid Stability

Chapter 2

Complex Oscillations in IBR-Dominated Networks

2.1 Introduction

The increased concerns about environmental protection and an emphasis on meeting the energy demands using green energy have sparked a paradigm shift for harnessing energy from non-conventional power sources, such as wind and solar. Whilst many countries increased their energy capacity through environment-friendly sources, significant growth persistently emerged in countries and regions like USA, Europe, and Asia, resulting in a total capacity of 1.63 Terawatt (TW) from RES sources [32]. Amongst these, China has been at the top with 1.63 Terawatt (TW) of RES capacity, following the USA with 352 GW, and other countries proportionally. Countries such as Scandinavia and Great Britain further promise this commitment towards sustainable and environment-friendly energy production, where 2035 aims for a complete transition towards net-zero energy. In a nutshell, there has been an enormous increase in the transition of energy from conventional sources to CO_2 emission-free and is targeted to increase further shortly [33].

This frequent proliferation of RES in power systems has been enabled by technological advancements in power converters, enabling a reliable and convenient integration of these highly intermittent power sources, specifically wind and solar. These converters aim as a backbone for modern power networks retrofitting the transmission, distribution, and power dispatch. For instance, the VSC are equipped with passive network components to improve the flexibility and stability of the transmission networks [34]. Similarly, whilst the inverters and MMC are employed for PV and HVDC applications, variants of power converter topologies are extended for integrating wind generation into the grid. Not only does integrating these energy sources necessitate power converters, but careful consideration must also be given to the corresponding control methodologies [7]. Therefore, as long as the frequent proliferation of RES in power systems has greatly helped in reducing the dependency on conventional power sources, the paradigm transition to IBRs has significantly posed great challenges to the power system stability -amongst which, the power system oscillations are of great concern [35]. These oscillations in a power network have a transition from conventional SSO to super-synchronous (SupSR) and complex oscillations, amplified by the abundant integration of non-conventional energy sources through power converters. Therefore, this chapter will briefly explain the evolution of the complex oscillations in the context of the IBRs-dominated network. The overview of the network-dependent oscillation mechanism is explained further by providing a general overview of the methods to examine the oscillations.

2.2 Evolution of Complex Oscillations

The earliest analysis of SSO in a power network emerged in 1937 by taking into consideration the series-compensated transmission line [36]. A growing trend of oscillatory current was observed in the network, which is comprised of a transmission line with a series of compensated capacitors and a synchronous generator (SG) connected at the sending end of the line. The frequency of such oscillations was observed below the nominal frequency of the system (60 Hz), and thus it was referred to as SSO. The post-study analysis of the event suggested that the problem is an analogy of the electrical resonance in the system where self-excited oscillations are triggered at that sub-synchronous resonance frequency. At this frequency, the SG at the sending end of the transmission line forms a radial connection with the series-connected line capacitors mimicking an RLC connection. It is suggested that at the resonance frequency, the SG and series capacitors in such formation prevail negative resistance. This is normally referred to as the Induction Generator Effect (IGE) and is considered the main explanation for the growing oscillations in the system current.

When the first SSO event was reported for the network in the Mohave power plant in 1971, it was considered that the dynamics of the SG connected at the sending end of the transmission line interact with the series capacitors at the resonance frequency. At this frequency, the dynamics of the SG interact with the series capacitors, exchanging periodic energy between the SG and the system components. This type of phenomenon was mainly referred to as SSR as the oscillations consequently emerged due to the resonance interaction between the torsional system of the SG and the series compensated transmission line [37].

Following this incident, power network SSO was observed involving the torsional dynamics of the SG excited by the Power System Stabilizer (PSS) [38, 39], the control system associated with the governor [40], or the control system of power converters constituting the high voltage DC (HVDC) transmission system [41]. All of these early incidents were reported in the networks without series compensated transmission lines. These early investigations suggest that the power network components operating with the control system have implicit interactions with SGs leading to unfavorable dynamic conditions of the torsional system, thus inciting SSO in the network. Therefore, the SSO cannot be confused with the SSR-driven oscillations and can be explicitly regarded as a device-dependent disturbance intimidating network with voltage/current oscillations [42].

Over the last decade, there have been many SSO events reported as illustrated in Fig. 2.1. These explicitly indicate the interaction of power converters associated with WTGs and grid components [43]. An example of such events is reported from the networks well penetrated with the WTGs based WFs such as ERCOT network in Texas, USA, and Guyuan, North China. The early event reported by the ERCOT network had SSO frequency modes between 20-30 Hz. Various events on this network are mainly triggered by either the changing operating condition of the network or modification in topology. These varying conditions have either induced the control based oscillations when weak grid conditions are formed or SSR with the installed line compensators when network topology has changed [44]. Similarly, the double circuit 500kv series compensated transmission line connecting the far located WFs in the Guyuan network of North China has reported the modes of oscillations between 6-9 Hz [45]. In both of these networks, the type-III WTGs based WFs are employed to the rest of the grid through a long transmission line involving series compensations. From the case studies reported, it has been identified that the converters of the WFs are explicitly involved in such type of SSO under varying operating conditons, pointing to concerns on the control associated with these converters in the WFs. Therefore, wide literature refers to such type of events as SSCI based oscillations. These events are in alignment with the IGE problem associated with conventional SGs and the terminology can be referred to as for assessing the SSCI events with frequency modes below the nominal system frequency. The uniqueness in events as reported above is that either the series compensation, the dynamics of SGs or both of them are involved. This means that the concept illustrated for the interaction of SG torsional dynamics or IGE can best explain the events, provided that the system involves a single/aggregated generation unit connected through a series of compensated transmission lines to the grid. Consequently. this concept can be persued to study the SSO mechanism with a single generation unit modeled with grid.

Figure 2.1: Timeline of the remarkable SSCI events around the world

Conversely, several events are reported after the aforementioned incidents which prevail distinct oscillation modes. For example, in 2015, the Hami network which is comprised of several distinct types of inverter based generation sources experienced oscillations. This network consist of type-IV permanent magnet synchronous generators (PMSGs), HVDC links, and PSS. Before the event took place in the Hami network, it was considered that PMSGs are less likely prone to network instability and SSOs. However, the post event analysis perused in the literature suggests that the event is mainly comprised of SSO modes above the system nominal frequency [46]. Thus, the oscillations with such modes are named as super-synchronous (SupSR) oscillations. It is to be noted that all these events are reported by the PMUs having fundamental reporting rates as (30-120fps). The efficacy and fidelity of reporting such events through PMU with limited observability will be highlighted in the later sections. However, this leave behind some questions, which have attracted wide interest and great concern from the research community and industry as many new factors emerged in this case.

- Firstly, SSO modes above the nominal frequency exist, but are they independent or associated and coupled with another frequency?
- Secondly, If, PMSG were considered to be highly immune to instability and SSO involvement, how this configuration of WTGs can be involved in the Hammi network incident? The network also involved HVDC links, however, no intact confirmation of their association in oscillations is discussed in some cases. This takes a wider interest in the involvement of control configuration in triggering oscillations.
- Last but not least, all the cases are investigated with DFT-based mecha-

nisms, the basic principle of such algorithms is that the estimation is based on the nominal frequency. Therefore, there could be modes that behave as inter-harmonics and prevail non stationary nature. So, the cases need further investigation as PMUs are less likely to report such modes.

The evolution of the SSO mechanism is briefly summarized in Fig.2.2. From all these discussion and the hierarchy map as illustrated in Fig.2.2, there seems an interest of the exploration towards the mechanism of oscillations which have no definite origin. Recent studies have emerged in literature that points towards such oscillation as the modes are distinct and complex as compared to conventional SSO [47, 48]. The early analysis prevail that such oscillations exhibit similar consequences in voltage and current waveforms, however the frequency modes are non stationary in nature, may or may not coupled with other frequencies and could have bandwidth varying from several hertz to kilo-hertz. The exemplary studies suggest the consequence of such events as rigorous involvement of the control mechanism in IBRs, however no consensus on its definite origination has been made yet. Therefore, this put emphasizes on their investigation through a mechanism that can detect non stationary signals, intelligent enough to detect and differentiate the complex modes and localize the source in a wider network.

2.3 Mechanism and Quantification of Oscillations

The oscillation frequency in the power network varies widely. This ranges from a few hertz to several hundred hertz in the modern power network. The bandwidth of oscillation frequency evolving as a consequence of varying generation sources and network topology is illustrated in Fig. 2.3. Based on the network configura-

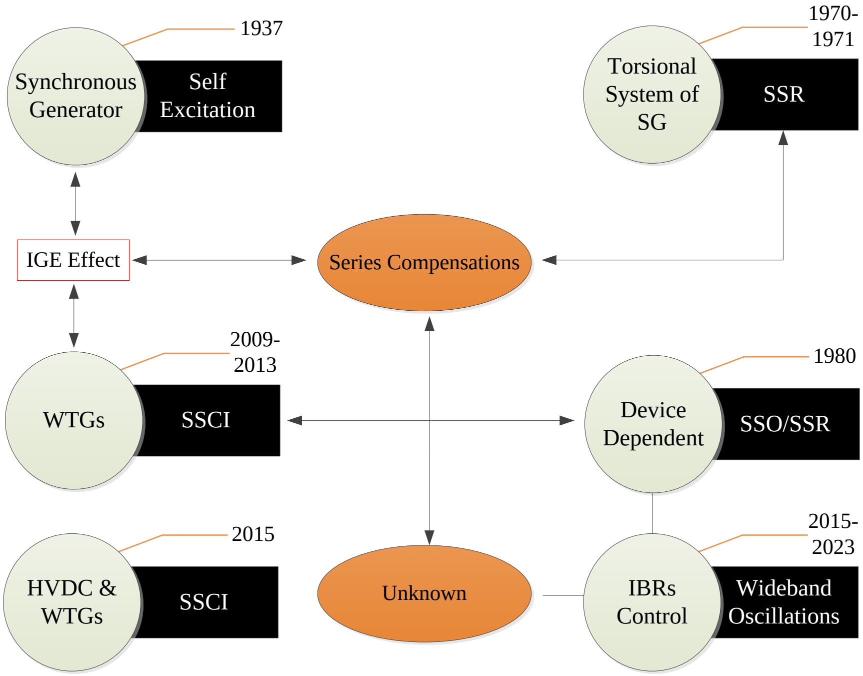

Figure 2.2: Evolution of complex oscillations

tion and type of generation source, the emerging oscillations may be categorized into low frequency , high frequency and complex oscillations. The low-frequency oscillation emerges as a natural characteristic of the power grid and generally varies between 0.1 Hz to 2.0 Hz. In between this range, both single-machine and inter-area oscillations are widely witnessed by the system operators. In single machine based oscillations, the periodic energy is exchanged with the network at 0.1-1.5 Hz by the control, prime-mover or excitation system of the generators with the local network components. In contrast, the generation sources oscillating against each other are generally reported for frequency modes of 1-2 Hz. Generically, the left half of Fig.2.3 depicts the conclusive illustration of low frequency oscillations. These mainly involve the exchange of energy between the power network components and the dynamics of conventional generators such as excitation and prime mover control. .

The nature of power networks is rapidly evolving with enormous penetration of power converter dominated generation sources. The mechanism of network disturbances and specifically nature of oscillations is getting complex as a result of this evolution. This specifically stems from the evolution in operating technology of these power sources as the topology of power converters and the switching mechanism explicitly varies for the type of generation sources. For example, the wind and solar when integrated into the power grid require an additional and substantial quantity of passive components for stable grid operation. These generation sources in addition to the passive network components forms a complex network involving inter-dependent controls explicitly reliant on the coordination of the various generation sources in the network. For instance, the dynamic con-trol of HVDC and VSCs often involves a fast current control loop in addition to the voltage control loop that operates with a lower bandwidth. The varying nature of such control mechanisms, in addition to the active/reactive power and PLL control, responds indistinctively to the power network disturbances. The net-work disturbances are here referred to as SSCI and SSR oscillations. Such types of oscillations become inadvertently challenging and adopt a complex nature. This complex nature usually stems as a consequence of distinct IBR's converters topology, control mechanism, and their interaction in the network when operating condition changes [49]. The range of such oscillations is shown in the right half of Fig.2.3, where the complex dynamics due to resonance, control, converters topology and network filters lead to new high-frequency stability and resonance issues, usually will be referred to as complex SSCI based oscillations in this thesis. The bandwidth of complex oscillations is mix, thus it include sub-synchrnous

(SubSR), super-synchronous (SupSR) and coupled frequencies in SubSR and SupSR bandwidths. The SubSR modes are the SSCI frequencies at which the IBRs or generation sources are exchanging the energy below the operating frequency of the network. Similarly, the SupSR modes have the frequencies above system nominal frequency and they may sometimes coupled with the SubSR modes. The origin of frequency coupling and complex SSCI is not intact, however the recent studies reveal their origination as a consequence of variation in control mechanisms, dynamic interaction between power network components and IBRs-based generation sources and explicit variation in the operating conditions of the IBRs-dominated power network leading to subsequent alteration in the network topology.

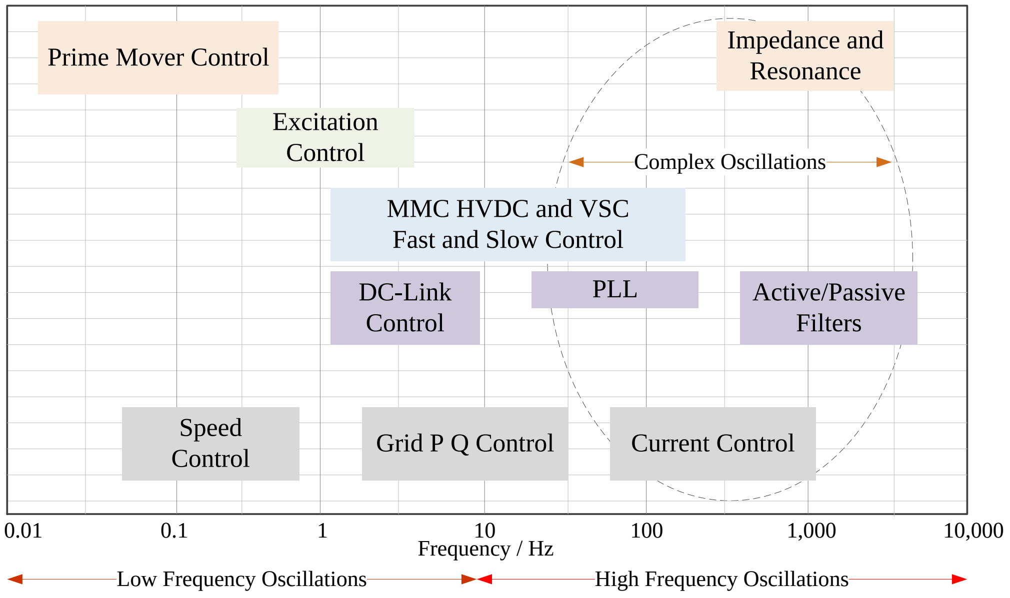

Figure 2.3: Overview of power network components and contribution to types of oscillations

2.4 Methods for Evaluation of System Oscillations

The oscillations in a power network can be classified into two basic categories i.e. The time and frequency analysis based methods. The time domain method is normally referred to as the modal analysis and is the most frequently used method for oscillations with known modes. However, if the modes of the oscillations are different from complex oscillations, the modal analysis prevails significant limitations, to be discussed in the later sections. The frequency domain methods normally includes the Damping Torque Analysis (DTA), complex torque analysis, and impedance model analysis. At this stage, only the basic methods are discussed.

2.4.1 Modal Analysis

Considering a power system, where the state ($\mathbf{X}$) of the system are represented by different dynamics such as, angle (δ_i) and speed (ω_i) etc of SG in a system. This system can be represented as,

$$\begin{aligned} \dot{x} &= f(x, y, u) \\ Z &= g(x, y, u) \end{aligned} \tag{2.1}$$

This set of systems can be linearized and represented with a MIMO system as,

$$\begin{aligned} \dot{X} &= \mathbf{A}X + \mathbf{B}U \\ \mathbf{Y} &= \mathbf{C}X + \mathbf{D}U \end{aligned} \tag{2.2}$$

Where, $X \in R^{n\times1}$ is the vector of state variables, $U \in R^{m\times1}$ is the control vector, normally referred as the inputs of the system, and the output vector is denoted by $U \in R^{l\times1}$. In addition, the matrix representing the states of the system obtained at normalized and equilibrium point is $\mathbf{A} \in R^{n\times n}$, $\mathbf{B} \in R^{n\times m}$ represent the control matrix, $\mathbf{C} \in R^{n\times l}$ is the output matrix, while $\mathbf{D} \in R^{l\times m}$ represent the forward matrix obtained at chosen inputs and the equilibrium point, respectively. Consequently, the system transfer function matrix can be written as,

$$H(s) = \mathbf{C}(s\mathbf{I} - \mathbf{A})^{-1}\mathbf{B} + \mathbf{D} \tag{2.3}$$

Where, $\mathbf{I_n} \in \mathbb{R}^{n\times n}$ represent an identity matrix.

The deterministic information about the system equilibrium point is synthesized through the characteristic equation obtained as,

$$\mathbf{det}|A - \lambda_i\mathbf{I}| = 0 \tag{2.4}$$

The solution of the characteristic equation in (2.4) for a system matrix $\mathbf{A}$ characterized at a specific equilibrium point provides the eigenvalues λ_i. The λ_i will be either the real or complex conjugate value, representing the system state, normally referred to as the modes. For the system matrix $\mathbf{A}$, the left and right eigenvector provides insights on the stability and can be obtained as,

$$\begin{aligned} \mathbf{A}\mathbf{v_i} &= \lambda_i\mathbf{v_i} \\ \mathbf{A}\mathbf{w_i}^{\mathbf{T}} &= \lambda_i\mathbf{w_i}^{\mathbf{T}} \end{aligned} \tag{2.5}$$

Where, $\mathbf{v_i}$ & $\mathbf{w_i}$ are any non-zero vectors, representing left and right eigenvectors; respectively. The modal matrix for the corresponding left and right eigenvectors can be written as,

$$\mathbf{V} = [\mathbf{v}_i \ldots \mathbf{v}_n] \text{ and, } \ \mathbf{W^T} = [\mathbf{W_i}^\mathbf{T} \ldots \mathbf{W_i}^\mathbf{T}] \tag{2.6}$$

Using this, the stability of the power system can be illustrated as,

$$\begin{aligned} \text{forall } \ i \ldots n\,, \zeta_i = \lambda_i \zeta_i + (\mathbf{WB})_i \mathbf{U}, \text{ with;} \\ (\mathbf{WB})_i \rightarrow i^{th} of (\mathbf{WB})_i \end{aligned} \tag{2.7}$$

The general solution for (2.7) in terms of eigenvalues can be written as,

$$\lambda_i = \sigma_i \pm j\omega_i \tag{2.8}$$

The (2.8) provides the solution for the system matrix $\mathbf{A}$ such that the stability of the system is prevailed by the number and location of eigenvalues. If $\sigma_i \in \mathbb{R}$, there are no oscillatory modes in the system. If λ_i is a conjugate value, this corresponds to the oscillatory modes. From (2.8), following relation can be interpreted,

$$\begin{aligned} &\text{Mode: } \lambda_i = \sigma_i \pm j\omega_i \\ &\text{Frequency of modes: } = \frac{\omega_i}{2\pi} \\ &\text{Damping: } = \zeta_i = -\frac{\sigma_i}{|\lambda_i|} = -\frac{\sigma_i}{\sqrt{\sigma_i^2 + \iota\omega^2}} \end{aligned} \tag{2.9}$$

This means that, if the eigenvalues for $\mathbf{A}$ are on the left-hand side of the complex plane, the system is stable. If the eigenvalues for $\mathbf{A}$ are on the right-hand side of the complex plane, the system is unstable. Any values on both sides of the complex plane determine the marginal stability of the system and vice versa. From (2.6) and (2.7), for any i^{th} oscillatory mode, the v_{ji} and w_{ji} are the element of $\mathbf{v}_i \in R^{n\times 1}$ and $\mathbf{w}_i \in R^{n\times 1}$ in the j^{th} and i^{th}, rows; respectively. From this, the association of the j^{th} state variable with the i^{th} oscillatory mode can be determined by the participation factor as follows,

$$PF_{jk} = \frac{|v_{ji}w_{ji}|}{\sum_{i=1}^{K} |v_{ji}w_{ji}|} \tag{2.10}$$

Using (2.6) and (2.7), the decomposed model of the original system as represented in (2.2) can obtained. This denote the equivalent transformation by letting $\mathbf{Z}$ as a new state variable vector and equivalent of (2.2) can be written as,

$$\begin{aligned} \dot{Z} &= \mathbf{\Lambda} X + \mathbf{W^T B} U \\ \mathbf{Y} &= \mathbf{CVZ} + \mathbf{D} U \end{aligned} \tag{2.11}$$

Where, $\Lambda = \text{diag}(\lambda_i) \in \mathbb{C}^{n\times n}$, and can be shown that $\mathbf{V}$ and $\mathbf{W}$ are orthogonal. From (2.11), it can be observed that the transformation does not affect the stability of the original system. Therefore, using (2.7), the decomposed model of the system can be obtained as shown in Fig.2.4 and the residue matrix can be obtained as follows.

$$\mathbf{R} = \mathbf{BCVW^T} \tag{2.12}$$

The obtained residue matrix refers to the conventional method that can be modified and used in positive and negative feedback loops to tune and modify the eigenvalues of the system and the corresponding poles of the system can be molded towards the right half plane.

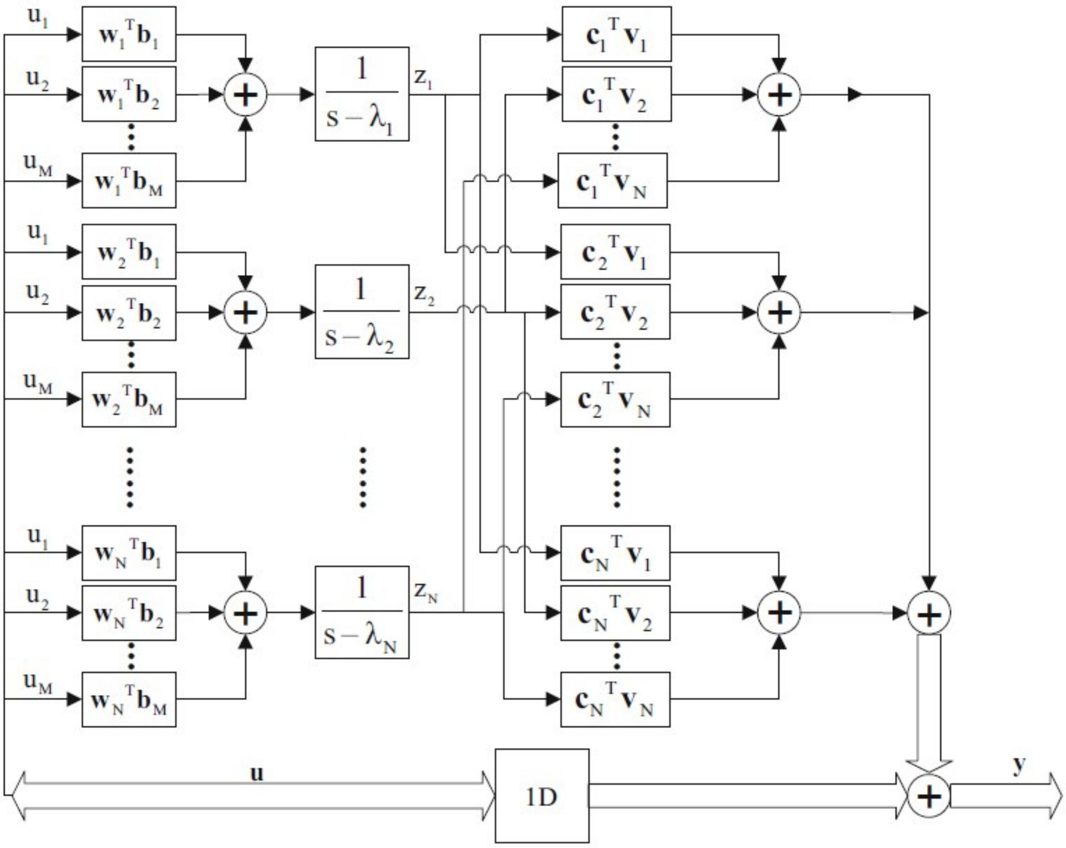

Figure 2.4: Representation of system space model through block diagrams of modal decomposition

2.4.2 Damping Torque Analysis

The DTA method is considered to be a valuable tool for assessing the damping stability of the system . The method is tailored for a single-machine infinite bus power system and has proven its feasibility for low-frequency oscillations concerned with single-machine networks. The mechanism is applied by measuring overall torque contribution from the network stabalizers such as PSS or Flexible

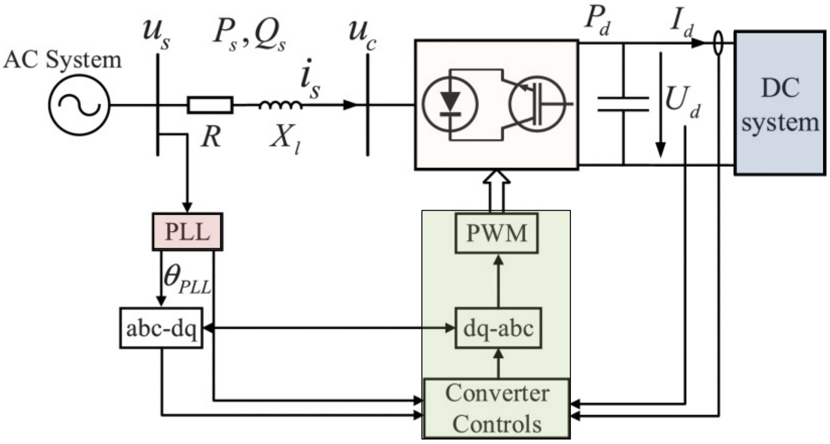

Figure 2.5: Representation of single machine VSC connection as PSS with AC system

AC Transmissions (FACTs) devices, and their overall impact on mitigating the oscillations are analyzed.

Considering a single machine network as shown in Fig.2.5, the (2.2) can be written for such network as [50],

$$\begin{bmatrix} \Delta\dot{\delta} \\ \Delta\dot{\omega} \\ \Delta\dot{Z} \end{bmatrix} = \begin{bmatrix} 0 & \omega_0 I & 0 \\ A_{21} & A_{22} & A_{23} \\ A_{31} & A_{32} & A_{33} \end{bmatrix} \begin{bmatrix} \Delta\delta \\ \Delta\omega \\ \Delta Z \end{bmatrix} + \begin{bmatrix} 0 \\ B_2 \\ B_3 \end{bmatrix} U_d \tag{2.13}$$

Where, the system states are $\dot{\mathbf{X}}^{\mathbf{T}} = [\Delta\dot{\delta}\ \Delta\dot{\omega}\ \Delta\dot{Z}]$ showing the power angle, generator speed and state variables of the VSC and generators, respectively. U_d is the control input representing the deviations in the $\mathbf{Y}$ vectors and adjusting it using the compensator $K(s)$. Thus this can be written as $U_d = K(s)\Delta\mathbf{Y}$, where $K(s)$ is the transfer function of compensation control tuned for specific λ_i at ω_s. Thus, the input of the system can be a complementary damping controller, which can be written as,

$$\Delta\mathbf{Y} = C(s)\,[\Delta\delta \;\; \Delta\omega \;\; \Delta Z]^T \tag{2.14}$$

The process of DTA is generalized in Fig.2.6. Where $C(s)$ refers to the transfer function of the second-order SSO system. The $\Delta\mathbf{X}$ denotes the states of the power system changing due to SSO event and $k(s)$ is the compensation provided if the SSO is triggered. The status of the SSO and its risk can be determined from the system frequency.

Let $\omega_{sso} = 2\pi f_{sso}$, where f_{sso} be the frequency of SSO in the system, the system transfer function as a function of SSO frequency can be written as,

$$\Delta X(j\omega_{sso}) = \; [\Delta X(j\omega_{sso})] + \Im\,[\Delta X(j\omega_{sso})] \tag{2.15}$$

The symbols $\Im$ denote the real and imaginary parts of the complex plane obtained for (2.15). From (2.15), the positive value of $\Im$ part indicates a stable system and no risk of SSO, while $\Im\,[\Delta X(j\omega_{sso})] < 0$ indicates the SSO associated with SSO components. It should be noted that the DTA approach requires prior information on the SSO frequency modes, so the compensator (k(s)) can be tuned accordingly and the SSO can be mitigated. Therefore, the accuracy of the approach is highly dependent on the estimation of frequency modes in the SSO event. In addition to that, the transition of DTA to a larger network encompassing a multi-machine power system introduces considerable complexity. Even in scenarios as straightforward as examining power oscillations along specific transmission lines like tie lines, the extended application of DTA presents challenges. This complexity stems from the necessity to consider contributions from numerous generators, thus magnifying the intricacy of DTA when applied

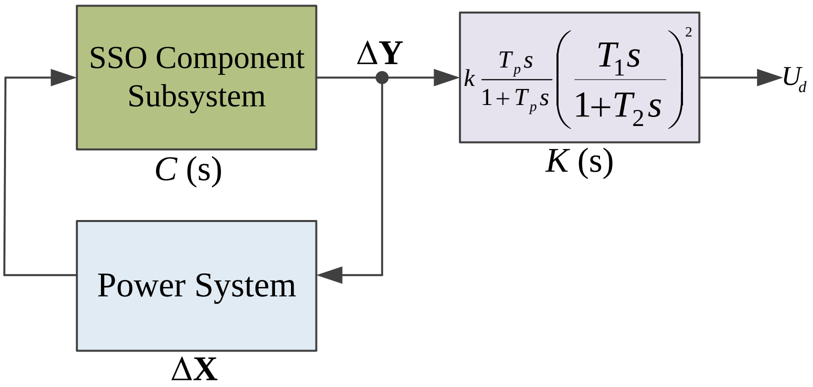

Figure 2.6: Block diagram of damping torque analysis approach

within multi-machine power systems.

2.4.3 Impedance Modal Analysis

The impedance model-based analysis has been widely used to assess the stability of the power network. The approach is generally used by simplifying the aggregated impedance of two sub-systems connected at any node in the network. An example of such a system is illustrated in Fig.2.7a, where an aggregated and simplified WTG is connected with a weak AC grid through the transmission line. This network model is deduced to an interconnected and simplified model as displayed in Fig.2.7b. For instance, Z_w is the transfer function of the WTG system representing the key relations associated with SSR and SSCI. Whereas, Z_G is the transfer function of the rest of the power system. This configuration provides a simplified yet adequate representation of the interconnected system for determining the nodal voltage (Δv_i) and current (Δi_i) with SSCI and SSR modes. The nodes (i, j) represent the point of common coupling (PCC) where the WTG and the rest of the power network are connected. For instance, the simplified relation for voltage and current can be deduced for a single node from Fig.2.7c as,

$$\Delta V = Z_W(s)\Delta i \tag{2.16}$$

$$\Delta I = Y_G(s)\Delta V \tag{2.17}$$

Where, $Y_G(s) = \frac{1}{Z_G(s)}$. Using (2.16) and (2.17), any SSR/SSCI modes can be examined using frequency spectrum analysis such that the obtained measurements qualify the Nyquist criteria for assessing the modes of interest. Once the SSR/SSCI modes are obtained from the voltage and currents obtained at PCC, the impedance of the rest of the network and WTGs (source) can be examined at that particular frequency. The generalized characteristic equation for the impedance can be obtained from Fig.2.8 as,

$$1 + Z_W(s)Z_G(s) = 0 \tag{2.18}$$

Therefore, the relation in (2.18) at a given frequency can be utilised to evaluate the system's stability. It is worth emphasising that frequency assessment plays a crucial role in identifying the precise modes, since both the impedance and stability of the system are directly dependent on them. At this stage, it becomes clear that a single-generator mechanism is no longer sufficient. Hence, an adaptive impedance model is needed, as multiple generation units with diverse control strategies are now involved.

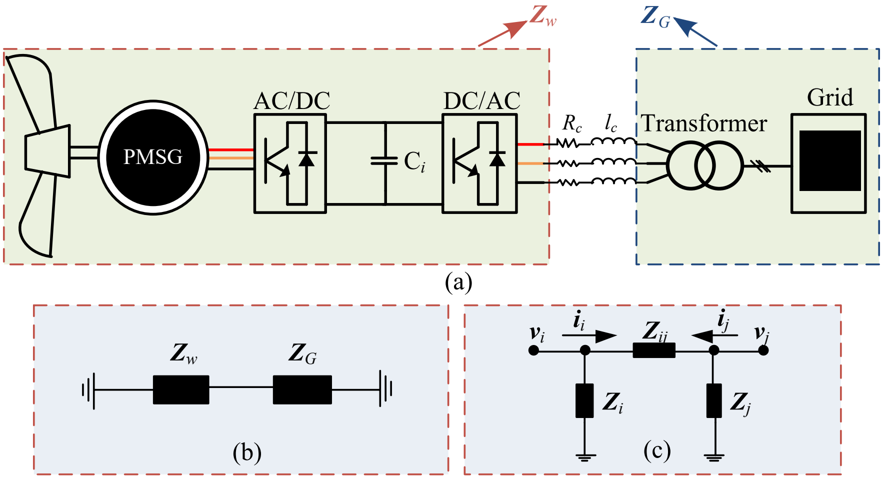

Figure 2.7: Schematic of type-IV WTG connection to grid through a transmission line.

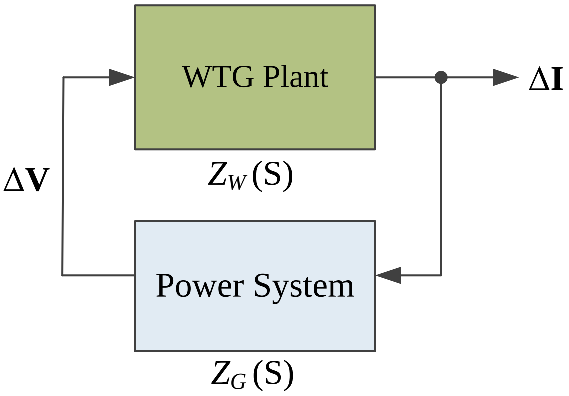

Figure 2.8: Block diagram of impedance modal analysis

2.5 Existing Methods of Detection

It is well known that stability of the power system, specifically related to the generation sources has been critically analyzed with well established methods, such as DTA and modal analysis [51,52]. These approaches are also frequently adopted to analyze the risk of oscillations in the power networks. However, these methods have limitations such as either identifying the stability points for a single operating point or only applicable for stationary and very low frequency oscillations. The intermittency and randomness of REs cause significant variations in the operating conditions of the power system. Therefore, this becomes critically challenging to model the network for all operating conditions and subsequently analyze the system for oscillation modes with respect to different operating conditions. In addition to that, the oscillations related to the power converter-based sources exhibit non-stationary and time-varying frequency modes. Therefore, detection approaches utilizing existing tools which explicitly rely on the synchro-phasors make it explicitly challenging to obtain information about these oscillations and design the detection and mitigation approach for convenient damping. This is mainly because the synchrophasor-based approaches explicitly rely on the estimation of parameters based on the fundamental frequency and its integral components. Conversely, a high bandwidth approach independent of estimating the fundamental components is required to identify the specific modes in the power network and with the highest accuracy. This section provides a brief summary of the methods proposed in the literature to estimate the modes of oscillations using i) SPMUs and WAMS, and ii) SWMUs and the monitoring framework. In summary, the emphasis is provided on the adoption of the SWMUs and their applicability in the modern network based on the state-of-the-art and identified literature.

2.5.1 SPMUs and Application for Oscillations Detection

The synchrophasor has been widely adopted for power system applications such as dynamic monitoring, fault detection and control of large-scale power networks. The synchrophasor are nothing but estimated phasors at each node of the network synchronized widely to each other through well-known methods such as Global Navigation Satellite System (GNSS), Precision Time Protocol (PTC), or Network Time Protocol (NTC) etc. The PMUs adopting this technology are integrated to central Phasor Data Concentrators (PDC) through the mentioned communication protocols.One typical example of such configuration for a power network is illustrated in Fig.2.9. Another definition for such configuration is mainly attributed to WAMS, widely reported for applications such as dynamic monitoring, control, and modeling of large-scale power networks [16–18].

The application of synchrophasor technology for low-frequency oscillations detection [53], predication in wind power system [54], and deriving appropriate damping control [55] based on such monitoring system is well elaborated in the literature. Similarly, reports have demonstrated that synchrophasor-based WAMS, utilizing PDC, can effectively extract nominal characteristics of SSR as discussed in [56–58]. However, it is worth highlighting that the reported mechanism of estimating phasors is explicitly designed for estimating the fundamental components i.e. 50/60Hz. Any other component received at the input of SPMU such as inter-harmonics or super synchronous components is dealt with noise and is treated as unfavorable, affecting the correct estimation of fundamental phasors.

Many efforts are reported to eliminate the effect of harmonics/inter-harmonics so that the fundamental components can be estimated precisely. A similar approach is proposed for a conventional DFT to estimate the fundamental phasors in the presence of a wide range of frequency components referred to as noise and inter-harmonics [59]. However, applications like these consider the oscillation modes as noise and are suppressed to achieve the output performance in order to comply with the standards such as C37.118.1-2011 [60] and C37.118.1a-2014 [61]. Usually, the information processed through such methods and received at PDCs are further used for control actions associated with power network and generation sources. Therefore, the key information of the specific components is critically essential at each stage in order to ensure stability and reliability in the network. It is noted that the standard reporting rate of PMUs ranges from 50/60 frames per second (fps) to 120 fps. However, challenges remain in conveying intrinsic information, as these approaches typically rely on filtering out harmonic, interharmonic, and subsynchronous components. Therefore, in other words, the filtering and limited reporting rates constrain the observability of oscillations modes. These modes are significantly important to be estimated precisely so that further localization and mitigation measures can be taken [62].

2.5.2 SWMUs and their Application to Oscillation Detection

The transient conditions and disturbances which may cause discontinuous reporting of waveforms significantly deteriorate the reporting of phasors using synchrophasor-based WAMS. This is mainly due to the limited reporting rate

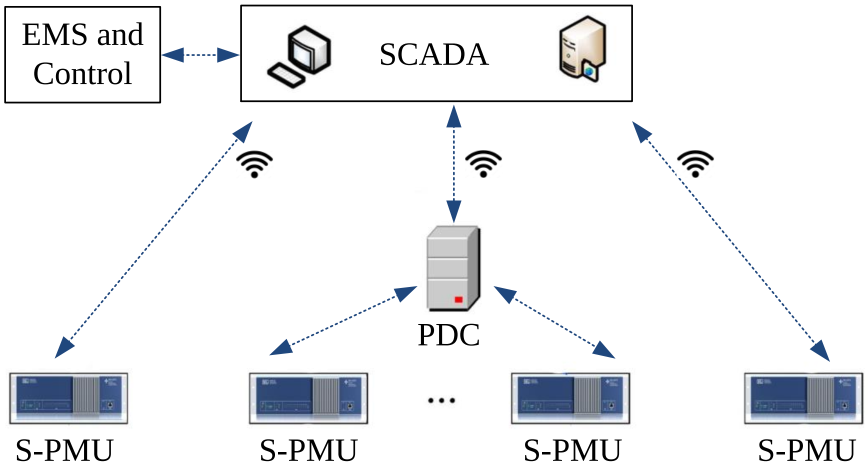

Figure 2.9: An example configuration of PMUs and PDC configuration for power network applications

and associated algorithms estimating the phasors, thus limiting the overall observability of the network for disturbances and/or modes of oscillations requiring wider bandwidth and precise sampling in order to report the accurate metrics of the oscillations.

The recently developed synchrnozied waveform measurement units (SWMUs), serve as valuable supplements for complex oscillations detection, localization and mitigation. Unlike PMUs which have constraints like low observability, limited reporting rate, dependence on filters, and latency, the SWMUs are high sampled synchronized signals data with time stamps. The emerging technology is adopted variously by different regions in the world foreseeing the potential of its applications.

Table 2.1 summarize the key regions where the SWMUs are adopted for difference applications. For example, continuous Point-on-Wave (CPOW) measurement devices reported from USA and Synaptec interrogators in the United Kingdom record continuous and synchronized waveform data [27,63]. In contrast, the other regions uses the waveform data for event-triggered applications and only process the data over a definite time period.

To meet the demand of modern power networks for enhanced observability against complex disturbances in the network, different methodologies regarding processing, storing, and transmitting SWUMs are extensively discussed in [64,65]. The major contributions are the academic community which has focused particularly on data pre-processing and storage techniques. For instance, [66] provides a resampling technique that employs filters, designed with window functions to accommodate varying sampling frequencies under different power system conditions, thereby optimizing storage efficiency. In [67], a SWMU capable of adaptively sampling synchronized waveform data at frequencies from 0.8 kHz to 12.8 kHz is introduced, applying higher sampling rates during transient states. Other resampling techniques, including B-spline interpolation [68], the Farrow structure [69], [70], polyphase FIR filters [71], and bandpass sampling [72], are also discussed for waveform resampling applications.

To distinguish between transient and steady-state conditions and adapt sampling frequencies accordingly, waveform discontinuity detection methods are essential. For example, [73] uses waveform similarity metrics to achieve this. Additionally, [74] introduces an adaptive sub-band compression technique for streaming synchronized waveform data, while [75] presents slipstream, a lossless compression method for such data. These techniques significantly reduce the communication and storage requirements for managing synchronized waveform data.

Similar to the WAMS, where synchro-phasors are integrated at PDC and the

Table 2.1: SWMUs and their Origin

Country	**Device**
Canada	Waveform measurement Unit [64, 65]
United Kingdom	CPOW device by Synaptec [27]
China	Synchronized waveform measurement device [67]
America	CPOW device [63]

PDC network is used for determining the power network operation, the SWMUs can be also integrated and utilized for the WAMS with higher observability and reduced constraints. Therefore, the waveform measurements collected by SWMUs are transmitted to the main station for various power system operation applications. The typical applications of SWMUs based WAMS system for the detection of power network oscillations are proposed in [76]. The proposed method leverage the synchronized waveform data typically available at both ends of the transmission line and uses an analytical approach to derive the parameters of the SSR event. However, this type of approach is only applicable to SSR which have stationary frequency components over a definite window length. Similarly, an effort to localize the source of SSR in power networks using SWMUs is reported in [77,78]. It is important to note that SWMUs are not limited to oscillation monitoring but are also applicable to other aspects of power system operation requiring extended observability. For instance, the authors in [79] propose a SWMU-based approach for situational awareness against high-frequency events in the distribution network. Similarly, the SWMUs based optimized high-sampled data obtained from different nodes of the power network is utilized to obtain the signatures for different events. These signatures are used for machine learning algorithms to train and identify the corresponding disturbance in the network [80, 81].

2.5.3 Open Challenges and Research Direction

Although, there has been rapid and rigorous work demonstrated on the SWMUs and phasors based WAMS in recent years, however, the identification and localization of complex oscillations remain open challenges, particularly with respect to defining and characterizing their fundamental nature. The question mainly stems from the latest developments in the control mechanism of IBRs and the penetration of power networks with the latest technology. Therefore, considering complex oscillation phenomena where the oscillation's frequency ranges widely from several Hz to kHz including the interharmonic components [82], it becomes explicitly challenging for phasors-based WAMS to detect these modes. This is because the observation window needs to be explicitly adaptive to accommodate all the frequency components. Therefore, this becomes explicitly challenging to optimize the window length for the oscillations modes varying rigorously with the operating conditions. The window length is one, but the other factors such as filters and their affect can be another research challenge to optimize the PMUs based WAMS for enhanced observability of network oscillations with complex dynamics. Also, the SWMUs based method is proven to be promising for fulfilling observability criteria, however the sampling rate would be higher and the reporting rate may correspond to several kHz. This could lead to a jeopardizing situation where handling such abundant data could become an open challenge. However, there have been many methods widely available on the methodology of sending compressed data to the central location and retrieving the accurate information, specifically for SWMUs as reported in [83–85].

Furthermore, it is vital to analyze the power network in accordance with the stability standards. It is widely known that the stability of a power network regarding oscillations is analyzed with a small signal model of the system. However, such cases are only applicable when the power network demonstrates its metrics for single operating conditions. Therefore, it is extremely difficult to demonstrate the stability of the network extremely penetrated with the IBRs of evolving technology and control mechanisms. An example of such cases is prominently the UK electricity market where significant drift towards REs is the target leading to explicit challenges such as integration of more inertial (GVA) resources etc as reported in the UK national grid [86]. Such type of latest integration primarily change the network topology and require significant alteration in the observability of the power system for reporting significant and complex phenomenons such as monitoring of wide-area complex oscillations [19]. Therefore, the limited observability constraints using PMUs-based WAMs make it significantly impossible to derive and provide an adaptive mechanism that can identify the complex oscillations and their modes for varying operating conditions. As discussed, the SWMUs based WAMS can be a significant approach for analyzing the system stability based on the varying operating conditions and adopting the power system operation according to those conditions [82]. Similarly, keeping in view the constraints of small signal stability analysis, the impedance based approach can be well adopted with precise information received through SWMUs-based WAMS system and impedance-based criteria can be applied to determine the unstable regions.

2.6 Existing Methods for Oscillations Mitigation

Power network oscillations are considered to be serious threat against network stability and reliability for modern power systems. Mainly, there exist numerous approaches for mitigating the power network oscillations, however; majorly the mitigation approaches can be categorized into system planning and operation, control and protection phases.

The system planning phase play an important role in mitigating the power system oscillations as the complex oscillations are mainly associated with the new interconnection integrated into the system. Therefore, it is explicitly important that the grid codes at the system planning level define stringent requirements to ensure the mitigation of such phenomenons in the network [87]. An example of this initiative can be learned from the UK and Australian energy markets, where considerable focus is to enhance the short circuit level (SCL) and inertia of the network. This is mainly motivated to be driven by the grid forming control (GFM), explicitly known for its inherent capability of mitigating network oscillations. However, an emphasized should be placed further on studying the complex oscillations and further amendments should be provided to enhance the stability of the grid regarding such issues. This way, the generators at the planning level can be bounded to provide a control mechanism able to suppress the networks oscillations, and specifically the complex oscillations in the network.

Similarly, the same jurisdiction can be applied to operators in order to update the mechanism in accordance with the evolution of the system topology and provide sufficiently appropriate algorithms for detecting and identifying complex oscillations in the network. The major contribution from an operational perspective is considered in the layover of efficient algorithms; for example, if oscillations emerge from a single wind farm (WF), the approach should be to localize and isolate the generators causing the oscillations rather than shutting down the entire WF. Conversely, the later approach can be integrated with the pre-installed generators and the vendors can be advised to update the control system of the pre-installed generators. However, this approach usually requires contract negotiations, etc. Similarly, the protection relay compliant to the complex oscillations need to be deployed by the generators and transmission owners for emergency protection.

The planning of system and protection levels primarily involves deploying new devices capable of injecting or absorbing power into the network to suppress or damp oscillations or isolate specific areas. However, as the mechanisms behind complex oscillations are predominantly associated with the control of generators within the power system network, this discussion will focus specifically on the active damping control mechanisms for asynchronous generators.

While the control methodology can be extended to other network components such as STATCOMs and reactors, using these devices solely for mitigating SSCI remains a costly approach [88]. Traditionally, the sources of complex oscillations in power networks have been attributed to asynchronous generators, which predominantly utilize VSCs or CSCs to provide controllable outputs.

Among the various types of asynchronous generation, VSC-based systems have been widely reported as significant contributors to power network oscillations, with wind generation systems being the most prominent sources of control-induced oscillations. As grid codes evolve to address stability requirements, the control mechanisms of these sources are also undergoing changes, leading to a notable increase in complex oscillations.

Therefore, this discussion will focus specifically on the control mechanisms of WTGs, their contributions to SSCI phenomena, and current research trends in addressing these challenges.

2.6.1 Control Mechanism of WTG

Conventionally, the type-3 and Type-4 wind turbine configurations are among the most widely used for large-scale grid integration. Type-3 employs a doubly fed induction generator (DFIG), which connects to the grid through a rotor-side converter (RSC) and a grid-side converter (GSC). Fig.2.10 illustrate the example of both types (type-3 and type-4) of WTGs based Wind Farms (WFs) connected to the grid via series-compensated transmission lines, respectively. The generic structure of the control is designed in the dq-axis reference frame. Generically, the GSC of the type-3 WTG is involved with controlling the DC link and stator terminal voltage. In contrast, the primary job of the RSC involves the regulation of electrical torque and reactive power on the stator side. In a nutshell, it is the WTG control system that actively indulges in the oscillations of the network as-sociated with WFs. Meanwhile, these oscillations can be mitigated significantly with different arrangements as proposed in [89]. It is important to note that the regulation of variables in RSC and GSC control primarily relies on propor-tional, integral, and derivative (PID) controllers. Consequently, modifying their parameters and evaluating the response through small-signal stability analysis has been shown to have a considerable impact on damping the subsynchronous SSCI modes, as discussed in [90,91]. In addition to that, the control loops in RSC

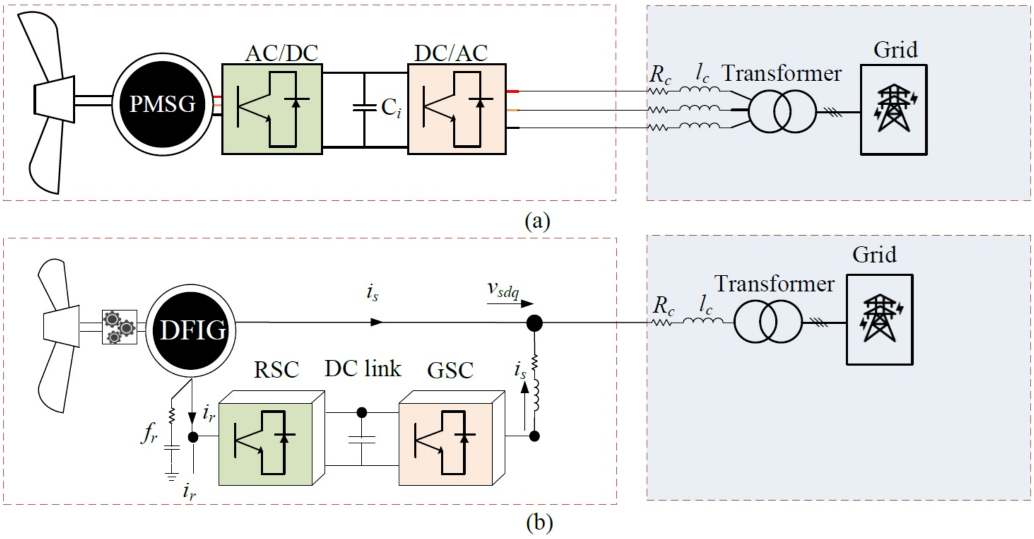

(a)

(b)

Figure 2.10: (a) Type IV PMSG based WTG, (b) Type III DFIG based WTG

of the WTG for torque and reactive power control have a significant impact on the escalation and deprivation of control based oscillations. It is shown that tuning the parameters for such variables can significantly deduce the risk of oscillations in the network [92]. Also, the authors in [93] propose an online approach where the WTG control parameters are varied based on detected synchronous modes. Other approaches considering the machine learning and stochastic approaches are reported in [94], where the WTG parameters are varied systematically to avoid the synchronous resonance in the network. Similarly, the response time of the controller is considered to have a significant impact on damping the SSCI based oscillations. A similar approach is being proposed by the authors in [95] where the rise time of controller is varied to improve the performance and mitigate the SSCI. It is incredibly acknowledged that control parameters have a considerable impact, however, all these reported methods haven't provided any reference to the relevance of satisfying the grid compliance for dynamics conditions such low voltage ride through (LVRT), high voltage ride through (HVRT) and stability for multiple fault events.

2.6.2 Modification in GSC Control

The structure and topology of the GSC in DFIG mimic the behavior of shunt-connected VSC. Thus, it provides an inherent capability of providing extra damping through appropriate control mechanisms and providing as similar behavior as a STATCOM [96]. Though the control modification in the GSC can provide extra damping, however, the overall stability cannot be guaranteed after system coupling. Similar approaches are reported in [30,97] by proposing an extra damping control loop to modify the voltage control loop for stator voltage on GSC of WTG. This is illustrated in Fig.2.11a, where the reference for the current control loop is modified by providing an additive damping control signal into the error generated by the stator voltage at GSC of the WTG. Conventionally, such modifications are only applicable for converters controls tuned at a single and specific oscillation mode. Therefore, to provide an extra flexibility for oscillation modes of different frequency range, multichannel damping controls are proposed in [98,99] as shown in Fig.2.11b. The main purpose of such an approach is steadily dependent on the system stability analysis and single operating condition. The control methodology is dependent on the pre-defined oscillation mode, and inject anti-phase current for that specific mode to damp the oscillation. Similarly, a reduced order state feedback control employing an arbitary gain and high pass filter is proposed by [8] and the modification can be observed in Fig.2.11c. The method also employ an LQR state observer estimating the state variable and adjust the output based on the deviations in the input reference as shown in Fig.2.11c. However, such type of methods are explicitly dependent on the system states requiring appropriate model reduction and making it mathematically complex to implement for a large-scale wind power systems.

It is important to highlight that the GSC control and its modification offer great flexibility for providing active damping control to mitigate the oscillations, however, the GSC provide limited flexibility in terms of changes for complex oscillations. The reason is twofold, firstly, the modifications are applicable for the stator voltage control loop and secondly, the damping capability is limited to a certain value of the nominal capacity [5].

2.6.3 Modification in RSC Control

Similar to the GSC control, the RSC control plays a pivotal role in the stability of the system and oscillations damping. The mechanism of modifying the RSC control provide similar behavior as damping stabilizers added into the excitation system of the conventional turbo generators. This is mainly achieved by increasing the damping at each oscillation frequency band and so the dynamic stability of the generator as well as the network can be improved. Similar to this mechanism, the RSC impedance can be modified using an appropriate control mechanism and thus understood as ”virtual impedance” to the grid adding extra resistance at the oscillations frequency and ensuring the stability [100].

The basic configuration of RSC control is illustrated in Fig. 2.12 where it plays a crucial role in the stability of the DFIG-based wind farm systems. In fact, the inner control loops designed to regulate the active and reactive power play a significant role in characterizing the oscillations specifically the SSCI-driven complex oscillations. The effective part of the impedance (resistance) comparing to the grid at the point of interface (POI) can be enhanced by amending the inner con-

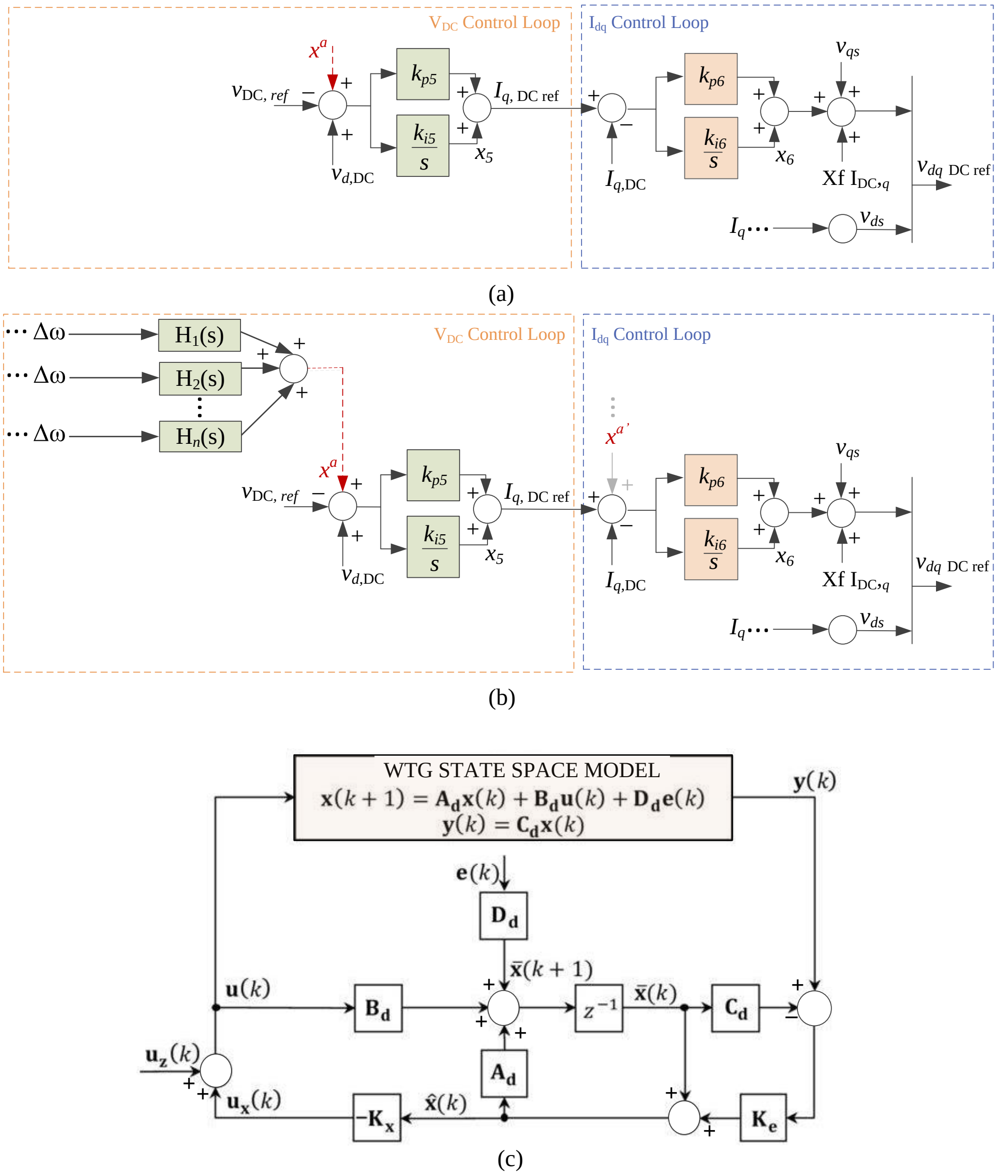

Figure 2.11: a) GSC q-axis loop modification with damping control, b) multi-channel frequency damping control with modifications in $q-axis$ voltage and current loops, c) state-feedback controller utilizing LQR as state observer.

trol loop at RSC. In fact, one approach is where a supplementary control signal is added into the voltage control to provide stabilize output for any deviations in the output caused by the oscillations [92,100]. Similarly, a subsynchronous damp-

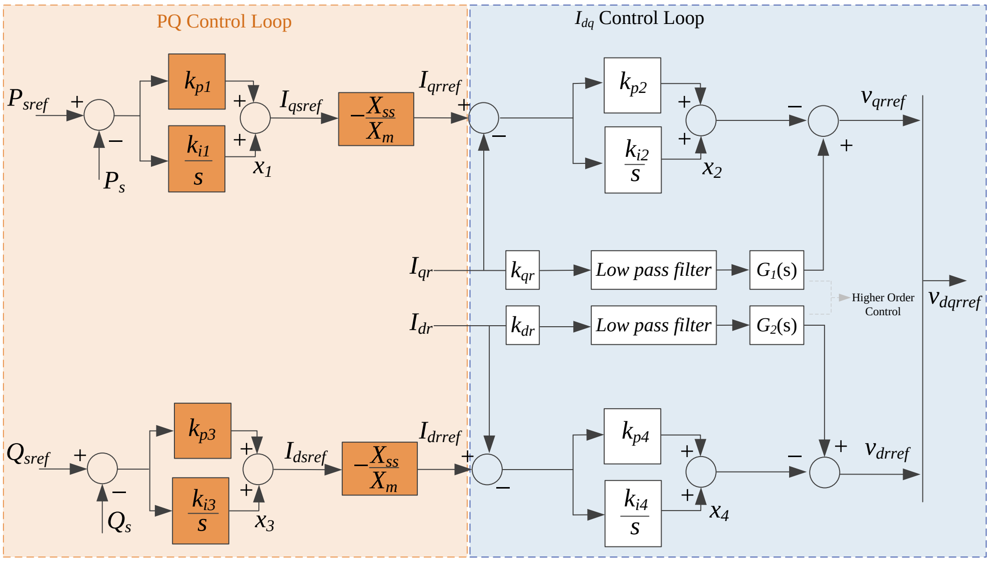

Figure 2.12: RSC control of DFIG

ing control is proposed in [13] where an optimal LQR control is used as a state observer for the locally available stator and rotor currents in the dq0-axis. The actual mechanism is proposed for the GSC stator voltage control and post-study analysis shows that the performance could have been enhanced if the observers are adopted for the output voltage loops in the RSC control. Additionally, filters based approaches are most frequently reported in the literature for damping the sub-synchronous and control induced oscillations [11, 31]. This include adding filters tuned at specific oscillation frequencies to the output of the voltage control loop driving the control input for the RSC control. A typical example of such an approach is illustrated in Fig.2.13 [11]. Typically, a bandpass filter is paired with a lead-lag compensator to generate an additional compensation signal corresponding to the filtered oscillation signal. The lead-lag compensator provides an anti-phase compensation to adjust the output signal and consequently provide

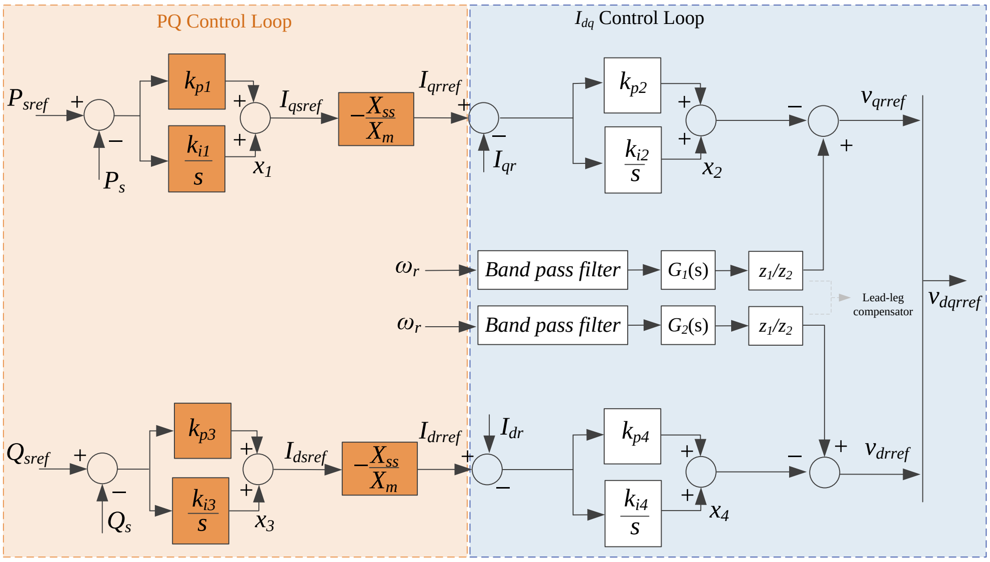

Figure 2.13: Band pass filters with lead-leg compensator for oscillations damping

active damping against oscillations. Similarly, a bandstop filter (BSF) based approach is proposed by the authors in [12], where the filters are specifically tuned to eliminate the subsynchronous components in the input signal. This approach is simple and require an optimal placement of the notch filters on the dq-transformed current loops. Several studies are reported in the literature regarding the optimal placement of notch filters as provided in [12, 29], thus suggesting its optimal placement in the d-axis inner controller providing control input as output voltage as illustrated in Fig.2.14. While the proposed methods are straightforward and cost-effective, as they do not require additional hardware resources or depend on system states, their applicability is limited to systems with a known oscillation frequency. SSCI-induced complex oscillations are heavily influenced by factors such as control mechanisms, network strength, operating conditions, and variability in constraints for intermittent power sources (VSC/CSC-based systems).

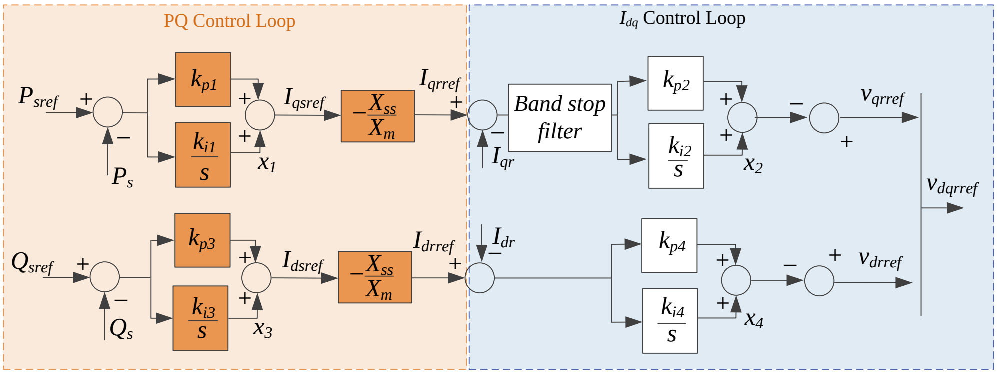

Figure 2.14: d-axis integrated notch filter based oscillations damping approach for RSC

Consequently, the oscillation frequency can vary within the same network under different operating conditions, making it particularly challenging to effectively deploy such filters in networks with dynamic operating conditions. Other approaches used for damping the SSCI include the partial feedback linearization (PFL) as reported in [9] and H-infinity based control given in [10]. These nonlinear control approaches provide significantly improved performance for different dynamic conditions, however, the performance of such is rigorously dependent on the system dynamics and its states. Non-linear control approaches that rely on optimization-based solutions often demand a deep understanding of mathematics for successful implementation, as well as an accurate model of the system to be controlled. It is crucial to note that the resulting controller is optimal only with respect to the defined cost function and may not align with conventional performance metrics, such as settling time or energy efficiency. Additionally, these methods typically struggle to handle non-linear constraints, such as saturation, effectively. Also, non-linear constraints such as saturation are generally not well-handled [101].

2.6.4 Open Challenges

A diverse range of SSCI control strategies has been reviewed in the literature, yet several challenges remain in developing effective and practical mitigation techniques:

Limited Access to WG Models: Most wind generator (WG) models are either inaccessible due to commercial confidentiality or insufficiently developed because of a lack of standardization and validation [102, 103]. This limitation prevents transmission system operators, utilities, and engineers from conducting subsynchronous studies during the planning stages.

Simplified Model Assumptions: For simplicity, simulation studies often assume that hundreds of WGs in a wind farm are identical and connected to a common bus. In reality, WFs may consist of diverse WG types and wind turbine control (WTC) strategies across various locations. As a result, the actual SSCI mitigation performance may differ significantly from the results obtained using these simplified models.

Lack of Practical Solutions: Most SSCI damping techniques discussed in the literature are theoretical and not tailored for practical implementation. There is an urgent need for straightforward strategies that can be easily applied in real-world systems.

Time-Varying Oscillation Frequency: SSCI oscillation frequencies vary over time, making it essential for mitigation schemes to account for this dynamic behavior. While some recent studies focus on tracking sub- and/or super-synchronous frequency components dynamically [104], [105], [106], challenges persist in simultaneously tracking fundamental and multiple sub- and super-synchronous components. Few studies have addressed the time-varying frequency aspect, which is critical for practical SSCI suppression techniques like adaptive filtering.

Dependence on Operating Conditions: SSCI is a global phenomenon influenced by factors such as the number of WGs in service, wind speed variations, and network topology changes. Mitigation strategies must be robust and capable of operating effectively across a broad spectrum of system conditions.

Addressing these challenges is essential to develop SSCI damping solutions that are both reliable and applicable in real-world scenarios.

2.7 Summary

This chapter provides the formulation of complex SSCI beginning with a thorough exploration of the evolution of oscillations within power networks. The chapter also deep dives into a detailed examination of how oscillations develop and propagate. To provide a precise assessment, the quantification of these oscillations and the emergence of complex SSCI are compared against the latest advancements in the field, as documented in the state-of-the-art literature.

A comprehensive analysis is conducted to reach a consensus on the involvement of various participants in initiating complex SSCI and the necessary observability bandwidth. This involves a comparative study of existing literature to summarize the key findings and agreements in the field. Following this, an extensive review of system analysis methods for detecting oscillations is presented. This review includes a detailed examination of various detection methodologies, evaluating their effectiveness and applicability in different scenarios.

Additionally, the analysis emphasizes an alternative approach that addresses the limitations posed by constrained observability. This approach aims to overcome these barriers, providing a more robust framework for monitoring and controlling oscillations.

Finally, the document lays a strong foundation by reviewing specific literature focused on the mitigation of oscillations within the network. It identifies and discusses the open challenges related to the detection, localization, and mitigation of these oscillations, offering insights into potential solutions and future research directions.

Chapter 3

System Modeling and Quantification of Oscillations

The IBRs dominated networks are of significant concern as improper modeling of the converter and tuning of the control system along with varying operating conditions can lead to the risk of complex oscillations. The dominant modes of SSO such as i.e. sub/super synchronous modes are specifically related to the dynamic conditions of IBRs connected to a weak grid network. Previously, a weak grid dominated by WTGs has been extensively studied in [107]. The study suggest that the dominance of IBRs in such grids effectively leads to the instability of the network. Similarly, the effect of PLL, which is widely adopted for controlling these IBRs, may destabilize the network if the parameters are not tuned correctly. The similar research is proposed in [108], emphasizing on the importance of PLL and arbitrary setting of the parameters in grid-connected WTG. Moreover, the effect of a faster control loop for current control and slow voltage control for DC bus has also shown key potentials of instability, if not configured correctly [109, 110]. Therefore, this chapter analytically examines the effect of these three factors on the grid-connected Wind Power Plant (WPP) and explains how these factors play a key role in amplifying the SSOs and destabilizing the power network. This is pursued with detailed mathematical analysis and derivation of the sufficient stability conditions for a grid connected WPP constituted by Type3/Type4 WTGs.

Therefore; firstly, a detailed full-order model of the WTG is derived. Then, the model is simplified to obtain a reduced-order model of the grid-connected WTG to reflect the effect of PLL, and control loops involved in current and DC bus voltage control, respectively. The respective mathematical models are used to establish the stability criteria and provide the necessary conditions for which the violation leads to the occurrence of the SSO. Finally, a detailed analysis explains the effect of these three terms, where violating the stability conditions leads to complex SSOs.

Finally, putting these as a foundational argument for the escalation of complex oscillations, effective methods are proposed in next chapter covering the essential requirements to detect and localize complex SSOs in IBRs dominated networks.

3.1 Modelling of the DFIG

The detailed model of the DFIG connected to a series compensated transmission line is shown in Fig. 3.1. The converter mainly include the Dual-fed Induction Generator (DFIG), the Grid Side Converter (GSC), the Rotor Side Converter (RSC), the control system associated with GSC and RSC, and the phase loop lock (PLL). In the following sections, the detailed model of DFIG is established from the linearized model of aformentioned components associated with the grid

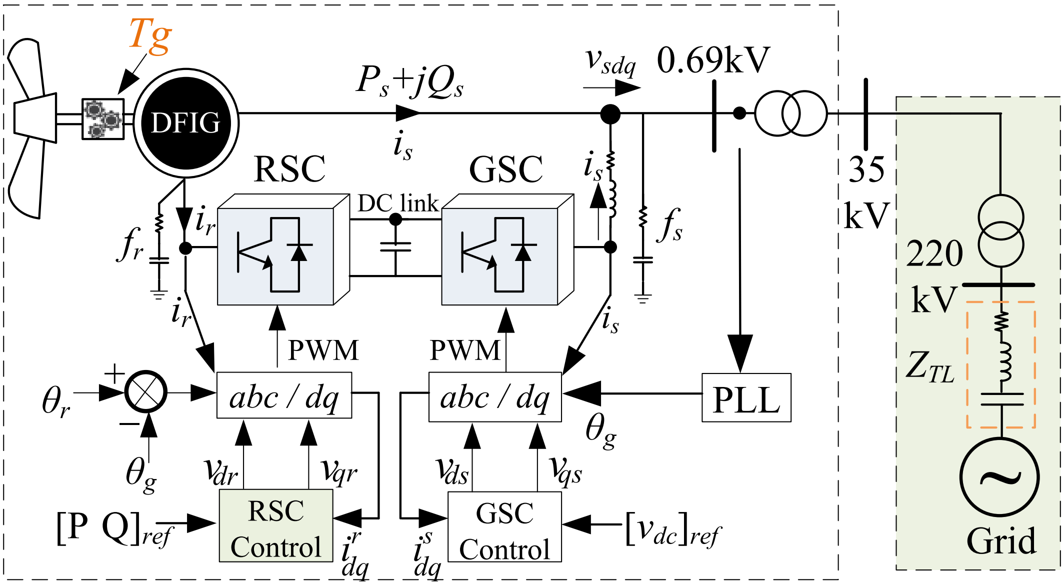

Figure 3.1: Detailed model of the DFIG, representing RSC and GSC voltage, current, and respective control

connected DFIG.

3.1.1 The Induction Generator

The DFIG equivalent model can be illustrated in the in Fig. 3.2. Representing the rotor side voltage with v_r and stator side voltage with v_s, the dynamics of the induction generator (IG) for an arbitrary speed ω can be written as,

$$v_s = R_s I_s + \frac{d}{dt}\phi_s + j\omega\psi_s \tag{3.1}$$

$$v_r = R_r I_r + \frac{d}{dt}\phi_r + j(\omega - \omega_r)\psi_r \tag{3.2}$$

The flux linkages with respect to the stator and rotor side converter as provided in Fig.3.2 can be written as,

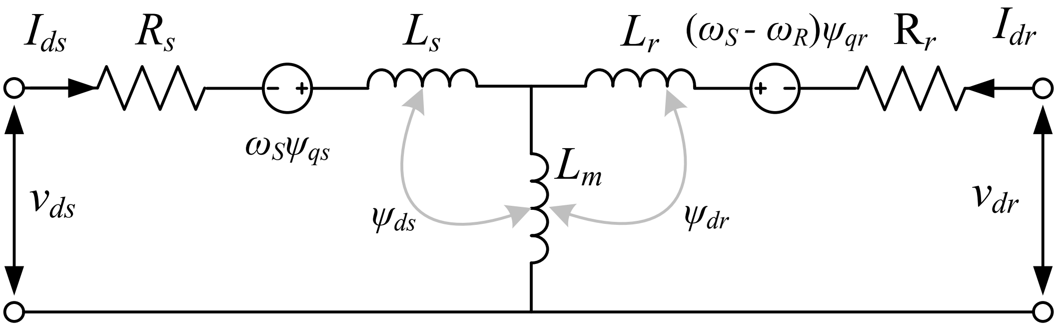

Figure 3.2: Equivalent circuit of the DFIG representing the stator and rotor side voltage and flux linkage

$$\psi_s = L_s I_s + L_m I_r \tag{3.3}$$

$$\psi_r = L_m I_s + L_r I_r \tag{3.4}$$

The DFIG-based WTG is strongly coupled with the grid through stator windings, therefore; to illustrate the dynamics due to this strong coupling, (3.1) can be amended by putting (3.3) and (3.2) by using (3.4) as given in details in [111]. Using mathematical manipulation, the equation for flux linkage on the stator side can be written as,

$$\begin{cases} \frac{d}{dt}\psi_{\mathrm{ds}} = \omega R_s I_{\mathrm{ds}} + \omega v_{\mathrm{ds}} + \omega \psi_{\mathrm{qs}} \\ \frac{d}{dt}\psi_{\mathrm{qs}} = \omega R_{\mathrm{s}} I_{\mathrm{qs}} + \omega v_{\mathrm{qs}} - \omega \psi_{\mathrm{ds}} \end{cases} \tag{3.5}$$

where v_{ds} and v_{qs} represent the stator side voltage; ψ_{ds} and ψ_{qs} stator side flux; and I_{ds}, I_{qs} stator side current in the d and q reference frame, receptively; ω is the synchronous speed; and R_s represent the resistance of the stator windings.

Similarly, the equation for the rotor side windings of the induction generator can be written as,

$$\begin{cases} \frac{d}{dt}\psi_{\mathrm{dr}} = \omega(RI_{\mathrm{dr}} + v_{\mathrm{dr}}) + \omega\left(1 - \omega_{\mathrm{r1}}\right)\psi_{\mathrm{qr}} \\ \frac{d}{dt}\psi_{\mathrm{qr}} = \omega(RI_{\mathrm{qr}} + v_{\mathrm{qr}}) - \omega\left(1 - \omega_{\mathrm{r1}}\right)\psi_{\mathrm{dr}} \end{cases} \tag{3.6}$$

In this context, v_{dr} and v_{qr} represent the d and q components of voltage, while ψ_{dr} and ψ_{qr} denote the d and q components of flux on the rotor side. Similarly, I_{dr} and I_{qr} are the d and q components of current in the rotor windings of the induction generator. Additionally, ω_{r1} is the angular speed of the high-speed shaft in the two-mass shaft system, and R_{r} is the resistance of the rotor windings.

Similarly, the flux of the stator and rotor in the $d - q$ domain can be written as,

$$\begin{cases} \psi_{\mathrm{ds}} = -X_{\mathrm{s}}I_{\mathrm{ds}} - X_{\mathrm{m}}I_{\mathrm{dr}} \\ \psi_{\mathrm{qs}} = -X_{\mathrm{s}}I_{\mathrm{qs}} - X_{\mathrm{m}}I_{\mathrm{qr}} \\ \psi_{\mathrm{dr}} = -X_{\mathrm{r}}I_{\mathrm{dr}} - X_{\mathrm{m}}I_{\mathrm{ds}} \\ \psi_{\mathrm{qr}} = -X_{\mathrm{r}}I_{\mathrm{qr}} - X_{\mathrm{m}}I_{\mathrm{qs}} \end{cases} \tag{3.7}$$

Where X_{r} and X_{s} are the self-inductance of the stator and rotor windings, respectively, while X_{m} refers to the mutual inductance between the stator and rotor side windings of the IG.

The two-mass rotational system of an induction generator comprises a high-speed shaft and a low-speed shaft, linked by a gearbox. The equations governing the motion of this two-shaft system are:

$$\begin{cases} J_{\mathrm{r1}}\frac{d}{dt}\omega_{\mathrm{r1}} = k_{\mathrm{m}}\theta_{\mathrm{r}} - T_{\mathrm{e}} - \zeta_{\mathrm{m}}\left(\omega_{\mathrm{r1}} - \omega_{\mathrm{r2}}\right) - \zeta_{\mathrm{r1}}\omega_{\mathrm{r1}} \\ J_{\mathrm{r2}}\frac{d}{dt}\omega_{\mathrm{r2}} = T_{\mathrm{m}} - k_{\mathrm{m}}\theta_{\mathrm{r}} - \zeta_{\mathrm{m}}\left(\omega_{\mathrm{r2}} - \omega_{\mathrm{r1}}\right) - \zeta_{\mathrm{r2}}\omega_{\mathrm{r2}} \\ \frac{d}{dt}\theta_{\mathrm{r}} = \omega\left(\omega_{\mathrm{r2}} - \omega_{\mathrm{r1}}\right) \end{cases} \tag{3.8}$$

where, J_{r1} and J_{r2} represent the constants of inertia for the low-speed and high-speed shafts, respectively. Similarly, T_{m} and ω_{r2} denote the mechanical torque and angular speed of the low-speed shaft, respectively. The k_{m} and ζ_{m} represent the elastic and mutual damping coefficient between the high-speed and low-speed shafts. Whereas, ζ_{r2} and ζ_{r1} refer to the self-damping coefficients of the high-speed and low-speed shafts, respectively. The relative angular position of the low-speed and high-speed shafts is denoted by $\theta_{\mathrm{r}} = \theta_{\mathrm{r2}} - \theta_{\mathrm{r1}}$. Here, θ_{r1} represents the angular position of the high-speed shaft, and θ_{r2} represents the angular position of the low-speed shaft. T_{e} signifies the electromagnetic output torque of the induction generator, which can be expressed as:

$$T_{\mathrm{e}} = X_{\mathrm{m}}\left(I_{\mathrm{ds}}I_{\mathrm{qr}} - I_{\mathrm{qs}}I_{\mathrm{dr}}\right) \tag{3.9}$$

Similarly, the equation for the active power can be written as,

$$P_{\mathrm{r}} = v_{\mathrm{dr}}I_{\mathrm{dr}} + v_{\mathrm{qr}}I_{\mathrm{qr}} \tag{3.10}$$

Assuming $\Delta T_m = 0$ and linearizing (3.5) to (3.1),

$$\begin{cases} \Delta\dot{\mathbf{X}}_1 = \mathbf{A}_1\Delta\mathbf{X}_1 + \mathbf{B}_1\Delta\mathbf{z}_1 + \mathbf{b}_1\Delta v_{\mathrm{qs}} + \mathbf{b}_2\Delta v_{\mathrm{ds}} \\ \Delta P_{\mathrm{r}} = \mathbf{c}_1^{\mathrm{T}}\Delta\mathbf{X}_1 + \mathbf{c}_2^{\mathrm{T}}\Delta\mathbf{z}_1 \end{cases} \tag{3.11}$$

where

$$\begin{aligned}\Delta\mathbf{X}_1 &= [\Delta\psi_{\mathrm{ds}}\Delta\psi_{\mathrm{qs}}\Delta\psi_{\mathrm{dr}}\Delta\psi_{\mathrm{qr}}\Delta\omega_{\mathrm{r1}}\Delta\omega_{\mathrm{r2}} \quad \Delta\theta_{\mathrm{r}}]^{\mathrm{T}} \\ \Delta\mathbf{z}_1 &= \begin{bmatrix} \Delta \mathrm{v}_{\mathrm{ds}} & \Delta \mathrm{v}_{\mathrm{qs}} \end{bmatrix}^{\mathrm{T}}\end{aligned} \tag{3.12}$$

$$A_1 = \left[\begin{array}{ccccccc}
\frac{X_{\mathrm{r}}\omega R_{\mathrm{s}}}{(X_{\mathrm{m}}^2-} & \omega & \frac{-X_{\mathrm{m}}\omega R_{\mathrm{s}}}{(X_{\mathrm{m}}^2-} & 0 & 0 & 0 & 0 \\
X_{\mathrm{r}}X_{\mathrm{s}} & & X_{\mathrm{r}}X_{\mathrm{s}} & & & & \\
-\omega & \frac{X_{\mathrm{r}}\omega R_{\mathrm{s}}}{(X_{\mathrm{m}}^2-} & 0 & \frac{-X_{\mathrm{m}}\omega R_{\mathrm{s}}}{(X_{\mathrm{m}}^2-} & 0 & 0 & 0 \\
 & X_{\mathrm{s}}X_{\mathrm{r}} & & X_{\mathrm{s}}X_{\mathrm{r}} & & & \\
\frac{X_{\mathrm{m}}\omega R_{\mathrm{r}}}{(X_{\mathrm{r}}X_{\mathrm{s}}-} & 0 & \frac{-X_{\mathrm{s}}\omega R_{\mathrm{r}}}{(X_{\mathrm{r}}X_{\mathrm{s}}-} & \omega(1-\omega_{\mathrm{r10}}) & -\omega\psi_{\mathrm{qr0}} & 0 & 0 \\
-X_{\mathrm{m}}^2 & & -X_{\mathrm{m}}^2 & & & & \\
0 & \frac{X_{\mathrm{m}}\omega R_{\mathrm{r}}}{(X_{\mathrm{r}}X_{\mathrm{s}}-} & -\omega(1-\omega_{\mathrm{r10}}) & \frac{-X_{\mathrm{s}}\omega R_{\mathrm{r}}}{(X_{\mathrm{r}}X_{\mathrm{s}}-} & \omega\psi_{\mathrm{rd0}} & 0 & 0 \\
 & -X_{\mathrm{m}}^2 & & -X_{\mathrm{m}}^2 & & & \\
(-X_{\mathrm{m}}X_{\mathrm{r}}I_{\mathrm{qr0}} & (X_{\mathrm{m}}I_{\mathrm{dr0}}X_{\mathrm{r}}+ & (X_{\mathrm{m}}I_{\mathrm{qr0}}+ & (-I_{\mathrm{rd}d0}X_{\mathrm{m}}^2- & (-\zeta_{\mathrm{m}} & & \\
-X_{\mathrm{m}}^2I_{\mathrm{qs0}}) & X_{\mathrm{m}}X_{\mathrm{s}}I_{\mathrm{ds0}}) & X_{\mathrm{m}}X_{\mathrm{s}}I_{\mathrm{qs0}}) & X_{\mathrm{m}}X_{\mathrm{s}}I_{\mathrm{ds0}}) & -\zeta_{\mathrm{r1}} & \underline{\zeta_{\mathrm{m}}} & \underline{k_{\mathrm{m}}} \\
(J_{\mathrm{r1}}X_{\mathrm{m}}^2- & (J_{\mathrm{r1}}X_{\mathrm{m}}^2- & (J_{\mathrm{r1}}X_{\mathrm{m}}^2- & (J_{\mathrm{r1}}X_{\mathrm{m}}^2- & J_{\mathrm{r1}} & \overline{J_{\mathrm{r1}}} & J_{\mathrm{r1}} \\
J_{\mathrm{r1}}X_{\mathrm{r}}X_{\mathrm{s}}) & J_{\mathrm{r1}}X_{\mathrm{s}}X_{\mathrm{r}}) & J_{\mathrm{r1}}X_{\mathrm{r}}X_{\mathrm{s}}) & J_{\mathrm{r1}}X_{\mathrm{s}}X_{\mathrm{r}}) & & & \\
 & & & & & (-\zeta_{\mathrm{m}} & \\
0 & 0 & 0 & 0 & \underline{\zeta_{\mathrm{m}}} & \underline{(-\zeta_{\mathrm{r2}})} & -\underline{k_{\mathrm{m}}} \\
0 & 0 & 0 & 0 & J_{\mathrm{r2}} < br > -\omega & \omega & \mathrm{Jr}^2 2 < br > 0
\end{array}\right]$$

$$\mathbf{B}_1 = \begin{bmatrix} 0 & 0 \\ 0 & 0 \\ \omega & 0 \\ 0 & \omega \\ 0 & 0 \\ 0 & 0 \\ 0 & 0 \end{bmatrix}, \quad \mathbf{b}_1 = \begin{bmatrix} 0 \\ \omega \\ 0 \\ 0 \\ 0 \\ 0 \\ 0 \end{bmatrix}, \quad \mathbf{b}_2 = \begin{bmatrix} \omega \\ 0 \\ 0 \\ 0 \\ 0 \\ 0 \\ 0 \end{bmatrix} \tag{3.13}$$
$$\mathbf{c}_1^{\mathrm{T}} = \begin{bmatrix} k_5 v_{\mathrm{dr0}} & k_7 v_{\mathrm{qr0}} & -k_6 v_{\mathrm{dr0}} & -k_8 v_{\mathrm{qr0}} & 0 & 0 & 0 \end{bmatrix},$$
$$\mathbf{c}_2^{\mathrm{T}} = \begin{bmatrix} I_{\mathrm{dr0}} & I_{\mathrm{qr0}} \end{bmatrix}$$

3.1.2 Dynamics of RSC and its Control

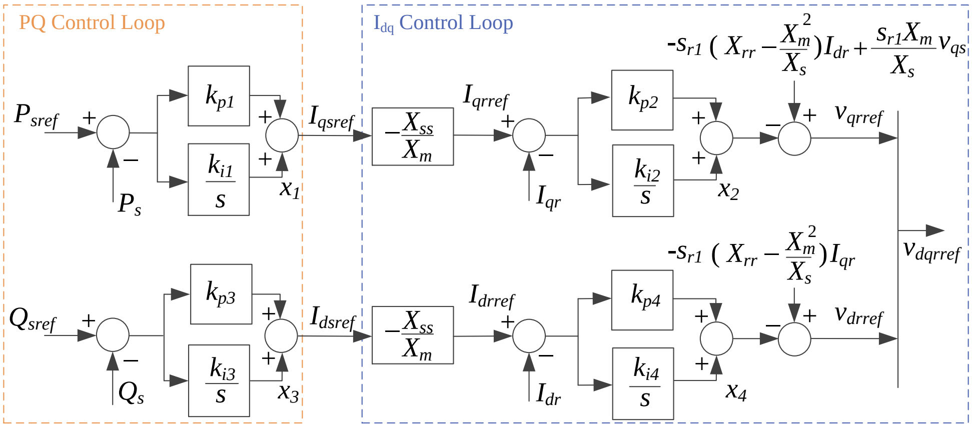

Figure 3.3: Control block of the RSC in the DFIG based WTG

The configuration of the RSC control system is illustrated in Fig.3.3. The current control inner loops regulate the d-axis and q-axis stator currents, I_{qs}

and I_{ds}, respectively. The outer loops manage the active and reactive power outputs from the stator side of the induction generator, given as P_{s} and Q_{s}, respectively. The slip of the high-speed shaft of the induction generator is defined as $s_{\mathrm{r1}} = 1 - \omega_{\mathrm{r1}}$. The relation for the control inputs and outputs can be written from Fig.3.3.

$$\begin{cases} \frac{d}{dt}x_1 = k_{i1}(P_{sref} - P_s) \\ \frac{d}{dt}x_2 = k_{i2}(I_{qrref} - I_{qr}) \\ \frac{d}{dt}x_3 = k_{i3}(Q_{sref} - Q_s) \\ \frac{d}{dt}x_4 = k_{i4}(I_{drref} - I_{dr}) \end{cases} \tag{3.14}$$

where k_i refers to the corresponding integral gains; while $P_{\mathrm{sref}}, Q_{\mathrm{sref}}$ are the reference set points for the active and reactive power; and I_{qrref}, and I_{drref} are the reference points for the current loops of q and d axis respectively.

Further to ease the simplification, the relation for the rotor side current in the $d-q$ domain can be obtained as,

$$\begin{cases} I_{qsref} = x_1 + k_{p1}(P_{sref} - P_s) \\ I_{dsref} = x_3 + k_{p3}(Q_{sref} - P_s) \\ \qquad \text{Similarly, for the rotor side,} \\ i_{qrref} = -\dfrac{X_s}{X_m} I_{qsref} \\ i_{drref} = -\dfrac{X_s}{X_m} I_{dsref} - \dfrac{v_{qs}}{X_m} \\ \qquad \text{and similarly, the rotor side voltage equations can be written as,} \\ v_{qrref} = -k_{p2}(I_{qrref} - I_{qr}) - x_2 - s_{r1}(X_{rr} - \dfrac{X_m^2}{X_s} I_{dr}) + \dfrac{s_{r1}X_m}{X_s v_{qs}} \\ v_{drref} = -kp_4(I_{drref} - I_{dr}) - x_{d4} + s_{r1}(X_{rr} - \dfrac{X_m^2}{X_s}) I_{qr} \end{cases} \tag{3.15}$$

where $k_{\mathrm{p1}}, k_{\mathrm{p2}}, k_{\mathrm{p3}}$, and k_{p4} are the constant proportional gains; I_{qsref} and I_{dsref} are the reference points for stator currents in $d-q$ domain; v_{qrref} and v_{drref} are the reference values for the control inputs managing the RSC voltage in $d-q$ domain, respectively.

Similarly, the active and reactive power can be written as,

$$\begin{cases} P_s = v_{qs}I_{qs} + v_{ds}I_{ds} \\ Q_s = v_{qs}I_{ds} + v_{ds}I_{qs} \end{cases} \tag{3.16}$$

The linearization of the equation (3.14)-(3.16) with assumption that $\Delta P_{sref} = 0$ and $\Delta Q_{sref} = 0$, we obtain,

$$\begin{cases} \Delta\dot{\mathbf{X}}_2 = \mathbf{A}_2\Delta\mathbf{X}_2 + \mathbf{B}_2\Delta\mathbf{X}_1 + \mathbf{b}_3\Delta v_{ds} + \mathbf{b}_4\Delta v_{ds} \\ \Delta\dot{\mathbf{z}}_1 = \mathbf{C}_1\Delta\mathbf{X}_2 + \mathbf{C}_2\Delta\mathbf{X}_1 + \mathbf{C}_3\Delta \mathrm{v}_{\mathrm{d}s} + \mathbf{C}_4\Delta\mathrm{v}_{\mathrm{ds}} \end{cases} \tag{3.17}$$

The output of the constituting matrix can be determined using,

$$\Delta\mathbf{X}_2 = \begin{bmatrix} \Delta x_1 & \Delta x_2 & \Delta x_3 & \Delta x_4 \end{bmatrix}^{\mathrm{T}},$$

$$\mathbf{A}_2 = \begin{bmatrix} 0 & 0 & 0 & 0 \\ \frac{-k_2X_{\mathrm{s}}}{X_{\mathrm{m}}} & 0 & 0 & 0 \\ 0 & 0 & 0 & 0 \\ 0 & 0 & \frac{-k_iX_{\mathrm{s}}}{X_{\mathrm{m}}} & 0 \end{bmatrix}$$

$$\mathbf{b}_3 = \begin{bmatrix} -k_{\mathrm{i1}} I_{\mathrm{qs0}} \\ \frac{k_{\mathrm{i2}} k_{\mathrm{p1}} X_{\mathrm{ss1}} I_{\mathrm{s}q0}}{X_{\mathrm{m}}} \\ -k_{\mathrm{i3}} I_{\mathrm{s}d0} \\ \frac{k_4 k_{\mathrm{p3}} X_{\mathrm{s}} I_{\mathrm{s}d0} - k_{i4}}{X_{\mathrm{m}}} \end{bmatrix}, \quad \mathbf{b}_4 = \begin{bmatrix} -k_{\mathrm{i1}} I_{\mathrm{s}d0} \\ \frac{k_{\mathrm{i2}} k_{\mathrm{p1}} X_{\mathrm{s}} I_{\mathrm{s}d0}}{X_{\mathrm{m}}} \\ k_{\mathrm{i3}} I_{\mathrm{qs0}} \\ \frac{-k_{\mathrm{i4}} k_{\mathrm{p3}} X_{\mathrm{s}} I_{\mathrm{qs0}}}{X_{\mathrm{m}}} \end{bmatrix},$$

$$\mathbf{C}_1 = \begin{bmatrix} 0 & 0 & \frac{k_{\mathrm{p4}} X_{\mathrm{s}}}{X_{\mathrm{m}}} & -1 \\ \frac{k_{\mathrm{p2}} X_{\mathrm{s}}}{X_{\mathrm{m}}} & -1 & 0 & 0 \end{bmatrix}$$

$$C_2^{\mathbf{T}} = \begin{bmatrix} \frac{k_{\mathrm{p3}} k_{\mathrm{p4}} X_{\mathrm{s}} X_{\mathrm{r}} v_{\mathrm{s}q0} + k_{\mathrm{p4}} X_{\mathrm{m}}^2}{X_{\mathrm{m}}(X_{\mathrm{r}} X_{\mathrm{s}} - X_{\mathrm{m}}^2)} & \frac{k_{\mathrm{p2}} k_{\mathrm{p1}} X_{\mathrm{s}} X_{\mathrm{r}} v_{\mathrm{s}d0}}{X_{\mathrm{m}}(X_{\mathrm{r}} X_{\mathrm{s}} - X_{\mathrm{m}}^2)} - \frac{s_{\mathrm{r10}} X_{\mathrm{m}}}{X_{\mathrm{s}}} \\ \frac{k_{\mathrm{p3}} k_{\mathrm{p4}} X_{\mathrm{s}} X_{\mathrm{r}} v_{\mathrm{s}d0}}{X_{\mathrm{m}}(X_{\mathrm{m}}^2 - X_{\mathrm{s}} X_{\mathrm{r}})} + \frac{s_{\mathrm{r10}} X_{\mathrm{m}}}{X_{\mathrm{s}}} & \frac{k_{\mathrm{p2}} k_{\mathrm{p1}} X_{\mathrm{s}} X_{\mathrm{r}} v_{\mathrm{s}q0} + k_{\mathrm{p2}} X_{\mathrm{m}}^2}{X_{\mathrm{m}}(X_{\mathrm{s}} X_{\mathrm{r}} - X_{\mathrm{m}}^2)} \\ \frac{k_{\mathrm{p3}} k_{\mathrm{p4}} X_{\mathrm{s}} v_{\mathrm{s}q0} + k_{\mathrm{p4}} X_{\mathrm{s}}}{X_{\mathrm{m}}^2 - X_{\mathrm{r}} X_{\mathrm{s}}} & \frac{k_{\mathrm{p2}} k_{\mathrm{p1}} X_{\mathrm{s}} v_{\mathrm{s}d0}}{X_{\mathrm{m}}^2 - X_{\mathrm{r}} X_{\mathrm{s}}} + s_{\mathrm{r10}} \\ \frac{k_{\mathrm{p3}} k_{\mathrm{p4}} X_{\mathrm{s}} v_{\mathrm{s}d0}}{X_{\mathrm{s}} X_{\mathrm{r}} - X_{\mathrm{m}}^2} - s_{\mathrm{r10}} & \frac{k_{\mathrm{p2}} k_{\mathrm{p1}} X_{\mathrm{s}} v_{\mathrm{s}q0} + k_{\mathrm{p2}} X_{\mathrm{s}}}{X_{\mathrm{m}}^2 - X_{\mathrm{s}} X_{\mathrm{r}}} \\ -I_{\mathrm{qr0}} \left(X_{\mathrm{r}} - \frac{X_{\mathrm{m}}^2}{X_{\mathrm{s}}} \right) & I_{\mathrm{dr0}} \left(X_{\mathrm{r}} - \frac{X_{\mathrm{m}}^2}{X_{\mathrm{s}}} \right) - \frac{v_{\mathrm{s}q0} X_{\mathrm{m}}}{X_{\mathrm{s}}} \\ 0 & 0 \\ 0 & 0 \end{bmatrix}$$

$$\mathbf{C}_3 = \begin{bmatrix} \frac{k_{\mathrm{p4}} - k_{\mathrm{p3}} k_{\mathrm{p4}} X_{\mathrm{s}} I_{\mathrm{s}d0}}{X_{\mathrm{m}}} \\ \frac{s_{\mathrm{r10}} X_{\mathrm{m}}}{X_{\mathrm{s}}} - \frac{k_{\mathrm{p2}} k_{\mathrm{p1}} X_{\mathrm{s}} I_{\mathrm{s}q0}}{X_{\mathrm{m}}} \end{bmatrix}, \quad \mathbf{C}_4 = \begin{bmatrix} \frac{k_{\mathrm{p3}} k_{\mathrm{p4}} X_{\mathrm{s}s} I_{\mathrm{s}q0}}{X_{\mathrm{m}}} \\ \frac{-k_{\mathrm{p2}} X_{\mathrm{s}} k_{\mathrm{p1}} I_{\mathrm{d}s} 0}{X_{\mathrm{m}}} \end{bmatrix}$$

$$B_2 = \begin{bmatrix} \frac{k_{\mathrm{i1}} v_{\mathrm{sd0}} X_{\mathrm{r}}}{X_{\mathrm{r}} X_{\mathrm{s}} - X_{\mathrm{m}}^2} & \begin{matrix} \frac{k_{\mathrm{i1}} v_{\mathrm{qs0}} X_{\mathrm{r}}}{X_{\mathrm{s}} X_{\mathrm{r}} - X_{\mathrm{m}}^2} \\ \binom{k_{\mathrm{p1}} k_{\mathrm{i2}} X_{\mathrm{s}} X_{\mathrm{r}} v_{\mathrm{qs0}}}{V_2^2} \end{matrix} & \frac{k_{\mathrm{i1}} V_{\mathrm{ds0}} X_{\mathrm{m}}}{X_{\mathrm{m}}^2 - X_{\mathrm{r}} X_{\mathrm{s}}} & \begin{matrix} \frac{k_{\mathrm{i1}} v_{\mathrm{qs0}} X_{\mathrm{m}}}{X_{\mathrm{m}}^2 - X_{\mathrm{s}} X_{\mathrm{r}}} \\ -k_{\mathrm{p1}} k_{\mathrm{i2}} X_{\mathrm{s}} v_{\mathrm{qs0}} \\ k_{\mathrm{S}} Y \end{matrix} & 0 & 0 \\ \begin{matrix} \frac{k_{\mathrm{p1}} k_{\mathrm{i2}} X_{\mathrm{s}} X_{\mathrm{r}} v_{\mathrm{sd0}}}{v_{\mathrm{v}}} \\ X_{\mathrm{m}}(X_{\mathrm{m}}^2 - X_{\mathrm{r}} X_{\mathrm{s}}) \end{matrix} & X_{\mathrm{m}}(X_{\mathrm{m}}^2 - X_{\mathrm{s}} X_{\mathrm{r}}) & \begin{matrix} \frac{-k_{\mathrm{p1}} k_{\mathrm{i2}} X_{\mathrm{s}} V_{\mathrm{ds0}}}{X^2 - X X} \\ X_{\mathrm{m}}^2 - X_{\mathrm{r}} X_{\mathrm{s}} \\ k_{\mathrm{i3}} v_{\mathrm{qs0}} X_{\mathrm{m}} \end{matrix} & \begin{matrix} \frac{-k_{\mathrm{i2}} X_{\mathrm{s}}}{X_1^2 - X_1 X_{\mathrm{m}}} \\ X_{\mathrm{m}}^2 - X_{\mathrm{s}} X_{\mathrm{r}} \\ -k_{\mathrm{i3}} v_{\mathrm{sd0}} X_{\mathrm{m}} \end{matrix} & 0 & 0 \\ \begin{matrix} \frac{k_{\mathrm{i3}} v_{\mathrm{qs0}} X_{\mathrm{r}}}{X_{\mathrm{r}} X_{\mathrm{s}} - X_{\mathrm{m}}^2} \\ k_{\mathrm{p3}} k_{\mathrm{i4}} X_{\mathrm{s}} X_{\mathrm{r}} v_{\mathrm{qs0}} \end{matrix} & \frac{k_{\mathrm{i3}} V_{\mathrm{ds0}} X_{\mathrm{r}}}{X_{\mathrm{m}}^2 - X_{\mathrm{s}} X_{\mathrm{r}}} & \begin{matrix} \frac{k_{\mathrm{i3}} v_{\mathrm{qs0}} X_{\mathrm{m}}}{X_{\mathrm{m}}^2 - X_{\mathrm{r}} X_{\mathrm{s}}} \\ -k_{\mathrm{p3}} k_{\mathrm{i4}} X_{\mathrm{s}} v_{\mathrm{qs0}} \end{matrix} & \frac{-k_{\mathrm{i3}} v_{\mathrm{ds0}} X_{\mathrm{m}}}{X_{\mathrm{m}}^2 - X_{\mathrm{s}} X_{\mathrm{r}}} & 0 & 0 \\ k_{\mathrm{i4}} X_{\mathrm{m}}^2 & -k_{\mathrm{p3}} k_{\mathrm{i4}} X_{\mathrm{s}} X_{\mathrm{r}} V_{\mathrm{ds0}} & -k_{\mathrm{i4}} X_{\mathrm{s}} & \underline{k_{\mathrm{p3}} k_{\mathrm{i4}} X_{\mathrm{s}} V_{\mathrm{ds0}}} & & 0 \end{bmatrix}$$

While, ΔX_1 and Δz_1 are defined from (3.11).

3.1.3 Dynamics of GSC and its Control

It is important to note that this thesis emphasize only on the explicit effect of RSC dynamics, its control, and the associated PLL in alliance with the complex SSO modes. The GSC derivations are only provided to facilitate the modeling of DFIG for grid-connected applications. Therefore, the dynamics equations are included in this section and further derivations related to the mechanical constraints can be obtained from [112]. It is important to note that, the GSC of the WTG regulates the DC bus voltage, mainly based on the DC voltage control loop operating at a bandwidth of $1/10^{th}$ times slower comparatively to the current control loops. Therefore, to facilitate the derivations, the voltage across the filter having reactance X_f can be written as,

$$\begin{cases} \dot{I}_{\mathrm{d,DC}} = \frac{\omega v_{\mathrm{d,DC}}}{X_{\mathrm{f}}} - \frac{\omega v_{\mathrm{ds}}}{X_{\mathrm{f}}} + \omega I_{\mathrm{q,DC}} \\ \dot{I}_{\mathrm{q,DC}} = \frac{\omega v_{\mathrm{q,DC}}}{X_{\mathrm{f}}} - \frac{\omega v_{\mathrm{qs}}}{X_{\mathrm{f}}} - \omega I_{\mathrm{d,DC}} \end{cases} \tag{3.18}$$

Where, $v_{d,DC}$ and $v_{q,DC}$ refer to the voltage on the GSC converter in the $d-q$ axis, respectively.

From Fig.3.4, the relation for the voltage across the bus capacitor (v_{dc}) can be written as,

$$Cv_{\mathrm{dc}}\frac{dv_{\mathrm{dc}}}{dt} = P_{\mathrm{r}} - P_{\mathrm{c1}} \tag{3.19}$$

Where C denotes the capacitance of the bus, P_{r} is rotor active power output and P_{c1} is the power injected into the GSC. This can be expressed as,

$$P_{\mathrm{c1}} = V_{\mathrm{d,DC}}I_{\mathrm{d,DC}} + v_{\mathrm{q,DC}}I_{\mathrm{q,DC}} \tag{3.20}$$

Similarly, the relation for the control outputs can be written as,

$$\begin{cases} I_{\mathrm{q,DC\ ref}} &= k_{\mathrm{p5}}\left(v_{\mathrm{DC,ref}} - v_{\mathrm{d,DC}}\right) + x_5 \\ v_{\mathrm{q,DCref}} &= k_{\mathrm{p6}}\left(I_{\mathrm{q,DCref}} - I_{\mathrm{q,DC}}\right) + x_6 + v_{\mathrm{qs}} + X_{\mathrm{f}}I_{\mathrm{d,DC}} \\ v_{\mathrm{d,DCref}} &= k_{\mathrm{p7}}\left(I_{\mathrm{d,DCref}} - I_{\mathrm{d,DC}}\right) + x_7 + v_{\mathrm{ds}} - X_{\mathrm{f}}I_{\mathrm{q,DC}q} \end{cases} \tag{3.21}$$

Where, $k_{\mathrm{p5}}, k_{\mathrm{p6}}$, and k_{p7} are the proportional control gains, and $v_{\mathrm{DC}ref}$, $I_{\mathrm{q,DC}ref}$, $I_{\mathrm{d,DC}ref}$ are the DC side voltage, $q-axis$ and $d-axis$ reference currents. The linearization of (3.18) - (3.21) provide us with,

$$\dot{\mathbf{X}}_3 = \mathbf{A}_3\Delta\mathbf{X}_3 + \mathbf{b}_5\Delta v_{\mathrm{ds}} + \mathbf{b}_6\Delta v_{\mathrm{qs}} + \mathbf{b}_7\Delta P_{\mathrm{r}} \tag{3.22}$$

Where,

$$\Delta\mathbf{X}_3 = \begin{bmatrix} \Delta I_{\mathrm{d,DC}} & \Delta I_{\mathrm{q,DC}} & \Delta v_{\mathrm{d,DC}} & \Delta x_5 & \Delta x_6 & \Delta x_7 \end{bmatrix}^{\mathrm{T}}$$

While the rest of the parameters can be obtained by solving using the linearization of the equation and mathematical manipulation for $\Delta\mathbf{X}$.

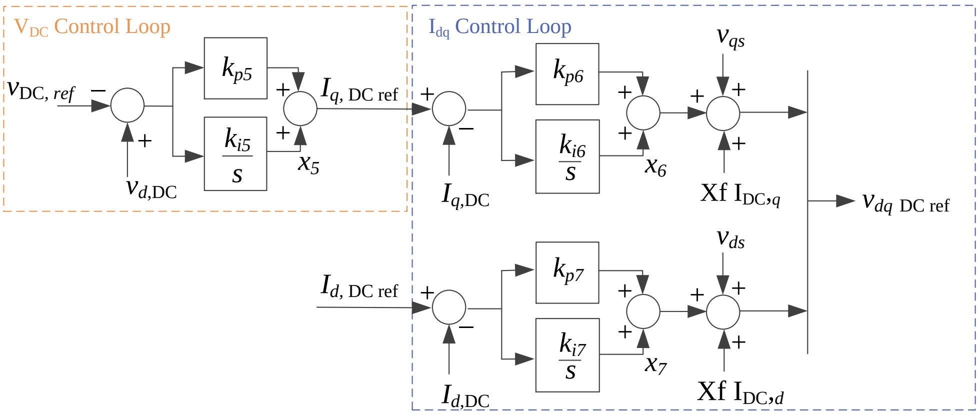

Figure 3.4: Configuration of the DC voltage control loop of DFIG

3.1.4 The dynamics of Phase Locked Loop

Typically, the PLL for a DFIG aligns its $d-q$ coordinate system's d-axis with the direction of the stator flux. When neglecting resistance, the flux lags behind the terminal voltage of the DFIG by 90°. Consequently, the direction of the DFIG terminal voltage corresponds to the q-axis. The PLL is designed to track the phase of the terminal voltage, aligning it with the q-axis of the $d-q$ coordinate system of the DFIG, as illustrated in Fig.3.5. The linearized model of the PLL for grid-connected DFIG can be obtained as,

$$\Delta\dot{\mathbf{X}}_4 = \mathbf{A}_4\Delta\mathbf{X}_4 + \mathbf{b}_8\Delta v_x + \mathbf{b}_9\Delta v_y \tag{3.23}$$

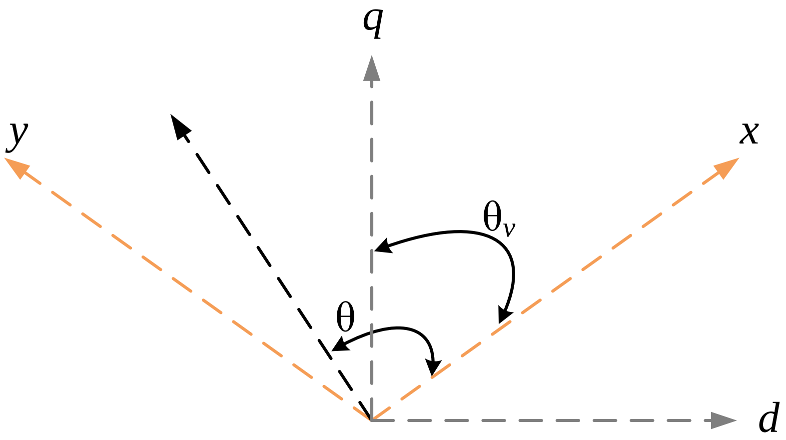

Figure 3.5: $d-q$ transformation and vectors distribution in the rotating reference frame

where $v\angle\theta = v_x + jV_y$ and refers to the stator's terminal voltage in the DFIG, expressed in the $x-y$ coordinate as;

$$\Delta\mathbf{X}_4 = \begin{bmatrix} \Delta x_\mathrm{p} & \Delta\theta_\mathrm{p} \end{bmatrix}^\mathrm{T}$$

$$\mathbf{A}_{\mathrm{d}4} = \begin{bmatrix} 0 & -k_\mathrm{i}v \\ 1 & -k_\mathrm{p}v \end{bmatrix}, \mathbf{b}_8 = \begin{bmatrix} -\frac{k_\mathrm{i}v_{\mathrm{y}0}}{v} \\ -\frac{k_\mathrm{p}v_y}{v} \end{bmatrix}, \mathbf{b}_9 = \begin{bmatrix} \frac{k_\mathrm{i}v_x}{v} \\ \frac{k_\mathrm{p}v_x}{v} \end{bmatrix}$$

The relation for current in the $x-y$ coordinates can be written as,

$$\begin{aligned} \begin{bmatrix} I_x \\ I_y \end{bmatrix} &= [\sin\theta_\mathrm{p} \cos\theta_\mathrm{p} - \cos\theta_\mathrm{p} \sin\theta_\mathrm{p}] \left(\begin{bmatrix} I_{\mathrm{d,DC}} \\ I_{\mathrm{q,DC}} \end{bmatrix} + \begin{bmatrix} I_{\mathrm{ds}} \\ I_s \end{bmatrix} \right) \\ \begin{bmatrix} v_{\mathrm{ds}} \\ v_{\mathrm{qs}} \end{bmatrix} &= [\sin\theta_\mathrm{p} - \cos\theta_\mathrm{p} \cos\theta_\mathrm{p} \sin\theta_\mathrm{p}] \begin{bmatrix} V_x \\ V_y \end{bmatrix} \end{aligned} \tag{3.24}$$

Linearizing the expression given in (3.24) gives us,

$$
\begin{aligned}
\begin{bmatrix} \Delta I_x \\ \Delta I_y \end{bmatrix} =& \begin{bmatrix} \cos\theta_{\mathrm{p0}} & -\sin\theta_{\mathrm{p0}} \\ \sin\theta_{\mathrm{p0}} & \cos\theta_{\mathrm{p0}} \end{bmatrix} \left(\begin{bmatrix} I_{\mathrm{d,DC0}} \\ I_{\mathrm{q,DC0}} \end{bmatrix} + \begin{bmatrix} I_{\mathrm{s0}} \\ I_{\mathrm{s0}} \end{bmatrix} \right) \Delta\theta_{\mathrm{p}} \\
&+ \begin{bmatrix} \sin\theta_{\mathrm{p0}} & \cos\theta_{\mathrm{p0}} \\ -\cos\theta_{\mathrm{p0}} & \sin\theta_{\mathrm{p0}} \end{bmatrix} \left(\begin{bmatrix} \Delta I_{\mathrm{d,DC}} \\ \Delta I_{\mathrm{q,DC}} \end{bmatrix} + \begin{bmatrix} \Delta I_{\mathrm{ds}} \\ \Delta I_{\mathrm{qs}} \end{bmatrix} \right) \\
=& \mathbf{p}_1 \Delta\theta_{\mathrm{p}} + \mathbf{P}_1 \left(\begin{bmatrix} \Delta I_{\mathrm{d,DC}} \\ \Delta I_{\mathrm{q,DC}} \end{bmatrix} + \begin{bmatrix} \Delta I_{\mathrm{ds}} \\ \Delta I_{\mathrm{qs}} \end{bmatrix} \right) \\
\begin{bmatrix} \Delta v_{\mathrm{ds}} \\ \Delta v_{\mathrm{qs}} \end{bmatrix} =& \begin{bmatrix} \cos\theta_{\mathrm{p0}} & \sin\theta_{\mathrm{p0}} \\ -\sin\theta_{\mathrm{p0}} & \cos\theta_{\mathrm{p0}} \end{bmatrix} \begin{bmatrix} v_x \\ v_y \end{bmatrix} \Delta\theta_{\mathrm{p}} + \begin{bmatrix} \sin\theta_{\mathrm{p0}} & -\cos\theta_{\mathrm{p0}} \\ \cos\theta_{\mathrm{p0}} & \sin\theta_{\mathrm{p0}} \end{bmatrix} \begin{bmatrix} \Delta v_x \\ \Delta v_y \end{bmatrix} \\
=& \mathbf{p}_2 \Delta\theta_{\mathrm{p}} + \mathbf{P}_2 \begin{bmatrix} \Delta v_x \\ \Delta v_y \end{bmatrix}
\end{aligned}
\tag{3.25}
$$

3.2 Quantification of Oscillations

This thesis only carries the mathematical analysis for the control loop operating at a faster time scale. The control loops such as voltage control and dynamic connected externally with the power plant control (PPC) mechanism are operated significantly at lower bandwidth, and thus have less subsequent effect on the complex SSCI.

3.2.1 Dynamics of Inner Control Loops of the RSC in the Current Timescale

From the current control inner loop of the RSC displayed in Fig.3.1, it can have ($s_{\mathrm{r1}} = 1 - \omega_{\mathrm{r}}$). Therefore, the relation for the voltage at the rotor side converter can be written as,

$$\begin{aligned}
v_{\mathrm{qr}} &= \left(k_{\mathrm{p2}} + \frac{k_{\mathrm{i2}}}{s}\right)\left(I_{\mathrm{qr}ref} - I_{\mathrm{qr}}\right) - (1-\omega)\left(X_{\mathrm{r}} - \frac{X_{\mathrm{m}}^2}{X_{\mathrm{s}}}\right) I_{\mathrm{dr}} + (1-\omega)\frac{X_{\mathrm{m}}}{X_{\mathrm{s}}} v_{\mathrm{qs}} \\
&= H_2(s)\left(I_{\mathrm{qr}ref} - I_{\mathrm{qr}}\right) - (1-\omega)\left(X_{\mathrm{r}} - \frac{X_{\mathrm{m}}^2}{X_{\mathrm{s}}}\right) I_{\mathrm{dr}} + (1-\omega_{\mathrm{r}})\frac{X_{\mathrm{m}}}{X_{\mathrm{s}}} v_{\mathrm{qs}} \\
v_{\mathrm{dr}} &= \left(k_{\mathrm{p4}} + \frac{k_{\mathrm{i4}}}{\mathrm{s}}\right)\left(I_{\mathrm{dr}ref} - I_{\mathrm{dr}}\right) + (1-\omega)\left(X_{\mathrm{r}} - \frac{X_{\mathrm{m}}^2}{X_{\mathrm{s}}}\right) I_{\mathrm{qr}} + (1-\omega)\frac{X_{\mathrm{m}}}{X_{\mathrm{s}}} v_{\mathrm{ds}} \\
&= H_4(s)\left(I_{\mathrm{drref}} - I_{\mathrm{dr}}\right) + (1-\omega)\left(X_{\mathrm{r}} - \frac{X_{\mathrm{m}}^2}{X_{\mathrm{s}}}\right) I_{\mathrm{qr}} + (1-\omega)\frac{X_{\mathrm{m}}}{X_{\mathrm{s}}} v_{\mathrm{s}}
\end{aligned} \tag{3.26}$$

Linearization of (3.26) provide us with,

$$\Delta \mathbf{v}_{\mathrm{dqr}} = \mathbf{Z}_1(s)\Delta I_{\mathrm{dr\ ref}} + \mathbf{Z}_2(s)\Delta I_{\mathrm{qr\ ref}} + \mathbf{Z}_3(s)\Delta \mathbf{I}_{dq} + \mathbf{Z}_4\Delta \mathbf{v}_{\mathrm{s}dq} + \mathbf{Z}_5\Delta\omega$$

where the subsequent matrices can be written as,

$$\begin{aligned}
&\Delta \mathbf{I}_{\mathrm{qr}} = \begin{bmatrix} I_{\mathrm{dr}} & I_{\mathrm{qr}} \end{bmatrix}^{\mathrm{T}}, \Delta \mathbf{v}_{\mathrm{qs}} = \begin{bmatrix} v_{\mathrm{ds}} & v_{\mathrm{qs}} \end{bmatrix}^{\mathrm{T}}, \Delta \mathbf{v}_{\mathrm{rq}} = \begin{bmatrix} v_{\mathrm{dq}} & v_{\mathrm{qr}} \end{bmatrix}^{\mathrm{T}}; \\
&\mathbf{Z}_1(s) = \begin{bmatrix} -H_4(s) \\ 0 \end{bmatrix}; \mathbf{Z}_2(s) = \begin{bmatrix} 0 \\ -H_2(s) \end{bmatrix}; \mathbf{Z}_3(s) = \begin{bmatrix} H_4(s) & \eta_0 \\ -\eta_0 & H_2(s) \end{bmatrix} \\
&\mathbf{Z}_4 = \begin{bmatrix} s_{\mathrm{r1}}\frac{X_{\mathrm{m}}}{X_{\mathrm{s}}} & 0 \\ 0 & s_{\mathrm{r1}}\frac{X_{\mathrm{m}}}{X_{\mathrm{s}}} \end{bmatrix}; \mathbf{Z}_5 = \begin{bmatrix} -\left(X_{\mathrm{r}} - \frac{X_{\mathrm{m}}^2}{X_{\mathrm{s}}}\right) I_{\mathrm{q0-r}} - \frac{X_{\mathrm{m}}}{X_{\mathrm{s}}} v_{\mathrm{d0-s}} \\ \left(X_{\mathrm{r}} - \frac{X_{\mathrm{m}}^2}{X_{\mathrm{s}}}\right) I_{\mathrm{d0-r}} - \frac{X_{\mathrm{m}}}{X_{\mathrm{s}}} V_{\mathrm{q0-s}} \end{bmatrix}
\end{aligned}$$

Usually, the transients due to magnetic linkage in stator winding are ignored such that, $\frac{d}{dt}\psi_{\mathrm{ds}} = \frac{d}{dt}\psi_s = 0$. Based on this, the stator winding voltage equation can be written as,

$$\begin{cases} R_{\mathrm{s}} I_{\mathrm{ds}} + v_{\mathrm{ds}} + \psi_{\mathrm{qs}} = 0 \\ R_{\mathrm{s}} I_{\mathrm{qs}} + v_{\mathrm{qs}} - \psi_{\mathrm{ds}} = 0 \end{cases} \tag{3.27}$$

Using the equation derived for the stator winding flux in the early section, i.e., the $d-q$ components are taken and the relation for the current can be written as,

$$\begin{cases} I_{\mathrm{ds}} = -\frac{X_{\mathrm{m}} X_{\mathrm{s}}}{X_{\mathrm{s}}^2 + R_{\mathrm{s}}^2} I_{\mathrm{dr}} + \frac{X_{\mathrm{m}} R_{\mathrm{s}}}{X_{\mathrm{s}}^2 + R_{\mathrm{s}}^2} I_{\mathrm{qr}} - \frac{R_{\mathrm{s}}}{X_{\mathrm{s}}^2 + R_{\mathrm{s}}^2} v_{\mathrm{ds}} - \frac{X_{\mathrm{s}}}{X_{\mathrm{s}}^2 + R_{\mathrm{ds}}^2} V_{\mathrm{qs}} \\ I_{\mathrm{qs}} = -\frac{X_{\mathrm{m}} R_{\mathrm{s}}}{X_{\mathrm{s}}^2 + R_{\mathrm{s}}^2} I_{\mathrm{dr}} - \frac{X_{\mathrm{m}} X_{\mathrm{s}}}{X_{\mathrm{s}}^2 + R_{\mathrm{s}}^2} I_{\mathrm{qr}} + \frac{X_{\mathrm{s}}}{X_{\mathrm{s}}^2 + R_{\mathrm{s}}^2} v_{\mathrm{s}} - \frac{R_{\mathrm{s}}}{X_{\mathrm{s}}^2 + R_{\mathrm{s}}^2} v_{\mathrm{qs}} \end{cases} \tag{3.28}$$

To ease the simplification, ω_{r1} is equal to ω and the linearized equation for the rotor's winding voltage can be obtained as,

$$\begin{cases} \frac{d}{dt}\Delta\psi_{\mathrm{dr}} = \omega R_{\mathrm{r}} \Delta I_{\mathrm{dr}} + \omega \Delta v_{\mathrm{dr}} + \omega\left(1 - \omega_{\mathrm{r0}}\right) \Delta\psi_{\mathrm{qr}} - \omega \psi_{\mathrm{qr0}} \Delta\omega_{\mathrm{r}} \\ \frac{d}{dt}\Delta\psi_{\mathrm{qr}} = \omega R_{\mathrm{r}} \Delta I_{\mathrm{qr}} + \omega \Delta v_{\mathrm{qr}} - \omega\left(1 - \omega_{\mathrm{r0}}\right) \Delta\psi_{\mathrm{dr}} + \omega \psi_{\mathrm{dr0}} \Delta\omega_{\mathrm{r}} \end{cases} \tag{3.29}$$

Similarly, the rotor's flux equation can be expressed in linearized form as,

$$\begin{aligned} \Delta\psi_{\mathrm{dr}} &= -X_{\mathrm{r}} \Delta I_{\mathrm{dr}} - X_{\mathrm{m}} \Delta I_{ds} \\ \Delta\psi_{\mathrm{qr}} &= -X_{\mathrm{r}} \Delta I_{\mathrm{qr}} - X_{\mathrm{m}} \Delta I_{\mathrm{qs}} \end{aligned} \tag{3.30}$$

and, the linearized version of (3.27), stator winding voltage can be manipulated and written as,

$$\begin{cases} \Delta I_{\mathrm{ds}} = -\frac{X_{\mathrm{m}}X_{\mathrm{s}}}{X_{\mathrm{s}}^2+R_{\mathrm{ds}}^2}\Delta I_{\mathrm{dr}d} + \frac{X_{\mathrm{m}}R_{\mathrm{s}}}{X_{\mathrm{s}}^2+R_{\mathrm{ds}}^2}\Delta I_{\mathrm{qr}} - \frac{R_{\mathrm{s}}}{X_{\mathrm{s}}^2+R_{\mathrm{ds}}^2}\Delta v_{\mathrm{ds}} - \frac{X_{\mathrm{s}}}{X_{\mathrm{s}}^2+R_{\mathrm{ds}}^2}\Delta v_{\mathrm{qs}} \\ \Delta I_{\mathrm{qs}} = -\frac{X_{\mathrm{m}}R_{\mathrm{s}}}{X_{\mathrm{s}}^2+R_{\mathrm{ds}}^2}\Delta I_{\mathrm{dr}d} - \frac{X_{\mathrm{m}}X_{\mathrm{s}}^2}{X_{\mathrm{s}}^2+R_{\mathrm{ds}}^2}\Delta I_{\mathrm{qr}} + \frac{X_{\mathrm{s}}^2}{X_{\mathrm{s}}^2+R_{\mathrm{ds}}^2}\Delta v_{\mathrm{ds}} - \frac{R_{\mathrm{s}}}{X_{\mathrm{s}}^2+R_{\mathrm{ds}}^2}\Delta v_{\mathrm{qs}} \end{cases} \tag{3.54}$$

Using (3.26), (3.28) (3.30), and (3.54), the relation for rotor side current in $d-q$ domain can be formulated as,

$$\begin{aligned} \Delta I_{\mathrm{dr}} &= H_{\mathrm{dr}}(s)\Delta I_{\mathrm{drref}} - H_{\mathrm{qs}}(s)\Delta v_{\mathrm{qs}} + H_{\omega\mathrm{dr}}(s)\Delta\omega_{\mathrm{r}} \\ \Delta I_{\mathrm{qr}} &= H_{\mathrm{qr}}(s)\Delta I_{\mathrm{qrref}} - H_{\omega\mathrm{qr}}(s)\Delta\omega_{\mathrm{r}} - H_{\mathrm{ds}}(s)\Delta v_{\mathrm{ds}} \end{aligned} \tag{3.31}$$

where

$$\begin{aligned} H_{\mathrm{dr}}(s) &= \frac{H_4(s)}{H_4(s) - \frac{1}{\omega}\left(\frac{X_{\mathrm{m}}^2X_{\mathrm{s}}}{X_{\mathrm{s}}^2+R_{\mathrm{s}}^2} - X_{\mathrm{r}}\right)s + \frac{s_{\mathrm{r10}}X_{\mathrm{m}}^2R_{\mathrm{s}}}{X_{\mathrm{s}}^2+R_{\mathrm{s}}^2} + R_{\mathrm{r}}} \\ H_{\mathrm{qs}}(s) &= \frac{\frac{\mathrm{r10}X_{\mathrm{m}}R_{\mathrm{s}}}{X_{\mathrm{s}}^2+R_{\mathrm{s}}^2}}{H_4(s) - \frac{1}{\omega}\left(\frac{X_{\mathrm{m}}^2X_{\mathrm{s}}^2}{X_{\mathrm{s}}^2+R_{\mathrm{s}}^2} - X_{\mathrm{r}}\right)s + \frac{\mathrm{r10}X_{\mathrm{m}}^2R_{\mathrm{s}}}{X_{\mathrm{s}}^2+R_{\mathrm{s}}^2} + R_{\mathrm{r}}} \\ H_{\omega\mathrm{dr}}(s) &= \frac{\frac{X_{\mathrm{m}}R_{\mathrm{s}}(v_{\mathrm{qs0}}+X_{\mathrm{m}}I_{\mathrm{dr0}})}{X_{\mathrm{s}}^2+R_{\mathrm{s}}^2}}{H_4(s) - \frac{1}{\omega}\left(\frac{X_{\mathrm{m}}^2X_{\mathrm{s}}}{X_{\mathrm{s}}^2+R_{\mathrm{s}}^2} - X_{\mathrm{r}}\right)s + \frac{s_{\mathrm{r10}}X_{\mathrm{m}}^2R_{\mathrm{s}}}{X_{\mathrm{s}}^2+R_{\mathrm{s}}^2} + R_{\mathrm{r}}} \\ H_{\mathrm{qr}}(s) &= \frac{H_2(s)}{\frac{1}{\omega}\left[-\frac{X_{\mathrm{m}}^2X_{\mathrm{s}}}{X_{\mathrm{s}}^2+R_{\mathrm{s}}^2} + X_{\mathrm{r}}\right]s + R_{\mathrm{r}} + \frac{s_{\mathrm{r10}}X_{\mathrm{m}}^2R_{\mathrm{s}}}{X_{\mathrm{s}}^2+R_{\mathrm{s}}^2} + H_2(s)} \\ H_{\omega\mathrm{qr}}(s) &= \frac{\frac{X_{\mathrm{m}}^2R_{\mathrm{s}}I_{\mathrm{qr0}}}{X_{\mathrm{s}}^2+R_{\mathrm{s}}^2}}{\frac{1}{\omega}\left[-\frac{X_{\mathrm{m}}^2X_{\mathrm{s}}}{X_{\mathrm{s}}^2+R_{\mathrm{s}}^2} + X_{\mathrm{r}}\right]s + R_{\mathrm{dr}} + \frac{\omega_{\mathrm{sr10}}X_{\mathrm{m}}^2R_{\mathrm{s}}}{X_{\mathrm{s}}^2+R_{\mathrm{s}}^2} + H_2(s)} \\ H_{\mathrm{s}d}(s) &= \frac{\frac{\omega_{\mathrm{sr10}}X_{\mathrm{m}}R_{\mathrm{s}}}{X_{\mathrm{s}}^2+R_{\mathrm{s}}^2}}{\frac{1}{\omega}\left[-\frac{X_{\mathrm{m}}^2X_{\mathrm{s}}}{X_{\mathrm{s}}^2+R_{\mathrm{s}}^2} + X_{\mathrm{r}}\right]s + R_{\mathrm{dr}} + \frac{\omega_{\mathrm{sr10}}X_{\mathrm{m}}^2R_{\mathrm{s}}}{X_{\mathrm{s}}^2+R_{\mathrm{s}}^2} + H_2(s)} \end{aligned} \tag{3.32}$$

3.2.2 Dynamics of Inner Control Loops of the GSC and Output Filter in the Current Timescale

Extending the equations obtained in the previous section for the detailed model of DFIG, GSC dynamics in the current timescale can be derived by considering the equation derived for DC link converter. Therefore, the linearization of (3.18) yields,

$$\begin{cases} \Delta\dot{I}_{\mathrm{d,DC}} = \frac{\omega\Delta v_{\mathrm{d,DC}}}{X_{\mathrm{f}}} - \frac{\omega\Delta v_{\mathrm{ds}}}{X_{\mathrm{f}}} + \omega\Delta I_{\mathrm{q,DC}} \\ \Delta\dot{I}_{\mathrm{q,DC}} = \frac{\omega\Delta v_{\mathrm{q,DC}}}{X_{\mathrm{f}}} - \frac{\omega\Delta v_{\mathrm{qs}}}{X_{\mathrm{f}}} - \omega\Delta I_{\mathrm{d,DC}} \end{cases} \tag{3.33}$$

From Fig.3.4 and using (3.18), the inner control loop of GSC with linearized dynamics can be written as,

$$\begin{cases} \Delta v_{\mathrm{q,DC}} = \left(k_{\mathrm{p6}} + \dfrac{k_{\mathrm{i6}}}{s}\right)\left(\Delta I_{\mathrm{q,DC}ref} - \Delta I_{\mathrm{q,DC}q}\right) + \Delta v_{\mathrm{qs}} + X_{\mathrm{f}}\Delta I_{\mathrm{DC}} \\ \qquad\quad = H_6(s)\left(\Delta I_{\mathrm{q,DCref}} - \Delta I_{\mathrm{q,DC}}\right) + \Delta v_{\mathrm{qs}} + X_{\mathrm{f}}\Delta I_{\mathrm{dc}} \\ \Delta v_{\mathrm{d,DC}} = \left(k_{\mathrm{p7}} + \dfrac{k_{\mathrm{i7}}}{s}\right)\left(\Delta I_{\mathrm{d,DCref}} - \Delta I_{\mathrm{d,DC}}\right) + \Delta v_{\mathrm{ds}} + X_{\mathrm{f}}\Delta I_{\mathrm{q,DC}} \\ \qquad\quad = H_7(s)\left(\Delta I_{\mathrm{d,DCref}} - \Delta I_{\mathrm{d,DC}}\right) + \Delta v_{\mathrm{ds}} + X_{\mathrm{f}}\Delta I_{\mathrm{q,DC}} \end{cases} \tag{3.34}$$

From (3.33) and using (3.34), the inner loop dynamics of the RSC including the output filter can be expressed as:

$$\begin{aligned} \Delta I_{\mathrm{q,DC}} &= \frac{\omega H_6(s)}{sX_{\mathrm{f}} + \omega H_6(s)}\Delta I_{\mathrm{q,DCref}} = H_{\mathrm{q,DC}}(s)\Delta I_{\mathrm{q,DC}ref} \\ \Delta I_{\mathrm{d,DC}} &= \frac{\omega H_7(s)}{sX_{\mathrm{f}} + \omega H_7(s)}\Delta I_{\mathrm{d,DCref}} = H_{\mathrm{d,DC}}(s)\Delta I_{\mathrm{d,DC}ref} \end{aligned} \tag{3.35}$$

3.3 Stability Criteria and Risk of Oscillations

3.3.1 Risk of Oscillations due to Dynamics of PLL

Unlike low-frequency oscillations or torsional oscillations in conventional wind power systems, recent studies show that complex electromagnetic oscillations in weak grids emerge due to SSCI between components of the weak grid and control of IBRs [35]. The phenomenon is demonstrated by incidents reported in the last decade [4], emerging primarily due to the employment of phase-locked loop (PLL) and d-q transformation-based IBR control [113], resulting in complex sub- and/or super-synchronous oscillations [114, 115]. Examples of such incidents are widely reported in power networks around the world, examples include Hami [115], ERCOT [116], and Guyuan [117] networks.

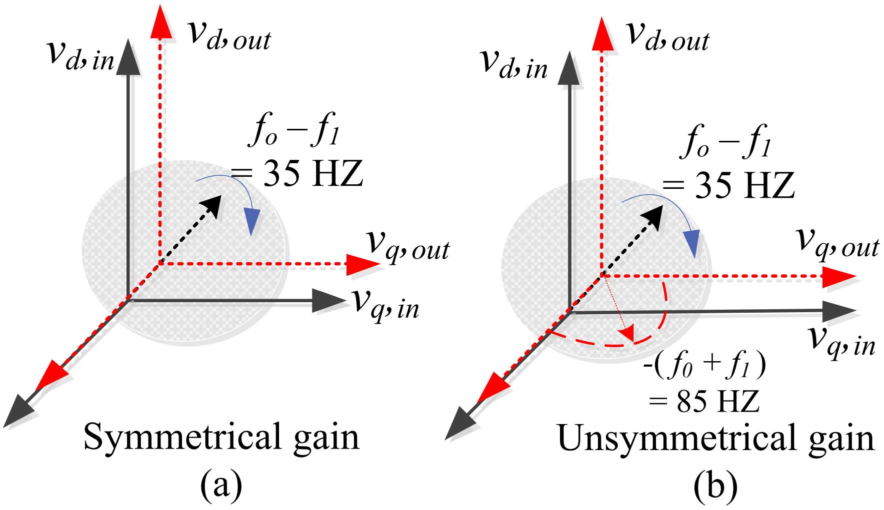

Figure 3.6: dq transformation and coupling frequency effect due to (a) symmetrical gains, (b) unsymmetrical gains.

When an IBR with PLL for control and grid synchronization experiences a disturbance with Inter-harmonic Frequency (IhF), subsequent effect in terms of coupled frequencies can be observed in the output [3] as shown in Fig. 3.6. For balanced grid and symmetrical gains of PLL as shown in Fig. 3.6a, the IhF with 15 Hz component in the dq rotating frame will appear as 35 Hz component at the control input. Similarly, for unsymmetrical gains and unbalanced grid conditions, an additional coupled frequency appears at the control inputs of current loops as a result of voltage perturbation by IhF [118]. To make it simple, the interpolation of these coupled frequency-based modes (sub-synchronous (subSR) and super-synchronous (supSR)) into fundamental frequency interacts with other network components and emerges as complex and multi-mode synchronous resonance (MSR) based oscillations in the network [119]. Therefore, the theoretical bounds suggest a potential increase in the complexity of the phenomena for networks dominated by IBRs, significantly impacting the PCC impedance at varying operating conditions due to complex modes [120]. Therefore, it is possible that dynamics of grid connected WTGs are dominated by the effective performance of the PLL when the weak grid is subject to operational variations. The dynamics of these PLLs appear as poorly damped modes when the control system of the WTG is challenged with operational uncertainties and disturbance in the network. Therefore, to gain a proper understanding of the involvement of the PLL-based oscillation modes that may intend to become poorly damped when the WTG is in weak grid conditions, it becomes important to analyse the system with the conventional method of stability analysis. Therefore, the detailed model derived in section 2 is used to analyse the effect of PLL on other dynamics of the grid-connected WTG. This is demonstrated analytically through the widely applicable technique used for analysing the stability of the system. Generally, the WTG system with sophisticated control mechanisms is attributed as high-order nonlinear dynamic system. However, to ease the simplicity for derivation and provide a foundational argument, the single grid connected WTG system can be considered as a linear dynamic system. Therefore, it is widely known in the control system that any dominated modes of oscillation present in a system are dominated over the dynamics of the whole network. Therefore, the WTG-based system can be approximated as the second-order system describing the dominant modes of oscillations by the PLL.

To obtain the reduced-order model of the WTG dominated by the dynamics of the PLL, the earlier equations; (3.25) derived from (3.23) for the PLL dynamics can be leveraged to simplify and obtain the stability limits [121]. This is achieved by linearizing the model of the DFIG and ignoring all the dynamics in a slow time scale except the PLL. Thus, the detailed linearization reduced order model of the DFIG given in [121] can be adopted to assess the affect of PLL in escalating the oscillations. To simplify, the dynamics are given as,

$$\begin{aligned}&\frac{d}{dt}\Delta\mathbf{X}_{\text{pll}} = \mathbf{A}_{\text{pll}}\Delta\mathbf{X}_{\text{pll}} + \mathbf{B}_{\text{pll}}\Delta\mathbf{V}_{xy}\\&\Delta\mathbf{I}_{xy} = \mathbf{C}_{\text{pll}}\Delta\mathbf{X}_{\text{pll}}\end{aligned} \tag{3.36}$$

where

$$\begin{aligned}
\Delta\mathbf{X}_{\mathrm{pll}} &= \Delta\mathbf{X}_4 = \begin{bmatrix} \Delta x & \Delta\theta \end{bmatrix}^{\mathrm{T}} \\
\mathbf{A}_{\mathrm{pll}} &= \begin{bmatrix} 0 & -k_{\mathrm{i}}v \\ 1 & -k_{\mathrm{p}}v \end{bmatrix}, \mathbf{B}_{\mathrm{pll}} = \begin{bmatrix} -\frac{k_{\mathrm{i}}v_y}{v} & \frac{k_{\mathrm{i}}v_x}{v} \\ -\frac{k_{\mathrm{p}}v_y}{v} & \frac{k_{\mathrm{p}}v_x}{v} \end{bmatrix} \\
\mathbf{C}_{\mathrm{pll}} &= \begin{bmatrix} 0 & \mathbf{k}_5 \end{bmatrix} = \begin{bmatrix} 0 & -I_y \\ 0 & I_x \end{bmatrix} \\
\mathbf{k}_5 &= \begin{bmatrix} -\sin\theta & -\cos\theta \\ \cos\theta & -\sin\theta_0 \end{bmatrix} \begin{bmatrix} I_{\mathrm{d0}} \\ I_{\mathrm{q0}} \end{bmatrix} = \begin{bmatrix} -I_y \\ I_x \end{bmatrix}
\end{aligned} \tag{3.37}$$

The PLL-dominated reduced order model can be obtained using mathematical alterations from the full-order state-space model of the grid-connected WTG as,

$$\begin{aligned}
\frac{d}{dt}\Delta\mathbf{X}_{\mathrm{pll}} &= \left(\mathbf{U}_{1pll} - \frac{X_{\mathrm{L}}}{\omega}\mathbf{B}_{\mathrm{pll}}\mathbf{C}_{\mathrm{pll}}\right)^{-1} \left(\mathbf{A}_{\mathrm{pll}} + X_{\mathrm{L}}\mathbf{B}_{\mathrm{pll}}\mathbf{U}_{2pll}\mathbf{C}_{\mathrm{pll}}\right)\Delta\mathbf{X}_{\mathrm{pll}} \\
&= \mathbf{A}_{\mathrm{pll}}\Delta\mathbf{X}_{\mathrm{pll}}
\end{aligned} \tag{3.38}$$

Let P and Q be the steady-state active and reactive power output from the WTG. It can have

$$\begin{aligned}
P &= I_x v_x + I_y v_y \\
Q &= I_x v_y - I_y v_x
\end{aligned} \tag{3.39}$$

Thus, the characteristic equation can be obtained as,

$$\begin{aligned}
\mathbf{A}_{\text{pll}} &= \left(\mathbf{U}_{1pll} - \frac{X_{\text{L}}}{\omega}\mathbf{B}_{\text{pll}}\mathbf{C}_{\text{pll}}\right)^{-1}\mathbf{A}_{\text{pll}} + X_{\text{L}}\mathbf{B}_{\text{pll}}\mathbf{U}_{2pll}\mathbf{C}_{\text{pll}} \\
&= \frac{1}{1-\frac{X_{\text{L}}}{\omega}k_{\text{p}}\frac{P}{v}}\begin{bmatrix} 1-\frac{X_{\text{L}}}{\omega}k_{\text{p}}\frac{P}{v} & \frac{X_{\text{L}}}{\omega}k_{\text{i}}\frac{P}{v} \\ 0 & 1 \end{bmatrix}\begin{bmatrix} 0 & X_{\text{L}}k_{\text{i}}\frac{Q_0}{v}-k_{\text{i}}v \\ 1 & X_{\text{L}}k_{\text{p}}\frac{Q_0}{v}-k_{\text{p}}v \end{bmatrix} \\
&= \frac{1}{1-\frac{X_{\text{L}}}{\omega}k_{\text{p}}\frac{P}{v}}\begin{bmatrix} \frac{X_{\text{L}}}{\omega}k_{\text{i}}\frac{P}{v} & a_1 \\ 1 & X_{\text{L}}k_{\text{p}}\frac{Q_0}{v}-k_{\text{p}}v \end{bmatrix}
\end{aligned} \tag{3.40}$$

where $a_1 = \left(1-\frac{X_{\text{L}}}{\omega}k_{\text{p}}\frac{P}{v}\right)\left(X_{\text{L}}k_{\text{i}}\frac{Q_0}{v}-k_{\text{i}}v\right) + \frac{X_{\text{L}}}{\omega}k_{\text{i}}\frac{P}{v}\left(X_{\text{L}}k_{\text{p}}\frac{Q_0}{v}-k_{\text{p}}v\right)$

3.3.2 Small-Signal Stability Limit of the Single Grid Connected WTG System Dominated by PLL Dynamics

Using (3.40), The characteristic equation for the grid connected WTG dominated by the dynamics of the PLL can be obtained as $|\lambda\mathbf{U}_{1pll} - \mathbf{A}_{\text{pll}}| = 0$. Solving this equation yields,

$$
\begin{aligned}
&\mid \lambda \mathbf{U}_{1pll} - \mathbf{A}_{\text{pll}} \mid \\
&\quad = \left[\lambda\left(1 - \frac{X_{\text{L}}}{\omega} k_{\text{p}} \frac{P}{v}\right) - \frac{X_{\text{L}}}{\omega} k_{\text{i}} \frac{P}{v}\right] \Bigg[\Bigg(\lambda\left(1 - \frac{X_{\text{L}}}{\omega} k_{\text{p}} \frac{P}{v}\right) - X_{\text{L}} k_{\text{p}} \frac{Q_0}{v} + k_{\text{p}} v\Bigg] \\
&\qquad - \left(1 - \frac{X_{\text{L}}}{\omega} k_{\text{p}} \frac{P}{v}\right)\left(X_{\text{L}} k_{\text{i}} \frac{Q_0}{v} - k_{\text{i}} v\right) - \frac{X_{\text{L}}}{\omega} k_{\text{i}} \frac{P}{v}\left(X_{\text{L}} k_{\text{p}} \frac{Q_0}{v} - k_{\text{p}} v\right) \\
&\quad = \left(1 - \frac{X_{\text{L}}}{\omega} k_{\text{p}} \frac{P}{v}\right)^2 \lambda^2 + \left(1 - \frac{X_{\text{L}}}{\omega} k_{\text{p}} \frac{P}{v}\right)\left(-\frac{X_{\text{L}}}{\omega} k_{\text{i}} \frac{P}{v} - X_{\text{L}} k_{\text{p}} \frac{Q_0}{v} + k_{\text{p}} v\right)\lambda \\
&\qquad + \frac{X_{\text{L}}}{\omega} k_{\text{i}} \frac{P}{v}\left(X_{\text{L}} k_{\text{p}} \frac{Q_0}{v} - k_{\text{p}} v\right) \\
&\qquad - \left(1 - \frac{X_{\text{L}}}{\omega} k_{\text{p}} \frac{P}{v}\right)\left(X_{\text{L}} k_{\text{i}} \frac{Q_0}{v} - k_{\text{i}} V\right)_0 - \frac{X_{\text{L}}}{\omega} k_{\text{i}} \frac{P}{v}\left(X_{\text{L}} k_{\text{p}} \frac{Q_0}{v} - k_{\text{p}} v\right) \\
&\quad = \left(1 - \frac{X_{\text{L}}}{\omega} k_{\text{p}} \frac{P}{v}\right)^2 \lambda^2 + \left(1 - \frac{X_{\text{L}}}{\omega} k_{\text{p}} \frac{P}{v}\right)\left(-\frac{X_{\text{L}}}{\omega} k_{\text{i}} \frac{P}{v} - X_{\text{L}} k_{\text{p}} \frac{Q_0}{v} + k_{\text{p}} v\right)\lambda \\
&\qquad - \left(1 - \frac{X_{\text{L}}}{\omega} k_{\text{p}} \frac{P}{v}\right)\left(X_{\text{L}} k_{\text{i}} \frac{Q_0}{v} - k_{\text{i}} v\right) = 0
\end{aligned}
\tag{3.41}
$$

Hence,

$$
\begin{aligned}
&\mid \lambda \mathbf{U}_{1pll} - \mathbf{A}_{\text{pll}} \mid \\
&\quad = \left(1 - \frac{X_{\text{L}}}{\omega} k_{\text{p}} \frac{P}{v}\right)\lambda^2 + \left(-\frac{X_{\text{L}}}{\omega} k_{\text{i}} \frac{P}{v} - X_{\text{L}} k_{\text{p}} \frac{Q_0}{v} + k_{\text{p}} v\right)\lambda \\
&\qquad + \left(\frac{Q_0}{v} + k_{\text{i}} v - X_{\text{L}} k_{\text{i}}\right) = 0
\end{aligned}
\tag{3.42}
$$

According to Routh-Hurwitz criteria (RHC), the characteristic equation should have a definite positive solution for the terms in (3.42) to ensure stability; therefore, this can be written as,

$$
\begin{aligned}
&\left(-\frac{X_\mathrm{L}}{\omega}k_\mathrm{i}\frac{P}{v}-X_\mathrm{L}k_\mathrm{p}\frac{Q_0}{v}+k_\mathrm{p}v\right)>0\\
&\left(1-\frac{X_\mathrm{L}}{\omega}k_\mathrm{p}\frac{P}{v}\right)>0\\
&\left(\frac{Q_0}{v}+k_\mathrm{i}v-X_\mathrm{L}k_\mathrm{i}\right)>0
\end{aligned}
\tag{3.43}
$$

(3.43)(2.63) can be rearranged to highlight the key elements contributing effectively towards the PLL-dominated instability in grid-connected WTGs,

$$
\begin{aligned}
&\frac{k_\mathrm{p}}{\omega}<\frac{v}{X_\mathrm{L}P}\\
&X_\mathrm{L}k_\mathrm{i}P+\omega X_\mathrm{L}k_\mathrm{p}Q_0<\omega k_\mathrm{p}v^2
\end{aligned}
\tag{3.44}
$$

The $X_\mathrm{L}Q_0 < v^2$ for the system to remain stable and this is determined by $X_\mathrm{L}k_\mathrm{i}P+\omega X_\mathrm{L}k_\mathrm{p}Q_0 < \omega k_\mathrm{p}v^2$ such that $\omega X_L Q_o k_p < v_2 k_p \omega$ for all values of $X_L Q_o k_p$.

Therefore, (3.44) can be re-arranged to obtain,

$$
\begin{aligned}
&\frac{k_\mathrm{p}}{\omega}<\frac{v}{X_\mathrm{L}P}\\
&\frac{k_\mathrm{i}}{\omega k_\mathrm{p}}+\frac{Q_0}{P}<\frac{v^2}{X_\mathrm{L}P}
\end{aligned}
\tag{3.45}
$$

The grid-connected WTG is mainly impacted by three major conditions, thus escalating control-dominated oscillations in the power network. The major factors can be enumerated as 1) weak grid conditions, 2) the improper setting of the PLL gains and the design of the control for the converters associated with WTG, analytically detailed in [7]. Weak grid condition is mainly determined by the rated voltage, active power capacity and line reactance, given as,

$$
\mathrm{SCR}=\frac{v^2}{P_\text{WTG-rated}\,X_\mathrm{L}}
\tag{3.46}
$$

where $P_{\text{WTG - rated}}$ is the rated capacity of the grid connected WTG. For ensuring stability, the SCR of the grid-connected WTG cannot be less than zero. However; generally the grid is considered weak if the SCR < 3. Therefore, (3.46) can be written as,

$$\text{SCR} = \frac{v^2}{X_{\text{L}} P_{\text{WTG-rated}}} \geq 1 \tag{3.47}$$

The $P_{\text{WTG-rated}}$ and v are taken in p.u to determine the SCR of the grid with the reactance of the transmission line. Therefore, this can be amended in p.u as,

$$\text{SCR} \approx \frac{1}{X_{\text{L}}} \geq 1 \tag{3.48}$$

Hence, the higher and varying x_{L} corresponds to the weakened SCR and is determined as a weak WTG-based grid connection, consequently. In addition to that, the SCR condition is in alignment with the early derived small signal stability limit (3.45). Thus, the relation between these two ((3.47) and (3.45)) clearly highlights the importance of the careful consideration of the grid reactance (X_L) and heavy loading condition (higher values of $P_{WTG-rated}$), consequently leading to the higher risk of instability for the grid connected WTGs. Further to that, the PLL dependent response of RSC and GSC controls is explicitly related to the grid conditions. Therefore, careful consideration should be given to the internal control gains of the PLL meeting the varying operating conditions of the gird, as improper settings violate the small signal stability condition given by (3.45), consequently leading to a higher risk of instability. From (3.45) and (3.46), it can be written as,

$$SCR = \frac{v^2}{X_{\text{L}} P_{\text{WTG-rated}}} \leq \frac{v}{X_{\text{L}} P} \tag{3.49}$$

Consider if the gains of the PLL controller are set as follows;

$$\begin{aligned} &\frac{k_{\mathrm{p}}}{\omega} \leq 1 \\ &\frac{k_{\mathrm{i}}}{\omega k_{\mathrm{p}}} + \frac{Q}{P} \leq 1 \end{aligned} \tag{3.50}$$

Then, (3.50) should satisfy the stability criteria defined in (3.45) and support (3.49) for the grid connected WTG to remain stable.

Generally, the grid codes emphasize operating the IBRs and specifically the WTG-based generation sources to provide ±0.95 power factor for normal operating conditions. Thus, referring to (3.50), the gains (k_p and k_i) should be chosen such that the cumulative value of the terms ($\frac{k_i}{\omega k_p}$) should remain less than one. For example, if the grid-connected WTG is operated with a certain power factor giving maximum value for Q/P equivalent to 0.30, then the gains in ($\frac{k_i}{\omega k_p}$) should be flexible enough that their overall value doesn't exceed 0.70. This way, the grid connected WTG system dominated by the dynamics of PLL remain stable.

3.4 Example Cases

From the previous mathematical analysis, it can be observed the stability of the control loops play a vital role in emerging the oscillations. This is mainly due to varying operating conditions affecting several factors at the POI. Thus, the gains of the whole control system and specifically the PLL should be adjusted to avoid such problems in the network. The example of such phenomena is illustrated by employing the full order model of the grid-connected DFIG as shown in Fig.3.1. To illustrate the stability dynamics with changing operation, the reference for

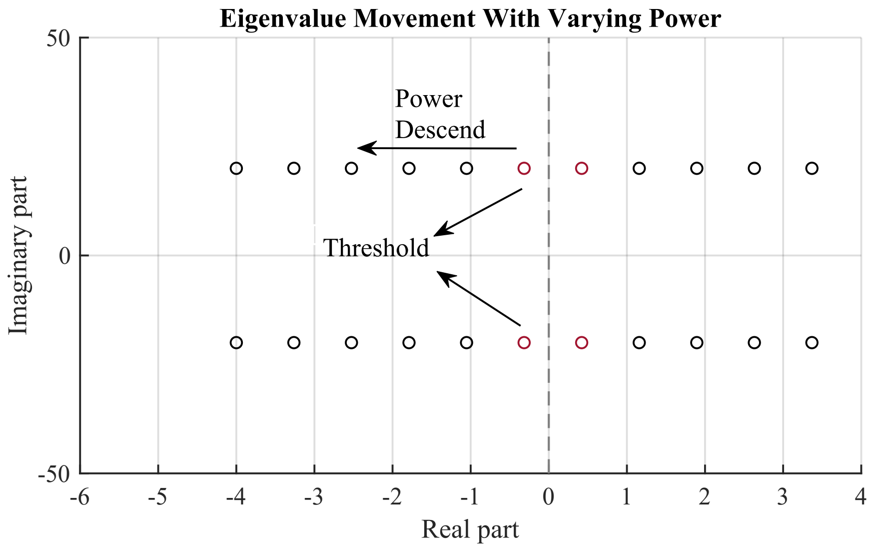

Figure 3.7: Effect of varying power on the stability of control mechanism

output active power is varied from 0.35pu to 0.8pu while X_L at POI is taken kept 1pu. The control gains are adjusted in order to provide a stable value of $\frac{k_i}{\omega k_p}$ as 0.3/200.

From (3.45), the varying output affects the overall value and is changing dynamically. It can be observed that 0.55pu output behave as a threshold barrier for the stability region. This is illustrated in Fig.3.7 where the poles are significantly moving to the right half after the increased power threshold. The effect in the output power can be observed in Fig.3.8 where considerable oscillations emerges as a consequence of instability in the control dynamics.

The validation of the mathematical conclusions provided in (3.45) is further verified through the two machine-power system networks with a grid-connected WTG-based wind farm. The wind farm is comprised of 267 WTGs aggregated with 1.5MW each. The details of the WTGs are given in [89], while the network parameters are obtained from [44]. From (3.49), it can be observed that variations in the X_L and P_{rated} significantly affect the X/R ratio of the grid. Therefore, the

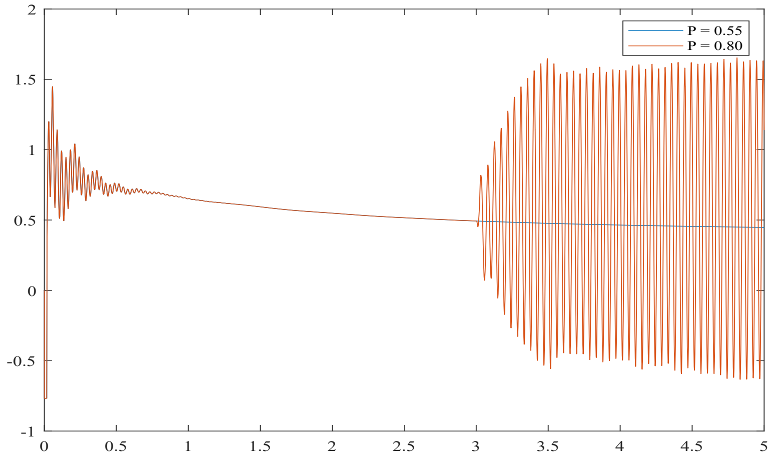

Figure 3.8: Simulation test for emerging oscillations due to control instability -Case 1

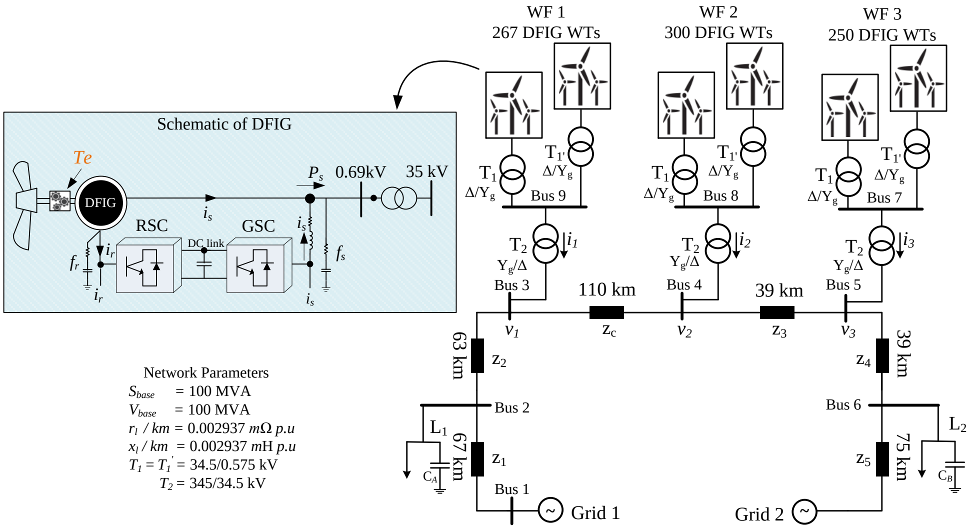

Figure 3.9: Network configuration used for simulation test case 2

nonlinear simulations are conducted for the grid with $X/R \leq 2.0$ to illustrate the control dynamics for a weak grid. For instance, the control gains are first selected as $k_p = 0.233$ and $k_i = 2.67$ for case-1, and the corresponding dynamics are examined by varying the POI voltage from 1.0 pu to 0.90 pu. To meet the grid code compliance, the WTG is supposed to provide stable-rated power at POI.

However, the variations in the voltage significantly affect the SCR and explicitly challenge the stability of control dynamics. For the same scenario in the case-2, when the control gains are adjusted ($k_p = 2.30$ and $k_i = 22.60$), though still oscillations persist, however the damping modes are considerably enhanced as illustrated in Fig. 3.10. Therefore, this section emphasize on the concept to illustrate the explicit attachment of control dynamics with the system stability and emergence of power network oscillations. These stability violations of the control loops for different time-scale affect the operation of the WTG system and consequently escalate significant oscillations in the network [7].

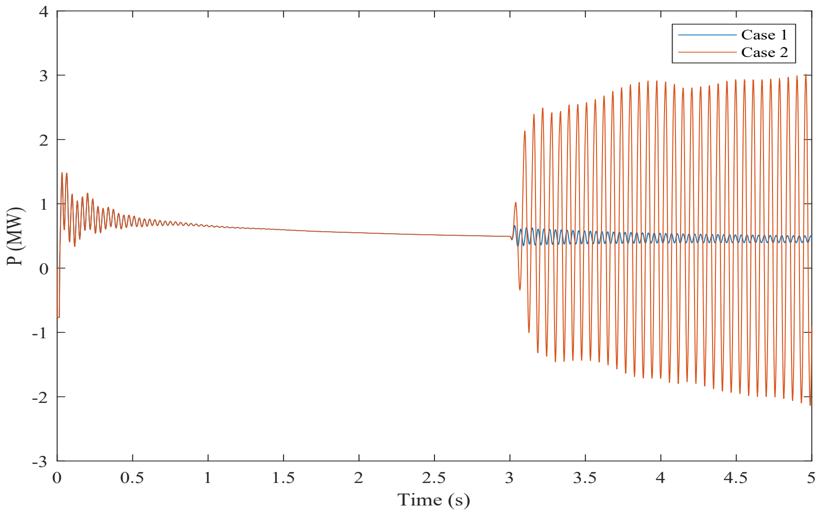

Figure 3.10: Simulation test for emerging oscillations due to control instability -Case 2

3.5 Summary

This chapter concludes a detailed modeling of the IBRs in the renewable energy dominated grids. The type III and type IV models of the WTG are specifically considered due to their versatile operating conditions and control functionalities.

Considering these, the basic mathematical model of the WTG is established. The dynamics of the rotor and grid side converters are modeled and detailed analysis of control functions along with PLL are provided. The oscillations quantification is justified by mathematically proving the effect of inner control loops on both rotor and grid side converters. Last but not least, the stability criteria based on the small signal stability analysis is provided. This explicitly explains the risk of oscillations due to the dynamics of PLL and the impact on the further network. Finally, the mathematical analysis are backed by example cases to provide foundational framework of understanding for the research work. The last section provide details analysis of how the various conditions increases the risk of instability and consequently the oscillations propagation in the network.

Chapter 4

Detection and Localization of Complex Oscillations

4.1 Introduction

Unlike low-frequency oscillations or torsional oscillations in conventional wind power systems, recent studies show that complex electromagnetic oscillations in weak grids emerge due to SSCI between components of the weak grid and control system of IBRs [35] in the power generation plants. A detailed summary of SSCI events occurred worldwide in different grids is provided in [4]. Detailed studies and post event analysis of these events suggest the involvement of phase-locked loop (PLL), and its dynamics associated with the voltage and current control loops inside the IBRs [113]. Thus, involvement of these dynamics along with network perturbations, results in complex SSCI [114,115]. Examples of such incidents are widely reported in power networks around the world, where practical examples include Hami [115], ERCOT [116], and Guyuan [117] networks.

It is widely recognized from the reported incidents that a key origin of these disturbances is the involvement of IBRs (WTGs and Solar) in the power networks. The findings in [4] suggest that the complex SSCI which stems from coupled frequency at sub and super synchronous modes, and their linkage is emphasized with type-3 and type-4 WTGs in line compensated networks and weak grid arrangements. This coupled frequency concept is reported to be evolved from the fast control mechanism of the IBRs and is a consequence of the PLL response to network disturbances and inter-harmonics, as illustrated in Fig. 4.1. For instance, in balanced grids and idle gains of PLL as shown in Fig. 4.1a, the inter-harmonic component with 15 Hz in the dq rotating frame will appear as a 35 Hz component at the control input. Similarly, for unsymmetrical gains and unbalanced grid conditions, an additional coupled frequency appears at the control inputs of current control loops as a result of voltage perturbations by inter-harmonic components [118]. To further explain, the interpolation of these coupled frequency-based modes (sub-synchronous and super-synchronous) into fundamental frequency of the IBRs plant interact with network components, consequently leading to SSR with complex modes based oscillations in the network [3, 119]. Therefore, the theoretical bounds as earlier derived in chapter 3, suggest a potential increase in the complexity of the phenomena for networks dominated by IBRs, significantly impacting the PCC impedance at varying operating conditions due to complex modes [120]. The precise information regarding oscillations comprising complex modes facilitate the accurate determination of impedance, hence allowing for the identification of the source of disturbance up/downstream of the connection point. Therefore, it is of great interest to detect all possible modes using a systematic approach such that preventive measures can be employed and thus contribute to realistic self-healing and resilient power systems.

Assuming that the oscillations have a single mode (e.g. subSR), and are stationary in nature over a designed window, it is relatively straightforward to detect its presence by using synchrophasors data, DFT based algorithms [122, 123], and designing bandpass filters [124]. However, the constraints on reporting rate and superimposition of data with filters typically limit the observability of network disturbances constituted by modes with indistinct frequency bandwidths and inter-harmonic orders. An approach reported in [15, 46] proposed a DFT based technique to detect the supSR modes while considering the theoretical constraints such as spectral aliasing and reporting rate limitations. However, this is only applicable for the events with stationary modes which are distinct and located at definite bins of DFT spectra.

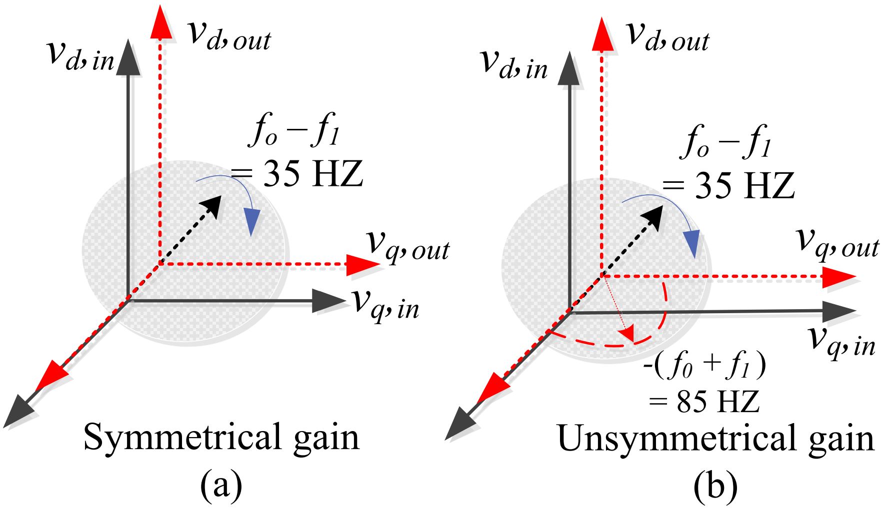

Figure 4.1: dq transformation and coupling frequency effect due to (a) symmetrical gains, (b) unsymmetrical gains.

Keeping in view the utmost importance of localizing the source of oscillations in the power network, this chapter offers the following insights.

- A detailed analytical approach is derived to provide a foundational background on the fidelity of measurements acquired through DFT based approaches integrated into monitoring devices. The approach's shortcomings are underscored by employing a state-of-the-art sliding DFT (SDFT) methodology to examine the simplest case of complex SSCI.

- Through detailed mathematical analysis and a review of the latest literature, this study emphasizes the adoption of SWMUs as monitoring devices. By adopting SWMUs, a novel realigned adaptive IFST (AIFST) is proposed to facilitate the accurate identification of complex oscillation modes under varying power network conditions.
- The admittance model subjugated by multi mode synchronous resonance due to coupled frequencies at the specific operating point conditions is derived from the reconstructed modes.
- Taking into account the reconstructed modes and the subsequent admittance model, the complex power flow is derived. This enables the characterization of the oscillation sources for the active/reactive oscillations in the network.

4.2 Motivation

In recent years, the reporting of SSR events has become more common due to the rapid penetration of power grids with renewable power sources. The SSR based oscillation events have been frequently observed for windfarm based power networks connecting it through line compensations. However, the new phenomena of complex oscillations have emerged due to the integration of IBRs interpolating range of frequencies in the fundamental frequency. Such events are significantly important to detect for stable operation of the system as the event results in escalating power oscillations in the network that can lead to the disconnection of generation sources and may damage the generators. Detection of such events using PMUs possess significant challenges in terms of their limited reporting rate, spectral leakage and picket fence effect, which intuitively report false amplitude and frequency of the modes of interest while detecting multi-mode resonance. Therefore, a systematic approach has been derived for the localization of such oscillations exhibiting complex frequency modes. This is achieved by leveraging novel synchro-waveforms that omit the prerequisites for qualifying the Nyquist criteria to achieve optimal samples. From these, novel AIFST is derived and adopted to achieve intact and precise determination of the SSCI modes. The approach provides confidence for identifying the source of SSCI in IBR-dominated networks using the augmented admittance model and SSCI-based power flow. In the goal of enhancing the sustainability and resilience of grids, the feasibility and applicability of the approach for real-world applications are demonstrated by employing real-world datasets. The results convey a strong justification for the adoption of the method as a step towards mitigating SSCI in IBR networks.

4.3 Fidelity of Synchro-Phasors in Reporting Complex SSCI

PMUs are widely deployed in power networks, providing synchronized phasors of the voltage and currents obtained in transmission and distribution sectors. Their specific applications are widely seen in WAMS, inertia estimation and power network stability. Since there has been significant change in the power network topology, network disturbances included SSCI based oscillations have similarly evolved. PMUs have been widely deployed in modern power networks to obtain synchrophasors and monitor power network oscillations. The principal concept of acquiring phasors using PMUs is the fundamental DFT based approach. Some advanced variants of this approach are adopted to detect the SSR based oscillations in the power network using WAMS. SSR based oscillations have typically bandwidth below 25 Hz and are readily observable with the current PMU reporting rate. On the contrary, complex oscillations exhibit frequency modes which are non-stationary and have inter harmonic modes. The bandwidth of these oscillations range from 5 Hz to 100 Hz in the case the modes are coupled; otherwise variations up to several hundred Hertz exist. Therefore, in this thesis such oscillation are referred to as complex and Multi Mode Synchronous Resonance (MSR) driven oscillations.

The MSR based oscillations originating due to the control interactions of IBRs in weak grids have been a focus due to a limited understanding of their origin [35]. The presence of complex modes in SSCI based oscillation is different compared to the mechanism of harmonics, low-frequency oscillations and forced oscillations due to time-varying frequency and damping characteristics. Typically, these oscillations encompass a wide range of frequencies. The dominant modes often exhibit coupled frequencies or a combination of coupled and other frequency modes, leading to MSR based oscillations [113]. They usually originate as a result of a PLL response to unbalanced grid conditions. Consequently, in such conditions the control system starts interacting with the power network components, resulting in complex oscillations, and making it challenging to detect. Such phenomena best aligns with the illustration of frequency coupled modes shown in Fig. 4.1

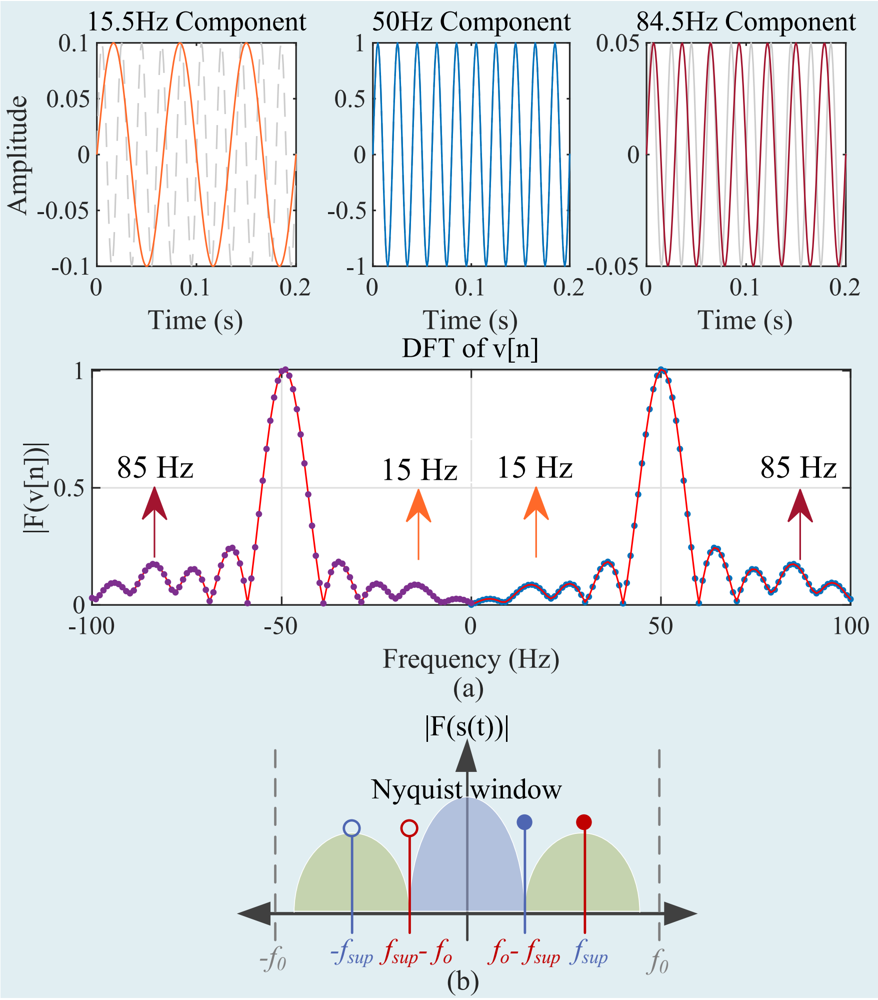

Figure 4.2: Performance of DFT for undersampled signals (a) signal with 84.5 Hz and 15.5 Hz modes and its spectrum, (b) role of Nyquist window for $f_i > f_n/2$ modes, and the folded spectral magnitude.

manifesting observability constraints for DFT based approaches as depicted in Fig. 4.2. To further explain the observability constraints using DFT based approach, consider a non-stationary, multi-component signal with sub synchronous component of frequency f_{sub} and super synchronous component of frequency f_{sup}, originating as a result of SSCI. The instantaneous signal comprised of fundamental component (f_0) and accompanied by sub-synchronous and super-synchronous modes can be modeled as,

$$x(t) = A_0 \cos(2\pi f_0 t + \phi_0) + \sum_{i=1}^{2} A_i e^{\sigma_i t} \cos(2\pi f_i t + \phi_i) \tag{4.1}$$

where, A_0, f_0 and ϕ_0 denote the amplitude, frequency and phase of the fundamental component, the subsequent indexes ($i = 1, 2$) for A_i, f_i and ϕ_i correspond to SSCI components (f_{sub}, f_{sup}), and σ_i represents the damping factor of each SSCI mode.

Typically, the reporting rate of PMUs for WAMS is between $10 - 100\, fps$ [59]. Considering a PMU with a fixed sampling rate $f_R = 100 fps$, the expression in (4.1) at n^{th} sample can be expressed as

$$x[n] = A_0 \cos(2\pi \hat{f}_0 n + \phi_0) + \sum_{i=1}^{2} A_i e^{\hat{\sigma}_i n} \cos(2\pi \hat{f}_i n + \phi_i) \tag{4.2}$$

where, $\hat{f}_0 = f_0/f_R$ and $\hat{f}_i = f_i/f_R$ is the normalized frequency of the fundamental and SSCI component, respectively. Similarly, $\hat{\sigma}_i$ denote the damping factor normalized at the fixed sampling rate.

Conventionally, a rectangular window of length $N_R = f_R/f_0$ is applied to obtain synchrophasors using a DFT based algorithm. The DFT window length and the sampling period determine the number of spectral bins and the respective inter-bin distance for the frequency components in (4.2). It is essential to note that acquiring the required number of samples in (4.2) necessitates the condition of satisfying the Nyquist criteria for sampling. Therefore, considering the $100\, fps$ reporting rate noted above with fixed DFT window length, the fundamental and subsequent frequency components can be expressed in spectral bins as

$$\hat{f}_n = \frac{f_0}{f_R} = \sum_{i=0}^{2} \frac{\Upsilon_i}{f_R}, \tag{4.3}$$

where $\Upsilon_i = \Gamma_i + \hbar_i$ represent the spectral bin of frequency components and their inter-bin location for fundamental and subsequent SSCI based components.Subsequently, $\pm\Upsilon_{sub}$ and $\pm\Upsilon_{sup}$ represent the spectral bins of SSCI components when synchrophasors with fundamental frequency ($f_0 = 50\,\mathrm{Hz}$) are generated using a rectangular window of length N_R for a signal presented in (4.2). The frequency component lies at integral bin for $\hbar = 0$ if $f_0 = \hat{f}_n$. However, for SSCI components where assuming $f_{sub} \in \left[1, 25\right]$ and $f_{sup} \in \left[60, 100\right]$, then $\Gamma_1 \neq \mathbb{Z}\,\& \leq 1$. Similar is the case for Υ_2, where $\Gamma_2 \neq \mathbb{Z}$ and this deduce $\hbar_i \neq 0$ which implies f_0 and subsequent f_i components do not lie on integral bins and estimated synchrophasors are affected with spectral leakage as illustrated in Fig.4.2.

The DFT spectrum of (4.1) for f_0 and superimposed by SSCI components (f_{SSCI}) is constituted by their respective positive and negative spectra [122], given as

$$[\nu] = \nu[k, \Gamma]^{\pm}_{f_0} + [k, \Gamma]^{\pm}_{f_{SSCI}} \tag{4.4}$$

(4.4) can be written for the $\pm\Gamma$ and using rectangular window taking samples at each n^{th} interval as

$$\breve{\nu}[n, \Gamma]^{\pm}_{f_0} = \hat{A}_0 \cos\left(2\pi \frac{\Gamma_0}{f_0 \cdot N_R}\,(n + \Gamma_0) + \phi_0\right) e^{-j2\pi\frac{\Gamma_0}{f_0}} \tag{4.5}$$

$$\begin{aligned}\check{\nu}[n,\Gamma]^{\pm}_{f_{SSCI}} =& \frac{1}{f_i \cdot N_R} e^{\frac{\hbar_i}{N_R}} \left[\sum_{i=1}^{f_i - 1} \hat{A}_i e^{\frac{\hbar_i}{N_R}} \right. \\ & \left. \cos\left(2\pi \frac{\Gamma_i}{f_i \cdot N_R}(n+\Gamma_i)+\phi_i\right) e^{-j2\pi\frac{\Gamma_i}{f_i}} \right]\end{aligned} \tag{4.6}$$

(4.5) and (4.6) can be simplified using Euler identity for $\cos(2\pi\frac{\Gamma_1}{N_R}(n+\Gamma_0)+\phi_0)$ to normalize the estimated phasors for corresponding reporting of the synchrophasors algorithm, as derived in [3]. Therefore, this can be written as

$$\begin{aligned}\Psi_0\left(\Gamma_0+n\right) &= \frac{1-e^{j2\pi(\Gamma_0+n)}}{1-e^{j2\pi\left(\frac{\Gamma_0-n}{\hat{f}_0}\right)}}, \\ \Psi_i\left(\Gamma_i+n\right) &= \frac{1-e^{j2\pi(\Gamma_i+n)+\frac{\hbar_i}{\hat{f}_n}}}{1-e^{j2\pi\left(\frac{\Gamma_i+n}{\hat{f}_n}\right)\cdot\frac{\hbar_i}{\hat{f}_n}}},\end{aligned} \tag{4.7}$$

where, Γ_0 and Γ_i denote the bin distance between f_o, f_{SSCI} in (4.1) and any n^{th} positive sequence harmonic content that illustrate the MSR and non-stationary complex signal. (4.7) implies that $\Psi_{(0,i)}$ for f_o and f_{SSCI} depends on the sampled signal reported at n^{th} interval by the synchrophasor. This leads to two important conclusions:

- The synchrophasor-based estimation algorithm primarily depends on f_o and assumes that $[\nu]$ has finite stationary cycles over the applied window.
- For any f_{SSCI} with $\omega_i(t) \neq \mathbb{Z}$ constituting $\nu[n]$ with $\sum_{i=1,2\cdots}^{t=0:k:1} \hat{A}_i cos(w_i t + \phi_i)$ as superimposed components, the N_R doesn't guarantee the minimum conditions for Nyquist theory.

This implies that if $N_R \ll 2f_{SSCI}$, the spectrum of frequencies for f_0 and f_{SSCI} folds up at each respective $\pm\Gamma$, and results in aliased spectral leakage as illustrated in Fig. 4.2(a, b). This affects the accurate estimation of synchrophasors which subsequently leads to erroneous estimation of the associated parameters, consequently misleading the impedance proportional to the respective modes and nominating the wrong candidate as a source of disturbance in the network. Therefore, this section provides a foundational understanding of the key limitations of the DFT based approach, which is widely used in PMUs. The mathematical analysis indicates that detecting such events crucially require either advanced variants of the DFT or an alternate approaches that utilize high resolution time-series data. To analyze advanced variant of the DFT, the complex SSCI modes are further examined using the state-of-the-art Sliding Discrete Fourier Transform (SDFT) in the next section. This highlights a fundamental challenge associated with the DFT-based approach commonly used in PMUs. A detailed discussion supports the adoption of SWMUs, based on the identified limitations of these methods.

4.3.1 Analysis using SDFT

The analysis using sliding window-based DFT is straightforward if the oscillation modes are stationary and have known bandwidth. Consider an example signal as illustrated below.

$$x[n] = A_0 \cos(2\pi f_0 \frac{n}{f_s} + \phi_0) \; + cos(2\pi f_i \frac{n}{f_s} + \phi_i) \tag{4.8}$$

Given the discrete sequence of data points for the signal in (4.8), the SDFT can be deduced initially from the DFT circular shift property by multiplying the time domain sequence with $e^{j\frac{2\pi}{N}}$. The detailed derivation for this is provided in Appendix A [125, 126], and the final relation for computing a DFT using sliding window based approach can be written as.

$$X_{t+1}[k] = e^{j\frac{2\pi}{N}k}\left(X_t[k] + x[t+N] - x[t]\cdot e^{-j\frac{2\pi}{N}kt}\right) \tag{4.9}$$

Where, $X_t[k]$ is the DFT obtained at bin k, $x[t+N]$ is the new sample acquired at N, and x_t is previous sample. Considering $x[n]$ in (4.8) as input signal for the SDFT and $X_t[k]$ being the output of the SDFT, the the z-transform of the signals can be denoted as $X(z)$ and $X_t(z)$, respectively. Thus, the transfer function for the input and output of the SDFT can be written as,

$$\begin{aligned} H_{SDFT}(z) &= \frac{X_t(n)}{X(n)} \\ &= (1 - z^{-N})\frac{e^{j\frac{2\pi k}{N}}}{1 - e^{j\frac{2\pi k}{Nz^{-1}}}} \end{aligned} \tag{4.10}$$

To further simplify (4.10) in order to lead it to the SSR specific applications, the $H_{SDFT}(z)$ is multiplied by $1 - e^{j\frac{2\pi k}{Nz^{-1}}}$ [126] in both denominator and numerator.

This yields,

$$H_{\mathrm{SDFT}}(z) = (1 - z^{-N})\cdot e^{j\frac{2\pi k}{N}}\frac{1 - e^{j\frac{2\pi k}{N}}z^{-1}}{(1 - e^{-j\frac{2\pi k}{N}}z^{-1})(1 - e^{-j\frac{2\pi k}{N}}z^{-1})} \tag{4.11}$$

Simplifying the above expression further yields to,

$$H_{SDFT}(z) = \underbrace{(1 - z^{-N})}_{\text{comb filter}}\underbrace{\frac{(1 - e^{-j\frac{2\pi k}{Nz^{-1}}})e^{-j\frac{2\pi k}{N}}}{1 - 2cos(\dfrac{2\pi k}{N})z^{-1} + z^{-2}}}_{K^{th} complexresonator} \tag{4.12}$$

(4.12) reflect two important parameters in order to adopt it for SSR based applications. The $1 - z^{-N}$ corresponds to the finite window length, thus restricting

the samples computation by N number of samples. Similarly, the denominator is a second order polynomial with real coefficients, thus implementing the recursive Goertzel algorithm. This can also be referred as second order infinite impulse response (IIR) resonance filter, tuned to a specific frequency. Thus, this act like a narrowband filter and accumulating energy at the specific frequency bins k.
It is essential to emphasize that the SDFT is particularly derived to extract signal components known frequency modes, thereby offering significantly greater computational efficiency compared to the conventional Fast Fourier Transform (FFT). This enhanced efficiency is primarily attributed to the SDFT's ability to update the spectral content incrementally on a harmonic-by-harmonic basis [126, 127], rather than recalculating the full frequency spectrum for each new data point, as required in the DFT.

The efficiency and selectivity of the SDFT are enabled by its resonator-based filter architecture, which facilitates recursive and frequency-targeted updates. This makes the SDFT particularly well-suited for applications involving signals with known frequency modes and bandwidths. As depicted in Fig. 4.3, the SDFT filter structure can be conceptualized as a comb filter cascaded with multiple complex resonators. In this configuration, the comb filter serves to pre-attenuate signal components, while each complex resonator selectively amplifies the desired harmonic components.

Importantly, both the comb filter and the complex resonators exhibit zero phase response at their designated frequencies, as detailed in [125, 127]. As a result, the SDFT achieves unity gain and zero phase shift at these frequencies, enabling accurate extraction of target signal components without introducing magnitude distortion or phase error [125, 128]. To implement advanced methods

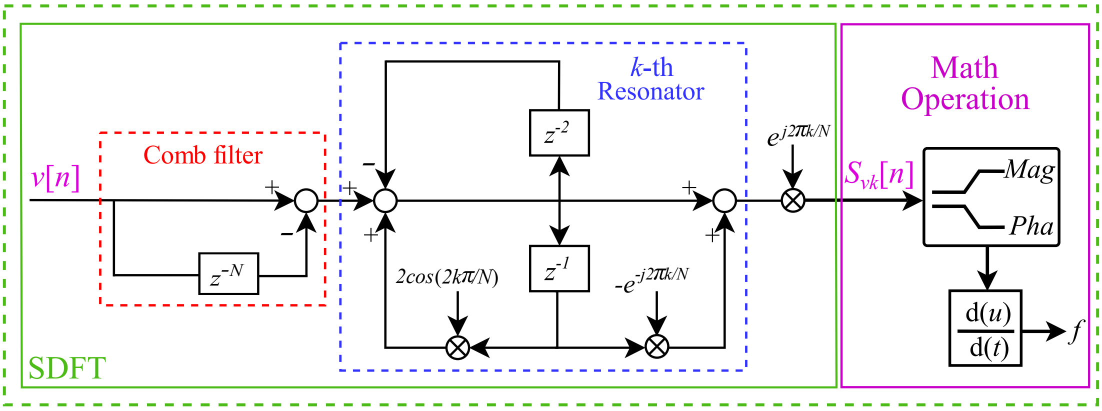

Figure 4.3: Comb filter based SDFT algorithm

such as SDFT for SSCI-related applications [125], real-time operation requires prior knowledge of the bandwidth and frequencies of the SSCI modes. Typically, these oscillatory modes in a power network for conventional SSR can be identified using various techniques, as discussed in an earlier chapter of this thesis. However, each method comes with its own limitations, all centered around a common challenge: the dependence of these modes on changing operating conditions. This dependency introduces two key constraints — first, the bandwidth of the modes is not fixed, and second, the modes exhibit significant time varying properties, particularly in networks with low SCR and inertia.

Fidelity of SDFT in Reporting SSCI modes

To demonstrate the concept of SSCI observability using the SDFT and to examine its limitations in tracking nonstationary and complex oscillations, a simplified yet representative network model is developed, as shown in Fig. 4.4. The simulation setup and system parameters are listed in Table 4.1. Firstly, to induce SSR, the transmission network and series compensation parameters are tuned accordingly. The step-up transformer connecting the DFIG (from 0.69kV to 35kV) has a

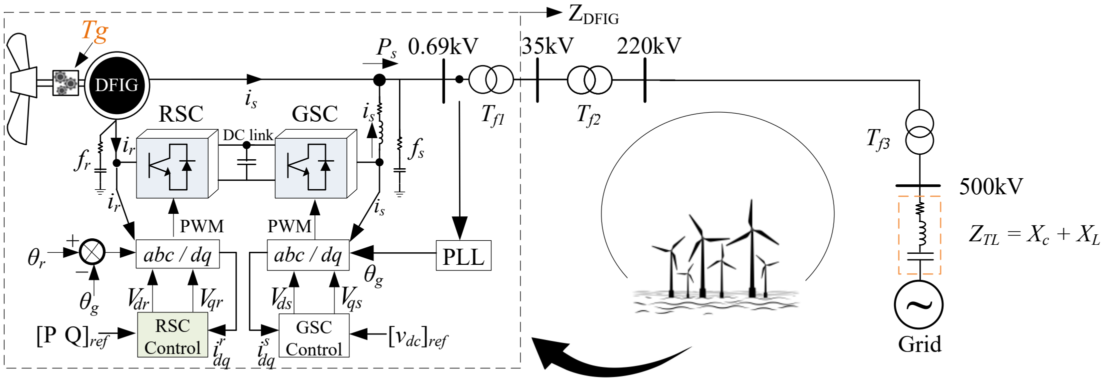

Figure 4.4: Schematic of power network showing the DFIG-based WTG and its connection to the grid through a compensated transmission line.

Table 4.1: Parameters of DFIG

Rated Power	1.5 MVA
Rated voltage	0.69 kV
Rated Current	2.173 kA
Moment of inertia ($J = 2H$)	0.79 s
Stator resistance (r_s)	0.022 pu
Rotor resistance (r_r)	0.027
Stator leakage inductance (L_s)	0.28 pu
Rotor leakage inductance (L_r)	0.31 pu
f	50 Hz

reactance of $X_{T_{f1}} = 0.019$pu and $X_{T_{f2}} = 0.039$pu. The transformer linking the transmission line and the series compensation has a reactance of $X_{T_{f3}} = 0.065$pu. The total reactance of the 220kV transformers and wind farms is $X_w = 0.0859$pu.

For the series compensation, the inductive and capacitive reactances are set as $X_L = 0.065$pu and $X_c = 0.01634$pu, respectively. The network is initially tuned such that the total inductive reactance becomes $X_L = 0.1413$pu, with the capacitive reactance unchanged at $X_c = 0.01634$pu. This configuration leads to a SSR with mode of $f_{ssr} = 17\,\text{Hz}$, calculated as follows:

$$f_{ssr} = f_o \times \sqrt{\frac{X_c}{\sum X_L}} \tag{4.13}$$

The voltage and current waveforms at PoC, obtained from the network model as illustrated in Fig.4.4, are depicted Fig.4.5. The oscillatory behavior in the waveforms illustrate the 17 Hz frequency component, corresponding to the resonance frequency for which the system has been tuned. Given that the SSR frequency is known in advance based on the intact knowledge of the system dynamics, the SDFT resonator is configured with a bandwidth below the nominal grid frequency f_o. Although this allows the grid-side observer to detect the dominant SSO frequency (f_o= 17 Hz), the limited bandwidth restricts the detection of higher-frequency components and coupled modes, which may be present.

Since as discussed in earlier sections that the oscillatory behavior cannot be limited to simple SSR mode when dealing with IBRs and control interactions, but this may include coupled frequency modes as well discussed in earlier chapter of this thesis. To capture these coupled modes, the SDFT resonator bandwidth is extended up to 100 Hz. As shown in Fig.4.6, this broader bandwidth enables the identification of coupled oscillatory modes, which are crucial for accurately tracing the source of oscillations in the network. Initially, with symmetric IBR control and only a 20% variation in line compensation at $t = 2s$, the system exhibits a clear 17 Hz SSO without observing coupled modes. This is expected, as the resonator bandwidth is still kept below f_o, limiting visibility into higher-order interactions.

It is important to note that the SSO frequency is derived based on the relationship in (4.13), and the stable waveform response shown in Fig.4.5 confirms system stability under these conditions. To analyze the influence of IBR control, the GSC parameters are asymmetrically adjusted to reduce the phase margin, thereby highlighting the effect of the Phase Loop Lock (PLL) instability. Although the wind speed is held constant at 11m/s across all cases, this asymmetry, combined with the earlier compensation change, leads to the appearance of SSCI with coupled modes, as depicted in Fig.4.6.

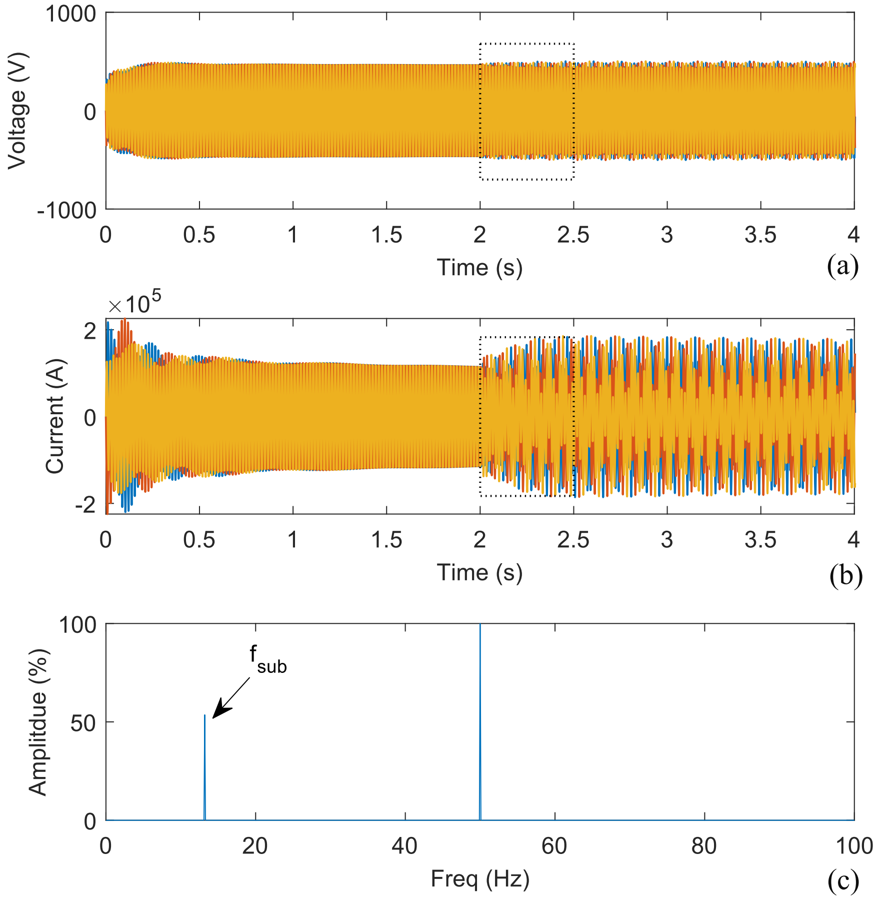

Figure 4.5: Voltage and current waveforms obtained at PCC of 0.69/35kV for SSO below f_o showing (a) voltage at PCC, (b) current at PCC, (c) the response of SDFT

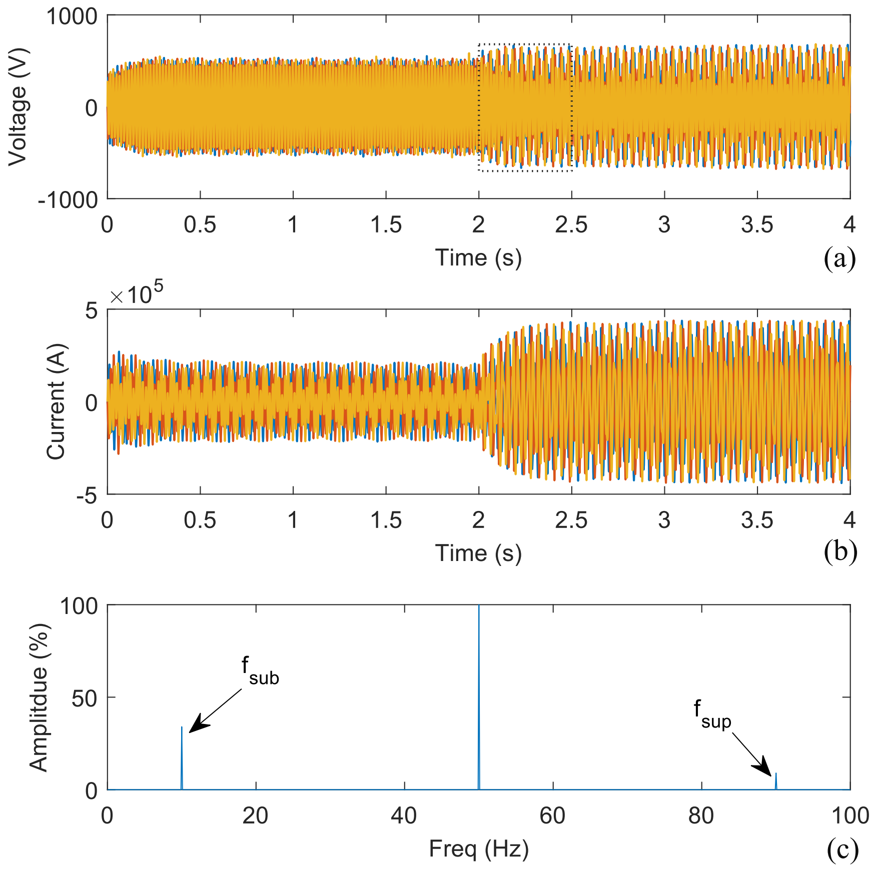

Figure 4.6: Voltage and current waveforms obtained at PCC of 0.69/35kV for SSO with coupled modes showing (a) voltage at PCC, (b) current at PCC, (c) the response of SDFT

It is also important to emphasize that the observed SSCI bandwidth corresponds to a single operating point. Since network operating conditions can vary significantly, it becomes impractical to fix the resonator bandwidth for all scenarios. Moreover, setting a large fixed bandwidth increases computational complexity and has been found to be ineffective for reliably detecting complex SSCIs in IBR-dominated systems [129].

To further evaluate the fidelity of SDFT-based observability in such conditions, the network is subjected to parameters that induce nonstationary SSCI behavior. As illustrated in Fig.4.7, SDFT produces inaccurate estimates under these conditions. This is primarily due to spectral leakage and the absence of proper bin alignment for discrete interharmonic components. Consequently, frequency modes become difficult to resolve, leading to inaccurate magnitude estimation and poor separation of individual SSCI modes. Thus, accurately estimating non-stationary modes with widely varying frequency bandwidths is significantly hindered by several critical challenges. These include the lack of clear guidance on selecting optimal window widths, the need for adaptability across a broad frequency spectrum, the complexity of tuning filters for specific frequencies, and, most notably, the reliance on estimation techniques that do not account for fundamental frequencies. These limitations in observability can lead to erroneously localization of oscillation sources within the network; potentially compromising the reliability and effectiveness of system analysis.

These findings underline the need for an alternative approach capable of handling nonstationary dynamics and complex frequency interactions. To address this, for the first time a synchro-transform method based on adaptive instantaneous frequency estimation is proposed. The approach leverage the state of the art SWMUs, which are nothing but a high resolution and synchronized data obtained through waveform units. The detailed analysis of this novel approach, its suitability for complex oscillations detection and localization is derived, assessed and discussed in the following sections.

4.4 Detection of Complex SSCI using SWMU

The involvement of non-stationary and coupled modes in complex SSCI necessitates high-resolution synchronized data for accurate estimation of the oscillation

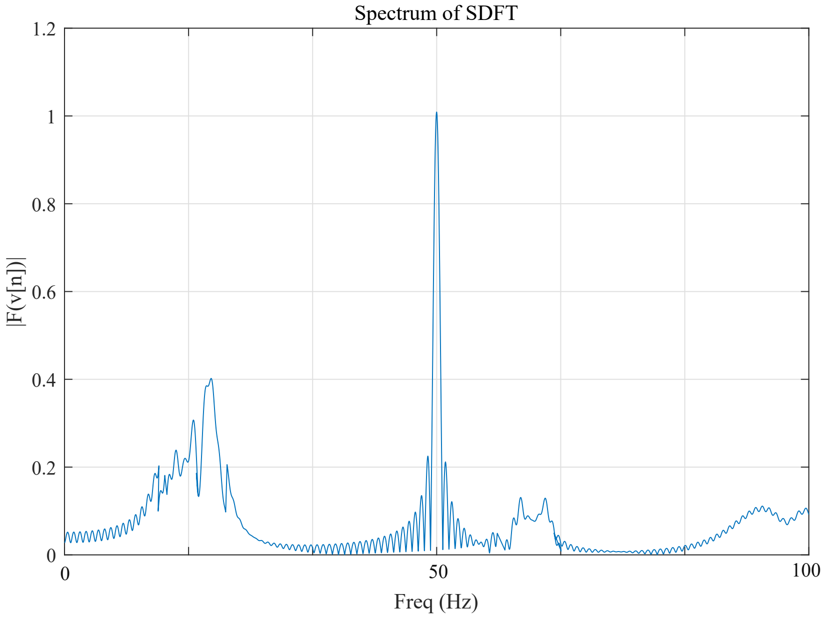

Figure 4.7: SDFT of non-stationary sinusoid for the DFIG based line compensated network

modes. Time-synchronized waveforms, also referred to as synchro-waveforms, are therefore adopted to address key observability and estimation challenges. Unlike conventional PMUs and PDC, SWMUs provide high-resolution time-synchronized data, effectively eliminating two major limitations: (1) the sampling constraints that restrict frequency range coverage, and (2) the reliance on estimation methods based solely on fundamental frequency-based approaches such as DFT. Additionally, the raw data obtained from SWMUs can support various advanced signal processing techniques to extract valuable information beyond traditional mode estimation. Thus, the high resolution time-synchronized waveform data serves as a foundational enabler for developing and implementing a more adaptive and precise method for estimating complex SSCI modes -laying the basis for the application of the novel Adaptive Instantaneous Frequency based Synchro Transform (AIFST) approach, discussed in the following section.

4.4.1 The Adaptive Instantaneous Frequency based Approach

To address the estimation of complex, time-varying modes, the proposed framework develops the AIFST. This allows the transformation of high-sampled SWMU data into a robust time-frequency representation, enabling the extraction of intact oscillation modes. These modes are further utilized to compute the impedance at each network node, which facilitates accurate localization of the oscillation source. Although time-frequency transformation of time-series data has been previously explored [22], conventional methods suffer from several critical issues: lack of frequency realignment, non-adaptive windowing, and significant energy dispersion around the ridges—particularly when analyzing strongly time-varying modes. Thus, the developed approach not only overcomes the limitations of earlier techniques but also enhances the accuracy of oscillation modes extraction for strongly time varying and coupled frequency modes. These precisely extracted modes are then used to derive the impedance model, which plays a critical role in accurately localizing the source of oscillations within the IBR-based network. The detailed derivations of the proposed method, its mathematical analysis and novel developments are discussed in the following sections.

4.4.2 Mathematical Background of Synchro-Transform

Assuming a non-stationary time-varying complex signal as illustrated in the following.

$$x(t) = A_0 \cos(2\pi f_0 t + \phi_0) + \sum_{i=1}^{2} A_i e^{\sigma_i t} \cos(2\pi f_i t + \phi_i) \tag{4.14}$$

We transform this into continuous time domain to facilitate the explanation and derivation of the SST. Thus, the Fourier Transform (FT) of (4.14) can be written as,

$$X(\omega) = \int_{-\infty}^{+\infty} x(t) e^{-jwt} dt \tag{4.15}$$

The STFT of $x(t) \in L^2(\mathbb{R})$ for real and even sliding window $g_\sigma \in L^2(\mathbb{R})$ is given as

$$S(t, \omega) = \int_{-\infty}^{+\infty} x(u) e^{-\jmath\omega(u-t)} g_\sigma(u-t) dx \tag{4.16}$$

The STFT calculates the FT of $x(t)g_\sigma(u-t)$ for shorter duration as $u \in [t-\Delta t, t+\Delta t]$. Therefore, for STFT it is essential to assume that the magnitude and phase components (ϕ_i) of the signal in (4.14) fulfill the criteria of $|A_i'(t)| \leq \varepsilon$ and $|\phi_i^{''}| \leq \varepsilon$, where ε is sufficiently small value. In addition, the components of the signal $x(t)$ should have sufficient separation distance as $2\Delta_\omega < \phi_k'(t) - \phi_{k-1}'(t)$ satisfies only if $\phi_{0,i}' \in x(t)$ are weakly time-varying.

With this condition, (4.14) is considered as a weakly time-varied sinusoidal signal and is approximated to have only harmonic components for all durations of u [130]. Using Taylor expansion, (4.16) can be modified to reflect a mono-component signal, and thuscan be approximated for a fixed time interval ($\hat{t}$) as

$$\begin{aligned} S(t, \omega) &= \int_{-\infty}^{+\infty} g_\sigma(u-\hat{t}) A(\hat{t})\, e^{\jmath\big(\phi(\hat{t})+\phi'(\hat{t})(u-\hat{t})\big)} e^{-\jmath\omega(u-\hat{t})} dx \\ &= A(\hat{t}) e^{\phi(\hat{t})} \hat{g}_\sigma(\omega - \phi^{'}(\hat{t})) \end{aligned} \tag{4.17}$$

(4.17) is generalized for fundamental (A_0, ϕ_0) and subsequent terms (A_i, ϕ_i) reflecting (4.16) and the components of $x(t)$. We further replace $\hat{t}$ with t for the ease of simplicity, while detailed mathematical derivation can be seen from [130]. This leads to the estimation of IF ($\phi^{'}$) in time-frequency frame with (t, w) as

$$\begin{aligned}\breve{\omega}_x(t,w) &= \mathfrak{Re}\left\{\frac{\delta_t\, S(t,w)}{\jmath\, S(t,w)}\right\}\\ &= \mathfrak{Re}\left\{\frac{\delta_t\, A_0(t)e^{\jmath\phi_0(t)}\hat{g}_\sigma(\omega-{\phi_0}'(t))}{\jmath\, A_0(t)e^{\jmath\phi_0(t)}\hat{g}_\sigma(\omega-{\phi_0}'(t))}\right.\\ &\quad+\frac{\delta_t\, A_i(t)e^{\jmath\phi_i(t)}\hat{g}_\sigma(\omega-{\phi_i}'(t))}{\jmath\, A_i(t)e^{\jmath\phi_i(t)}\hat{g}_\sigma(\omega-{\phi_i}'(t))}\\ &\text{Where by solving for } \delta_t,\\ &= \phi_0'(t)+\phi_i'(t),\end{aligned} \tag{4.18}$$

where $\Re e$ is the real part of the reassigned frequency ($\breve{\omega}_v(t,w)$) accumulated from the energy spread at time t of the original instantaneous frequency (ω). (4.17) and (4.18) provide a biased estimate of the modes in $x(t)$, with unsymmetrical alignment of $\phi(t)^{'}$ to $|A(t)|$ and thus leading to scattered energy concentration around the ridges. It is important to note that ridges are nothing but traces in the time-frequency plane that track the dominant modes in the signal. Thus, to gain concentrated information and squeeze energy in the region around the coefficients of modes in the signal, $\forall\, \phi_i \in x(t)$, the reassignment operator can be employed as Dirac delta function for ω as

$$\tilde{T}(t,\psi) = \int_{-\infty}^{+\infty} S(t,\omega)\delta\left[\psi - \breve{\omega}_x(t,w)\right] d\omega \tag{4.19}$$

Therefore, substituting (4.17) and (4.18) into (4.19) provided that condition for sufficient separation of modes is met, the coefficients are reallocated from $S(t,w)$

$\rightarrow$ $(t, \breve{\omega}_S(t,w))$ using the coefficient reconstruction as

$$\breve{a}_k(t) \approx \frac{1}{2\pi g_\sigma} \int_{\left|\omega - \phi_k'(t)\right| < \tau_{SSCI}} \tilde{T}(t,\psi) d\psi \tag{4.20}$$

This implies the following argument proved in [131]

$$\frac{1}{2\pi g_\sigma} \int_{|\omega - \phi'_k(t)| < \tau_{SSCI}} \tilde{T}(t,\psi) dpsi - \breve{a}_k(t) \leq \kappa\tilde{\varepsilon} \tag{4.21}$$

Where τ_{SSCI} controls the bandwidth for reconstructing the coefficients, κ is a constant, and $\varepsilon << 1$ is a precision for ensuring that each component is reconstructed with a tiny error, and the coefficients are tightly concentrated in their respective bands $(t, \phi_k^{'}(t))$.

To extract a concentrated coefficient with intact information, the STFT is iterated to obtain SST, however, it has the following limitations:

- The input signal for SST is assumed to be weakly varying in time, an assumption not practical for IBR-dominated networks. As a result, any input signal of complex oscillations with non-stationary modes will be approximated as a counterpart of harmonic oscillations for determining the SST coefficients.

- SST employs a fixed window that is not sufficient for acquiring concentrated information around ridges for calculating the coefficients. of a signal containing varying components. Thus, non stationary and high frequencies require a window with precise and high time resolution, where as lower frequencies can be adequately analyzed with high frequency resolution. Thus, there is tradeoff that fixed window based SST cannot satisfy.

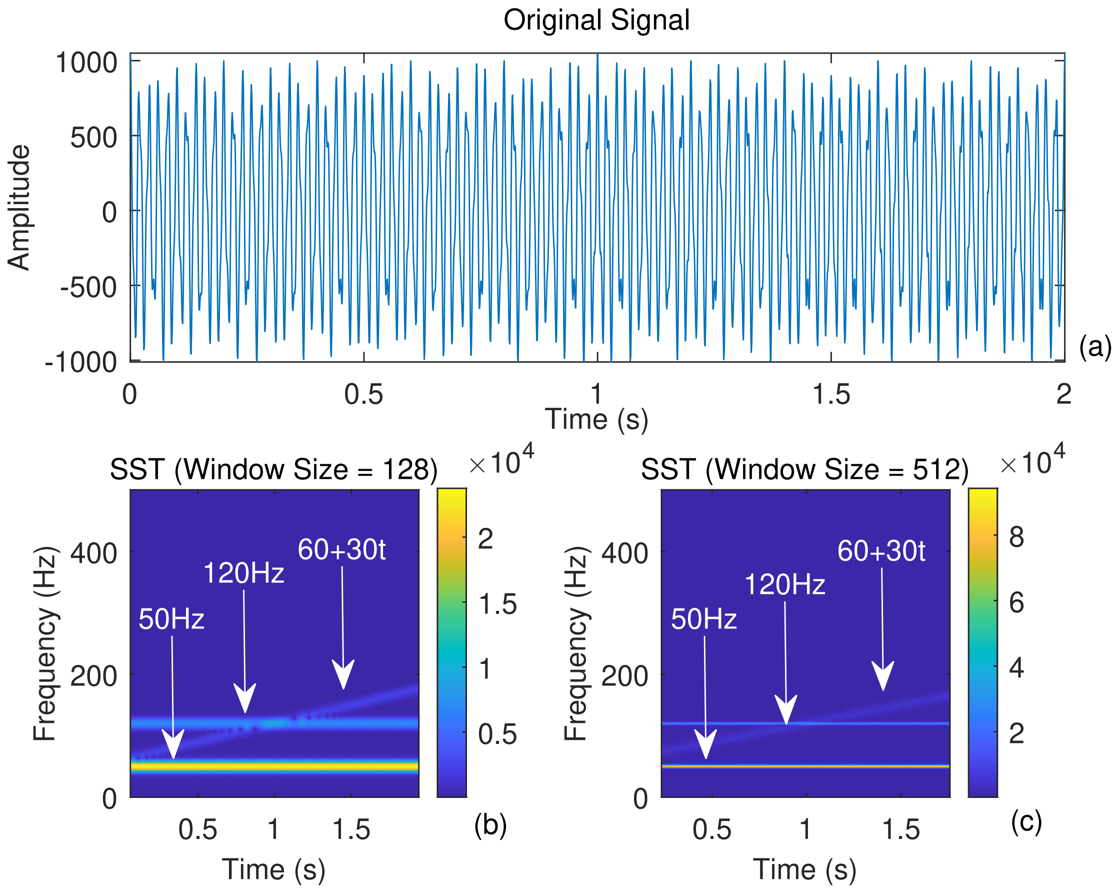

Figure 4.8: Analysis of SST with fixed window for time varying complex SSCI modes showing (a) Original signal, (b) 128 samples window, (c) 520 samples window

The aforementioned statements are justified through an example illustration depicted in Fig.4.8. Consider the system shown in Fig.4.4, where an SSCI event is generated through marginally stable control gains. This generates two SSCI modes, where the first mode is strongly time varying and the second is station-ary i.e. $f_1 = 60 \rightarrow 180$ Hz and $f_2 = 120$ Hz, respectively. The PCC voltage is shown in Fig.4.8 where resolution of 1 kHz sampling is used. This signal is initially analyzed with SST of 0.128 s (128 samples) window. Though for a 1 kHz sampled signal, this window size offer higher time resolution but poor frequency resolution. In other words, this allows the SST to capture fast time variations in the signal; however, the poor resolution of frequency results in smeared frequency representation. This can be well interpreted from the boundary thickness of the frequency components of 50 Hz and 120 Hz in Fig.4.8b as compared to Fig.4.8c where the window size is chosen as 512 later. Notably, a window size of 512 samples yields high-frequency resolution, enabling precise localisation of constant-frequency components like the 50 Hz and 120 Hz. However, this comes at the cost of time resolution, causing smearing or lag in tracking time-varying components like for the signal (f_1) which is varying over time from 60 → 180 Hz. The SST sharpens these representations by reassigning energy based on instantaneous frequency estimates, but its accuracy still fundamentally depends on the chosen window. Thus, short windows are better for resolving rapid frequency changes, while long windows excel at revealing stationary frequency content—highlighting the importance of window selection in interpreting and extracting ridges that represent dominant signal modes.

Thus, there is significant trade-off between the higher resolution in frequency and time when selection of the window is not optimal and adaptive, the SST is further evolved by making the window selection adaptive to wide range of frequencies that can capture the time-varying SSCI modes more precisely. This is explained in the following section.

4.4.3 Adaptive SST

The energy concentration of SST is improved by an iterative process of STFT using a constant window as discussed earlier. However, the concentration around ridges still deteriorates when subject to strong noise and time-varying signals

[132]. Since, the choice of window size plays a critical role in determining the trade-off between time and frequency resolution, an adaptive time-varying window is considered for this study that appropriately adjust optimal resolution to capture all dynamics in the signal following the estimation of the instantaneous frequency. Thus, it is critically important to align the ω precisely so that resolution of the window can be adopted accordingly. We begin this by considering a Gaussian window whose Fourier transform is given as

$$\hat{g}_{\sigma}(t) = \frac{1}{\sqrt{2\pi}\sigma} e^{\frac{-t^2}{2\sigma^2}} \tag{4.22}$$

where, σ is computed as $\sqrt{\frac{\sum |t-\bar{t}|^2}{n-1}}$ at each $n-1$ sample of N. Based on (4.22), (4.17) can be rewritten as

$$S(t,\omega) = \int_{0}^{\infty} A(t+u) \frac{1}{\sqrt{2\pi}\sigma} e^{\frac{-u^2}{2\sigma^2}} e^{-j\omega u} du \tag{4.23}$$

To facilitate the derivation, a constant chirp signal-based approximation of $x(t)$ is considered as $x(t) = Ae^{\left[\phi_0(t)+\phi'(t)(u-t)+\frac{1}{2}\phi''(t)(u-t)^2\right]}$ [133] that yields

$$S(t,\omega) = \int_{-\infty}^{+\infty} Ae^{j\left[\phi_0(t)+\phi_0'(t)u+\frac{1}{2}\phi_0'(t)w^2\right]} \frac{1}{\sqrt{2\pi}\sigma} e^{-\frac{u^2}{2\sigma^2}} e^{-j\omega u} du \tag{4.24}$$

$$S(t,\omega) = \frac{A}{\sqrt{2\pi}\sigma} e^{j\phi_0(t)} \int_{-\infty}^{+\infty} e^{-\frac{1}{2}\left[\frac{1}{\sigma^2}-j\phi_{\emptyset}'(t)\right]u^2-j[\omega-\phi_{\circ}(t)]u} du \tag{4.25}$$

The partial derivative of (4.25) yields

$$\partial x(t,\omega) = x(t,\omega) \left\{ j\phi'(t) + \frac{\phi''(t)[\omega-\phi'(t)]}{\frac{1}{\sigma^2}-j\phi''(t)} \right. \tag{4.26}$$

Substituting (4.26) in (4.19), the IF can be estimated as

$$\breve{\omega}_x(t,w) = \frac{\phi''(t)^2}{1+\phi''(t)^2}[\omega - \phi'(t)] + \phi'(t) \tag{4.27}$$

Recalling the condition in (4.21) for frequency modes closely located to each other, (4.27) can be written as

$$|\breve{\omega}_v(t,w) - \phi'(t)| < \varepsilon \left|1 - \frac{1}{1+\phi''(t)^2}\right| \tag{4.28}$$

From (4.25), if the $x(t)$ has MSR components that are varying slowly in time, then ε is small enough to assume oscillation components as an approximation of harmonic order of $x(t)$. Therefore, the condition satisfies if $\breve{\omega}_v(t,w) = \phi'$, otherwise, it can be observed from (4.27), that the estimate of $\breve{\omega}_v(t,w)$ depends on $\phi''(t)$ which is rate of change of IF. It is clear that for slow variation, the $\phi''(t)$ is small and is negligible, however for strongly time-varying signals, the $\phi''(t)$ is large enough to provide a biased estimate of IF using (4.27). Therefore, the continuous iteration of (4.27) provides concentrated Time Frequency Representation (TFR) with reduced error between $\breve{\omega}_v(t,w)^N$ and $\breve{\omega}_v(t,w)^{N-1}$ for optimal solution of $\tilde{\varepsilon}$. Thus,

$$\tilde{T}(t,\psi) = \int_{-\infty}^{+\infty} S(t,\omega)\delta\left[\psi - \breve{\omega}_v^N(t,w)\right] d\omega < \tilde{\varepsilon} \tag{4.29}$$

Theocratically, the above solution converges as the TF coefficients are reassigned to $(t, \breve{\omega^N})$, however, the frequency estimator in discrete implementation is rounded to the nearest $\mathbb{Z}$ to satisfy $\omega = \phi^{'}(t)$. This leads to a non-realignment issue with IF estimators $(\breve{\omega^N})$ and results in a deviated approximation of MSR modes in discrete implementation.

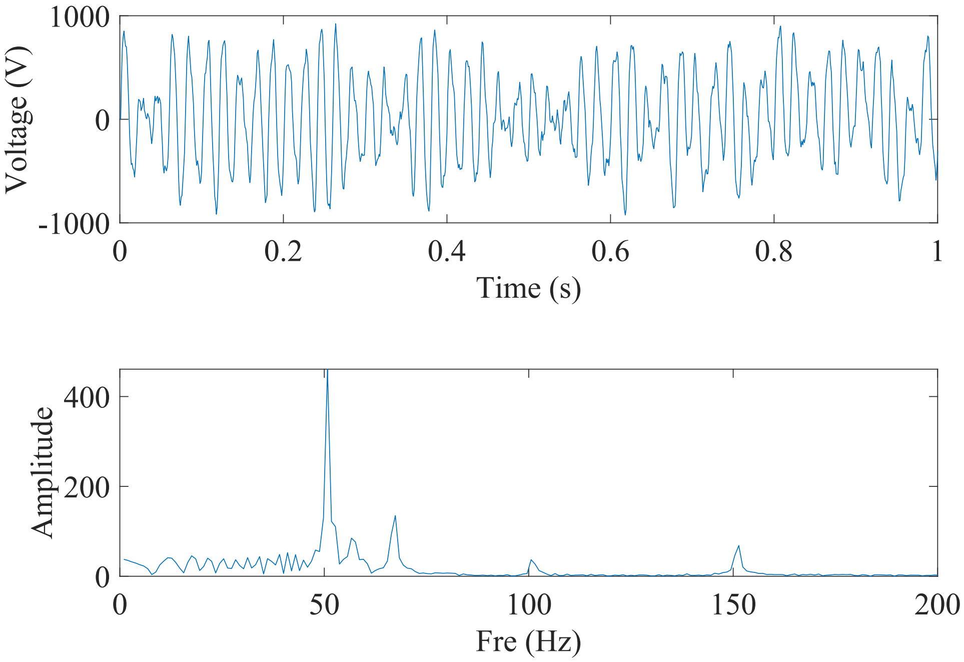

Figure 4.9: Voltage waveform with complex SSCI modes varying with time and closely spaced to the fundamental frequency

The estimation of frequency modes due to non-realignment issues are shown in Fig.4.10, which illustrate the TFRs of the voltage waveform shown in Fig.4.9. The TFRs obtained in Fig.4.10 shows a voltage signal with strongly time-varying modes including both harmonic and inter-harmonic components closely placed to the fundamental frequency. Further to that, the voltage waveform is contaminated with noise which is usually present when such data is obtained through SWMUs. Fig. 4.10 illustrates how the performance of TFR is significantly influenced by spectral leakage and the misalignment of energy components across the each IF. This misalignment, or non-realignment, occurs when the IF of the signals are not accurately tracked, resulting in energy dispersion across the time-frequency plane and thus, leading to poor localization and reconstruction of modes in the signal. This becomes more challenging when the optimal selection of the window length are not well aligned to the non stationary components of the signal. Recalling from the previous section, it is worth to highlight that the IBRs driven SSCI occurs with MSR, involving frequency modes which have wide bandwidth and are typically time-varying. Thus, for example, a 120 ms window yields a reasonably accurate estimation of the signal's original frequencies. However, misaligned windowing leads to spectral leakage causing more energy scattering around the modes making accurate estimation of the IF challenging. Furthermore, the use of different window sizes, as shown in Fig.4.10, demonstrates that without adaptive methods to appropriately match the window size to the signal's frequency content, the TFR struggles to distinguish between closely spaced or time-varying components, resulting in distorted representations. Thus, these observations highlight the need to derive an approach that can effectively adopt the window size according to the frequency modes and solely address both spectral leakage and IF re-alignment issue. The accurate re-alignment of IF is emphasized because the optimal choice of the window is explicitly dependent on the IF estimates.

Therefore, it is ensured that IF estimator is correctly aligned to its realignment region for approximation of all MSR (ϕ^i) modes. Thus, it is important to ensure accurate reference for obtaining the accurate estimation of ω. For these reasons, the reassignment operator is further modified as $\delta[\omega - \breve{\omega}(\hat{t})]$ [130]. This modification also has the effect of sharpening the frequency localization of the SST and reducing the interference between adjacent frequency components, resulting in a clearer and more interpretable TFR of the signal. Therefore, the new reference can be written as $\tilde{w}_{ref} = \breve{\omega}(\hat{t}) - \omega = 0$. It is best to center-align the IF estimator for each MSR component, as this enables accurate identification of the

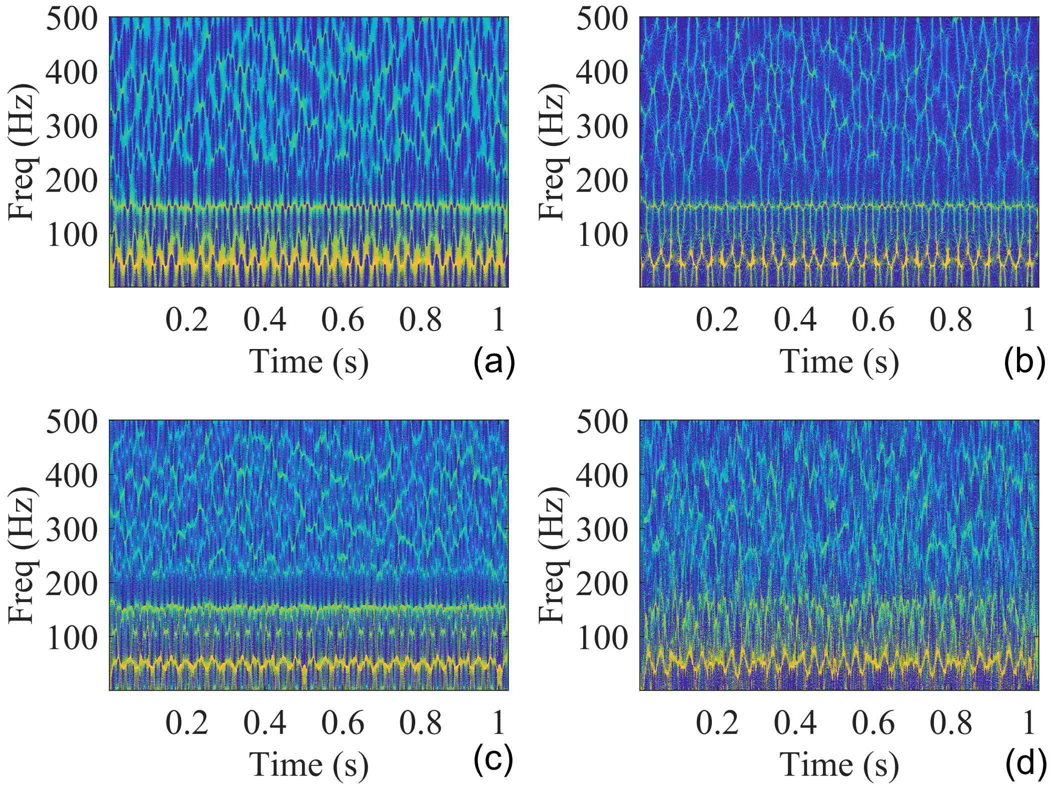

Figure 4.10: TFR of the voltage signal shown in Fig.4.9 showing effect of misaligned IF and spectral leakage as a result of (a) 240 ms window, (b) 120 ms window, (c) 50 ms window and (d) 25 ms window.

band center of all modes before performing the realignment of $\breve{\omega}(\hat{t})$ [132]. Therefore, (4.18) is discretized at $k = (1, 2, \cdots, K)$ and can be formulated for IF band center as

$$\tilde{w}_{ref} = \left\{ k_\omega \;\middle|\; \begin{array}{l} \Delta k_\omega > |\breve{\omega}_v(t, k_\omega) - k_\omega| \\ 1 \;> \partial_\omega \breve{\omega}_x\,(t, k_\omega) \\ |\breve{\omega}_v(t, k_\omega) - k_\omega + 1| \geq |\breve{\omega}_v(t, k_\omega) - k_\omega| \end{array} \right\} \tag{4.30}$$

Here, $\tilde{w}_{ref} \subset \omega$ such that $\omega \in \left[\tilde{w}^{+}_{ref}, \tilde{w}^{-}_{ref}\right]$, and limits of $\Delta\tilde{w}_{ref} = \tilde{w}^{-}_{ref} < \omega < \tilde{w}^{+}_{ref}$. The boundary limits of the new IF for the k^{th}_ω bandwidth can be written in discrete domain as

$$\Delta\tilde{w}_{ref} = \begin{cases} \tilde{w}^{-}_{ref}, & {}_{\max}\delta_{\omega}\breve{\omega}_v(t,k_{\omega}) \geq 1 || \ \omega < \tilde{w}^{i}_{ref} \\ \tilde{w}^{+}_{ref}, & {}_{\min}\delta_{\omega}\breve{\omega}_v(t,k_{\omega}) \geq 1 || \ \omega > \tilde{w}^{i}_{ref} \end{cases} \tag{4.31}$$

where the subscript $i = [1, 2 \cdots]$ refers to frequency bands of the corresponding MSR modes. From (4.31), the IF estimator can be realigned across $i = [1, 2 \cdots]$ bands of frequencies in (4.9) and $\breve{\omega}_v(t,w)$ for i^{th} modes is written as

$$\breve{\omega}_v(t,w) = \left[\begin{array}{ll} \breve{\omega}_v(t,k_{\omega})_{i=1}, & \tilde{w}^{-}_{ref,i=1} < k^{th}_{\omega} < \tilde{w}^{+}_{ref,i=1}; \\ \quad\vdots & \qquad\qquad\vdots \\ \breve{\omega}_v(t,k_{\omega})_{i=n}, & \tilde{w}^{-}_{ref,i=n} < k^{th}_{\omega} < \tilde{w}^{+}_{ref,i=n}; \end{array} \right. \tag{4.32}$$

where $\tilde{w}^{\pm}_{ref,i}$ refers to the frequency boundaries of IF bands of $\breve{\omega}_v(t,w)$ aligned at its center. This realignment of the IF significantly enhances the TFR of the voltage signal shown in Fig.4.9 and the result can be observed in Fig.4.11, which is the estimated TFR using the AIFST. It can be observed clearly that the modes are more concentrated and precisely determined against the noise and harmonic components. The boundary width of each frequency component is significantly reduced and tracked more precisely over time and frequency transitions. Thus, this highly precise and accurate estimation of the IF leads to definite reconstruction of the modes which subsequently help in localization the origin of the complex SSCI source in the network. Thus, the coefficients of STFT can be reallocated by using these realigned IF estimators across each frequency band's center as

$$\tilde{T}_v(t,\breve{\omega}) = \sum_{\frac{\Delta k_{\breve{\omega}}}{2} > |\breve{\omega}_v - k_{\breve{\omega}}|} S(t,\breve{\omega})\Delta k_{\breve{\omega}} \tag{4.33}$$

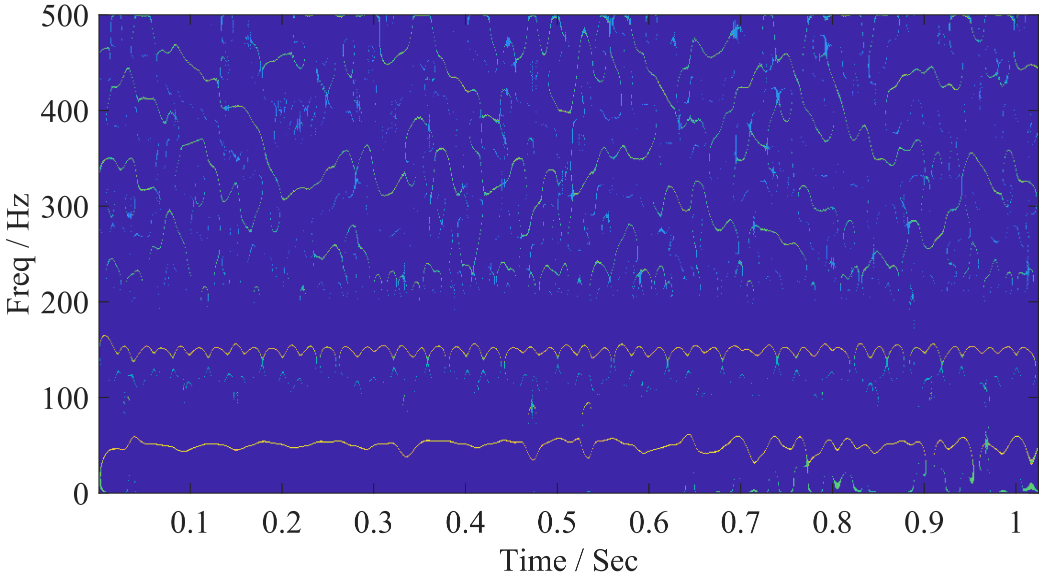

Figure 4.11: TFR of the signal shown in Fig.4.9 using AIFST

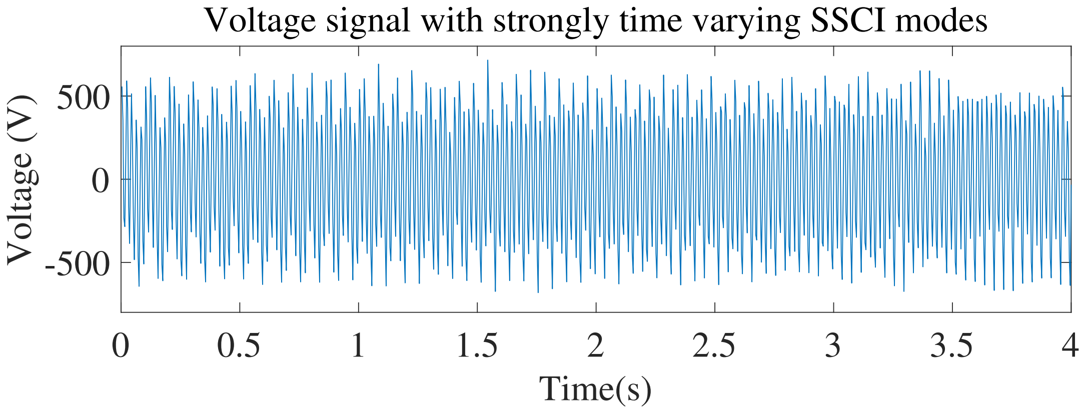

Figure 4.12: Time varying sinusoid with subsynchronous and supersynchronous modes

Following the realignment process for each mode, the coefficients in the discrete domain can be reconstructed using the adaptive and realigned IF based SST, frequently called as AIFST in this work,

$$\breve{a}_k = \frac{1}{2\pi g_\sigma(0)} \sum_{\tau_{SR} > |k_{\breve{\omega}} - \breve{\omega}|} \tilde{T}_v(t, \breve{\omega}) \Delta k_{\breve{\omega}} \tag{4.34}$$

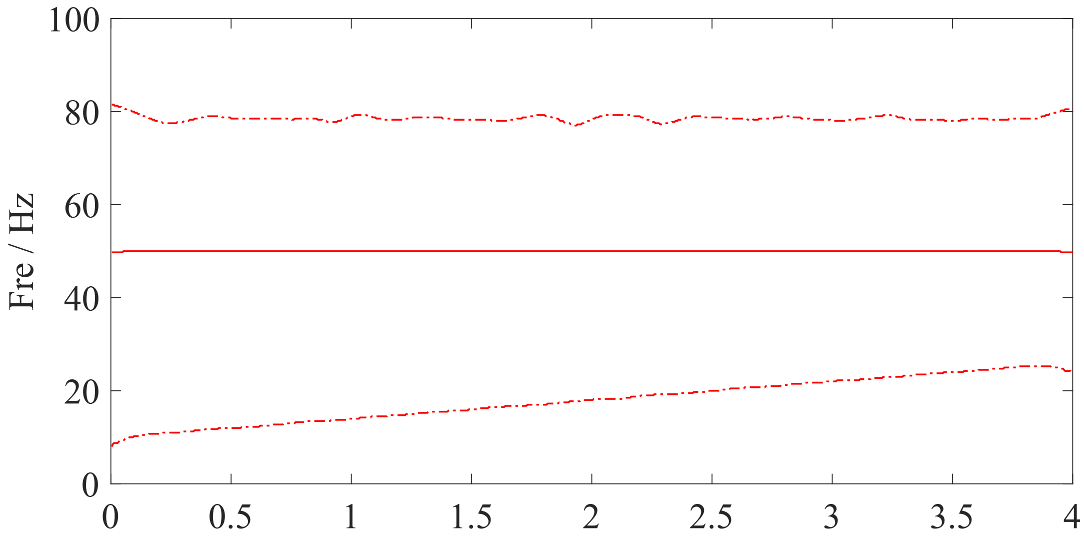

Figure 4.13: **Modes obtained using AIFST for strongly time-varying signal**

To illustrate the effectiveness of the developed (AIFST) approach for accurate estimation of the modes, a SSCI-based oscillations event is produced in the network shown in Fig.4.4. The voltage signal obtained at PCC of TF1 is shown in Fig.4.12. This time, the SSCI event contains a frequency mode varying with time from 10 → 21 Hz and a nearly constant mode of 80 Hz. The TFR representation of the modes is depicted in Fig.4.13 where both modes along with the fundamental frequency can be clearly observed. The precise estimation of the frequency modes leads to the accurate reconstruction of the frequency components involved in the complex SSCI event. The reconstructed modes as demonstrated in Fig.4.14 are obtained through the mathematically derived relation as given in (4.33). Therefore, accurately estimated modes provide a foundational basis for localizing the SSCI source within the network. These extracted modes are used to decompose the complex power flow, which consists of power exchanges at the PCC both at the fundamental and SSCI frequency components. Consequently,

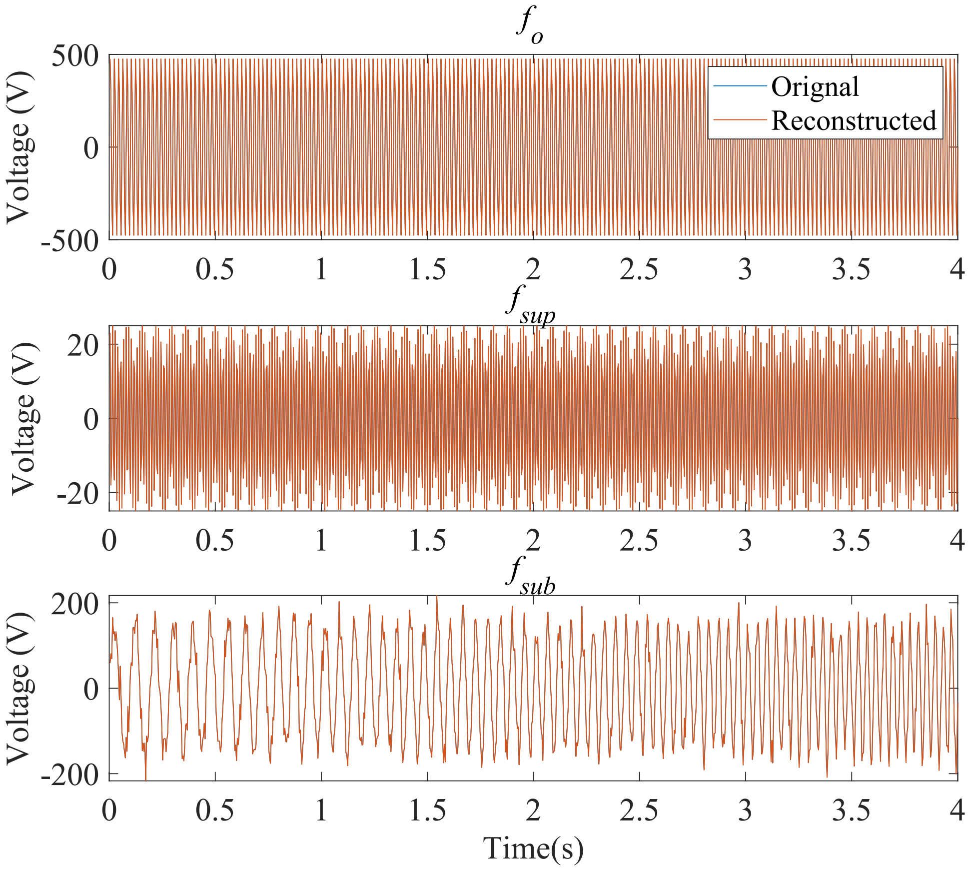

Figure 4.14: Modes obtained using AIFST for strongly time-varying signal

these modes are further leveraged to derive the complex power flow that explicitly reveals the contribution of each mode to the SSCI event. It is important to note that this chapter only provides the step-wise derivation and assessment of the developed approach and its detailed analysis to more complicated test cases is provided in the next chapter.

4.5 Localization

The power oscillations observed at any node in the power network result from the exchange of active and/or reactive power at specific SSCI modes. The source/origin of SSCI can be localized by decomposing the complex power flow at that node into the fundamental and SSCI components. Thus, the direction of power flow at SSCI modes provide significant evidence of source/region contributing towards oscillations in the network. Therefore, the modes reconstruction as discussed in the earlier sections play a significant role in characterizing the complex power flow.

Building on this foundational understanding and assuming that all branches and nodes connecting the IBRs and conventional power sources are fully observable in a simplified network (as shown in Fig.,4.15), the complex power at a specific node can be expressed as:

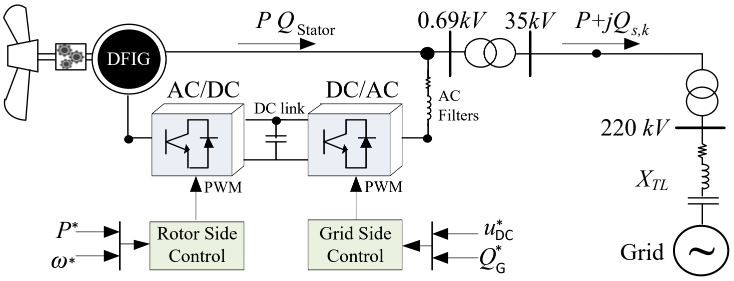

Figure 4.15: Simplified DFIG network connected to the grid through 220kV line compensated transmission line.

$$S_{j\to k} = \sum_{i=0}^{n} P_{j\to k} + \Im \sum_{i=0}^{n} Q_{j\to k} \tag{4.35}$$

where assuming that the DFIG based wind farm is connected at node j and exchanging $S_{j\to k}$ with the other nodes in the network, referred as “k”. Also, ”$\Im$” refers to the complex operator and “i” refers to the complex SSCI modes in (4.35). The active and reactive power at the nodes can be deduced from (4.35) as

$$\begin{aligned} P_{j\to k} &= P_o + \sum_{i=1}^{n} V_i I_i^{*} cos(\theta_{i,V} - \theta_{i,I}) \\ Q_{j\to k} &= Q_o + \sum_{i=1}^{n} V_i I_i^{*} sin(\theta_{i,V} - \theta_{i,I}) \end{aligned} \tag{4.36}$$

where P_o, Q_o refers to the fundamental frequency components, the subscript (i) refers to the modes (i.e., $subSR$, $supSR$ and harmonic noise), and operator "$*$" refers to the conjugate. From (4.35) and (4.36), it can be said that the resultant power at any specific node is the sum of fundamental and non-fundamental components of the system. The identification of frequency modes relies on (4.33) and (4.34), however, source localization intrinsically depends on the network admittance model (AM). The complex power for MSR-based oscillations is accurately observable if the system admittance is computed at that specific operating point. Previously, the source localization for SSR and SSCI interaction is illustrated on the basis of a single operating point [28, 134]. However, it is not practical for an IBR-dominated network to consider a model solely derived for a single operating point [135] due to intermittent nature of IBRs. This results in the lack of confidence in deriving an accurate relationship between the MSR and the system model. Therefore, the relation between the MSR modes and the admittance matrix (AM) obtained at varying operating points can be written as

$$\begin{bmatrix} v_{sub} \\ v_{sup} \end{bmatrix}_{(s,z_\kappa)} = \begin{bmatrix} \boldsymbol{Y}_{(s,z_\kappa)} \end{bmatrix}^{-1} \begin{bmatrix} i_{sub} \\ i_{sup} \end{bmatrix}_{(s,z_\kappa)} \tag{4.37}$$

where i_{sub}, i_{sup}, v_{sub}, v_{sup} are sub synchronous and super synchronous current and voltage modes respectively, z_κ denotes the operating point condition and $[\boldsymbol{Y}]$ is the AM. The frequency coupled AM ($\boldsymbol{Y}_{FCAM}$) can be obtained by modifying

(4.37) as

$$Y_{FCAM}(s, z_\kappa) = \begin{bmatrix} Y(s, z_\kappa)_{ii} & Y(s, z_\kappa)_{ij} \\ Y(s, z_\kappa)_{ji} & Y(s, z_\kappa)_{jj} \end{bmatrix} \tag{4.38}$$

where $\boldsymbol{Y}(s, z_\kappa)_{ii}$ and $\boldsymbol{Y}(s, z_\kappa)_{ij}$ represent the elements of the admittance matrix at the specific operating point (z_κ). For simplicity, (4.37) and (4.38) can be further manipulated by taking into account $[Y_{sub}](s, z_\kappa) = [i_{sub}] \times [v_{sub}]^{-1}$ and $[Y_{sup}](s, z_\kappa) = [i_{sup}] \times [v_{sup}]^{-1}$ at each operating condition (z_κ). The frequency coupled AM in (4.38) can be updated subsequently and in accordance with the obtained voltage and current modes. This can be written in a simpler form by representing in complex plane as

$$\begin{bmatrix} Y_{sub} \\ Y_{sup} \end{bmatrix}^{i}_{(s, z_\kappa)} = \begin{bmatrix} \boldsymbol{G}_{sub} + \Im\, \boldsymbol{B}_{sub} \\ \boldsymbol{G}_{sup} + \Im\, \boldsymbol{B}_{sup} \end{bmatrix}^{i} \tag{4.39}$$

Using (4.37), (4.38) and (4.39), the power for each MSR mode can be deduced as

$$\begin{bmatrix} s_{sub} \\ s_{sup} \end{bmatrix}^{i}_{(s, z_\kappa)} = \begin{bmatrix} \frac{i_{sub}^2}{Y_{ii}} + \frac{\Im\,(i_{sub}^* i_{sup}^*)}{Y_{ij}} \\ \frac{i_{sup}^2}{Y_{jj}} + \frac{\Im\,(i_{sub}^* i_{sup}^*)}{Y_{ji}} \end{bmatrix}^{i} \tag{4.40}$$

The $\boldsymbol{Y}_{ii}$ and $\boldsymbol{Y}_{jj}$, refer to WTG and grid side impedance, while the diagonal terms $(\boldsymbol{Y}_{ij} = \boldsymbol{Y}^*_{ji})$ refer to the impedance due to coupled frequencies, respectively. Simplifying (4.40) further yields

$$\begin{bmatrix} s_{sub} \\ s_{sup} \end{bmatrix}^{i}_{(s, z_\kappa)} = \begin{bmatrix} i_{sub}^2 \\ i_{sup}^2 \end{bmatrix} \begin{bmatrix} 1/\boldsymbol{G}_{sub} + \Im\, \boldsymbol{B}_{sub} & 0 \\ 0 & 1/\boldsymbol{G}_{sup} + \Im\, \boldsymbol{B}_{sup} \end{bmatrix} \tag{4.41}$$

Subsequently, (4.35) can be modified using (4.41) to compute the complex SSCI based power, and identify the region/source that either injected or absorbed power at the respective node as

$$\begin{aligned} S(s, z_\kappa) &= s_{sub} + s_{sup} = \boldsymbol{P} \pm \Im \boldsymbol{Q} \\ &= \left(\frac{i_{sub}^2}{\boldsymbol{G}_{sub}} + \frac{i_{sup}^2}{\boldsymbol{G}_{sup}} \right) \pm \Im \left(\frac{i_{sup}^2}{\boldsymbol{B}_{sub}} + \frac{i_{sup}^2}{\boldsymbol{B}_{sup}} \right) \end{aligned} \tag{4.42}$$

From (4.42), any IBR-induced oscillations in a weak grid can be of two types i.e., active and reactive power oscillation. The source can inject or absorb either mode of the oscillations by varying the impedance of the node at that specific operating condition. Therefore, (4.42) concludes that negative $\boldsymbol{P}$ and $\boldsymbol{Q}$ implies the node as an active source of oscillations and vice versa. Thus, the detailed analysis of this method is applied to realistic world cases and data, briefly discussed in the next chapter.

4.5.1 Method for Source Localization

This section provides a summary of overall method for source localization. The overview of the proposed method is illustrated in Fig.4.16, where the source can be localized using five main steps as provided in algorithm 1. In the first step, the initialization is ensured to confirm the data meets the minimum sampling requirements and is well synchronized. This is achieved with SWMUs as they are capable of capturing data with high samples at nodes where the WTGs are connected. Therefore, we ensure that data at the central location where algorithm 1 is used for localization is synchronized with the wider network and has no missing data and outliers. If so, the bad and missing data is replaced with

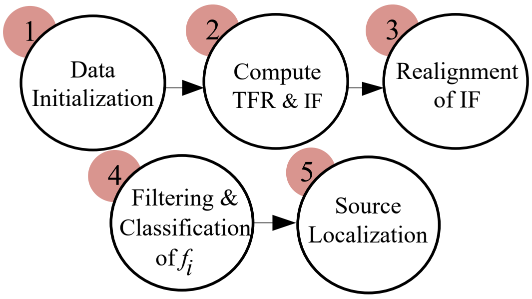

Figure 4.16: Methodology of the proposed method for modes detection and source/region localization

interpolation. In the second step, the SST is applied using (4.29). In this step, the preliminary information on instantaneous frequency ($\tilde{\omega}_v$) and phase ($\phi^{'}$) is obtained. In the third step, the $\tilde{T}(t,\psi)$ is obtained using (4.33) to retrieve the intricate TFR. This is achieved by computing $\tilde{w}_{ref} = \check{\omega}(\hat{t}) - \omega = 0$ using (4.30). In this step $\tilde{\omega}_v$ is realigned to its center location for each mode. This avoids mixing low and high-frequency modes and provides the intricate TFR of the event. In the fourth step, the frequency modes are selected based on conditional selection and the SSCI modes are reconstructed using (4.34). Finally, the complex SSCI power flow is derived using (4.42) at that specific operating point. The source of SSCI is localized by assessing the direction of power flow derived from the SSCI modes. The efficacy of the proposed method is demonstrated through numerical examples and a detailed case study.

4.6 Summary

This chapter proposes a systematic approach for deriving complex power flow and identifying sources associated with SSCI-driven oscillations. First, it is analytically found that the detection of these oscillations using synchrophasors and DFT-

Algorithm 1 Complex SSCI Detection & Localization

```
STEP 1:INITIALIZATION
Compute: $\hat{g}_\sigma$, Length (N): of signal From (4.2),
Sampling frequency (1/T), Nominal $f_0$.
STEP 2: COMPUTE STFT & $\breve{\omega}_v$                ▷ using (4.29) & (4.28)
STEP 3: REALIGNMENT OF IF
for $t = 1 : N$ do
    Calculate $\tilde{w}_{ref}$                          From (4.30)
                                                         ▷ Compute $k$
    for $n = 1 : k$ do
        Compute $\tilde{w}^{+}_{ref}$ & $\tilde{w}^{-}_{ref}$          From (4.31)
        Calculate $\breve{\omega}_v$                     From (4.32)
    end for
end for
Output: $\tilde{T}_v(t, \breve{\omega})$
STEP 4: CLASSIFICATION OF $f_i$
$f_i \leftarrow \breve{\omega}$                          From (4.29)
while $f_i \in [f_{sub}, f_{sup}] \times \mathtt{N}$ do
    if $f_i = [\tilde{T}_v(t, \breve{\omega})]^{\mathbf{2\times 1}}$ & sum $= 2 \cdot f_0$ then
        $[X]^{\mathbf{2\times 1}} \leftarrow \breve{a}_k$            ▷ Multimode SSCI
    else if $f_0 \leq f_i$ & $f_i \notin [n^{th} \cdot f_0]$ then
        $f_{sup} \leftarrow f_i$
        $X \leftarrow \breve{a}_k$                       From (4.34)
    else if $f_i \leq f_0$ & $f_i \notin [n^{th} \cdot f_0]$ then
        $f_{sub} \leftarrow f_i$
        $X \leftarrow \breve{a}_k$                       From (4.34)
    end if
end while
STEP 5: Source Localization
for $t = 1 : N$ do
    $X \in \mathbb{R}$
    while $|X| \neq 0$ do
        Compute Admittance Matrix                        From (4.39)
        Compute Power Flow                               From (4.42)
    end while
end for
for $i = 1 : j$ do
    $S(s, z_\kappa)^i$                                   Find power flow direction
end for
```

based algorithms leads to erroneous estimation of modes having time-varying frequencies. Then, the limitation of SST is highlighted using an analytical approach to ascertain that its performance is affected by noise and strongly time-varying signals. Consequently, AIFST is proposed to improve the accuracy of modes detection and so the corresponding particulars of SSCI-driven oscillations can be estimated adaptively in the presence of noise. Based on the identified modes at that particular operating point, a global admittance matrix is derived to identify the origin of SSCI-based oscillations. To localize the active/reactive source or sink of oscillations, modes-based power flow is derived at each observable node and source localization is carried out based on the active/reactive power flow. The robust and effective performance of the proposed approach is compared in four cases against the state-of-the-art methods by employing numerical simulations in the following chapter. The adaptivity and applicability for real-world applications are further demonstrated by using real-world data obtained from networks experiencing SSCI-driven oscillations, discussed in detail in next chapter. Therefore, as a result, a new diagnostic tool to support IBR-dominated grids may thus be realized, supporting effective mitigation of SSCI-driven oscillations.

Chapter 5

Validation of Modes Detection and Localization through Network Models

5.1 Introduction

Power network oscillations due to resonance and control interactions among inverter-based resources (IBRs) lead to voltage and current instabilities, challenging overall system stability and, in extreme cases, resulting in widespread outages. These oscillatory events are especially critical in power networks with high share of IBRs, where such dependencies lead to weak grid conditions and increased network complexity due to diverse topologies and control schemes involved. While previous studies have largely focused on low-frequency torsional and inter-area oscillations [4], the observability and localization challenges associated with SSCI have been overlooked, especially in real-time applications.

Notable system disturbances such as the North China Grid event due to wind farms control and HVDC control interactions, consecutive tripping of wind farm tripping in the ERCOT due to weak network configuration, and control-related issues in U.S. solar farms have emphasized the increasing impact of SSCI [4,82,136]. Most reported SSCI cases involve type-3 or type-4 WTGs and solar PV plants, where control interactions results in oscillatory power. These events are generally reported and linked to stationary sub-synchronous modes due to assumptions made as consequence of observability constraints. However, in practice, SSCI often involves more complex and inter-harmonics modes, including coupled modes that are not easily identified using system analysis considering single operating condition or neglecting the observability constraints as discussed in details in earlier chapters.

These complex oscillations propagate in the network with weak configuration, especially where Short Circuit Level (SCL) and reactive current contributions are explicitly low. The propagation mechanism is mainly driven by the internal control loops of IBRs, as few to name are those responsible for active and reactive power regulation, grid synchronizations and inertial emulations. Thus, during SSCI in weak network configurations, instability in one unit's (power park) control loop can lead to oscillations power injection at complex SSCI frequencies. Thus, neighboring IBRs, responding to such events may experience control saturation or feedback instability, further reinforcing the oscillations. Therefore, this mutual energy exchange between generation units at complex frequency modes complicates detection and localization. An example of such events is briefly discussed in [4, 43, 48, 137–141].

Therefore, keeping in view the understanding of complex SSCI existence in the weak or IBRs dominated network configuration, the methodology developed in Chapter 4 provides a foundational framework to identify the explicit SSCI modes and localize the particpating region/source in the network. Recalling the mathematical derivations from Chapter 4, where (4.33) and (4.34) allows identification of the complex SSCI modes, the SSCI based power flow can be formulated using (4.35). Following this, the contribution of active/reactive power at SSCI modes can be traced, leading to the localization of participating source in the network. These derivations enable identification of both source and sink components at SSCI frequencies, providing insight into which control loop or IBR is most responsible for the SSCI disturbance/event in the network.

Thus, this approach not only supports SSCI source localization but also contributes to understanding the SSCI power flow under dynamic conditions. Therefore, this chapter discusses the applications of the proposed method across several test cases, highlighting its effectiveness in accurately identifying the complex SSCI modes and tracing the origin and propagation of SSCI power. The results are analyzed in terms of Time-Frequency representation of the SWMUs waveforms, power flow behavior, and control response, providing significant insights into system dynamics and the implications. These findings also support targeted mitigation strategies by identifying the specific IBR control loops that require adjustment and are addressed in the next chapter.

5.2 Methodology of Validation

The proposed method is initially validated using a synthetic signal to demonstrate its detection accuracy in the presence of noise and time-varying frequencies. The effectiveness is then evaluated for real-world cases that involve SSR-driven oscillations and SSCI events. Dataset for two real events [1], one obtained through replication of an event through a PSCAD simulation and another recorded through PMUs, is used to verify the accuracy of modes detection. The detection accuracy is compared against state of the art methods recently reported in the literature, i.e., improved DFT (IpDFT) [46] and Prony analysis provided in [142]. Further, a modified IEEE-9 bus network is used for source localization, replicating the ERCOT incident [143].

The identification and localization algorithm is implemented in MATLAB/Simulink running on a desktop computer with a Core i7-11700 processor and 32GB random access memory. The algorithm takes an average computational time of 400 ms for the proposed method when the voltage and current waveforms are sampled at 1.6kHz. This sampling rate is sufficient enough to satisfy the Nyquist criteria for observing the complex SSCI modes up to 1 kHz. The computational time increases to approximately 800 ms when the waveforms are severely contaminated by noise and harmonics.

5.3 Verification through synthetic data: Case 1

The accuracy of the proposed method for a synthetic signal with time-varying frequency modes as M_1 and M_2 is verified through Matlab/Simulink studies. M_1 vary from 13.80 Hz→23.89 Hz and M_2 from 104.93 Hz→145.75 Hz with time. The signal is further corrupted with 40 dB noise and inter-harmonic components of magnitudes less than 1% to achieve an overall THD of 7.3%. Fig. 5.1 shows the modes detection comparison using the proposed method (AIFST), IpDFT, and

Prony method. The TFR of the synthetic signal is obtained using the proposed method and shown in Fig. 5.1b. It can be observed that AIFST detects the modes with high accuracy as compared to IpDFT and Prony methods as shown in Fig. 5.1c and Fig. 5.1d, respectively. Comparatively, the IpDFT performance significantly deteriorates when the input signal is constituted with time-varying modes and is affected by noise above 40 dB. It is clear from Fig. 5.1b, that the coefficients of DFT do not lie within the integral bins and so the exact magnitudes at corresponding frequencies cannot be determined. In contrast, the Prony method is dependent on a fix window function and thus requires a large window to estimate the modes in the signal. In addition to that, the modes M_1 and M_2 in this case are determined as an average over the period of the window and fail to provide accurate information on computing the frequencies at each operating interval. This limits the viability of the Prony method for constructing an admittance matrix for complex modes and at varying operating conditions. Alternatively, the proposed method precisely detects the modes (M_1, M_2) constituting the synthetic signals.

5.4 The Hammi Power Network

5.4.1 Description of the Network

The accuracy of mode detection and its feasibility for real-world systems is further evaluated by selecting the Hami power grid in northwest China. The network covers a diverse geographic area ranging from arid deserts to mountainous terrains, presenting both opportunities and challenges for generation and its transmission over the wide area. The north part of this grid is particularly notable for its

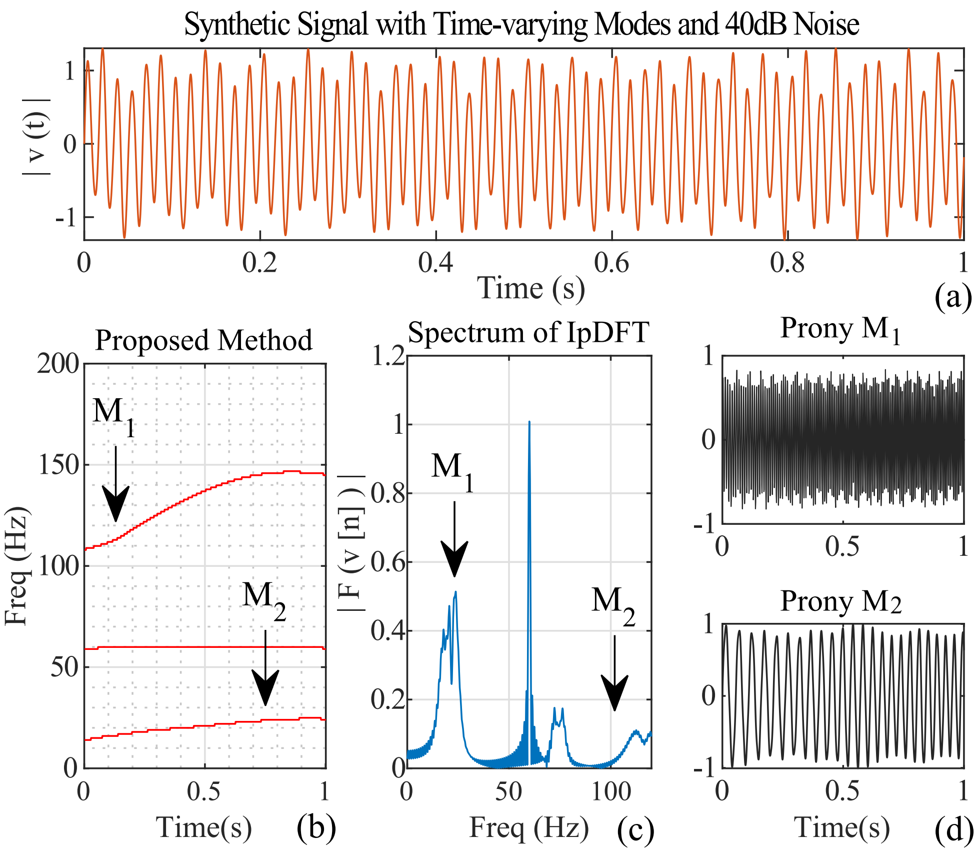

Figure 5.1: Modes detection in strongly time varied sinusoidal signal as shown in (a), using (b) TFr of the proposed method, (c) Spectrum of IpDFT, (d) Prony method.

significant renewable energy potential, making it a key focus for developing and adopting the existing infrastructure to accommodate intermittent power sources. The network is mainly comprised of static var compensators (SVCs), wind farms with mix of type-III and type-IV WTGs, and a transmission network of AC and ultra HVDC with the highest portion coming from the thermal energy as depicted in Fig. 5.2. The simplified network topology is illustrated in Fig. 5.3. The power from the WTGs is mainly collected through 220-kV lines, while a 500-kV double circuit line is used to export power to the Inner Mongolia and Northern grids. The double circuit lines are series compensated with maximum of 45% and 40%

compensation levels [144].

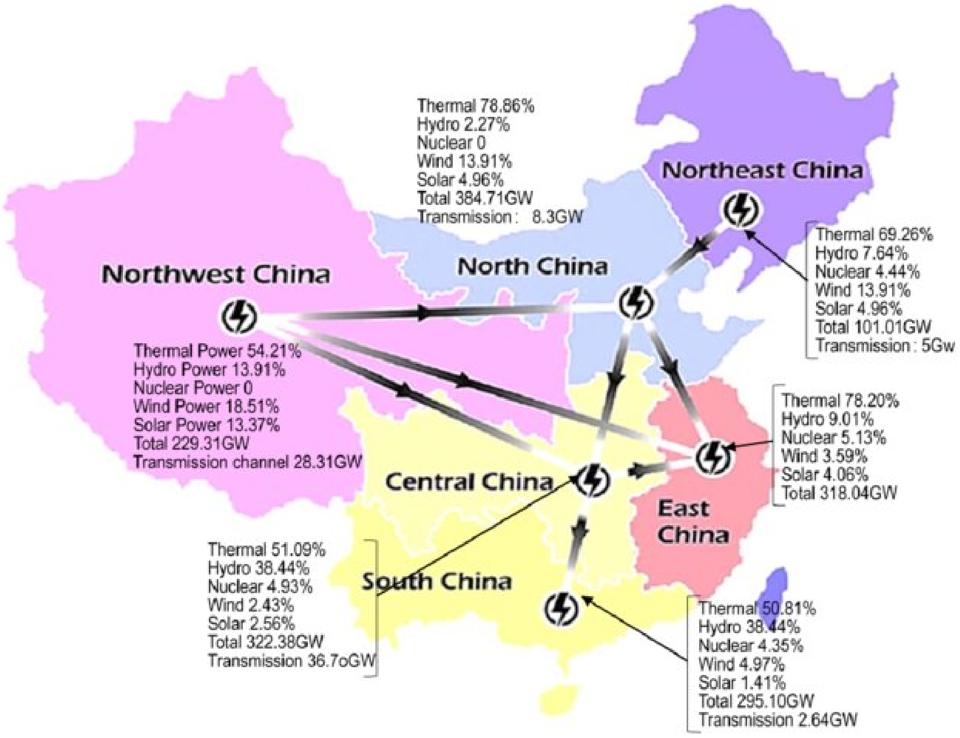

Figure 5.2: Illustration of Chinese Grid experiencing SSO events

5.4.2 Prior SSO Events in the Network

Over time, the Northwest and northeast parts have seen several oscillations event, highlighting the complexities of managing the new interconnection of modern power system. Notable events of oscillations include both SSO and SSCI, occurred timely from 2009 to 2017. The SSOs are mainly triggered by the interaction of large-scale wind farms with a series compensations. Over this period, there has been a notable increase in the reporting of SSO and SSCI events, likely concerning due to the active operation of the series compensations on all 500-kV lines and the involvement of control response to different events. This work looks into two major portions of the Northwest China grid covering SSCI events only. Firstly, we look into the SSO event reported in 2016 which had a frequency range of 19-24 Hz. This event specifically stem from the resonance between the type-3 WTGs and the series compensation. However, phenomena cannot be speculated as torsional based sub synchronous resonance (SSR) events due to a major difference in the topology of the generation mechanism as compared to the one in the Mohave power plant. This is mainly due to the reason that the phase current frequency in WTGs is less than 30 Hz. Therefore, this phenomena can be referred to as the SSR event as a consequence of the induction generator effect (IGE) explained in details in the next chapter. Secondly, the west China oscillation event is taken into consideration prevailing the primer effect of the phase-loop-lock (PLL) in the SSCI-driven oscillations. The event reported in 2015 mainly involved the type-IV WTGs, significantly injecting SSCI oscillations in the weak grid due to the inappropriate configuration of the PLL. The EMT studies in [145] further suggest that weak grid mode determined by type-IV WTGs can further interact with the torsional mode of the thermal generators, leading to high-frequency oscillations in the network. Subsequently, two distinct SSCI events are selected. For the first case, the instantaneous waveforms are obtained through PSCAD/EMTDC while incorporating factors producing the nearest replica of the event. Whereas, the dataset of the second event is recorded by both PMUs and waveform recorders [1, 15]. For both cases, the comparative evaluation of the proposed method with IpDFT and Prony analysis is presented next.

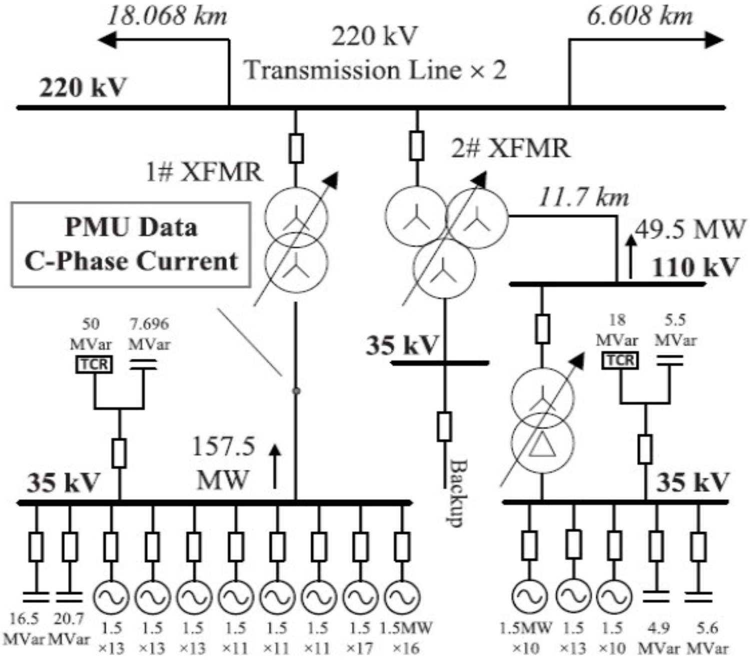

Figure 5.3: Network of North-China power grid experiencing SSO incident [1].

5.4.3 Validation of Event 1: Case 2

Fig. 5.4 (a) shows the current waveforms obtained through PSCAD/EMTDC simulation of the network shown in Fig. 5.3. Fig. 5.4 (b) shows the TFR of the SSCI event that occurs due to dynamic interaction between different network components, such as wind farms and SGs. The nearest estimation of f_o, f_{sub}, and f_{sup} using Prony analysis are 49.9 Hz, 24.575 Hz and 75.425 Hz, respectively. The TFr of Fig. 5.4 (a) shows a distinct mode having coupled frequencies (f_{sub} and f_{sup}) at 24.600 Hz and 75.400 Hz. The reconstructed modes at these frequencies are shown in Fig. 5.4 (c)-(e), and the key distinctions against both methods are summarized in Table (5.1).

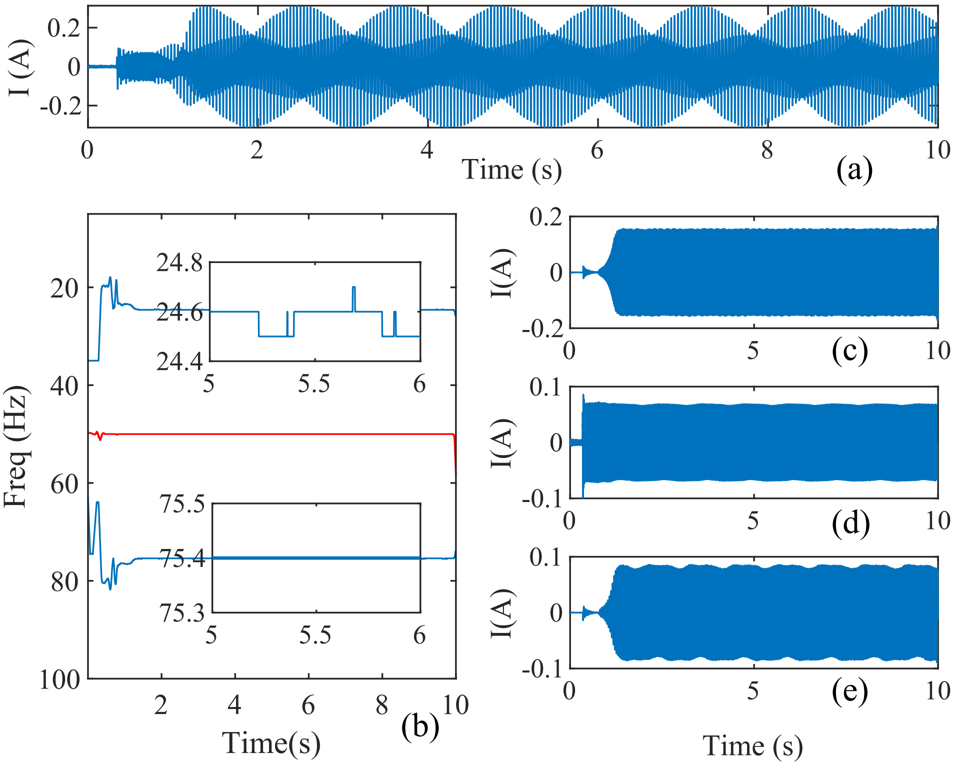

Figure 5.4: Simulation result of Hammi network showing, (a) instantaneous signal of current, (b) TFr of detected modes, (c) Mode at 24.6 Hz, (d) Mode at 50 Hz, (e) Mode at 75.4 Hz.

5.4.4 Validation of Event 2: Case 3

The efficacy and sensitivity of the proposed method are further evaluated on the real data of the SSCI event as shown Fig. 5.5. A brief comparison is provided in Table 5.1 for the proposed, IpDFT and Prony method. It can be concluded from the results that the ipDFT method reports the f_{sub} and f_{sup} only when the intact information on respective bins is constant and doesn't interpolate in the subsequent bins. Conversely, the Prony method estimates the nearest instantaneous frequency of both modes as $f_{sub} \rightarrow 8.278$Hz, $f_{sup} \rightarrow 91.6999$Hz, however, the mode detection subsequently deteriorate when strong variations in frequency are observed. Conversely, the proposed method is adaptive to frequency variations, flexibly adjusts the window and detects $f_{sub} \rightarrow 7.195\,\mathrm{Hz}$, $f_{sup} \rightarrow 92.807\,\mathrm{Hz}$, and consequently constructs the corresponding modes as shown in Fig. 5.5 (c-e). This concludes that both ipDFT and Prony methods capture the nearest modes if the noise ratio is above 40 dB. Furthermore, both approaches yield the mean values of the overlapping bins due to resolution limitations which inherently pose challenges in precise characterization of the modes. Alternatively, this can lead to indeterminacy of source localization and deteriorate the overall identification and localization process.

Table 5.1: TABLE I: Identified Modes in Case I, Case II, Case III, Case IV, and Comparisons with IpDFT and Prony Methods

	Case I			Case II			**Case III**			**Case IV**		
Results	Simulation results of time varying modes with noise			Simulation results of the Hammi network without noise			Actual data of the Hammi network with noise only			EMT simulation of ERCOT with harmonics and noise		
Methods	IpDFT	Prony	AIFST (Improved)	IpDFT	Prony	AIFST (Improved)	IpDFT	Prony	AIFST (Improved)	IpDFT	Prony	AIFST (Improved)
f_o	60	59.891	60	50	49.99	50	49.9935	49.9946	50	59.1022	59.6	60
f_{sub}	/	11.21, 27.55	13.8, 23.89	24.5753	24.5751	24.6008	8.287	8.2788	8.2570	12.11	11.3058	10.19
f_{sup}	/	100.83, 140.27	104.93, 145.75	75.4247	75.4252	75.4005	91.7129	91.6999	92.805	107.5998	108.7982	109.8

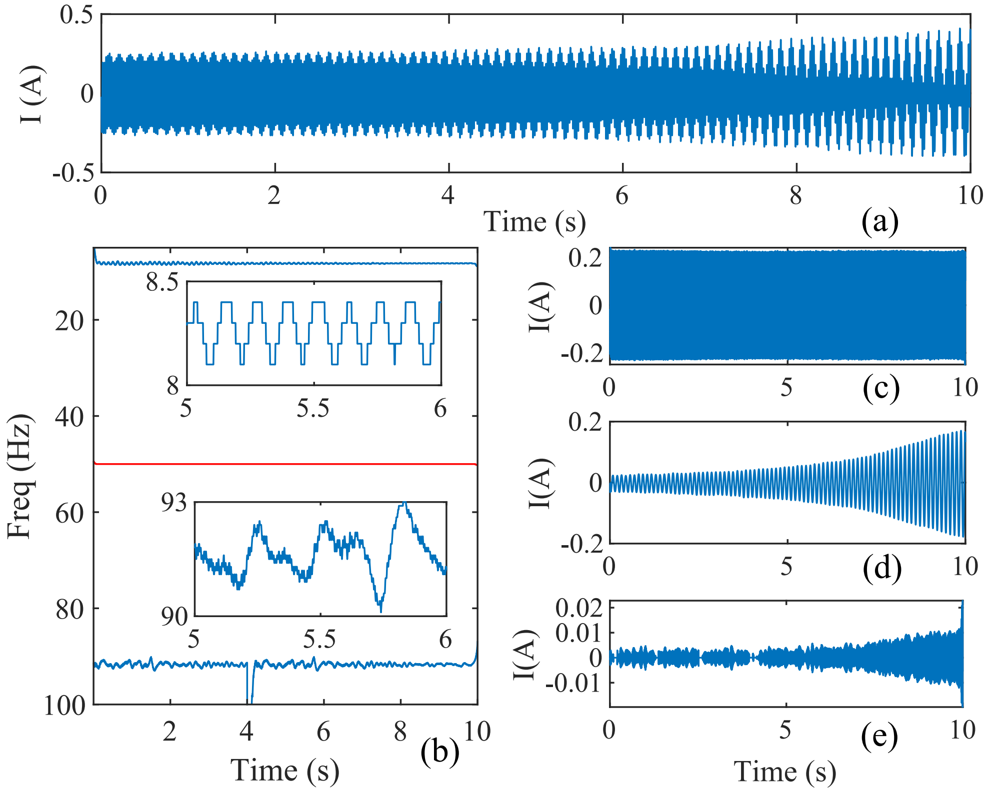

Figure 5.5: Real data of SSCI event in North China grid showing, (a) instantaneous signal of current, (b) TFr of detected modes, (c) time-varying Mode at 8.4 Hz, (d) constant Mode at 50 Hz, (e) strongly time-varying Mode at 91.6 Hz.

5.5 The ERCOT Network

The Electric Reliability Council of Texas (ERCOT) is one of the largest state's networks, feeding more than 26 million customers and covering almost 90% of the state load. The ERCOT serves as the primary operator of the grid and oversees the complex and expansive transmission network. The network includes over 650 generation units, encompassing a diverse integration of conventional and non-conventional energy sources. The diverse mix of these sources is dispatched over

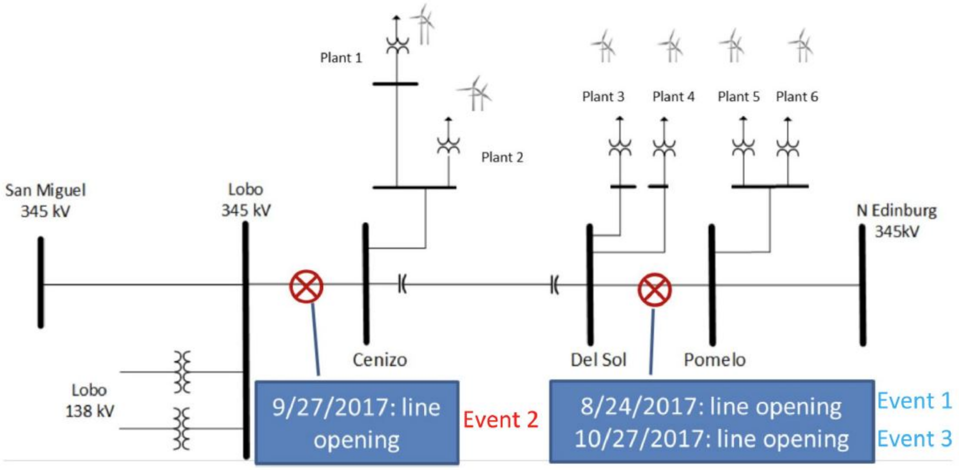

Figure 5.6: Section of ERCOT network reported in [2]

46,500 miles of high-voltage transmission lines network incorporated with series compensations. The Texas grid keeps evolving and is highly penetrated with wind and solar based intermittent sources. Specifically, the southside of ERCOT network is of great interest as the region has been heavily integrated with WPP of different capacity and network compensations. This part of the network as shown in Fig.5.6 has seen rigorous SSO events since 2007. The network illustrated shows only the south region limiting its boundary at San Miguel and N Edinburg stations, connecting to the rest of the grid with 345-kV transmission lines. There has been numerous studies taken out to analyse the stability and reliability of the network regarding the installed WPP [146–148], however none of these provide intrinsic information on the developed test-beds and the parameters adopted. Previously, the authors in [146] developed a PSCAD/EMTDC model for the Silverton station, however the model doesn't incorporate detailed parameters and makes it difficult to replicate the event with unknown parameters. Similarly, the authors in [147, 149, 150] investigate the type-III WPP for SSR for the particular section of the Texas grid and provide limited information on the parameters required to replicate the event. Similarly, [148] replicates the part of the Texas grid for scanning the overall reactance of the network. The authors only provide transmission line and transformer impedance and do not convey the WPP parameters.

5.5.1 Prior SSO Events in Texas/ERCOT Network

The Texas network has experienced two major events in 2007-2009 and in 2015. In 2009, a 680MW WPP is connected to the 345-kV main transmission line. The WPP is mainly a cluster of 3 WPP with type-III configuration of the WTGs and was connected at Ajo station. The transmission line has further expension at Rio Hondo where two stage compensation of 33% and 17% is installed. This compensation corresponds to the total of 50% reactance of the transmission line between Rio Hondo and Lon Hill. In 2009, the Ajo-Lon Hill line was tripped due to a fault. This tripping of the line causes the WPP in radial connection with the series compensation leaving it to experience a total of 80% effective compensation level. This triggers high voltage oscillations and results in damage to the crowbar circuit of the WTGs and the installed series capacitors. The modes of these oscillations are reported between 20-30 Hz and emerge within 100-150 ms of time. After the incident, a temporary solution was provided by installing an SSR relay to prevent further damage. Later on, during the upgrading and reconstruction of the Lon Hill and Rio Hondo transmission lines, the compensation level was reduced to 30% to avoid future occurrences of such events. However, the problem was permanently resolved after the WPP owners confirmation for installing SSR dampers.

Similar to the event reported in 2009, the southside region of the network experienced three different events in 2017. All these events are related to the type-III WTGs-based WPP who had previously installed the damping controllers. However, the installed damping controllers were designed on the limited information regarding SSO bandwidth and frequency modes. The other strong justification for this could be the inaccuracy in the modeling and analysis of the network [143]. It is noteworthy to say that all these events were reported within a three-month timeframe and took place on the 345kV transmission line between Lobo and N Edinburg. There are six WPPs installed over this transmission line as shown in Fig.5.6, pair of each connecting at Cenizo, Del-Sol, and Pome-lo stations. The transmission line is compensated between Cenizo and Del Sol and further ends at San Miguel and N Edinburgh station, connecting it to the rest of the network. The summary of the three events is as follow: The first event took place on 24th August, when the Del Sol-Pomelo line was tripped. This left the WPP connecting at Del Sol station in radial connection with the rest of the grid and installed series compensators. The modes reported for this event are 25.6 Hz and are observed through DFRs installed at the station bus. The second event was reported on September 27th, when the Lobo-Cenizo line was tripped. This scenario is similar to the one reported in the first incident, however the reported frequency of SSO is slightly less than 25.4 Hz. The SSR reported on this station was nearly 22.5 Hz and the corresponding waveform for voltage and current were recorded in [44]. Similarly, the third event appeared after one month with an SSO frequency of 26.5 Hz. However, the event didn't trip the SSR relays and protection devices installed for WPP connecting to the Del Sol station. The discrepancies in the reported frequency and SSO modes compel further investigation to replicate and analyse the events. This is because the first and third events are the same regarding the network and system parameters, however the reported modes lay at different frequencies. The second event make practical sense as the compensation and overall reactance are different, however this doesn't provide enough confidence for the reported modes to peruse for source localization. Therefore, the ultimate goal is to investigate and replicate the testbed developed by the University of Florida [143], verify it for the reported SSO frequency modes using the AIFST, and further configure it with type-IV WTGs to investigate the complex SSCI.

5.5.2 Modeling of ERCOT Network

It is always difficult and challenging to replicate the previous grid events to demonstrate the exact parameters. This is mainly due to the uncertainty, accuracy, and fidelity associated with the measurements observing the power network disturbance and the involved network components. Previously, a testbed was developed by the University of Florida for the ERCOT network, mimicking the events reported due to SSO as a consequence of SSR. The testbed parameters are provided in [143], however, it only employs the type-III based WTGs. Therefore, this work replicates the testbench developed for the three events to ensure the accuracy of the AIFST for detecting the SSR modes. Then, the model is further incorporated with type-IV WTGs to analyse the complex SSCI characteristic as a consequence of future up-gradation to the PMSG-based WPP. The complex SSCI is adopted as a test case to demonstrate the localization of the source/origin. The two foremost challenges for replicating the testbed are the information about the network component parameters and the event. The network component parameters are mostly extracted from the available information through public reports and mathematical analysis. The information on the capacity of the wind farms is found in the [44,143], where accumulated and aggregated models are used to achieve that capacity. Regarding system parameters and WTGs, the vendors never disclose information about the converters' topology, control parameters, and associated power plant controllers (PPCs). Therefore, two-level VSCs are employed for both type-III and type-IV DFIGs. The control system structure is based on the GE 1.5MW wind turbine model [151] which employs the *dq* transformation-based volt/var control. In addition to that, the event-related parameters are unknown to replicate the SSR, such as wind speed, the fault location, and the number of online wind turbines. These parameters effectively disturb the network impedance and contribute essentially to the induction generator effect. Therefore, considerate attention is paid to this part of the modeling and the nearest modes are achieved by the hit-try method. The rest of the parameters and modeling is carried out as follows.

Modelling of Wind Farms:

The wind farms are developed using the detailed model of the WTG. The 1.5MW GE generic model is adopted to develop all the wind farms. For the SSR-based topology, the aggregated detailed model of DFIG is used. A two-level IGBT-based VSC is employed for both GSC and RSC. The harmonic suppression filters and the VSC control for active/reactive power control are adopted from the model detailed in Chapter 3. The detailed parameters for a single unit DFIG are provided in Table 5.2 For all three wind farms, 734 WTGs of 1.5MW are assumed. The number of WTGs to each WPP is assigned from the detailed

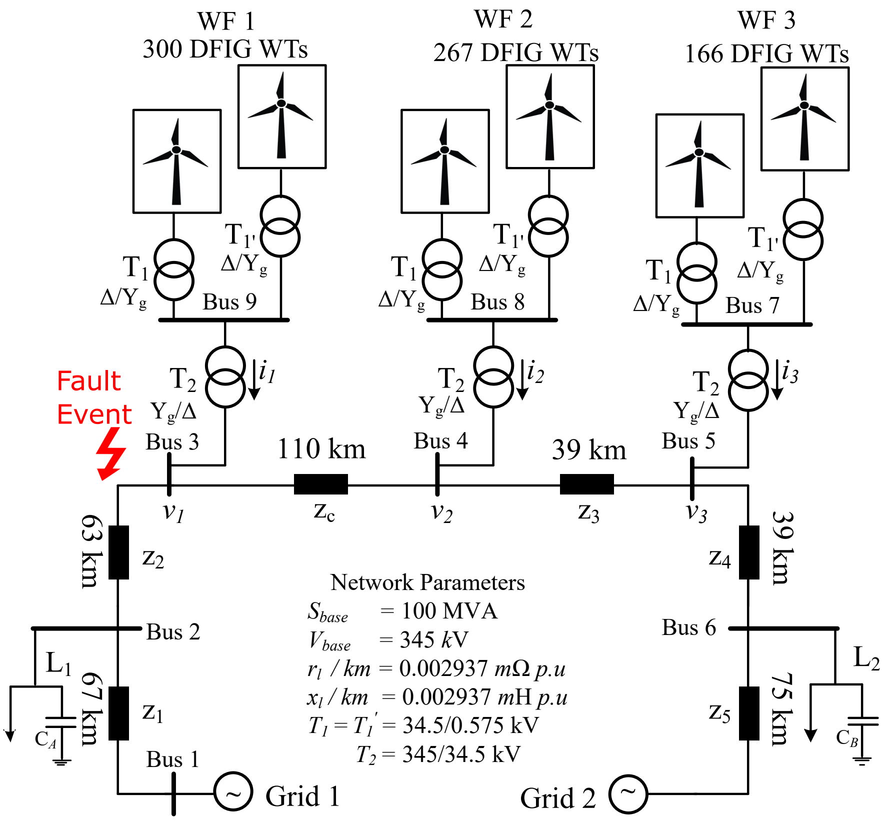

Figure 5.7: Circuit schematic of ERCOT replication using IEEE 9 bus network.

information provided in [44]. Following the information provided in [143,152,153], the capacity of WPP connected at bus 3 (Cenizo station), bus 4(Del Sol), and bus 5(Pomelo) is approximated as 450 MW, 400 MW, and 250 MW, respectively. All of the six WPPs employ the same model of DFIG, aggregated for the estimated power at each bus as shown in Fig. 5.7. The rest of the parameters for the capacity of WPP corresponding to each event are given in Table 5.3.

Modeling of Transmission Line:

The transmission line data is obtained from the public project reports of Electric Transmission Texas (ETT) [44, 143, 152]. The transmission network is comprised of six 345 kV stations, three of which namely Cenizo, Del Sol, and Pomelo are

Table 5.2: Parameters of Single WTG

Parameter	Value (SI)	Per-unit (pu)
Rated power	1.5MW	0.9
DC-link voltage	1150 V	
Rated voltage	575 V	1
Nominal freq.	60 Hz	1
Wind speed at Pmax	11 m/s	$0.18, 0.023$
$L_{l_s}\left(X_{ls}\right), R_s$	$94.5\mu\mathrm{H}, 5.6\ \mathrm{m}\Omega$	$0.16, 0.016$
$L'_{lr}\Big(X'_{l)}, R'_r$	$84.0\mu\mathrm{H}, 3.9\ \mathrm{m}\Omega$	2.9
$L_m\left(X_m\right)$	1.5mH	
Inertial, poles	$8.03\ \mathrm{J}, 6$	
Friction factor	0.01	
C_{dc}	10mF	$0.3, 0.03$
$L_c\left(X_{Lc}\right), R_c$	$0.16\mathrm{mH}, 0.59\ \mathrm{m}\Omega$	0.267
$C_1\left(B_1\right)$	2.9mF	$K_{pig} = 0.83, K_{iig} = 5$
Current control (GSC)		$K_{pdc} = 8, K_{idc} = 400$
DC-link control		$K_{pac} = 8, K_{iac} = 400$
V_{ac} control		$K_{pir} = 0.6, K_{iir} = 8$
Current control (RSC)		$K_{pq} = 0.4, K_{iq} = 40$
Q control		$K_p\mathrm{PLL} = 60$
PLL		$K_{i\mathrm{PLL}} = 1400$

Table 5.3: PARAMETERS OF WIND FARMS (1.5 MW EACH TURBINE)

	Capacity (MW)	Total	Event 1	Event 2	Event 3
WF1 (#WTs)	450	300	267	110	200
WF2 (#WTs)	400	267	250	220	200
WF3 (#WTs)	250	167	167	167	167
Wind Speed (m//s)		11	7.5	7.9	10.5

connected to the WPP. The endpoints of the transmission system, San Miguel and North Edinburgh, are linked to the main grid and represented as an infinite bus, and denoted as Grid1 and Grid2, respectively. The transmission line spans 393 km from San Miguel station to North Edinburgh station. The Cenizo and Del Sol stations are stretched by 110 km; whereas, the two stations, i.e., Deol Sol to Pomelo and Pomelo to North Edinburgh are evenly located and have a distance of 39 km. The testbed and network of the transmission system are developed in Matlab/Simulink and the pu line impedance parameters are calculated using the Matlab Simpower system toolbox. The rest of the parameters for the transmission network are given in Table 5.4.

5.5.3 Determining the Compensation Level:

The compensation level of the line from Lobo to North Edinburgh is approximately 49%. The total reactance of the two series capacitors, installed between Cenizo and Del Sol stations, is 48 Ω. Table 5.4 summarizes the per-unit and real values for the transmission system, including the transmission lines and transformers. For the simulation of Event 2, the DFIG is replaced with PMSG at Pomelo station for complex SSCI, and the impedance z_5 and z_4 were determined through trial and error to match the ratio of the SSR component at 22.5 Hz to the fundamental component at 60 Hz (320A/230A). Note that XT1 and RT1 represent the total impedance of T1 for each entire wind farm.

Table 5.4: Transmission System Parameters

Parameter	Value	Per-unit (pu)
S_{base}	100 MW	
V_{base}	34.5 kV	
$X_{T1} = L_{T1} + R_{T1}$	31.6uH + 1.2 mΩ	0.002, 0.0002
$X_{T2} = L_{T2} + R_{T2}$	3.16mH + 0.12Ω	0.002, 0.0002
V_{base}	345 kV	
$z_c = R + (X_l + X_c)$	4.76Ω + (114 mH + 55 uF)	0.004, 0.0362 + 0.041
z_1	2.26Ω + 69 mH	0.0019 + 0.022
z_2	2.26Ω + 66 mH	0.0019 + 0.021
z_3	1.43Ω + 41 mH	0.0012 + 0.013
z_4	1.43Ω + 41 mH	0.0012 + 0.013
z_5	2.63Ω + 79 mH	0.0022 + 0.025

5.5.4 The Replication of the ERCOT Events: Case 4

Firstly, the developed ERCOT model is validated for the disturbance that produced the oscillation event. The event is initiated by a 3-phase fault leading to a line outage between Bus2 and Bus3. This outage leads to a radial connection between the series compensated line and wind farms connected at Bus3 and Bus4 as illustrated in Fig.5.7.

The voltage profiles obtained through simulation results on buses connecting the WTGs are shown in Fig.5.8. The instantaneous values are sampled at 1.2 kHz and the TFrs obtained through AIFST are shown in Fig.5.8(b, d, f). These results demonstrate and provide the early intervention of SSR modes at those particular nodes due to network disturbance. It is evident from Fig.5.8, that fault perturbs the voltage on all nodes, however, the oscillations emerge due to alteration in the topology of the network. In addition to that, the authors in [28, 143] analyze this event with a DFT-based algorithm which consequently estimates only subSR modes due to its bandwidth limitations. However, analyzing such an event using the proposed method demonstrates an additional mode involved in the SSCI-based oscillations as shown in Fig.5.8(b, d, f).

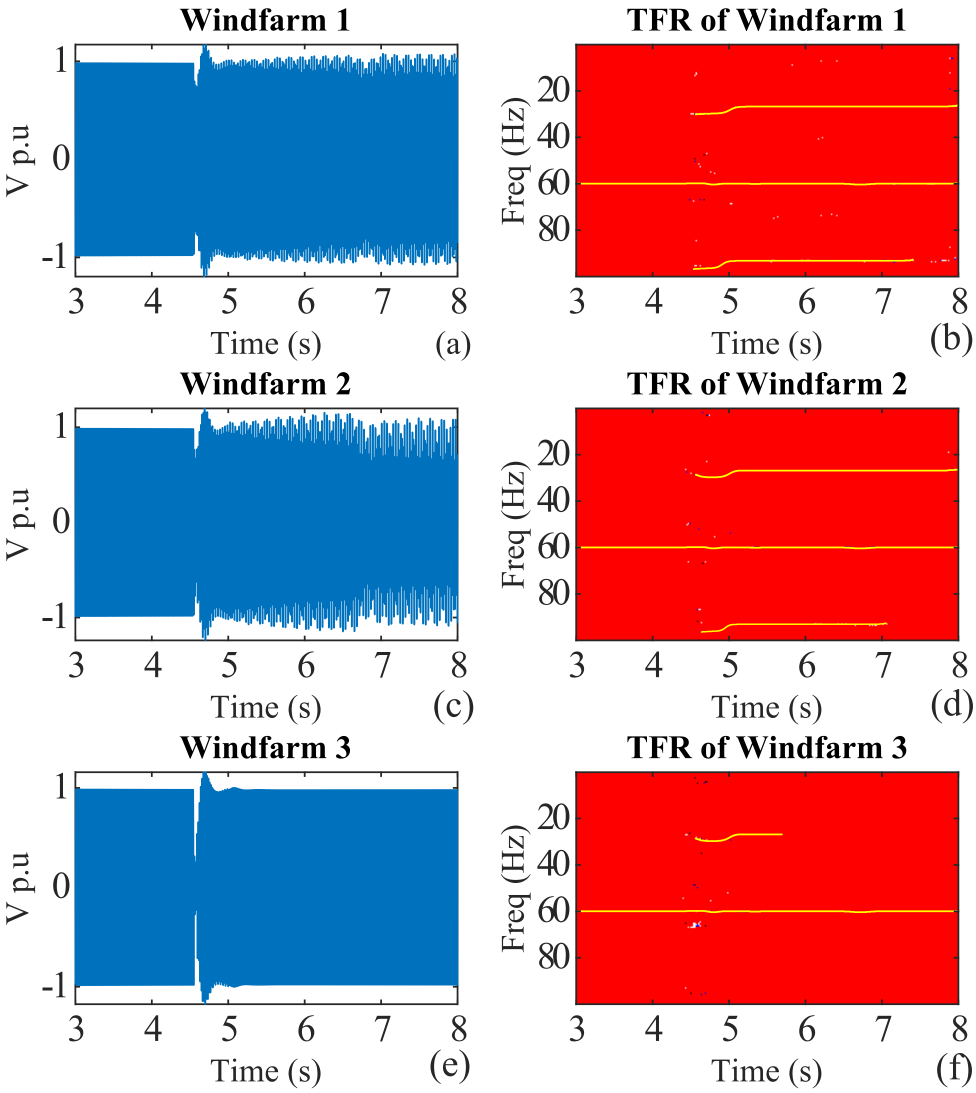

Figure 5.8: Fault triggered SSCI showing voltage waveforms and TFr of modes obtained using AIFST for (a) WF1, (b) WF2, (c) WF3.

The TFRs reveal that the fault triggers control interactions, impacting all three WFs, as shown in Fig.5.9. WF3 helps mitigate the effect by damping the oscillations and maintaining stable active/reactive power. However, it becomes evident that isolating the faulty section leaves WF1 and WF2 connected radially to the line compensation (Z_c), as illustrated in Fig.5.7. The triggered SSCI modes indicate that WF1 and WF2 contribute most to the subSR and supSR modes, while the TFR of WF3 shows only the subSR mode, lasting approximately 500 ms. This suggests that the DFT-based approach, with its limitations and measurement fidelity, can only detect a single subSR mode. In contrast, the proposed approach, which accurately estimates and detects modes while adapting to frequency variations under different operating conditions, identifies coupled-frequency-based modes for the event. Therefore, it is clear from the network topology that WF1 and WF2 are radially connected to the series compensation, providing strong evidence of their involvement in SSCI-driven oscillations.

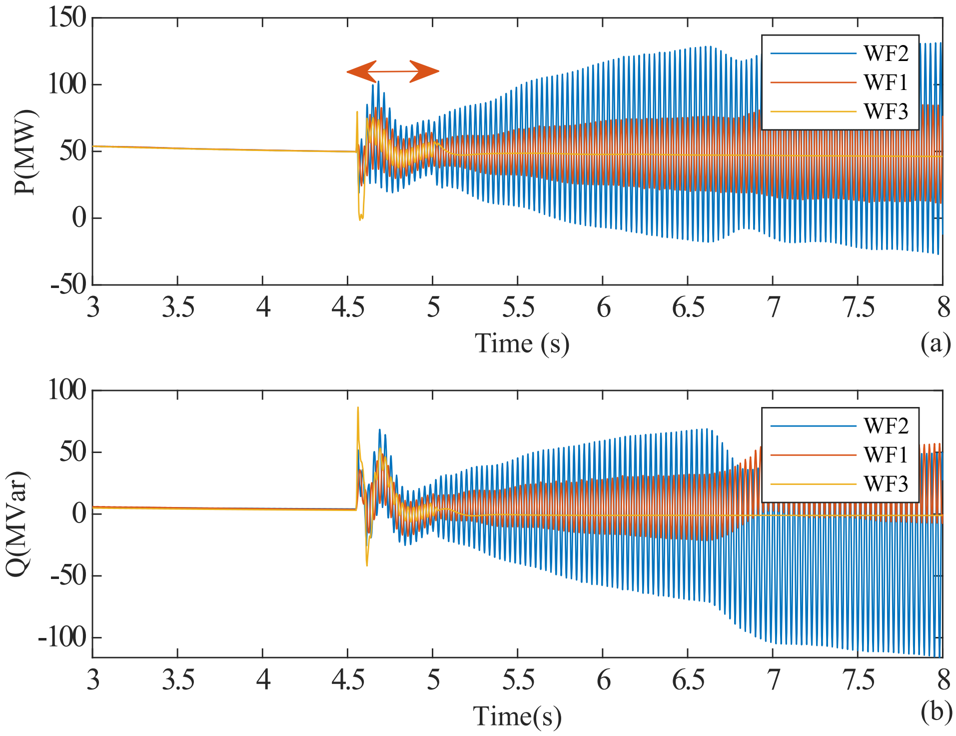

Figure 5.9: Performance of Wind farms in response to fault triggering SSCI showing, (a) active power oscillations, (b) reactive power oscillations.

On the contrary, this becomes severely challenging if the network components are not isolated, oscillating and threatening the whole network with explicit variations in the active/reactive power regulation. Therefore, to verify the proposed method for deriving SSCI-based power flow due to IBRs injecting both $subSR$ and $supSR$ modes in a network, the network is further modified by tuning the parameters of the PMSG and transmission line impedance. Recalling from the discussion of the previous chapters, the topology and configuration of the WTG explicitly change the SSCI modes. Therefore, in this scenario, the DFIG-based WPP at bus5 is replaced with PMSG to ascertain the amplitude of complex SSCI modes.

The key results from this test can be concluded as follows: Fig. 5.10 illustrates the current and voltage waveforms of windfarms connected at Bus $9, 8, 7$ for the network shown in Fig. 5.7. The instantaneous values are sampled at 1.2 kHz at their respective nodes for modes identification and source localization. The TFrs of the current and voltage waveforms are shown in Fig 5.10 (d-f) and Fig. 5.10 (j-l), respectively. The system parameters and control variables are deliberately tuned to induce harmonics and noise in the current and voltage waveforms to verify the sensitivity and efficacy of the proposed method against noise discrimination. At $t = 2.5$ s, the SSCI oscillations start in the system by varying the wind speed from 11 m/s to 7 m/s. Fig. 5.11 (a, d), Fig. 5.11 (b, e) and Fig. 5.11 (c, f) present the corresponding MSR modes for current values, while Fig. 5.11 (j, m), Fig. 5.11 (k, n) and Fig. 5.11 (l, o) represent modes for voltages obtained at intercon-necting nodes of WF1, WF2 and WF3, respectively.

The source localization is persuaded on the basis of the power flow direction, injected/absorbed by each SSCI participant. From (4.42), the power flow

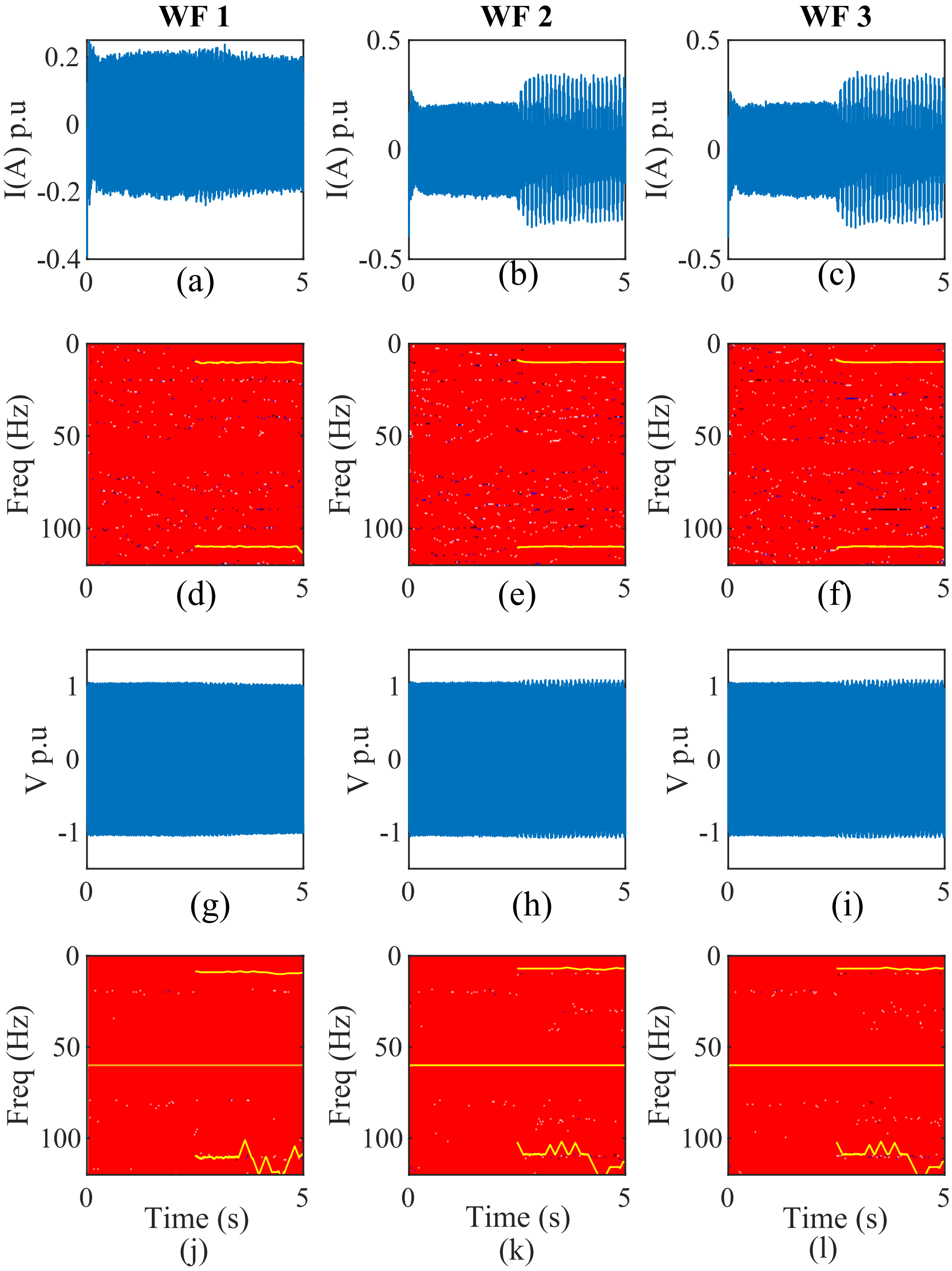

Figure 5.10: Wind triggered SSCI showing, (a-c) current waveforms, (d-f) TFrs of detected modes in current waveforms, (g-i) voltage waveforms, (j-l) TFrs of detected modes in voltage waveforms.

is solely derived on the basis of detected SSCI modes for the network shown in Fig.5.7. Further, the admittance matrix in alignment with the coupled frequencies is constructed from these modes, and the corresponding complex admittance is computed. According to the definition of (4.42), the substantial indications regarding the SSCI power flow determine the origin of the SSCI source. The SSCI -participant localization can be illustrated in Fig. 5.11 (m, p), Fig. 5.11 (n, q) and Fig. 5.11 (o, r), analyzing the active and reactive power flow at each interconnected node of respective windfarms. It can be observed that WF3 initiates both ac-tive and reactive power oscillations in the network with a major contribution of 1.4 MW active power and 0.15 MVAR reactive power injected into the system. This illustrates that WF3 is the prominent source of both active and reactive power oscillations in the network. Conversely, the WF1 and WF2 act as a sink for active power oscillations and absorb an equivalent of 0.45 MW and 1.2 MW. The control behaviour in SSCI-governed oscillations can be interpreted through an analysis of WF1 reactive power. In a stable system, the performance of the constant droop coefficient for the reactive power control loop is optimal and main-tains the reactive power to the reference until $t = 2.5$ s. However, the constant droop coefficient demonstrates limited adaptability when the system undergoes state transitions. It becomes evident that WF1 initially absorbs the reactive power oscillations, subsequently transitioning to become the source, primarily due to the variations in the impedance offered by the generator's rotor. There-fore, all three WFs behave either as a source or sink of active/reactive power and or both and vice versa.

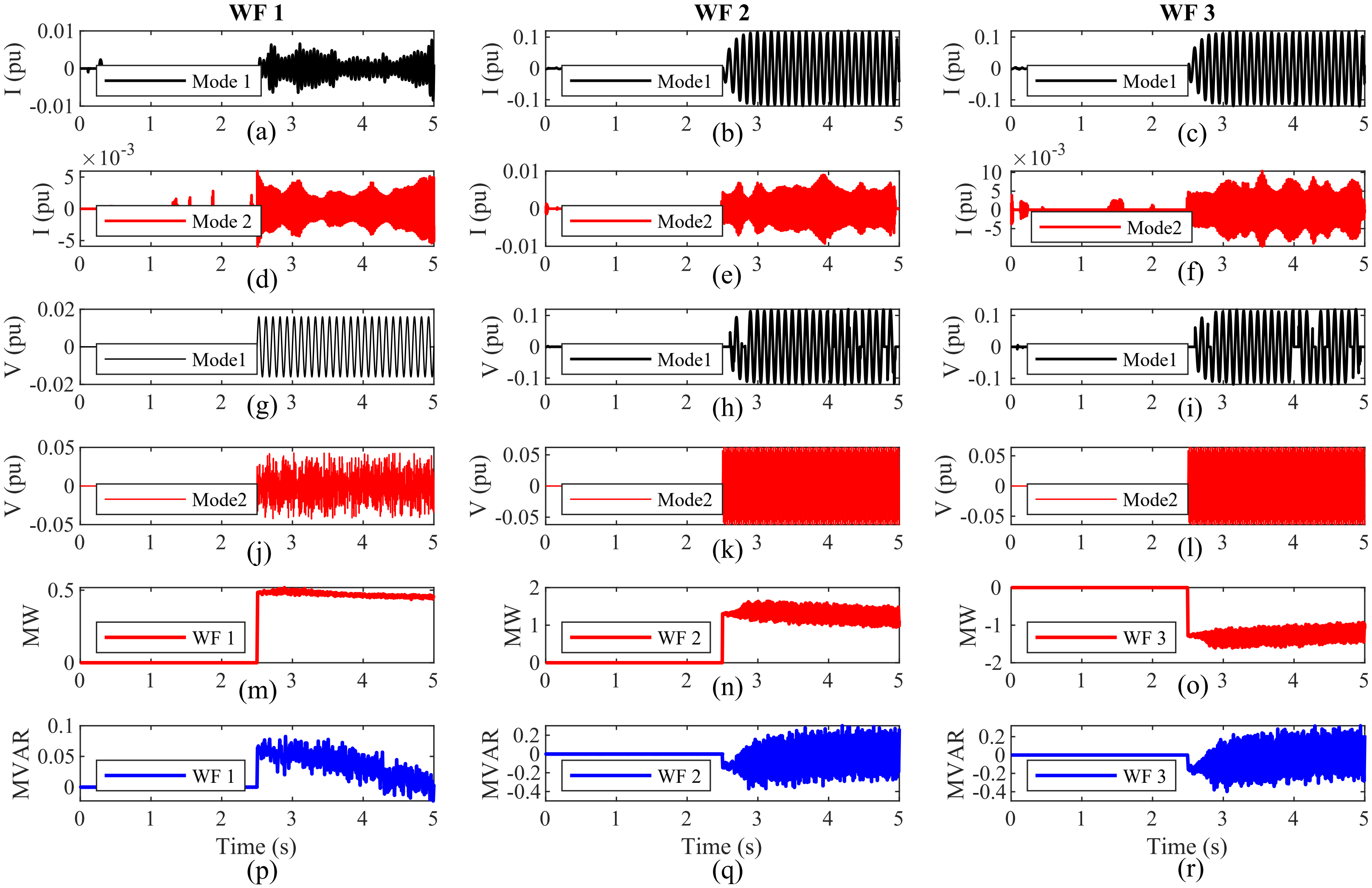

Figure 5.11: Illustration of modes reconstruction and power flow characterization from SSCI-event showing:(a-c) sub_{SR} modes in current for WFI, WF2 and WF3, (d-f) sup_{SR} modes in current for WFI, WF2 and WF3, (g-i) sub_{SR} modes in voltage for WFI, WF2 and WF3, (j-l) sup_{SR} modes in voltage for WFI, WF2 and WF3, (m-o) active power flow at detected modes for WFI, WF2 and WF3, (p-r) reactive power flow at detected modes for WFI, WF2 and WF3.

The comparative evaluation of the proposed method in contrast to IpDFT and Prony demonstrates that both techniques determine all the modes (f_o, f_{sub}, f_{sup}). However, this accuracy is contingent upon the condition that the data under the applied window is not time-varying and the noise ratio is considerably low as shown in Fig. 5.4. Otherwise, this results in an inadequate estimate of the f_{sub}, f_{sup} and its associated parameters. This is demonstrated in Case III where control parameters are deliberately tuned to get 9.8% ThD. A 20 dB noise in the voltage and current waveforms is further included to examine the sensitivity for real-world complex systems. It is evident from the comparative data in Table. 5.1, that the proposed method provides an accurate estimate of all frequencies and associated parameters, such as phase and impedance, and consequently realizes appropriate localization of the source.

5.6 Summary

The complex SSCI-based SSO requires a systematic, precise, and accurate approach to localize and identify the origin of SSCI and the participating sources. This requires a brief and systematic approach, where; firstly, the modes of oscillations are accurately determined. These modes are time-varying and explic-itly change with the operating condition of the network. In addition to that, the IBRs-dominated network is pertinent to complex SSCI with inter-harmonics modes with significant network noise. Therefore, the modes detection approach should be adaptive and selective enough to detect the SSCI modes only.

Secondly, Based on the identified modes at that particular operating point, a global admittance matrix is derived to identify the origin of SSCI-based oscillations.

To localize the active/reactive source or sink of oscillations, modes-based power flow is derived at each observable node and source localization is carried out based on the active/reactive power flow. Typically, the control of the IBRs is involved in the SSCI. Therefore, to identify the IBRs control contributing to the SSCI-based SSO, the relations derived in Chapter 4 are used to localize the origin where the control mechanism is explicitly contributing to the SSO. To prove the robust and effective performance of the proposed approach, the detection and localization approach is mainly validated through three main cases. Firstly, to ensure the adaptivity and robustness of the AIFST against time-varying and noisy signals, the modes detection is validated by testing using synthetic signals. Secondly, it is of utmost importance that the proposed method should be adoptable to real grid applications. Therefore, the modes detection approach is further val-idated through a real-world data set obtained from the northwest China grid. Finally, the overall mechanism of detection and localization is further analysed with the real-world dynamic system by developing the EMT models of the ER-COT south-region network. To conclude, the proposed approach is compared with the state-of-the-art and benchmark methods in all four test cases, and its feasibility is affirmed for real-world applications by its extensive performance.

Chapter 6

Mitigation of Complex Oscillations

6.1 Introduction

The widespread adoption of inverter-based resources IBRs into the existing grids has greatly reduced the dependence on conventional generation sources, however, this brings significant challenges related to the operational dynamics of the power system. Amongst the challenges associated with IBRs as discussed in the earlier chapters, the complex SSO with a wide range of frequencies are emerging as a specific concern [154]. Globally, power networks have encountered numerous SSO events, when IBRs and particularly WTGs are integrated in the network with the reactive components. Notably, events in wind farms-based power networks such as ERCOT in the USA, Guyuan in China, and Great Britain are primarily recorded because of SSR or SSCI between the series compensated lines and IBR's power electronics [4]. During these events, substantial oscillations in voltage and current are recorded, disturbing the whole network, consequently leading to disconnection of generation sources and damage to the protection system.

Numerous methods have been proposed to cope with the instability emerging due to SSCI or SSR phenomena on both generation and network sides [155]. The network sides are generally equipped with auxiliary damping devices such as synchronous voltage condensers (SVCs) and more power converter-induced topologies such as FACTs [156–158]. Typically, these devices are supposed to operate the system at nominal frequency and if augmented for SSR or SSCI frequency operation, severe voltage fluctuations in the DC link can be triggered. The operation of such a case is reported from the Guyuan system for the closest VSC to the SSCI source [159]. Solely employing these devices for mitigating the phenomena is an expensive solution, however, the strategy proves its feasibility only if such devices are already installed in the network and augmentation in control is provided to operate at specific SSCI frequencies. However, tunning the controllers for the exact modes of the SSCI is challenging as the frequency modes are usually not known and vary with the operating condition of the power network [3].

In recent times, there has been a surge in interest towards cost-effective control-based solutions for mitigating the SSO in the network. These are primarily based on the WTGs model and are explicitly reliant on the control parameters to prove their robustness and adaptivity to SSCI events. In these regards, [160] proposes a linear quadratic regulator as a damping controller by employing a reduced-order model to suppress the SSOs. Similarly, a nonlinear controller leveraging the partial feedback linearization technique is proposed to alleviate the oscillations in the DFIGs-based wind farms [161]. Similarly, a state space model-based linearized sliding mode controller is proposed in [162] to tackle SSO in the power network. Moreover, [163] uses the system Hamiltonian model and proposes an energy-shaping damping control to support the system with extra damping control ability. Meanwhile, [5, 31] is optimizing the parameters of the damping control by obtaining the impedance model of a DFIG-based wind farm network and assessing the performance of the proposed method via hardware-in-the-loop simulations and field tests. Enhancements to the damping control effectiveness in DFIGs are further explored through eigenvalue analysis and by employing optimization algorithms [164]. It is important to note that the accuracy of such control methods hinges on the intricate and precise modeling of the WTGs. However, the linearized models often fall short of representing the exact dynamics of real-world systems as complex nonlinearities are omitted while modeling the controllers. Additionally, given the need for tuning the parameters to optimal values, these CSDC are not guaranteed to deliver optimal performance across all operating conditions of the network.

Adapting to variations in operating conditions is crucial for effectively damping oscillations across a wide range of scenarios. In these regards, various methods are proposed to ensure the adaptive and robust performance of CSDC for a wide range of operational conditions. For instance, a variable gain super twisting sliding mode control is proposed in [165] adaptable to diverse conditions. Similarly, [166] proposes a model reference adaptive control to enhance damping under varying system operating conditions and wind speeds. Similarly, the CSDC-based approach reported in [167] is optimized through eigenvalue analysis, making the controller adaptive by dynamically adjusting the control parameter to variations in the compensation levels and wind speeds. Moreover, [168] extends the method proposed in [166] and employs a Multiple Model Adaptive Control strategy. This strategy is designed to provide a supplementary damping control capable of alleviating the SSO emerging across a broad spectrum of operating conditions. Despite the effectiveness of these methods, they often rely on the assumption of a known mathematical model or parameterized uncertainty. However, large-scale significant variations in operating conditions may prove the performance of these controllers inadequate for mitigating the SSO and providing sufficient damping.

Recently, model-free methods have emerged as a promising solution to various challenges associated with model uncertainties [169]. Some of the methods reported in the literature employ solely the data-driven approach, developing the control law by constructing dynamic linearization data models at various operating points using pseudo-partial derivatives [170]. The authors in [171–173] leverage these methods to train the system and control the SSO for various operating conditions. However, these methods are explicitly dependent on the online input data and require operational details of the system to achieve asymptotic stability of the control [174]. In addition to that, the dependence on the single control loop may inherently degrade the performance for other dynamics conditions such as the fault-ride-through (FRT) ability of the DFIGs in weak AC systems. To overcome these issues, model-free methods incorporating additional damping control loops are proposed previously by the authors in [5,31,175]. These involve triggering auxiliary damping control loop at SSR frequencies to mitigate the controller instability and prevent SSO. However, the damping control loop involves the integration of filters with specific bandwidth to filter the SSR modes and trigger at that frequency. This limits the viability of the approach rigorously depending on the prior knowledge of SSR frequencies [3].

The practical applications of frequency-dependent CSDC demonstrate constrained feasibility when dealing with SSCI-based SSO, where the modes of oscillations are non-stationary and are not definite due to varying operating conditions [176]. Therefore, to circumvent the reliance on frequency-dependent CSDC, this work proposes a DVIC that employs a single-layer-feed-forward learning algorithm to predict the error in the control signal due to large disturbance or SSCI triggering SSO in the WTGs; accordingly vary the RSC impedance and effectively mitigate the SSO driven be SSCI. Compared to the state of the art, the DVIC is an industrial-grade controller outperforming the CSDC due to its unique features such as: 1) It employs a data-driven auxiliary control loop to stabilize the *dq* control when a large disturbance or SSCI triggers the SSO. It does not need any offline training and triggers only on a limited set of neurons. 2) The functionality of the DVIC is adaptive and robust for all operating conditions and ensures asymptotic stability for boundary conditions. 3) The computational complexity is lower and the simplicity prevails lower costs for industrial implementation. 4) The proposed method doesn't consider heuristic assumptions to perceive monotonic convergence of tracking error.

Therefore, following up the findings in the previous chapter and leveraging the detection and localization approach which effectively nominate the control mechanism of the WTG involved in the SSCI, the DVIC control is proposed to mitigate the SSCI in finite time. The controller is implemented in the identified WTG and is verified through two realistic network systems. The key features of the developed method and proposed research are as follow:

1. Firstly, the proposed method is as simple as CSDC in structure and independent of the model states, making the implementation of the approach straightforward.

2. Prior knowledge of SSR modes and frequency bandwidths is not required as the DVIC is only based on the *dq* current states.

3. The generalized Hebbian learning law works as an auxiliary damping control loop. This approach makes the control adaptive and adjusts the rotor side converter (RSC) impedance in finite time by injecting a compensated signal to the *dq* control loop. The variation take place only when SSCI or large disturbance triggers system instability, thus making it stable for all varying conditions.

4. The method is implemented in one of the identified WTGs in the ERCOT network. These results demonstrate the effectiveness of the proposed method for real-world applications.

6.2 Research Motivation

It is widely recognized that IBRs, especially WTGs featuring complex power networks give rise to different types of stability challenges such as SSR and SSCI between the network components and WTGs. The severity of these disturbances are of critical concern, as these lead to network instability and induce complex oscillations. Promptly addressing these oscillations is crucial for ensuring dependable operations. Their mitigation relies on the prior identification of the frequency modes and the precise localization of the unit needing control upgrades. To achieve this, a systematic and precise method is required. This involves first identifying the SSCI modes and localizing the unit requiring the up-gradation to its control, as discussed in Chapters 4 and 5, which is an initial step in the mitigation scheme, followed by proposing a control scheme.

While numerous control methods have been proposed to tackle these oscillations, fictitious variation in damping using *dq*-based control of WTGs is seen as both cost-effective and dependable. Nevertheless, such methods are dependent on the prior knowledge of SSCI frequency modes and their effectiveness diminishes when the SSCI-oriented oscillations contain non-stationary and complex frequency modes. To enhance the WTGs control performance adaptive to diverse oscillation modes, this work proposes a single-layer feed-forward-based control approach, where the damping of WTG is fictitiously strengthened by the adaptive mechanism of Generalized Hebbian learning algorithm integrated into the *dq* vector control of WTG. The proposed method dynamically reacts to any SSR or SSCI occurrence and adjusts the WTG impedance to forestall oscillation initiation within a finite time. Through simulations and diverse test cases, the effectiveness and feasibility of the proposed method are demonstrated, marking its potential for real-world applications for the first time.

6.3 The Impedance Model of the System

6.3.1 A Typical DFIG based Series Compensated Network

A series compensation is an old technology to support an increase in line loading capacity and transmit quality power without voltage collapse. Fig.6.1 shows the typical series compensated transmission line system connected with grid at one end and DFIG based wind power plant (WPP) at the other end. The series compensator is a bulky passive component providing reactive power being proportional to the square of the current flowing through it. However, besides fault current and changing constraints for operating time of protection system, the series compensation present notable challenge which involve the dynamic interaction with the network components and initiating resonance at certain electrical and mechanical frequency.

For an IBRs-based simplified network as shown in Fig.6.1, the series compensation interacts with the converter control and incites resonance generating SSO with inter-harmonic and coupled frequency modes, thus referred to as complex SSCI [177]. This interaction occurs purely at electrical modes and has no definite bandwidth. The DFIG-based WPP in a series compensated power network can be essentially considered as series RLC resonance-based circuit, where the electrical resonance frequency can be written as,

$$f_e = f_0 \sqrt{\frac{X_c}{\sum X_L}} \tag{6.1}$$

Here, f_0 is the nominal frequency of the system with X_c as the cumulative capacitive reactance of the series compensation and transmission line, while $\sum X_L$ refers to the cumulative inductive reactance of the WPP, the transformers, and the transmission line. The resonance in such a system occurs due to the self-excitation of the induction generator (IG) as a consequence of negative slip. The general relation for slip is given as,

$$s = \frac{f_e - f_r}{fe} \tag{6.2}$$

Given in (6.2), f_r represent the rotor's electrical frequency and this can be deduced into Laplace transform as,

$$s = \frac{s - j\omega_m}{s} \tag{6.3}$$

In order to operate the machine in generator mode, usually the $f_e < f_r$; implying a negative slip. It is obvious that at negative slip, the rotor resistance is negative due to the lagging of magneto motive force (MMF) produced by armature current at f_e and thus it moves at a slower speed as compared to the speed of the rotor. On the contrary, since the stator of the DFIG is connected to the grid, the cumulative resistance on the grid side present positive resistance. The triggering of self excitation leading to oscillations in voltage and current are triggered only if the rotor's resistance magnitude at this resonance frequency is higher than the grid side resistance magnitude. The oscillations in the armature of the generator also involve the converter control and thus the control interactions are induced at this sub-synchronous frequency. Since the SSCI involve the converters control, the modes of the oscillations are essentially different as those involved in the synchronous generators (SG) due to induction generator effect (IGE). This is mainly because the RSC and GSC control are not involved in the SG and so the oscillation modes are only related to the mechanical dynamics. However, the IG effect can be illustrated as an assumption of growing SSCI by taking into account the dynamics of the RSC and GSC control effects. The RSC control explicitly aggravates the equivalent resistance of the rotor, however, this needs a mathematical derivation from the detailed model of the series compensated DFIG.

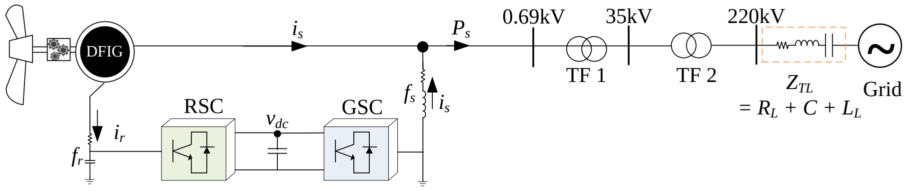

Figure 6.1: A schematic of series compensated transmission line with connection to DFIG and grid.

For instance, the equivalent resistance on the rotor side can be written as [5],

$$R_{eq} = \frac{sR_r}{s - j\omega_m} \tag{6.4}$$

where, ω_m is referred to as the mechanical speed of the rotor in (6.4). Therefore, given the importance of the rotor equivalent resistance and its affiliation with the RSC control, the IGE can be considered as foundational argument to explain the complex SSCI in the grid connected WTG with series compensated transmission line. A detailed analysis will be provided in the next section, which includes an in-depth modeling of the DFIG with a series compensated transmission line. This analysis will lead to a simplified yet sufficient circuit model that represents the effect of rotor resistance and the control parameters.

6.3.2 Derivation of an Equivalent Circuit Model of DFIG

The operation of a line-compensated DFIG is significantly influenced by factors other than the slip of the induction generator itself in relation to SSO. The most primitive development in complex SSCI due to DFIG is a consequence of equivalent rotor resistance, This is affected by dynamic parameters such as variations in wind, torque control, and the turbine converter control. This has been extensively studied in [178, 179] and [5]. Since the DFIG in grid connection represents strongly coupled topology, detailed modelling is required to reflect the dynamic effect of the control in efforts to mitigate the complex SSCI. Therefore, it is best to consider the internal dynamics of DFIG with the rotor and its control extorting the system stability with changing dynamics of the grid. Fig.6.2 represent the DFIG connected to the grid through VSCs with grid following control. The VSC is employed at both sides of the DFIG as an RSC and GSC with an induction generator (IG) connected through a shaft system. The IG can be represented in dq frame as [165]

$$\begin{aligned} v_{ds} &= \hat{R}_s I_{ds} + \frac{d}{dt}\psi_{ds} - \omega_s \psi_{qs} \\ v_{qs} &= \hat{R}_s I_{qs} + \frac{d}{dt}\psi_{qs} + \omega_s \psi_{ds} \\ v_{dr} &= \hat{R}_r I_{ds} + \frac{d}{dt}\psi_{dr} + \omega_{slip} \psi_{qr} \\ v_{qr} &= \hat{R}_r I_{qr} + \frac{d}{dt}\psi_{qr} + \omega_{slip} \psi_{dr} \end{aligned} \tag{6.5}$$

with

$$\psi_{ds} = \hat{L}_s I_{ds} + M I_{dr},\ \psi_{qs} = \hat{L}_s I_{qs} + M I_{qr}$$

$$\psi_{dr} = \hat{L}_r I_{dr} + M I_{ds},\ \psi_{qr} = \hat{L}_r I_{qr} + M I_{qs}$$

where the subscript r, s refers to the rotor and stator side variables in the dq reference frame, respectively; with ψ, M, I, v and ω_s as the flux linkage, magnetizing inductance, current, voltage and angular frequency, respectively. The equivalent resistance at stator side $\hat{R}_s$ and inductance $\hat{L}$ at both sides with dynamics of a compensated transmission line can be expressed as

$$\begin{aligned} \hat{R}_s &= R_s + R_{SC},\ \hat{L}_r = L_r - M^2/\hat{L}_s \\ \hat{L}_s &= L_s + L_{SC} + L_{SC} - 1/\left(\omega_s^2 C_{SC}\right) \end{aligned} \tag{6.6}$$

where R_{SC}, L_{SC} and C_{SC} refer to the resistance and, inductance of the transmission line and capacitance of the series compensator, respectively. The RSC dynamics can be obtained from (6.5) and (6.6) as,

$$\begin{aligned} v_{dr} &= R_r I_{rd} + \hat{L}_r \frac{\mathrm{d}}{\mathrm{dt}} I_{rd} - \omega_{slip} \hat{L}_r I_{rq} \\ &+\frac{M}{\hat{L}_s}\left[v_s - \hat{R}_s I_{sd} + \omega_s \left(\hat{\mathrm{L}}_{\mathrm{s}} I_{\mathrm{sq}} + \mathrm{M} I_{rq}\right)\right] \\ v_{qr} &= \hat{R}_r I_{rq} + \hat{L}_s \frac{d}{dt} I_{qr} + \omega_{slip} \hat{L}_r I_{rd}, \\ &+\frac{M}{\hat{L}_s}\left[-\hat{R}_s I_{sq} - \omega_s \left(\hat{\mathrm{L}}_{\mathrm{s}} I_{sd} + M I_{\mathrm{rd}}\right)\right] \end{aligned} \tag{6.7}$$

For ease of simplicity, (6.5) can be transformed into states space as,

$$\begin{aligned} \mathbf{v}_s &= \mathbf{i}_s \hat{R}_s + j\omega_e L_s \mathbf{i}_s + \mathcal{D}\mathbf{i}_s L_s + \mathcal{D}\mathbf{i}_r L_M + j\omega_e L_M \mathbf{i}_r, \\ \mathbf{v}_r &= \mathbf{i}_r \hat{R}_r + j\omega_s L_M \mathbf{i}_s + \mathcal{D}\mathbf{i}_s L_M + \mathcal{D}\mathbf{i}_r L_r + j\omega_s L_r \mathbf{i}_r. \end{aligned} \tag{6.8}$$

where the operator $\mathcal{D}$ represents the integer-order differentiation of the states. For sake of completeness, we transform (6.8) into $\mathcal{L}$-domain by replacing "$\mathcal{D}$" with operator "s". This provides us,

$$\begin{aligned} \mathbf{v}_s(\mathrm{s}) =& \mathbf{i}_s(\mathrm{s}) \hat{R}_s + \mathbf{i}_s(\mathrm{s}) j\omega_e L_s + \mathrm{s}\mathbf{i}_s(\mathrm{s}) L_s + \mathrm{s}\mathbf{i}_r(\mathrm{s}) L_M \\ &+ j\omega_e L_M \mathbf{i}_r(\mathrm{s}) \\ \mathbf{v}_r(\mathrm{s}) =& \mathbf{i}_r(\mathrm{s}) \hat{R}_r + \mathbf{i}_s(\mathrm{s}) j\omega_s L_M + \mathrm{s}\mathbf{i}_s(\mathrm{s}) L_M + \mathrm{s}\mathbf{i}_r(\mathrm{s}) L_r \\ &+ j\omega_s L_r \mathbf{i}_r(\mathrm{s}) \end{aligned} \tag{6.9}$$

To facilitate the derivation for rotor current, (6.9) can be manipulated as,

$$\mathbf{i}_r(\mathrm{s}) = \frac{\mathbf{v}_r(\mathrm{s}) - \mathrm{s}\mathbf{i}_s(\mathrm{s}) L_M - \mathbf{i}_s(\mathrm{s}) j\omega_s L_M}{R_r + L_r(\mathrm{s} + j\omega_s)} \tag{6.10}$$

Simplifying (6.9) by putting $\mathbf{i}_r(\mathrm{s})$ from (6.10) and doing mathematical manipulations to solve for $\mathbf{v}_s(\mathrm{s})$,

$$\begin{aligned}\mathbf{v}_s(\mathrm{s}) = \mathbf{i}_s(\mathrm{s})&\left[\hat{R}_s + \mathrm{s}\left(L_M^2 L_s \frac{(\mathrm{s}-j\omega_m)}{\hat{R}_r + L_r(\mathrm{s}-j\omega_m)}\right)\right]\\ &+ \mathbf{v}_r(\mathrm{s})\left[\frac{\mathrm{s}L_M}{\hat{R}_r + L_r(s-j\omega_m)}\right]\end{aligned} \tag{6.11}$$

where ω_m refers to the angular speed of DFIG and is given as $\omega_m = \omega_e - \omega_s$.

The Thevenin equivalent model of DFIG can be obtained in alignment with the equation obtained from (6.11) and is illustrated in Fig.6.3. This provides the foundation for exploiting the equivalent model of DFIG for manipulating the rotor-side impedance to minimize the negative resistance affected by the interaction of the internal control loop. Therefore, we neglect the outer control loops of both side converters (i.e. RSC and GSC) as these have negligible imposition on the SSO characterization [180].

The expression for the rotor current can be written in "*dq*" domain as,

$$\begin{aligned}\dot{I}_{dr} &= \frac{1}{\sigma\hat{L}_r}(v_{dr} - \hat{R}_r I_{dr} + \mathrm{S}\hat{L}_r\omega_s I_{qr}\sigma)\\ \dot{I}_{qr} &= \frac{1}{\sigma\hat{L}_r}(v_{qr} - \hat{R}_r I_{qr} - \mathrm{S}\hat{L}_r\omega_s I_{dr}\sigma)\end{aligned} \tag{6.12}$$

The rotor current dynamics in (6.12) can be re-written as follows,

$$\dot{\mathrm{x}} = \mathbf{A}\mathrm{x} + \mathbf{B}\mathrm{u_r} + \mathbf{D} \tag{6.13}$$

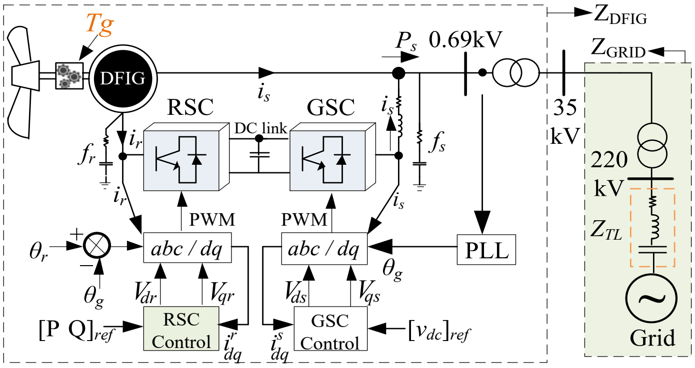

Figure 6.2: A series compensated network with DFIG and conventional control for grid side and rotor side converters

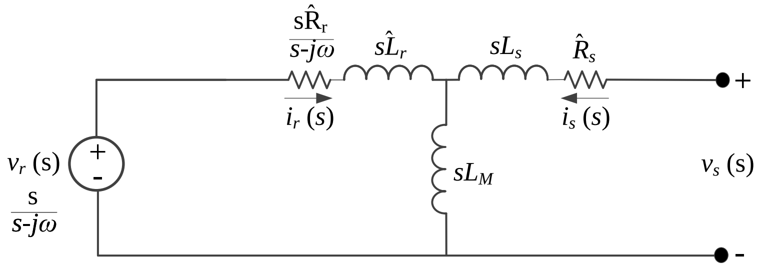

Figure 6.3: Equivalent circuit model of DFIG with Rotor dynamics

where $\dot{x} = \begin{bmatrix} \dot{I}_{dr} & \dot{I}_{qr} \end{bmatrix}^{\mathbf{T}}$ and $x = \begin{bmatrix} I_{dr} & I_{qr} \end{bmatrix}^{\mathbf{T}}$. While matrices,

$$\mathbf{A} = \begin{bmatrix} -\frac{R_r}{L_\sigma - j\omega_s} & 0 \\ 1 & 0 \end{bmatrix} \quad \mathbf{B} = \begin{bmatrix} -\frac{1}{L_\sigma} \end{bmatrix}$$

$$\mathbf{D} = \begin{bmatrix} \frac{L_m}{L_s L_\sigma}(v_s + R_s i_s) \end{bmatrix}^{\mathbf{T}}, \text{ and } \mathrm{u_r} = \eta \begin{bmatrix} v_{dr} & v_{qr} \end{bmatrix}^{\mathbf{T}}$$

6.3.3 Candidate of Instability in DFIG and Its Reshaping with Control

The impedance of the RSC is characterized by the resistance and leakage inductance of the RSC. This dynamic transitional behavior is accompanied by the states compensating gains used in control laws. Since, the objective of this work is to provide a foundational argument for the control effect on rotor dynamics, we consider the internal control loop of RSC only. The in-depth derivation on the current control loop are given in [181] in detail. Conversely, to make it simple and show the relevance of the inner control loop with rotor impedance, the "dq" axes of current inputs can be deduced from the basic control illustrated in Fig.6.2 [156]. This provides us with,

$$\mathrm{v}_{\mathrm{dr}} = e_{dr}\left(k_{pr} + \frac{k_{ir}}{\mathrm{s}}\right) \tag{6.14}$$

$$\mathrm{v}_{\mathrm{qr}} = e_{qr}\left(k_{pr} + \frac{k_{ir}}{\mathrm{s}}\right) \tag{6.15}$$

where, $e_{dr} = [i_{dr}^{ref} - i_{dr}]$, and $e_{qr} = [i_{qr}^{ref} - i_{qr}]$ shows the deviations in the "dq" axes of control inputs.

(6.14) and (6.15) can be written in more generalized form by replacing s with $s - j\omega_e$.

$$\mathrm{v}_r(s) = \left(\mathbf{i}_r^{ref}(\mathrm{s}) - \mathbf{i}_r(\mathrm{s})\right)\left(\frac{\mathrm{s}}{\mathrm{s} - j\omega_e}\right)\left(k_{pr} + \frac{k_{ir}}{s - j\omega_e}\right) \tag{6.16}$$

Considering the dynamics of the rotor in the control inputs, the final expression can be modified by using (6.10) and putting it in (6.16), (for detailed derivations, please see [136]), we get,

$$\mathrm{v}_r(\mathrm{s}) = \left[\mathbf{i}_r^{ref}(\mathrm{s}) - \frac{\mathbf{v}_r(\mathrm{s}) - \mathrm{s}\mathbf{i}_s(\mathrm{s})L_M - \mathbf{i}_s(\mathrm{s})j\omega_s L_M}{R_r + L_r(\mathrm{s}+j\omega_s)}\right] \left(\frac{\mathrm{s}}{\mathrm{s}-j\omega_e}\right)\left(k_{pr} + \frac{k_{ir}}{s-j\omega_e}\right) \tag{6.17}$$

Thereby, rearranging (6.17) for $\mathrm{v}_r(\mathrm{s})/\left(\mathbf{i}_r^{ref}(\mathrm{s}) - \mathbf{i}_r(\mathrm{s})\right)$ provides us with the final expression for varying rotor impedance imposed by control variables. This can be obtained as,

$$\mathrm{Z_r} = s\hat{L}_m + \frac{s}{s-j\omega_r}(\hat{R}_r + k_{pr} + \frac{k_{ir}}{s-j\omega_0}) \tag{6.18}$$

The expression in (6.18) is in alignment with Fig.6.4 (a) which expresses the mathematical dynamics of the rotor, including the effect of control dynamics "$Z_{CS}\frac{s}{s-j\omega}$" early derived in (6.14). Thus, the first part of Fig.6.4 (a) is the conventional approach that characterises the rotor-side impedance using control gains by a factor of "η" as shown in (6.14). This provides additional damping to RSC resistance and consequently results in stabilizing the system for varying operating conditions. However, the major drawback of tuning these parameters for avoiding SSCI events will deteriorate the additional performance of the WTG such as low voltage ride-through (LVRT) capability and dynamic performance for unplanned events [182]. Therefore, to enhance the dynamic performance of the WTGs and ensure stability against SSO events, additional damping is incorporated into existing RSC dynamics by fictitious impedance as shown in Fig.6.4 (b), commonly referred to as sub-synchronous damping control. However, this conventional sub-synchronous damping control (CSDC) requires careful design considerations and

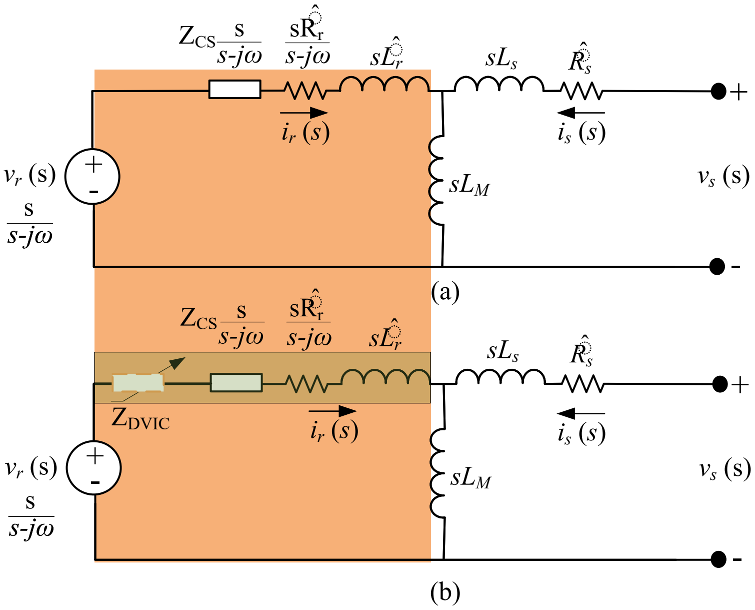

Figure 6.4: Equivalent circuit model of DFIG with Rotor dynamics representing (a) reshaping of rotor impedance with conventional control, (b) reshaping using DVIC.

has a subsequent impact on dynamics performance if not tuned diligently.

6.3.4 Limitation of CSDC

Though the addition of CSDC SSO mitigation is a convenient approach, there are significant challenges associated with this method, as detailed below.

The typical structure of CSDC is shown in Fig.6.5. It incorporates the integration of a bandpass filter, a phase compensator, and an amplifier to generate the control signal [164]. The critical aspects of such an approach are centred around three major challenges [175].

- The fixed bandwidth of the bandpass filter restricts the adaptability of control in addressing SSO with time-varying frequency components [3]. This places frequency-dependent constraints on the controller, where complex components with out-of-band frequencies may significantly impact the accuracy of the input signal for converter controllers in the WTGs system.

- The phase compensator with fixed bandwidth is employed in conventional CSDC to stabilize the control for conventional SSO. However, the complex SSOs with time-varying components explicitly introduce complex phase lags, potentially compromising the performance of fixed phase compensator ($[(ST1+1)/(ST2+1)]^2$) [3, 31].

- Explicitly in extreme conditions of the network, the control system associated with WTGs converter provides complex SSCI modes. These modes are constituted as a result of coupled SSCI frequencies interpolated with network noise and harmonics. Therefore, such modes are network-dependent and vary with the operating conditions. Thus the performance of conventional CSDC deteriorates for such modes and the root cause of SSCI mitigation becomes challenging.

Therefore, CSDCs are typically designed for a single operating point of the power network. As a result, their parameters remain fixed and are not updated in real-time to accommodate evolving network dynamics. This limits the damping performance in mitigating SSO, particularly under conditions where complex modes are amplified due to operational variability. Thus, in IBRs dominated networks, especially those integrated with compensator and weak network configuration, the limitations become more pronounced. Therefore, control strategies in such systems must be self adaptive to effectively accommodate varying network conditions. To address this challenge, a novel, self-adaptive control approach is proposed and presented for the first time in the following section.

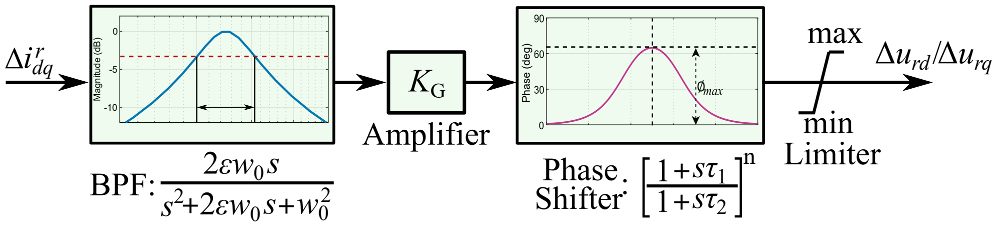

Figure 6.5: Block diagram of CSDC-based approach for SSCI mitigation.

6.4 The Adaptive DVIC Control Method

Controlling the rotor side current I_{dq} with dynamic and adaptive feedback control can effectively mitigate the complex oscillations emerging due to SSCI or SSR involved with line compensator. This can be achieved by considering the control loop as a virtual impedance responding proportionally to the RSC current perturbation due to SSR based oscillations. The finite time compensation of this perturbation effectively changes the DFIG impedance, preventing the destabilization of the control loop and consequently mitigating the SSO.

6.4.1 ANN based Adaptive Control

To address the identified issue, this thesis propose an artificial neural network (ANN) based single-layer feed-forward model-free control mechanism that can mitigate the SSCI in finite time for varying operating conditions of the network. The principle of the proposed approach is similar to that of CSDC and is shown in Fig.6.6. The control method is independent on the system states, communication links, and prior information of SSCI modes to mitigate the SSR in finite time. The method uses system state x_{dqr} as its input, measures $\Delta x[k] = x[k] - x[k-1]$, and adjusts output $y(k)$ online. The $y(k)$ is a stabilizing signal injected into the dq control of the DFIG, strengthening the output impedance of the RSC in finite

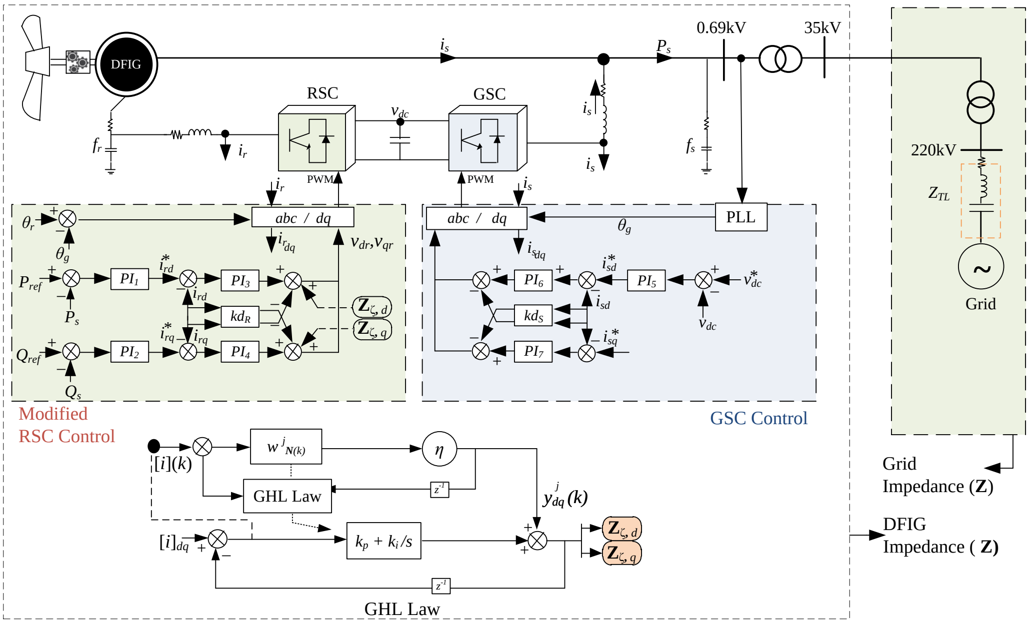

Figure 6.6: Proposed method for RSC control of DFIG, (a) RSC control modified with DVIC (b) Structure of proposed method for $\mathbf{Z}_\zeta$.

time.

For instance, the GHLL for the system described in (6.13) with input states $\mathbf{x}_{dqr}$ can be written as [183],

$$\begin{aligned}\Delta w^{ij}(k+1) = w^{ij}(t) + \eta \times \Big[& y^i_{dq}(t)\Delta x^j_{dq}(t) - \\ & y^i_{dq}(t)\sum_{k\le i} w^{kj}(t)\, y^k_{dq}(t) \Big]\end{aligned} \tag{6.19}$$

In the above, w^{ij} is the synaptic weight updated at each round of (t) from its previous value by taking into account the input vectors $x^j_{dq}(t)$ and resulting in the activation function, which is the product of the input state vector and w at $t-1$. Also, η represents the learning rate and can be tuned to achieve convincing convergence of the states to the reference value.

6.4.2 Derivation of Dynamic Virtual Impedance Control Law

The impedance model (IM) of DFIG can be derived from the analytical model discussed in the earlier section as

$$Z_{DFIG} = (Z_m || Z_r) + Z_s \tag{6.20}$$

where

$$\begin{cases} Z_r(s) = s\hat{L}_m + \frac{s}{s-j\omega_r}(\hat{R}_r + k_{pr} + \frac{k_{ir}}{s-j\omega_0}) \\ Z_m(s) = sM \\ Z_s(s) = \hat{R}_s + s\hat{L}_s \end{cases}$$

The proposed method functions as a DVIC, actively reshaping the RSC impedance $Z_r(s)$ to mitigate the effects of SSO. This is accomplished by attenuating the impact of external disturbances, thereby preventing the RSC impedance from exhibiting adverse or negative impedance characteristics during SSR or SSCI events. Assuming $\mathbf{Z}_\zeta$ is the output of the DVIC as shown in Fig. 6.6b, the new impedance for the RSC can be updated at each operating state as

$$Z_{r,(s,z_\kappa)} = s\hat{L}_m + \frac{s}{s-j\omega_r}(\hat{R}_r + k_{pr} + \frac{k_{ir}}{s-j\omega_0} + \mathbf{Z}_\zeta) \tag{6.21}$$

where $\hat{L}_m, k_{ir}, k_{pr}$ are the field excitation inductance, integral, and proportional gains of the RSC loop, respectively. z_κ refers to the operating mode. In (6.21), $\mathbf{Z}_\zeta$ can be determined by using GHLL as discussed earlier. This manipulates $Z_{r,(s,z_\kappa)}$ for any condition that initiates deviations in the states vector $\mathbf{x}_{dq}(t)$ due to SSCI phenomena. Thereby, (6.19) can be re-written as,

$$\Delta w_{\mathbf{N}}^{j}(k+1) = \mathbf{w}^{ij}(t) + \left[\mathbf{x}_{dq}^{i}(t)\mathbf{y}_{dq}^{j}(t) - \mathbf{y}_{dq}^{i}(t)\sum_{k\leq i} w^{kj}(k)\mathbf{y}_{dq}^{k}(t)\right] \tag{6.22}$$

The Δ here refers to the update in the $w_{\mathbf{N}}^{j}$ at t, while $\mathbf{x}_{dq}^{i}(t) = \mathbf{x}_{dq,ref} - x_{dq}$. Using mathematical simplifications, the (6.22) can be generalized for Z_{ζ} as

$$\mathbf{Z}_{\zeta} = \sum_{\mathbf{N}=1\ldots\eta} [\Delta w_{\mathbf{N}}(k)] \times (k_p \mathbf{x}_{dq}^{r} + k_i \int \mathbf{x}_{dq}^{r}) \tag{6.23}$$

The final value of the synaptic weights ($\Delta w_{\mathbf{N}}^{j}$) is decided when the connection between neurones is strengthened and error is minimised by ensuring an optimum correlation between the reference and output values. Therefore, the training data and learning relation are updated online every time step of the corresponding input state vector. This eventually alters the rotor side impedance in finite time for any variations, providing explicit virtual damping and ensuring mitigation. The effectiveness of the proposed method is provided in the next section, where a deliberate comparison is persuaded to gain insights on the performance of the method.

6.5 Case Study

6.5.1 System Under Consideration

This work considers an EMT model of the network provided in this chapter, previously used for the detection and localization of the WTG as shown in Fig.6.7.

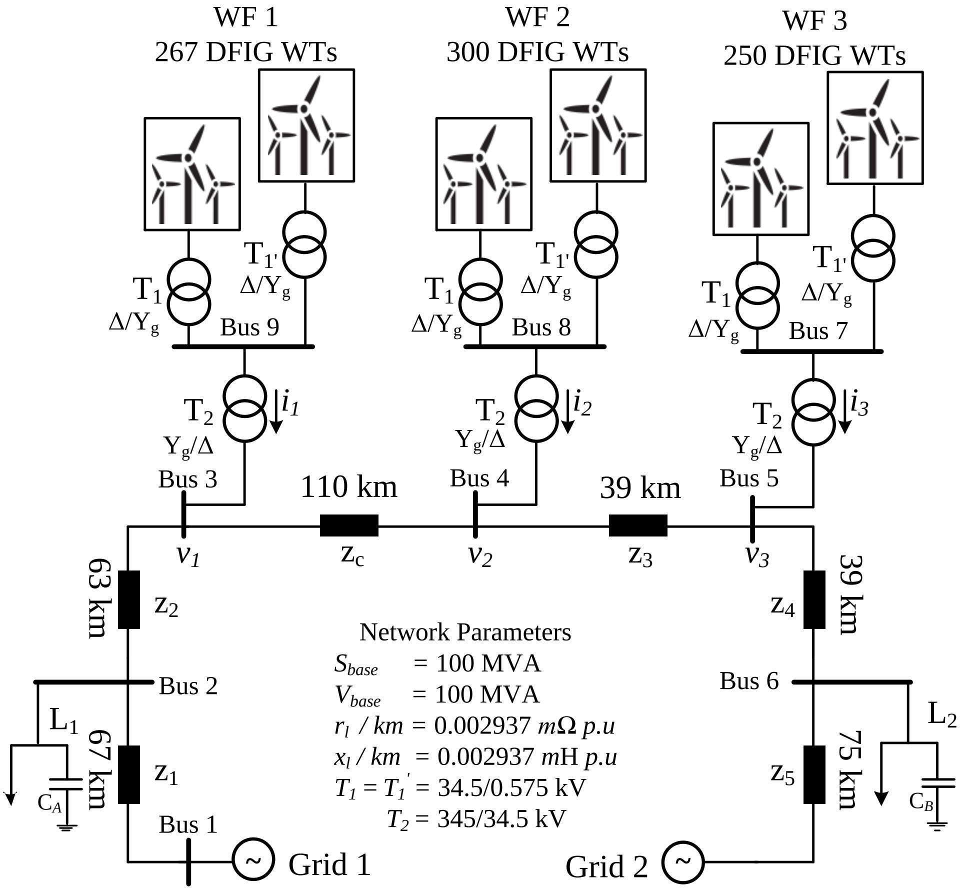

Figure 6.7: Configuration of an example of ERCOT network replication for studying SSCI/SSR

Recalling case 4 from Chapter 5, where the network has reported SSR-based events due to resonance with network components and has demonstrated significant oscillations in voltage and currents at the PCC of the wind farms. Three events have been reported demonstrating the SSCI and SSR modes in voltage and current oscillations. Two events are related to changes in the network topology resulting from the tripping of a section of the line. The alteration in network topology is initiated by a fault, which triggers protection devices and leads to line outages. Consequently, this results in the radial connection of WF1 and WF2 to the series-compensated line positioned between Bus 3 and Bus 4 for the reported events. The reported SSR frequencies for these events range from 22 Hz to 27 Hz. Similarly, the last event does not trip the protection device; however, the radial connection with the line compensation significantly affects the voltage/current loops and produces significant SSCI-based oscillations. These three events were previously replicated solely to demonstrate the effectiveness of AIFST. Following the AIFST-based SSCI power flow, which nominates the WPP connected to bus5 as a major contributor of SSCI instability, the control system for WF3 is updated with DVIC, consequently. The efficacy and robustness of the approach is illustrated through detailed studies, wherein simulation examples are conducted for various operating conditions to verify the dynamic performance, ensuring compliance with regulations aimed at maintaining grid stability.

6.5.2 Simulation Results

Various operational uncertainties associated with wind farms contribute to the emergence of different types of power system oscillations. Key operating parameters that significantly influence the mitigation of these oscillations include variations in wind speed, controlled active and reactive power, and changes in the compensation level of the transmission line. These factors are directly linked to both SSCI and SSR, as they affect the impedance of the RSC in WTGs at SSR-related frequencies. Under such conditions, the RSC resistance can exhibit negative impedance characteristics relative to the grid impedance, potentially leading to severe system instability if not appropriately managed.

The complex nature of these disturbances presents significant challenges in

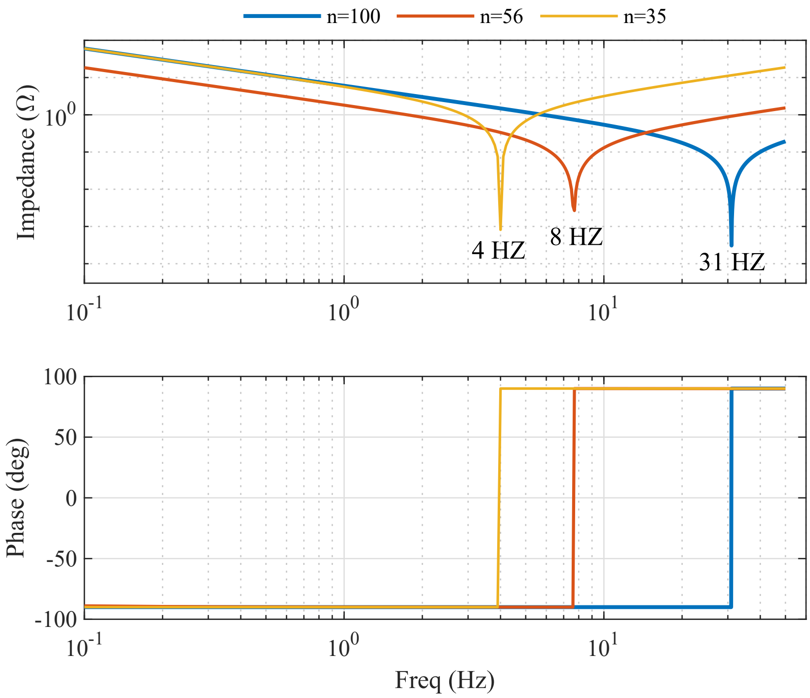

Figure 6.8: Effect of Wind on RSC impedance.

defining an optimal SSCI bandwidth for CSDC methods. To address this issue, a series of test studies have been carried out, focusing on the control behavior of the RSC in WTGs and its influence on impedance characteristics. These studies reveal that SSCI frequencies vary considerably under different operating conditions, highlighting the particular need for a control strategy that is robust and independent of specific SSCI frequencies.

Validation of DVIC for Varying Wind Speed

Before the damping performance of the proposed method is analysed, the effect of uncertain operating conditions on RSC impedance is demonstrated in Fig. 6.8. For ease of understanding, only the PCC measurements of Bus 5 are shown for the network depicted in Fig. 6.7. Three different wind profiles are analysed, varying from $6\,m/s$ to $15\,m/s$ and leading to certain disconnection of random WTGs where the wind speed is unfavourable. The control parameters are intuitively tuned to trigger the SSCI in the system to demonstrate the effect of operating conditions on the RSC impedance. Owing to such conditions, Fig.6.8 illustrates that the SSCI modes explicitly vary with the operating conditions. For instance, when the number of offline WTGs (n) is 100 and the line compensation ($Z_c = 15\,\%$), the SSCI mode, it is 31 Hz with the highest participation of negative impedance at PCC. This SSCI frequency varies inherently when the number of offline WTGs reduces to 35 from 56, giving a transition in SSCI frequency from $8 \rightarrow 4$ Hz.

The aforementioned SSCI frequencies significantly change by employing the damping control. To demonstrate this, the CSDC and DVIC control are employed while keeping the operating conditions as wind speed $v_w = 9\,\mathrm{m/s}$, reactive power $Q_{WTG} = 0$ MVAR, active power $P_{WTG} = 50$ MW, $Z_c = 20\,\%$ and $n = 817$ initially. For case 1, where v_w changes from 9 m/s → 13 m/s, the SSCI oscillations can be seen emerging at $t = 4\,\mathrm{s}$ as shown in Fig.6.9 (a). Similarly, Fig.6.9 (b) demonstrates the same modes for wind speed varying from $9 \rightarrow 6\,\mathrm{m/s}$ with similar network conditions. The FFT results at $t = 4.1s$ for 120 electrical cycles for both cases demonstrate that the DVIC control actively modifies the $\mathbf{Z}_{\zeta}$ to prevent the onset of SSCI-induced oscillations. Further to that, this is particularly illustrated from the FFT magnitudes shown in Fig.6.9 (a, b), that the DVIC approach shows extensive stability against the changing operating conditions and have explicitly lower magnitudes. The effect of these magnitudes can be seen in the active and reactive power in Fig.6.10 (a, b). Therefore, the proposed method has a dominant performance for mitigating the SSCI event by varying the $\mathbf{Z}_{\zeta}$ in

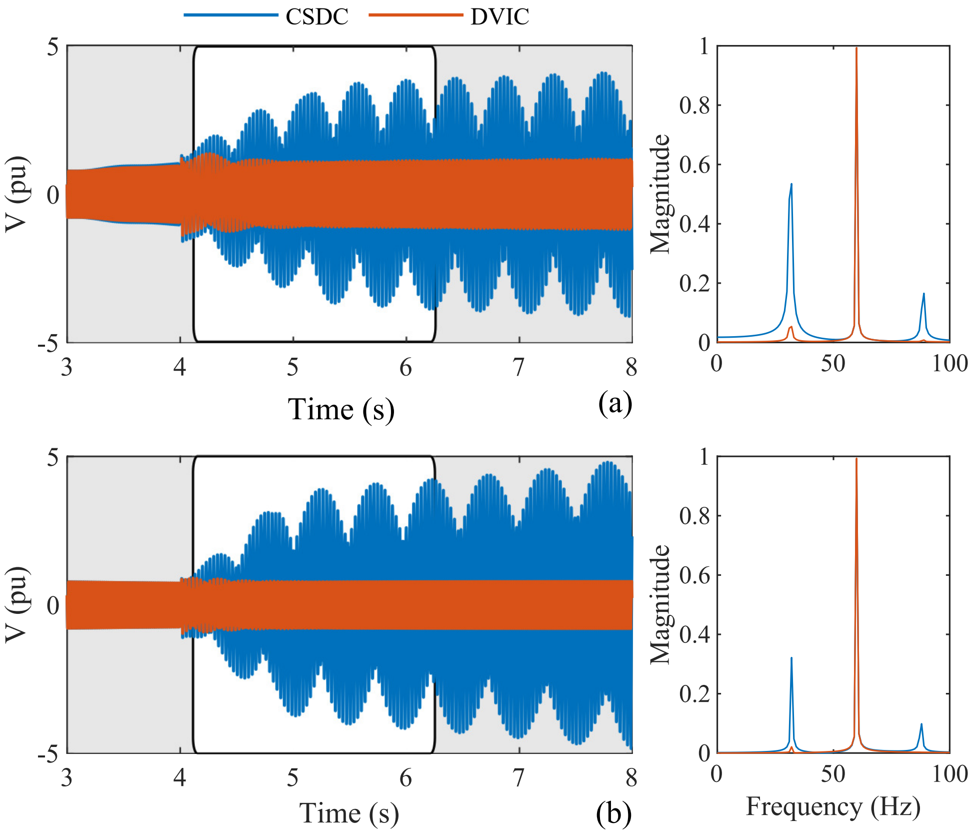

Figure 6.9: CSDC and DVIC performance showing voltage and SSCI modes for (a) $v_w = 9\,m/s \rightarrow 13\,m/s$, (b) $v_w = 9\,m/s \rightarrow 6\,m/s$.

finite time.

Validation of DVIC for Varying Compensation

The performance of the proposed method is further evaluated in comparison with the CSDC-based approach for different compensation levels. Initially, the line is compensated for $15\,\%$, v_w is 7.5 m/s, reference for $Q_{WTG} = 0\,\mathrm{MVAR}$ and active power $P_{WTG} = 50$ MW. At $t = 4\,\mathrm{s}$, the Z_c is doubled to $30\,\%$ while both CSDC and DVIC controllers are active. We illustrate this in Fig.6.11 by assessing the dynamics conditions of the system for both controllers using the time-frequency

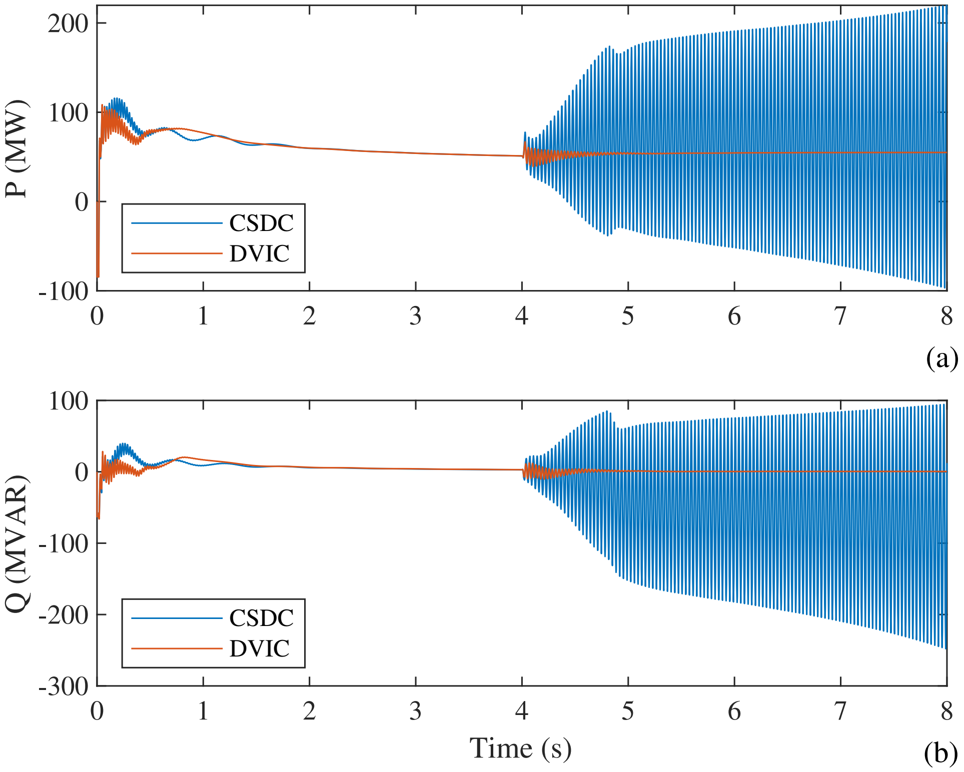

Figure 6.10: CSDC and DVIC performance for changing windspeed showing (a) Active power control, (b) Reactive power control.

representation (TFrs) of the oscillation modes. It can be observed that varying Z_c at $t = 4\,s$ initiate oscillations for both controllers as illustrated in Fig.6.11$(\mathrm{a,c})$, however, the DVIC-based approach mitigates it in finite time in comparison to the CSDC as shown in Fig.6.11$(\mathrm{c,d})$. The proposed method does not need prior information about SSCI modes as compared to CSDC but is adaptive enough to mitigate the effect of changing Z_c.

The performance of both approaches is further assessed by a more realistic test case where the Z_C is increased from 15 % → 50 % at $t = 4$ s. For simplicity and ease of comparison, Fig.6.12a and Fig.6.12c shows the $p.u$ current of the WTGs

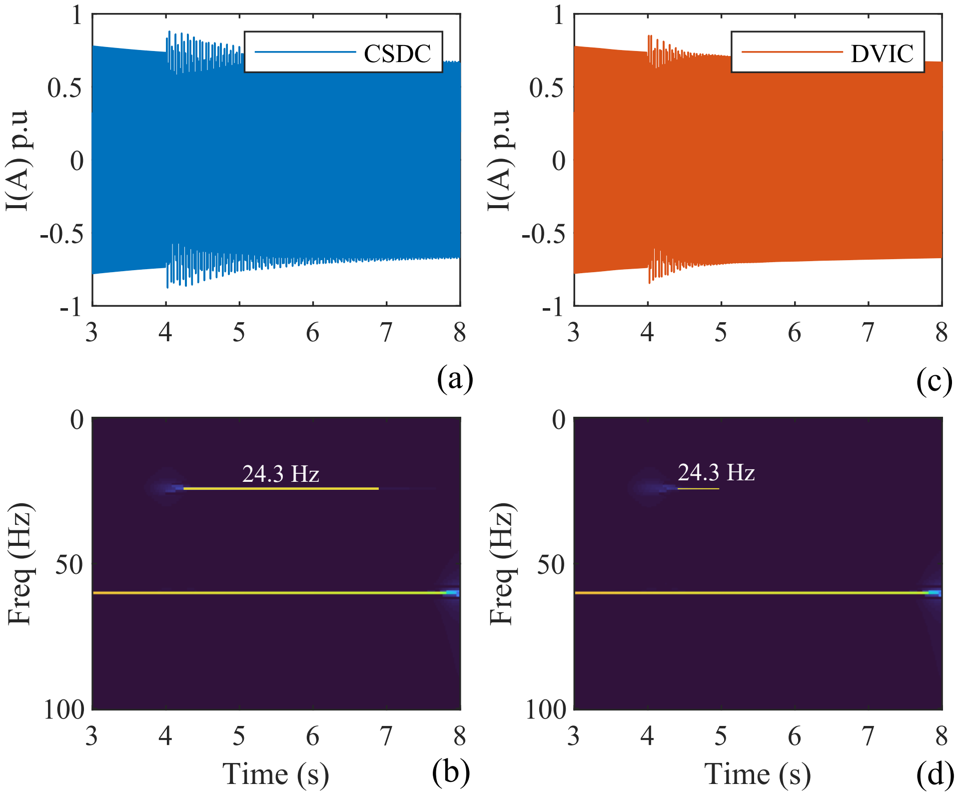

Figure 6.11: Variation in line compensation by 30 % showing p.u Current for (a) CSDC, (b) TFR of modes under CSDC, (c) DVIC, (d) TFR of modes under DVIC.

connected at Bus 9 only. The TFRs of the CSDC show the SSR mode starting after the switching of the compensation and increasing exponentially as compared to DVIC. On the contrary, the TFRs of the DVIC show that the variation in compensation triggers this mode as shown in Fig.6.12 d, however, is mitigated in approximately 120 electrical cycles. This is further illustrated in Fig.6.13 which is in alignment with Fig.6.12 for compensation variation of 15 % → 50 % at $t = 4\,s$. Fig.6.13 shows the reactance-frequency crossover criterion obtained through the analytical simplifications of the impedance model of the network at the node connecting wind farm 1. When SSCI begins due to switching of the

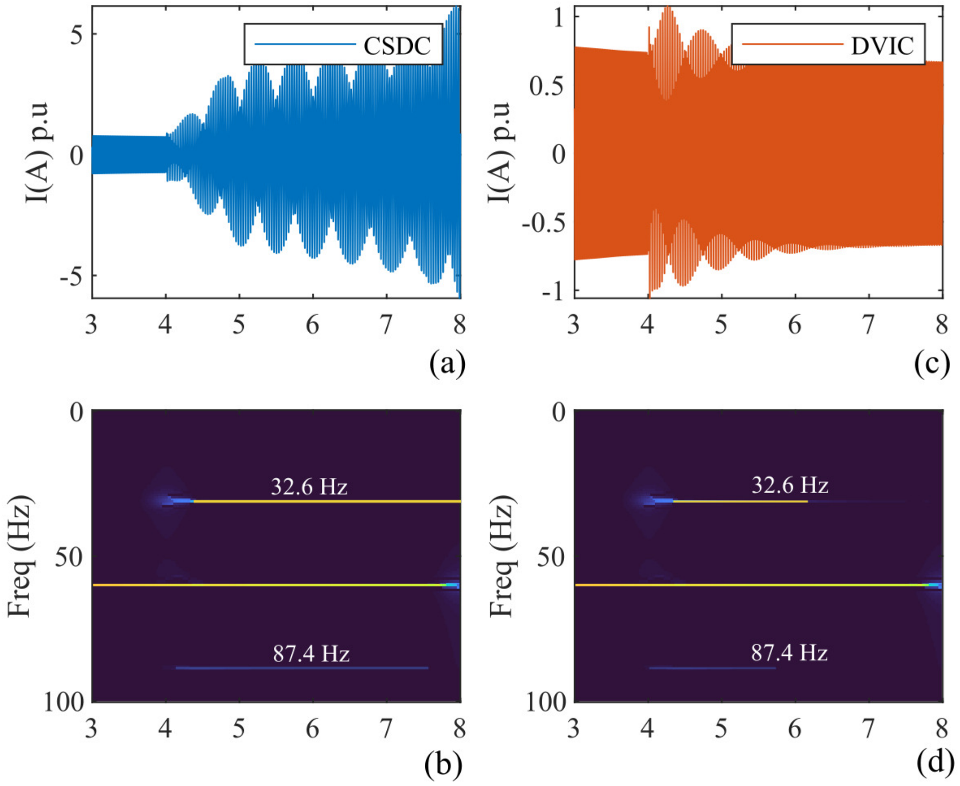

Figure 6.12: Variation in line compensation by 50 % showing p.u Current for (a) CSDC, (b) TFR of modes under CSDC, (c) DVIC, (d) TFR of modes under DVIC.

extra compensation, the variations in the frequency-dependent resistance (R) and reactance (X) can be observed in Fig.6.13a. According to the frequency crossover criteria defined in [136], the SSCI event emerges when the source resistance (R) is negative for $X = 0$ at a specific frequency. The zoomed version of Fig.6.13 shows the comparison of both controllers when the SSCI occurs at approximately 32.6 Hz. The DVIC approach reshapes the overall impedance at $f_{ssr} = 32.6\,\text{Hz}$ while mitigating the event in finite time by injecting a stabilizing signal to adjust Z_ζ. The stabilising signal by the DVIC-based approach is shown in Fig.6.14 for Z_c variations of 50 %.

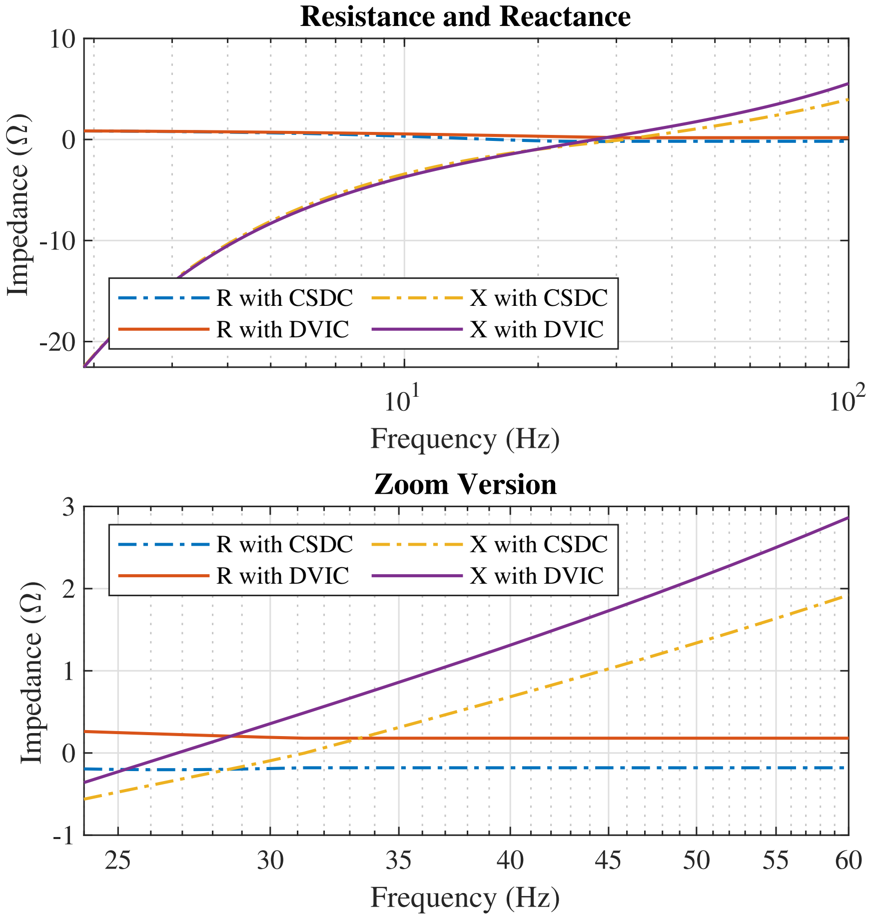

Figure 6.13: Variation of impedance (R & X) for 50 % change in line compensation by DVIC and CSDC.

It is clear that the proposed method responds in a definite time to the SSR event and adjusts the control signal by varying the impedance of the source to prevent the instability of the RSC converter. In addition to that, the difference in the performance of both controllers is further evaluated by taking the Discrete Fourier Transform (DFT) of both controllers for 120 electrical cycles for the events shown in Fig.6.11 and Fig.6.12. Only modes with magnitudes higher than 1% are shown here as the lower modes have no relation with the SSCI-based

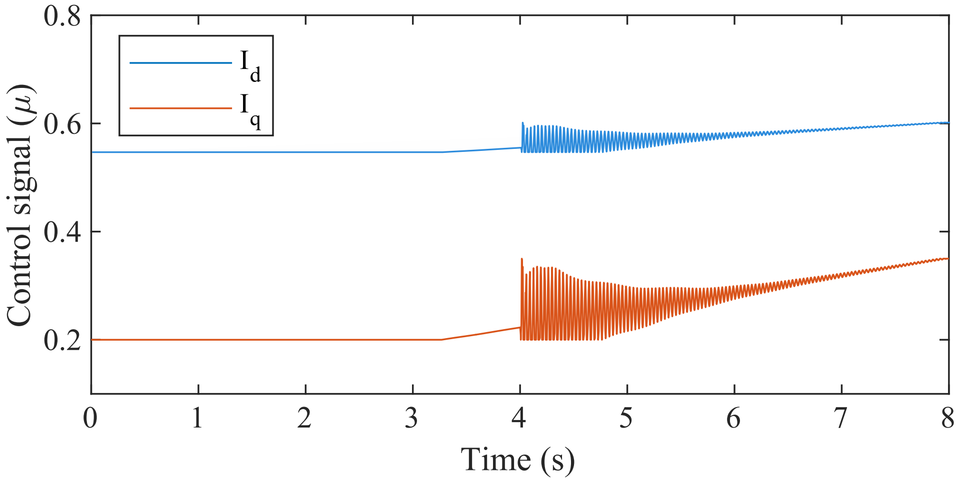

Figure 6.14: Performance of DVIC for varying rotor virtual impedance using signal injection for 50 % compensation.

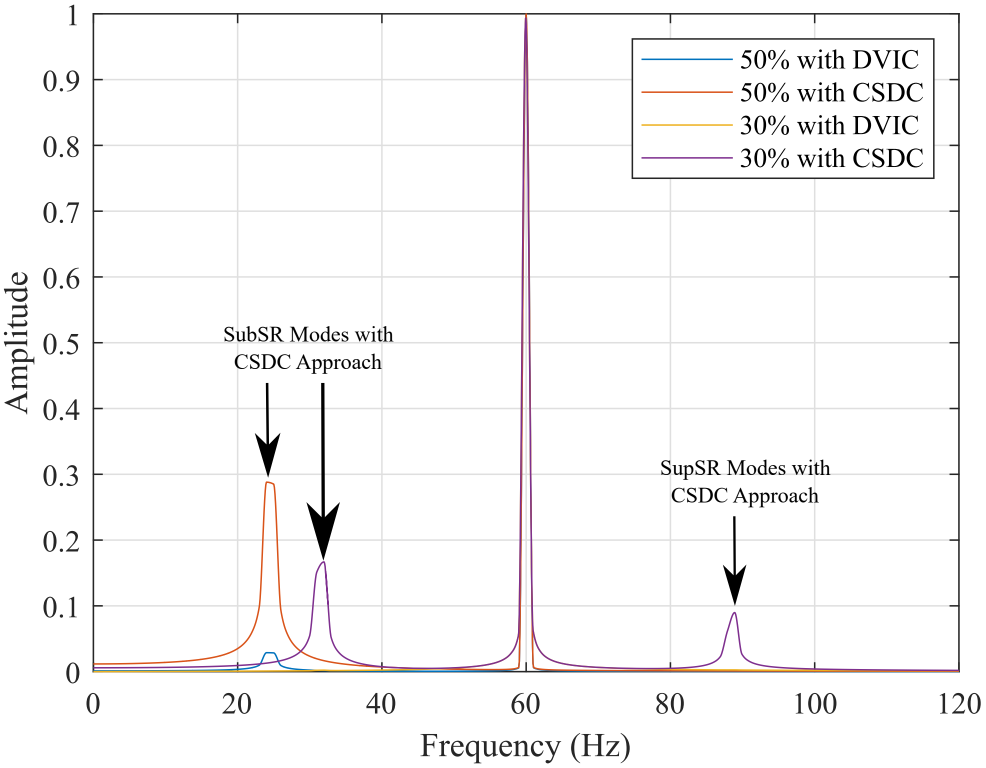

Figure 6.15: Mitigation of oscillation modes by CSDC and DVIC for changing compensation of 30 % and 50 %.

oscillations. Therefore, it can be observed that the magnitude of SSCI modes using the DVIC approach is considerably low as compared to the CSDC for both cases (30 % and 50 % compensations). The subSynchronous mode (SubSR) for DVIC is only $|f_{SubSR}| = 3\%$ as compared to CSDC, where $|f_{SubSR}|$ is 29% of the 60 Hz component for 50% variations in the compensation levels. It is also important to note that, the severe perturbation in the impedance of the source results in higher magnitudes of severe oscillations.

Dynamic Performance for FLRT and LVRT conditions

The power grid and regulating authorities define grid codes to ensure the stability of the network. The grid codes are inherently applicable to the power generation vendors connecting their assets to the transmission infrastructure. The grid codes impose strict rules for these connecting assets to meet the minimum criteria of fault ride-through (FLRT) and low voltage ride-through (LVRT) conditions.

In Great Britain (GB), the WTGs are required to remain connected for 140 ms during low voltage and fault conditions. In these scenarios, the IBRs (WTGs) are required to support the grid by minimizing the active power while maximizing the injection of reactive currents into the grid. To illustrate the performance of the proposed method for such conditions, a three-phase fault is initiated at 4 s lasting for 200 ms, and 500 ms as shown in Fig.6.16 and Fig.6.17. This test aims to verify the efficacy and robustness of the proposed method for extreme events. It can be observed from the active and reactive power of both Fig.6.16 and Fig.6.17 that the system returns to normal operations after fault clearance and provides stable power without anticipating any oscillatory modes. The performance of the proposed method is further assisted for a more severe scenario where grid voltage

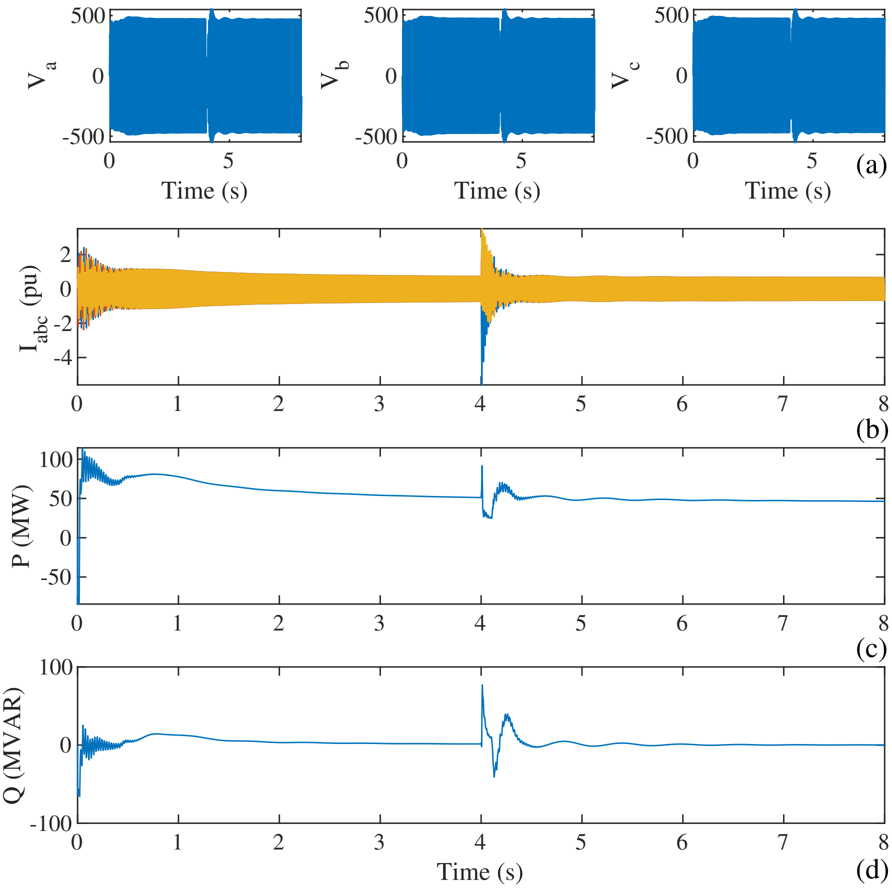

Figure 6.16: FLRT performance of DVIC for 3-Phase fault showing (a) voltage, (b) current, (c) active power, and (d) reactive power at PCC for 200 ms

dip falls to 70% of its nominal value as illustrated in Fig.6.18. It can be observed that the proposed controller significantly varies the current without prevailing any overshoot and undershoots in the current. The significant variations in the grid voltage is supported by the adaptive performance of the proposed controller, where significant reactive power is injected at the same time to support the grid.

Overall, the case studies demonstrate significant improvement in the dynamic performance of the WTGs by incorporating a DVIC-based approach. The ap-

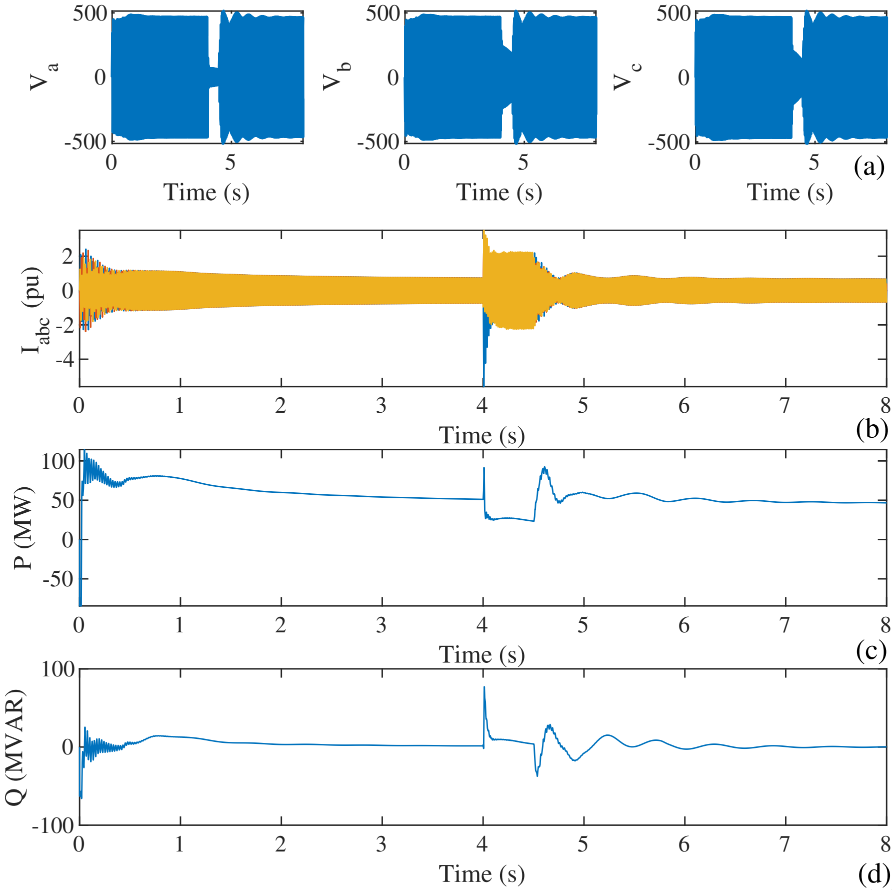

Figure 6.17: FLRT performance of DVIC for 3-Phase fault showing (a) voltage, (b) current (c) active power, and (d) reactive power at PCC for 500 ms

proach provides robust performance for the mitigation of SSCI modes by injecting a stabilising signal only when the GHLL detects it. Therefore, it is evident from the results that the proposed approach does not require any prior information about SSR modes and doesn't affect the performance of WTGs in any conditions.

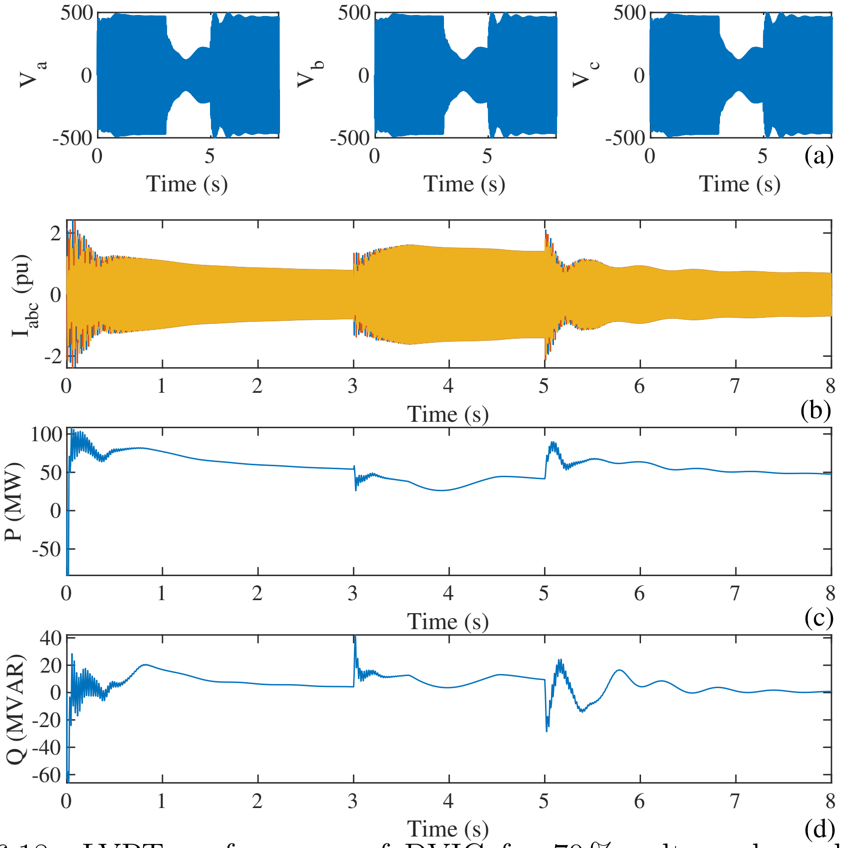

Figure 6.18: LVRT performance of DVIC for 70 % voltage drop showing (a) voltage, (b) current, (c) active power, and (d) reactive power

6.6 Future Research direction

The proposed controller demonstrates effective performance for the problem under consideration, as discussed in the preceding sections. Nevertheless, several research aspects remain open, particularly concerning the application of the ANN-driven control strategy. Specifically, the interaction of the control loop with the Power Plant Controller (PPC) must be carefully analyzed to ensure adaptivity within multilayer control hierarchies under varying grid conditions. The control loop exhibits a bounded settling time in response to disturbances and input variations. However, appropriate tuning of controller gains is critical to avoid excessive overshoot and undershoot in the system response. Furthermore, additional nonlinear modelling is required to formally characterise the region of attraction of the control law, thereby ensuring asymptotic stability across a wide range of grid disturbances. The proposed control algorithm has been shown to tolerate input noise magnitudes of up to 30% of the nominal signal without significant degradation of performance. While this does not imply instability or unacceptable performance for higher noise levels, further investigation is required to refine the control law and enhance robustness margins.

6.7 Summary

This work proposes a novel RSC control scheme for WTG to enhance the resiliency of *dq* axes control loop for mitigating SSCI oscillations. The proposed method works as an auxiliary loop and acts as a dynamic virtual impedance for the DFIG control system. The proposed scheme mitigates the effect of SSCI event in the *dq* axes current control loops with improved steady and, transient system performance. No requirement of prior knowledge of SSCI frequencies, their types, and their bandwidth sets apart this work. The proposed method does not deteriorate the nominal operation of the system and responds only when detecting the SSCI event. The simulation results demonstrate the efficacy of the proposed method for different test scenarios and prove its viability for further exploration and real grid applications.

Chapter 7

Conclusions and Future Work

7.1 Conclusions

It is widely recognized that inverter-based resources (IBRs), particularly wind turbine generators (WTGs) with complex power network configurations, introduce various types of stability challenges into their respective grids. Amongst these, the subsynchronous resonance (SSR) and subsynchronous control interactions (SSCI) between the network components and WTGs are of critical concern, as these can induce complex oscillations and lead to network instability. These oscillations emerge as a consequence of due interactions between the network components and generation sources. The characteristics and complexity of these oscillations are governed by system-wide dynamics and vary across different IBR-integrated power network configurations. The complex modes associated with SSCI oscillations are characterized by time-varying frequency and damping properties, setting them apart from the relatively stationary modes seen in harmonics, low-frequency oscillations, and forced oscillations. Moreover, these modes can become dynamically coupled under certain conditions, making their explicit detection and characterization particularly challenging. This complexity is further exacerbated under varying operating conditions in the power network, where the dynamic nature of these modes is more pronounced. Traditional detection methods, such as those relying on discrete Fourier transform (DFT)-based algorithms employed in phasor measurement units (PMUs), struggle to accurately capture these time-varying and coupled modes. As a result, the reliability of such methods is compromised, increasing the risk of undetected instabilities. Thus this fundamental limitation in observability drives towards significant challenges in the development and implementation of effective mitigation strategies for SSCI-related phenomena.

Therefore, keeping in view the critical aspects of complex SSCI to grid stability, this work focuses on addressing two major aspects of this challenge.

1) To develop a systematic approach that can efficiently detect the complex and time varying modes of such phenomena.

2) Identify the root cause of the instability in the network and propose mitigation strategies to address the emerging oscillations in the network. The conclusions drawn from the main contributions of this research are given below.

1. Fidelity of PMU based Observability for Complex Oscillations [184]:

To address the challenges of detecting and mitigating complex oscillations in IBR-dominated power networks, this work introduces key contributions that advance the understanding and observability of these phenomena.

For the first time, this approach provides a significantly more comprehensive and detailed analysis compared to prior methods such as DFT and Prony analysis. It highlights an increased risk of instability and inaccuracies when addressing complex SSCI within WAMS control mechanisms using the conventional approaches. Importantly, this work establishes a foundational framework through rigorous analytical examination, offering strong evidence to support the adoption of synchronized waveform measurement units (SWMUs) for assessing complex SSCI oscillations.

The complex oscillations in IBR-dominated power networks exhibit complex modes. Typically, such oscillations involve a wide band of frequencies, where the dominating modes have coupled frequencies resulting in multi-mode synchronous resonance-based oscillations. Detecting such modes with complex and wide bands of frequencies is challenging with the existing methods such as DFT, its variants and benchmark approaches such as as Prony analysis.

Therefore, critical analysis of the existing DFT-based methods is carried out to assess the observability requirements of complex oscillations in the IBRs-dominated network. It is widely recognized that the fundamental variant of the DFT approach is explicitly used in PMUs adopted for wide area monitoring system (WAMS) due to its simple and less computational industrial design. However, for the sake of comparison this work adopts the latest and state-of-the-art sliding DFT approach to assess the observability of multimode complex SSCI oscillations. It has been identified through analytical analysis that DFT and its variants are susceptible to erroneous estimation of SSCI modes, particularly those which are strongly time varying and complex in nature. Accordingly, the stability and accuracy of this approach is further assessed for WAMS prevailing enhanced risk and uncertainties in mitigating the complex SSCI for control mechanism. This method provides a far more comprehensive and detailed analysis than previous works and provides a foundational layout based on analytical analyses enabling the adoption of synchronized waveform based assessment of complex SSCI oscillations.

2. Source Localization of Complex SSCI using Modes based Power Flow [184, 185]:

A systematic diagnostic tool is developed for the first time by employing a synchro-transform concept with the pioneering use of SWMUs to localize the source of complex SSCI within power networks. This process is achieved in two main stages: first, identifying the presence of complex SSCI, and second, determining their source within the network. In these regards, the following novel contributions are made:

- For the first time, an adaptive TFT method is proposed for complex SSCI detection. This method resolves the inherent challenge of handling non-stationary complex signals, often erroneously treated as estimates of harmonic oscillations. By introducing an adaptive window, it mitigates the necessity of relying on a fixed window for a diverse range of mixed frequencies. Consequently, this adaptation facilitates the retrieval of SSCI modes without necessitating permanent adjustments to the window size.

- Further to that, a novel adaptive and realigned Instantaneous Frequency (IF)-based Time- Frequency Transform (TFT) approach is developed to resolve the non-realignment issues for the signals contaminated with high noise ratio and harmonic components located closely to the SSCI modes. This approach improves the accuracy of the modes detection and estimate the exact modes with 99.9% accuracy thus resolving the non-realignment issue for the oscillations with complex frequency modes. The non-realignment issue fundamentally emerges as a consequence of the erroneous estimation of the SSCI modes which are closely spaced to the harmonic and inter-harmonic contents. Thus, while transforming time-series data into TFT, the accuracy of coefficient approximation is deteriorated from the ridges. Therefore, this leads to significant inaccuracy in digital implementation; if the IF estimator is not correctly aligned in its realignment region.

- For the first time, the localization of the origin and source of complex SSCI in IBRs dominated network is accomplished by a novel, SSCI driven power flow. The power flow leverages the admittance model of complex SSCI components, explicitly obtained through the AIFST. The proposed method eliminates inaccuracies stemming from the reliance on obtaining system states for a single operational condition. Consequently, it remains applicable across various operating conditions, allowing for the derivation of SSCI modes. By considering the reconstructed modes and the subsequent admittance model, the complex SSCI power flow is calculated. This leads to the solution of a critical challenge: the identification of frequency modes and localization of complex SSCI sources in the IBRs dominated network.

3. Mitigation of Complex Oscillations [186], [187] , [188]:

The mitigation of oscillations in a network depend on the identification of the contributing source. Once the source is identified, it is explicitly important to update or replace the control system. In order to accomplish this, this work proposes for the first time a novel DVIC. The proposed method employs the state of the art, single-layer-feed-forward learning algorithm which predict the error in system dynamics generated as consequence of complex SSCI and provide a compensated control inputs to mitigate the effect.

The state of the art in literature proposes either frequency dependent or sophisticated system states based controllers to alleviate the instability as a consequence of SSO modes. However, this is particularly challenging because the oscillation modes for complex SSCI are non-stationary and have wider bandwidth, changing with varying operating conditions of the network. Thus, designing such controllers based on aforementioned properties exhibit significant challenges in-terms of stability and effective mitigation of complex phenomena.

To support this argument, a state-of-the-art model-based optimal control is derived to assess the performance of WTG in an IBRs-dominated network. This is the first time where an advanced constraints-based optimal control is proposed to assess the stability of a WTG for varying operating conditions. Though the mechanism proves its viability in-terms of performance for optimal tracking of the reference values for real-world disturbances, the implementation of the control require additional computational resources [189]. Also, the control law is explicitly dependent on system states and the performance deteriorates for oscillation frequencies above subsynchronous range.

Therefore, to circumvent the reliance on the system states and frequency-dependent filters, the novel contribution is accomplished as follows:

- The proposed method employs a data-driven auxiliary control loop to stabilize the *dq* control when a large disturbance or SSCI triggers the SSO. It does not need any offline training and triggers only on a limited set of neurons.

- The generalized Hebbian learning law works as an auxiliary damping control loop. This approach makes the control adaptive and adjusts the rotor side converter (RSC) impedance in finite time by injecting a compensated signal to the dq control loop. The variation takes place only when SSCI or large disturbance triggers system instability, thus making it stable for all varying conditions.

- The functionality of the DVIC is adaptive and robust for all operating conditions and ensures asymptotic stability for boundary conditions as prior knowledge of SSR modes and frequency bandwidths is not required.

- The proposed method does not consider heuristic assumptions to perceive monotonic convergence of tracking error.

- The proposed DVIC is effective for both type-3 and type-4 WTGs and applicable to weak grid configurations or networks with line compensations. This is substantiated by rigorous EMT simulations and small signal perturbation for impedance measurements.

- It is further corroborated that the DVIC responds only to the SSCI dynamics and does not affect the normal operation of the WTGs for grid stability constraints such as dynamic conditions and low voltage ride through performance.

- The computational complexity is lower and the simplicity supports lower costs for industrial implementation.

4. Validation with realistic test cases [185, 187]: Finally, this study presents the demonstration of the proposed methods with real world test cases replicated through EMT simulations. This is accomplished as follows:

- Real-world data sets are used to verify the detection accuracy of the AIFST. Four explicit test studies are conducted and the performance evaluated in comparison with SDFT, Prony analysis and IpDFT, as recently reported in the literature.

- An ERCOT model is developed based on a network which has significantly experienced such oscillations. The network is modified with different WTG configurations and considerable network noise to affirm the validation of the proposed approach for real-world applications. The study for this case reveal that under various dynamic conditions, the accuracy of AIFST stands 99.9% for fundamental components. In addition to that, the Prony and DFT based methods shows a significant deviations in the detection of original modes, while the proposed method detect this with 99.9% accuracy. Similarly, for the test case where the modes of oscillations are highly time varying, the IpDFT fails to estimate these. In contrast, the Prony method detected these, however the detection accuracy is approximately 18% less than the proposed AIFST method.

5. Contributions to Research Publications:

The research reported in this thesis has been published in the following journal and conferences.

[184] **T. Zaman,** Z. Feng, M. Syed, B. Pilscheur, D. Flynn, G. Burt, "Multimode synchronous resonance detection in converters dominated power system using synchro-waveforms." in 27th International Conference on Electricity Distribution (CIRED 2023), 2023, pp. 3620–3624

[185] **T. Zaman**, M. Syed, Z. Feng and G. Burt, "A Realigned Instantaneous Frequency Approach for SSCI Oscillation Localization in Power Networks," in IEEE Transactions on Power Systems, 2024, doi: 10.1109/TPWRS.2024.3474177.

[186] **T.Zaman**, Z. Feng, G. Burt, "A Finite Time Dynamic Virtual Impedance Control for SSCI mitigation in IBRs Dominated Network." in IEEE Transaction on Energy Conversion, 2025 -*under review.*

[187] **T. Zaman**, Z. Feng, M. Syed and G. Burt, "Mitigation of SSCI-Driven Complex Oscillations using Dynamic Virtual Impedance Based Control," 2024 IEEE Power & Energy Society General Meeting (PESGM), Seattle, WA, USA, 2024, pp. 1-5, doi: 10.1109/PESGM51994.2024.10689206.

[188] A.Issah, **T. Zaman**, M. Syed, H. Yue, G. Burt and M. S. E. Moursi, "Linear Parameter varying model predictive control of a Wind Energy Conversion System" in IEEE Transaction on Sustainable Energy, 2024, doi: 10.1109/T-STE.2024.3512997

[190] **T. Zaman**, Z. Feng, S. Mitra, M. Syed, S. Karanki, L. Villa, and G. M. Burt, "ANN Driven FOSMC Based Adaptive Droop Control for Enhanced DC Microgrid Resilience," in IEEE Transactions on Industry Applications, vol. 60, no. 2, pp. 2053-2064, March-April 2024, doi:10.1109/TIA.2023.3328577.

Appendix A

Derivation of the Sliding DFT used in Chapter 4

The DFT of a window of length N for a signal $X_t[k]$ can be written as:

$$X_t[k] = \sum_{n=0}^{N-1} x_t[n] \cdot e^{-j\frac{2\pi}{N}kn}$$

where $x_t[n]$ is the n-th sample in the window at time t.

When a new sample $x[t+N]$ is added to the window and the oldest sample $x[t]$ is removed, the new windowed sequence $x_{t+1}[n]$ is:

$$x_{t+1}[n] = \begin{cases} x_t[n+1], & \text{for } n = 0, 1, \dots, N-2 \\ x[t+N], & \text{for } n = N-1 \end{cases}$$

The DFT of the new windowed sequence at time $t+1$, $X_{t+1}[k]$, can be written as:

$$X_{t+1}[k] = \sum_{n=0}^{N-1} x_{t+1}[n] \cdot e^{-j\frac{2\pi}{N}kn}$$

Substituting the new windowed sequence $x_{t+1}[n]$ into the DFT expression:

$$X_{t+1}[k] = \sum_{n=0}^{N-2} x_t[n+1] \cdot e^{-j\frac{2\pi}{N}kn} + x[t+N] \cdot e^{-j\frac{2\pi}{N}k(N-1)}$$

This can be rewritten as:

$$X_{t+1}[k] = e^{j\frac{2\pi}{N}k} \sum_{n=1}^{N-1} x_t[n] \cdot e^{-j\frac{2\pi}{N}k(n-1)} + x[t+N] \cdot e^{-j\frac{2\pi}{N}k(N-1)}$$

Note that:

$$\sum_{n=1}^{N-1} x_t[n] \cdot e^{-j\frac{2\pi}{N}k(n-1)} = \sum_{n=0}^{N-2} x_t[n+1] \cdot e^{-j\frac{2\pi}{N}kn}$$

This is essentially the DFT $X_t[k]$ without the oldest sample $x[t]$:

$$\sum_{n=0}^{N-2} x_t[n+1] \cdot e^{-j\frac{2\pi}{N}kn} = X_t[k] - x[t] \cdot e^{-j\frac{2\pi}{N}kt}$$

Therefore:

$$X_{t+1}[k] = e^{j\frac{2\pi}{N}k} \left(X_t[k] - x[t] \cdot e^{-j\frac{2\pi}{N}kt} \right) + x[t+N] \cdot e^{-j\frac{2\pi}{N}k(N-1)}$$

Simplify:

$$X_{t+1}[k] = e^{j\frac{2\pi}{N}k} X_t[k] - e^{j\frac{2\pi}{N}k} x[t] \cdot e^{-j\frac{2\pi}{N}kt} + x[t+N] \cdot e^{-j\frac{2\pi}{N}k(N-1)}$$

Since $e^{-j\frac{2\pi}{N}k(N-1)} = e^{j\frac{2\pi}{N}k} \cdot e^{-j\frac{2\pi}{N}kN} = e^{j\frac{2\pi}{N}k}$:

$$X_{t+1}[k] = e^{j\frac{2\pi}{N}k} \left(X_t[k] - x[t] \cdot e^{-j\frac{2\pi}{N}kt} \right) + x[t+N] \cdot e^{j\frac{2\pi}{N}k}$$

$$X_{t+1}[k] = e^{j\frac{2\pi}{N}k} X_t[k] + e^{j\frac{2\pi}{N}k}(x[t+N] - x[t] \cdot e^{-j\frac{2\pi}{N}kt})$$

Thus, the Sliding DFT update formula is:

$$X_{t+1}[k] = e^{j\frac{2\pi}{N}k} \left(X_t[k] + x[t+N] - x[t] \cdot e^{-j\frac{2\pi}{N}kt} \right)$$

References

[1] F. Zhang, “Simulated synchrophasors in SSOs and phasor measurement data recorded during a subsynchronous oscillation incident in an actual power system,” 2021.

[2] S. H. Huang and Y. Gong, “South texas ssr,” *ERCOT ROS Meeting*, 2018, austin, TX, USA, May 2018. [Online]. Available: http://www.ercot.com/content/wcm/key_documents_lists/139265/10._South_Texas_SSR_ERCOT_ROS_May_2018_rev1.pdf.

[3] T. Zaman *et al.*, “Multimode synchronous resonance detection in converters dominated power system using synchro-waveforms.” in *27th International Conference on Electricity Distribution (CIRED 2023)*, 2023, pp. 3620–3624.

[4] L. Meegahapola *et al.*, “Review on oscillatory stability in power grids with renewable energy sources: Monitoring, analysis, and control using synchrophasor technology,” *IEEE Trans. Ind. Electron.*, vol. 68, pp. 519–531, 2021.

[5] J. Shair, X. Xie, Y. Li, and V. Terzija, “Hardware-in-the-loop and field validation of a rotor-side subsynchronous damping controller for a series

compensated DFIG system," *IEEE Trans. Power Del.*, vol. 36, no. 2, pp. 698–709, 2021.

[6] G. Yu, "A multisynchrosqueezing-based high-resolution time-frequency analysis tool for the analysis of non-stationary signals," *Journal of Sound and Vibration*, vol. 492, p. 115813, 2021.

[7] W. Wang, G. Li, and G. He, *Analysis and Mitigation of Broadband Oscillation in Renewable Energy Generation and AC/DC Transmission Systems.* Singapore: Springer, 2023. [Online]. Available: https://link.springer.com/book/10.1007/978-981-99-1568-2

[8] H. A. Mohammadpour, A. Ghaderi, H. Mohammadpour, and E. Santi, "Ssr damping in wind farms using observed-state feedback control of DFIG converters," *Electric Power Systems Research*, vol. 123, pp. 57–66, 2015.

[9] M. A. Chowdhury and G. M. Shafiullah, "Ssr mitigation of series-compensated DFIG wind farms by a nonlinear damping controller using partial feedback linearization," *IEEE Transactions on Power Systems*, vol. 33, no. 3, pp. 2528–2538, 2018.

[10] Y. Wang, Q. Wu, R. Yang, G. Tao, and Z. Liu, "H∞ current damping control of DFIG based wind farm for sub-synchronous control interaction mitigation," *International Journal of Electrical Power & Energy Systems*, vol. 98, pp. 509–519, 2018.

[11] J. Yao, X. Wang, J. Li, R. Liu, and H. Zhang, "Sub-synchronous resonance damping control for series-compensated DFIG-based wind farm with im-

proved particle swarm optimization algorithm," *IEEE Trans. Energy Convers.*, vol. 34, no. 2, pp. 849–859, 2018.

[12] H. Liu, X. Xie, Y. Li, H. Liu, and Y. Hu, "Mitigation of ssr by embedding subsynchronous notch filters into DFIG converter controllers," *IET Generation, Transmission & Distribution*, vol. 11, no. 11, pp. 2888–2896, 2017.

[13] A. E. Leon and J. A. Solsona, "Sub-synchronous interaction damping control for DFIG wind turbines," *IEEE Trans. Power Syst.*, vol. 30, no. 1, pp. 419–428, 2015.

[14] X. Xie, Y. Zhan, H. Liu, W. Li, and C. Wu, "Wide-area monitoring and early-warning of subsynchronous oscillation in power systems with high-penetration of renewables," *International Journal of Electrical Power Energy Systems*, vol. 108, pp. 31–39, 2019. [Online]. Available: https://www.sciencedirect.com/science/article/pii/S014206151832427X

[15] F. Zhang *et al.*, "An improved interpolated DFT-based parameter identification for sub-/super-synchronous oscillations with synchrophasors," *IEEE Trans. Power Syst.*, vol. 38, no. 2, pp. 1714–1727, 2023.

[16] F. Aminifar, M. Fotuhi-Firuzabad, A. Safdarian, A. Davoudi, and M. Shahidehpour, "Synchrophasor measurement technology in power systems: Panorama and state-of-the-art," *IEEE Access*, vol. 2, p. 1607 – 1628, 2014. [Online]. Available: https://www.scopus.com/inward/record.uri?eid=2-s2.0-85006230924&doi=10.1109%2fACCESS.2015.2389659&partnerID=40&md5=5f5bcd131d6627b8c4ddd9fc7b8bf3b5

[17] A. Chakrabortty, J. H. Chow, and A. Salazar, “Interarea model estimation for radial power system transfer paths with intermediate voltage control using synchronized phasor measurements,” *IEEE Transactions on Power Systems*, vol. 24, no. 3, pp. 1318–1326, 2009.

[18] J. De La Ree, V. Centeno, J. S. Thorp, and A. G. Phadke, “Synchronized phasor measurement applications in power systems,” *IEEE Transactions on Smart Grid*, vol. 1, no. 1, pp. 20–27, 2010.

[19] W. Xu, Z. Huang, X. Xie, and C. Li, “Synchronized waveforms x2013; a frontier of data-based power system and apparatus monitoring, protection, and control,” *IEEE Transactions on Power Delivery*, vol. 37, no. 1, pp. 3–17, 2022.

[20] Y. Jia, V. Stanojevic, X. Xie, S. Djurovic, L. Ding, and V. Terzija, “A novel adaptive linear prediction-based parameter estimation method for monitoring sub-/inter-harmonics during ssi events,” *International Journal of Electrical Power Energy Systems*, vol. 132, p. 107133, 2021. [Online]. Available: https://www.sciencedirect.com/science/article/pii/S0142061521003720

[21] F. Auger, P. Flandrin, Y.-T. Lin, S. McLaughlin, S. Meignen, T. Oberlin, and H.-T. Wu, “Time-frequency reassignment and synchrosqueezing: An overview,” *IEEE Signal Processing Magazine*, vol. 30, no. 6, pp. 32–41, 2013.

[22] T. Oberlin, S. Meignen, and V. Perrier, “The fourier-based synchrosqueezing transform,” in *2014 IEEE International Conference on Acoustics, Speech and Signal Processing (ICASSP)*, 2014, pp. 315–319.

[23] Y. Zhao, H. Cui, H. Huo, and Y. Nie, “Application of synchrosqueezed wavelet transforms for extraction of the oscillatory parameters of subsynchronous oscillation in power systems,” *Energies*, vol. 11, no. 6, 2018. [Online]. Available: https://www.mdpi.com/1996-1073/11/6/1525

[24] G. Zheng, H. Wang, S. Liu, and M. M. Farrokhifard, “2021 ieee-naspi oscillation source location contest: Team woodpecker,” in *2022 IEEE Power Energy Society General Meeting (PESGM)*, 2022, pp. 1–5.

[25] B. Wang and S. Maslennikov, “Ieee-naspi oscillation source location contest - case development and results,” North American SynchroPhasor Initiative, Tech. Rep., 2021. [Online]. Available: https://www.naspi.org/node/890

[26] S. Biswas, J. Follum, E. Andersen, and J. S. Banning, “Big data analysis of synchrophasor data - outcomes of research activities supported by doe foa 1861,” Pacific Northwest National Laboratory, Tech. Rep. PNNL-33548, 2022. [Online]. Available: https://www.naspi.org/sites/default/files/reference_documents/pnnl_33548_foa_1861_meta-analysis.pdf

[27] L. Chen, X. Xie, J. He, T. Xu, D. Xu, and N. Ma, “Wideband oscillation monitoring in power systems with high-penetration of renewable energy sources and power electronics: A review,” *Renewable and Sustainable Energy Reviews*, vol. 175, p. 113148, 2023.

[28] X. Xie, Y. Zhan, J. Shair, Z. Ka, and X. Chang, "Identifying the source of subsynchronous control interaction via wide-area monitoring of sub/super-synchronous power flows," *IEEE Trans. Power Del.*, vol. 35, pp. 2177–2185, 2020.

[29] H. Liu, X. Xie, J. He, H. Liu, and Y. Li, "Damping DFIG-associated ssr by adding subsynchronous suppression filters to DFIG converter controllers," in *2016 IEEE Power and Energy Society General Meeting (PESGM)*. IEEE, 2016, pp. 1–5.

[30] M. T. Ali, M. Ghandhari, and L. Harnefors, "Mitigation of sub-synchronous control interaction in DFIGs using a power oscillation damper," in *2017 IEEE Manchester PowerTech*. IEEE, 2017, pp. 1–6.

[31] R. Peña-Alzola, J. Roldán-Pérez, E. Bueno, F. Huerta, D. Campos-Gaona, M. Liserre, and G. Burt, "Robust active damping in lcl-filter-based medium-voltage parallel grid inverters for wind turbines," *IEEE Trans. Power Electron.*, vol. 33, no. 12, pp. 10 846–10 857, 2018.

[32] International Renewable Energy Agency (IRENA), "Renewable capacity statistics 2023 highlights," IRENA, Tech. Rep., Mar. 2023, accessed: 2025-05-17. [Online]. Available: https://www.irena.org/-/media/Files/IRENA/Agency/Publication/2023/Mar/IRENA_-RE_Capacity_Highlights_2023.pdf

[33] "G. zhang, z. li, b. zhang, and w. a. halang, "power electronics converters: Past, present and future," renewable and sustainable energy reviews, vol. 81, no. may 2016, pp. 2028–2044, 2018, doi: 10.1016/j.rser.2017.05.290."

[34] R. K. Varma and R. Salehi, “Ssr mitigation with a new control of pv solar farm as statcom (pv-statcom),” *IEEE Transactions on Sustainable Energy*, vol. 8, no. 4, pp. 1473–1483, 2017.

[35] U. Nations, “Paris agreement,” *Accessed Dec*, vol. 21, p. 2020, December 2015. [Online]. Available: https://unfccc.int/sites/default/files/english

[36] H. M. Rustebakke and C. Concordia, “Self-excited oscillations in a transmission system using series capacitors,” *IEEE Transactions on Power Apparatus and Systems*, 1970.

[37] “Proposed terms and definitions for subsynchronous oscillations,” IEEE Transactions on Power Apparatus and Systems, Tech. Rep., 1980.

[38] G. F. W. R A Lawson, D A Swann, “Minimization of power system stabilizer torsional interaction on large steam turbine-generators,” *IEEE Transactions on Power Apparatus and Systems*, 1978.

[39] M. E. C. W Watson, “Static exciter stabilizing signals on large generators-mechanical problems,” *IEEE Transactions on Power Apparatus and Systems,*, 1973.

[40] G. J. R. D C Lee, R E Beaulieu, “Effects of governor characteristics on turbo-generator shaft torsionals,” *IEEE Transactions on Power Apparatus and Systems,*, 1985.

[41] R. J. P. e. a. M Bahrman, E V Larsen, “Experience with hvdc-turbine-generator torsional interaction at square butte,” *IEEE Transactions on Power Apparatus and Systems,*, 1980.

[42] IEEE-Subsynchronous-Sesonance-Working, “Terms definitions and symbols for subsynchronous oscillations,” *IEEE Transactions on Power Apparatus and Systems*, 1985.

[43] Y. Cheng, L. Fan, J. Rose, S.-H. Huang, J. Schmall, X. Wang, X. Xie, J. Shair, J. R. Ramamurthy, N. Modi, C. Li, C. Wang, S. Shah, B. Pal, Z. Miao, A. Isaacs, J. Mahseredjian, and J. Zhou, “Real-world subsynchronous oscillation events in power grids with high penetrations of inverter-based resources,” *IEEE Transactions on Power Systems*, vol. 38, no. 1, pp. 316–330, 2023.

[44] J. Adams, C. Carter, and S.-H. Huang, “Ercot experience with subsynchronous control interaction and proposed remediation,” in *PES TD 2012*, 2012, pp. 1–5.

[45] L. Wang, X. Xie, Q. Jiang, H. Liu, Y. Li, and H. Liu, “Investigation of ssr in practical DFIG-based wind farms connected to a series-compensated power system,” *IEEE Transactions on Power Systems*, vol. 30, no. 5, pp. 2772–2779, 2015.

[46] X. Yang, L. Yang, X. Xiao, and Y. Wang, “A novel detection method for supersynchronous resonance from synchrophasor data,” *IEEE Trans. Power Syst.*, pp. 1–13, 2022.

[47] X. Lu, W. Xiang, W. Lin, and J. Wen, “Analysis of wideband oscillation of hybrid mmc interfacing weak ac power system,” *IEEE Journal of Emerging and Selected Topics in Power Electronics*, vol. 9, no. 6, pp. 7408–7421, 2021.

[48] C. Yin, X. Xie, S. Xu, and C. Zou, “Review of oscillations in vsc-hvdc systems caused by control interactions,” *The Journal of Engineering*, vol. 2019, no. 16, pp. 1204–1207.

[49] J. Sun, L. Mingjie, X. Zhang, Zhigang, H. W. Jingbo He, and G. Li, “Renewable energy transmission by hvdc across the continent: System challenges and opportunities,” *CSEE Journal of Power and Energy Systems*, vol. 03, no. 4, 2017.

[50] N. Prabhu and K. R. Padiyar, “Investigation of subsynchronous resonance with vsc-based hvdc transmission systems,” *IEEE Transactions on Power Delivery*, vol. 24, no. 1, pp. 433–440, 2009.

[51] X. Zhou and S. Bu, “Damping torque analysis for mechanical oscillation of pmsg based wind generation system,” in *12th IET International Conference on Advances in Power System Control, Operation and Management (APSCOM 2022)*, vol. 2022, 2022, pp. 182–187.

[52] M. Netto, V. Krishnan, L. Mili, P. Sharma, and V. Ajjarapu, “Real-Time Modal Analysis of Electric Power Grids—The Need for Dynamic State Estimation,” National Renewable Energy Laboratory, Golden, CO, NREL/CP-5D00-76124 Preprint, May 2020, available: https://www.nrel.gov/docs/fy20osti/76124.pdf.

[53] J. Ma, P. Zhang, H.-j. Fu, B. Bo, and Z.-y. Dong, “Application of phasor measurement unit on locating disturbance source for low-frequency oscillation,” *IEEE Transactions on Smart Grid*, vol. 1, no. 3, pp. 340–346, 2010.

[54] T. Sadamoto, A. Chakrabortty, T. Ishizaki, and J.-I. Imura, “Retrofit control of wind-integrated power systems,” *IEEE Transactions on Power Systems*, vol. 33, no. 3, p. 2804 – 2815, 2018, cited by: 40; All Open Access, Hybrid Gold Open Access. [Online]. Available: https://www.scopus.com/inward/record.uri?eid=2-s2.0-85031783487&doi=10.1109%2fTPWRS.2017.2750411&partnerID=40&md5=930a3db0602d5c274330b9b379da6a51

[55] S. Zhang and V. Vittal, “Design of wide-area power system damping controllers resilient to communication failures,” *IEEE Transactions on Power Systems*, vol. 28, no. 4, pp. 4292–4300, 2013.

[56] T. Rauhala, A. M. Gole, and P. Jarventausta, “Detection of subsynchronous torsional oscillation frequencies using phasor measurement,” *IEEE Transactions on Power Delivery*, vol. 31, no. 1, p. 11 – 19, 2016, cited by: 49. [Online]. Available: https://www.scopus.com/inward/record.uri?eid=2-s2.0-84962439683&doi=10.1109%2fTPWRD.2015.2436814&partnerID=40&md5=7e40d9d126e23c61b517b76f1a61c988

[57] H. Liu, T. Bi, J. Li, S. Xu, and Q. Yang, “Inter-harmonics monitoring method based on pmus,” *IET Generation, Transmission and Distribution*, vol. 11, no. 18, p. 4414 – 4421, 2017, cited by: 23. [Online]. Available: https://www.scopus.com/inward/record.uri?eid=2-s2.0-85040792341&doi=10.1049%2fiet-gtd.2017.0375&partnerID=40&md5=a7b7eca11d95820b939c79b2f29fbb15

[58] F. Zhang, L. Cheng, W. Gao, and R. Huang, “Synchrophasors-based identification for subsynchronous oscillations in power systems,” *IEEE Transactions on Smart Grid*, vol. 10, no. 2, pp. 2224–2233, 2019.

[59] L. Zhan, Y. Liu, and Y. Liu, “A clarke transformation-based dft phasor and frequency algorithm for wide frequency range,” *IEEE Transactions on Smart Grid*, vol. 9, no. 1, pp. 67–77, 2018.

[60] “Ieee standard for synchrophasor measurements for power systems,” *IEEE Std C37.118.1-2011 (Revision of IEEE Std C37.118-2005)*, pp. 1–61, 2011.

[61] “Ieee standard for synchrophasor measurements for power systems,” *IEEE Std C37.118.1a-2014*, 2014.

[62] T. Zaman and et all, “27th international conference on electricity distribution (cired 2023),” *Multimode synchronous resonance detection in converter dominated power system using synchro-waveforms*, vol. 2023, no. 06, 2023.

[63] A. Silverstein, J. Follum *et al.*, “High-resolution, time-synchronized grid monitoring devices,” *PNNL-29770. Richland, WA: Pacific Northwest National Laboratory. Available online at NASPI Archive: https://www. naspi. org/node/819*, 2020.

[64] W. Xu, Z. Huang, X. Xie, and C. Li, “Synchronized waveforms–a frontier of data-based power system and apparatus monitoring, protection, and control,” *IEEE Transactions on Power Delivery*, vol. 37, no. 1, pp. 3–17, 2021.

[65] A. F. Bastos, S. Santoso, W. Freitas, and W. Xu, “Synchrowaveform measurement units and applications,” in *2019 IEEE Power & Energy Society General Meeting (PESGM)*. IEEE, 2019, pp. 1–5.

[66] H. Liu, J. Lin, S. Xu, T. Bi, and Y. Lao, “A resampling method based on filter designed by window function considering frequency aliasing,” *IEEE*

Transactions on Circuits and Systems I: Regular Papers, vol. 67, no. 12, pp. 5018–5030, 2020.

[67] H. Liu, T. Bi, S. Xu, J. Li, J. Lin, Z. Zhao, F. Yang, H. Ding, J. Shang, and S. Liu, "A full-view synchronized measurement system for the renewables, controls, loads, and waveforms of power-electronics-enabled power distribution grids," *IEEE Transactions on Smart Grid*, vol. 13, no. 5, pp. 3879–3890, 2021.

[68] X. Huang, Y. J. Guo, and J. A. Zhang, "Sample rate conversion using b-spline interpolation for ofdm based software defined radios," *IEEE Transactions on Communications*, vol. 60, no. 8, pp. 2113–2122, 2012.

[69] C. Ghafari, H. Almasalma, B. Raison, N. Hadjsaid, R. Caire, and E. Martin, "Phasors estimation at offnominal frequencies through an enhanced-sva method with a fixed sampling clock," *IEEE Transactions on Power Delivery*, vol. 32, no. 4, pp. 1766–1775, 2016.

[70] C. W. Farrow, "A continuously variable digital delay element," in *1988., IEEE International Symposium on Circuits and Systems.* IEEE, 1988, pp. 2641–2645.

[71] A. Kumar, S. Yadav, and N. Purohit, "Generalized rational sampling rate conversion polyphase fir filter," *IEEE Signal Processing Letters*, vol. 24, no. 11, pp. 1591–1595, 2017.

[72] T. Rampone, A. Hallal, H. Khaleghi, and A. Sharaiha, "Down-conversion gain of an all-optical soa-mzi-based mixer using bandpass sampling," *IEEE Photonics Technology Letters*, vol. 26, no. 4, pp. 411–413, 2013.

[73] A. F. Bastos and S. Santoso, "Universal waveshape-based disturbance detection in power quality data using similarity metrics," *IEEE Transactions on Power Delivery*, vol. 35, no. 4, pp. 1779–1787, 2019.

[74] S. Blair and J. Costello, "Slipstream: High-performance lossless compression for streaming synchronized waveform monitoring data," in *2022 International Conference on Smart Grid Synchronized Measurements and Analytics (SGSMA)*. IEEE, 2022, pp. 1–6.

[75] ——, "Slipstream: High-performance lossless compression for streaming synchronized waveform monitoring data," in *2022 International Conference on Smart Grid Synchronized Measurements and Analytics (SGSMA)*. IEEE, 2022, pp. 1–6.

[76] B. Gao, R. Torquato, W. Xu, and W. Freitas, "Waveform-based method for fast and accurate identification of subsynchronous resonance events," *IEEE Transactions on Power Systems*, vol. 34, no. 5, pp. 3626–3636, 2019.

[77] W. Xu, Z. Huang, X. Xie, and C. Li, "Synchronized waveforms–a frontier of data-based power system and apparatus monitoring, protection, and control," *IEEE Transactions on Power Delivery*, vol. 37, no. 1, pp. 3–17, 2021.

[78] B. Gao, Y. Wang, W. Xu, and G. Yang, "Identifying and ranking sources of ssr based on the concept of subsynchronous power," *IEEE Transactions on Power Delivery*, vol. 35, no. 1, pp. 258–268, 2019.

[79] M. Izadi and H. Mohsenian-Rad, "A synchronized lissajous-based approach to achieve situational awareness using synchronized waveform measure-

ments," in *2021 IEEE Power Energy Society General Meeting (PESGM)*, 2021, pp. 01–05.

[80] ——, "A synchronized lissajous-based method to detect and classify events in synchro-waveform measurements in power distribution networks," *IEEE Transactions on Smart Grid*, vol. 13, no. 3, pp. 2170–2184, 2022.

[81] ——, *Event Detection, Classification, and Location Identification with Synchro-Waveforms*. John Wiley Sons, Ltd, 2024, ch. 31, pp. 729–759. [Online]. Available: https://onlinelibrary.wiley.com/doi/abs/10.1002/9781119890881.ch30

[82] L. Chen, X. Xie, J. He, T. Xu, D. Xu, and N. Ma, "Wideband oscillation monitoring in power systems with high-penetration of renewable energy sources and power electronics: A review," *Renewable and Sustainable Energy Reviews*, vol. 175, p. 113148, 2023. [Online]. Available: https://www.sciencedirect.com/science/article/pii/S1364032123000047

[83] M. P. Tcheou, L. Lovisolo, M. V. Ribeiro, E. A. Da Silva, M. A. Rodrigues, J. M. Romano, and P. S. Diniz, "The compression of electric signal waveforms for smart grids: State of the art and future trends," *IEEE Transactions on Smart Grid*, vol. 5, no. 1, pp. 291–302, 2013.

[84] X. Wang, Y. Liu, and L. Tong, "Adaptive subband compression for streaming of continuous point-on-wave and pmu data," *IEEE Transactions on Power Systems*, vol. 36, no. 6, pp. 5612–5621, 2021.

[85] S. Blair and J. Costello, "Slipstream: High-performance lossless compression for streaming synchronized waveform monitoring data," in *2022 Inter-*

national Conference on Smart Grid Synchronized Measurements and Analytics (SGSMA). IEEE, 2022, pp. 1–6.

[86] National Grid Electricity System Operator. (2020, January) How our new spin on grid stability is a boost for renewable generation. Accessed: 2024-11-22. [Online]. Available: https://www.neso.energy/news/national-grid-eso-outline-new-approach-stability-services-significant-step-forwards-towar

[87] National Grid ESO, "GC0137: Minimum Specification Required for Grid Forming Capability," National Grid ESO website, Feb. 2022, Approved by Ofgem and incorporated into the Grid Code. [Online]. Available: https://www.nationalgrideso.com/industry-information/codes/grid-code-old/modifications/gc0137-minimum-specification-required

[88] J. Shair, X. Xie, and G. Yan, "Mitigating subsynchronous control interaction in wind power systems: Existing techniques and open challenges," *Renewable and Sustainable Energy Reviews*, vol. 108, pp. 330–346, 2019. [Online]. Available: https://www.sciencedirect.com/science/article/pii/S1364032119302060

[89] L. Fan, R. Kavasseri, Z. L. Miao, and C. Zhu, "Modeling of DFIG-based wind farms for ssr analysis," *IEEE Transactions on Power Delivery*, vol. 25, no. 4, pp. 2073–2082, 2010.

[90] Z. An, C. Shen, Z. Zheng, F. Liu, X. Chang, and W. Wei, "Scenario-based analysis and probability assessment of sub-synchronous oscillation caused by wind farms with direct-driven wind generators," *Journal of Modern Power Systems and Clean Energy*, vol. 7, no. 2, pp. 243–253, 2019.

[91] C. Zhu, M. Hu, and Z. Wu, “Parameters impact on the performance of a double-fed induction generator-based wind turbine for subsynchronous resonance control,” *IET Renewable Power Generation*, vol. 6, no. 2, pp. 92–98, 2012.

[92] P.-H. Huang, M. S. El Moursi, W. Xiao, and J. L. Kirtley, “Subsynchronous resonance mitigation for series-compensated DFIG-based wind farm by using two-degree-of-freedom control strategy,” *IEEE Transactions on Power Systems*, vol. 30, no. 3, pp. 1442–1454, 2014.

[93] S. Chernet, M. Bongiorno, G. K. Andersen, T. Lund, and P. C. Kjaer, “Online variation of wind turbine controller parameter for mitigation of ssr in DFIG based wind farms,” in *2016 IEEE Energy conversion congress and exposition (ECCE)*. IEEE, 2016, pp. 1–8.

[94] A. Chen, D. Xie, D. Zhang, C. Gu, and K. Wang, “Pi parameter tuning of converters for sub-synchronous interactions existing in grid-connected DFIG wind turbines,” *IEEE Transactions on Power Electronics*, vol. 34, no. 7, pp. 6345–6355, 2018.

[95] U. Karaagac, J. Mahseredjian, S. Jensen, R. Gagnon, M. Fecteau, and I. Kocar, “Safe operation of DFIG-based wind parks in series-compensated systems,” *IEEE Transactions on Power Delivery*, vol. 33, no. 2, pp. 709–718, 2017.

[96] M. S. El-Moursi, B. Bak-Jensen, and M. H. Abdel-Rahman, “Novel statcom controller for mitigating ssr and damping power system oscillations in a

series compensated wind park," *IEEE Transactions on Power electronics*, vol. 25, no. 2, pp. 429–441, 2009.

[97] C. Zhu, L. Fan, and M. Hu, "Control and analysis of DFIG-based wind turbines in a series compensated network for ssr damping," in *IEEE PES General Meeting*. IEEE, 2010, pp. 1–6.

[98] S. O. Faried, I. Unal, D. Rai, and J. Mahseredjian, "Utilizing DFIG-based wind farms for damping subsynchronous resonance in nearby turbine-generators," *IEEE Transactions on Power Systems*, vol. 28, no. 1, pp. 452–459, 2012.

[99] X. Gao, U. Karaagac, S. Faried, and J. Mahseredjian, "On the use of wind energy conversion systems for mitigating subsynchronous resonance and subsynchronous interaction," in *IEEE PES Innovative Smart Grid Technologies, Europe*. IEEE, 2014, pp. 1–6.

[100] S. Chernet, M. Beza, and M. Bongiorno, "Investigation of subsynchronous control interaction in DFIG-based wind farms connected to a series compensated transmission line," *International Journal of Electrical Power & Energy Systems*, vol. 105, pp. 765–774, 2019.

[101] G. Zames, "Feedback and optimal sensitivity: Model reference transformations, multiplicative seminorms, and approximate inverses," *IEEE Transactions on Automatic Control*, vol. 26, no. 2, pp. 301–320, 1981.

[102] A. Honrubia-Escribano, E. Gómez-Lázaro, J. Fortmann, P. Sørensen, and S. Martin-Martinez, "Generic dynamic wind turbine models for power sys-

tem stability analysis: A comprehensive review," *Renewable and Sustainable Energy Reviews*, vol. 81, pp. 1939–1952, 2018.

[103] S. Zhao and N.-K. Nair, "Assessment of wind farm models from a transmission system operator perspective using field measurements," *IET renewable power generation*, vol. 5, no. 6, pp. 455–464, 2011.

[104] X. Xie, Y. Zhan, H. Liu, and C. Liu, "Improved synchrophasor measurement to capture sub/super-synchronous dynamics in power systems with renewable generation," *IET Renewable Power Generation*, vol. 13, no. 1, pp. 49–56, 2019.

[105] X. Xie, H. Liu, Y. Wang, Z. Xu, and J. He, "Measurement of sub-and supersynchronous phasors in power systems with high penetration of renewables," in *2016 IEEE Power & Energy Society Innovative Smart Grid Technologies Conference (ISGT).* IEEE, 2016, pp. 1–5.

[106] H. Liu, T. Bi, J. Li, S. Xu, and Q. Yang, "Inter-harmonics monitoring method based on pmus," *IET Generation, Transmission & Distribution*, vol. 11, no. 18, pp. 4414–4421, 2017.

[107] J. Hu, B. Wang, W. Wang, H. Tang, Y. Chi, and Q. Hu, "Small signal dynamics of DFIG-based wind turbines during riding through symmetrical faults in weak ac grid," *IEEE Transactions on Energy Conversion*, vol. 32, no. 2, pp. 720–730, 2017.

[108] Y. Song and F. Blaabjerg, "Analysis of middle frequency resonance in DFIG system considering phase-locked loop," *IEEE Transactions on Power Electronics*, vol. 33, no. 1, pp. 343–356, 2018.

[109] J. Hu, Y. Huang, D. Wang, H. Yuan, and X. Yuan, “Modeling of grid-connected DFIG-based wind turbines for dc-link voltage stability analysis,” *IEEE Transactions on Sustainable Energy*, vol. 6, no. 4, pp. 1325–1336, 2015.

[110] D. Wang, L. Liang, J. Hu, N. Chang, and Y. Hou, “Analysis of low-frequency stability in grid-tied DFIGs by nonminimum phase zero identification,” *IEEE Transactions on Energy Conversion*, vol. 33, no. 2, pp. 716–729, 2018.

[111] L. Fan, R. Kavasseri, Z. L. Miao, and C. Zhu, “Modeling of DFIG-based wind farms for ssr analysis,” *IEEE Transactions on Power Delivery*, vol. 25, no. 4, pp. 2073–2082, 2010.

[112] J. Liu, W. Yao, J. Wen, J. Fang, L. Jiang, H. He, and S. Cheng, “Impact of power grid strength and pll parameters on stability of grid-connected DFIG wind farm,” *IEEE Transactions on Sustainable Energy*, vol. 11, no. 1, pp. 545–557, 2020.

[113] W. Ren and E. Larsen, “A refined frequency scan approach to sub-synchronous control interaction (SSCI) study of wind farms,” *IEEE Trans. Power Syst.*, vol. 31, no. 5, pp. 3904–3912, 2016.

[114] D. Shu *et al.*, “Sub-and super-synchronous interactions between statcoms and weak AC/DC transmissions with series compensations,” *IEEE Trans. Power Electron*, vol. 33, pp. 7424–7437, 2018.

[115] H. Liu *et al.*, “Subsynchronous interaction between direct-drive PMSG based wind farms and weak AC networks,” *IEEE Trans. Power Syst.*, vol. 32, no. 6, pp. 4708–4720, 2017.

[116] J. Adams *et al.*, “ERCOT experience screening for sub-synchronous control interaction in the vicinity of series capacitor banks,” *2012 IEEE Power and Energy Society General Meeting*, pp. 1–5, 2012.

[117] L. Wang *et al.*, “Investigation of SSR in practical DFIG-based wind farms connected to a series-compensated power system,” *IEEE Trans. Power Syst.*, vol. 30, no. 5, pp. 2772–2779, 2015.

[118] W. Liu, Z. Lu, X. Wang, and X. Xie, “Frequency-coupled admittance modelling of grid-connected voltage source converters for the stability evaluation of subsynchronous interaction,” *IET Renewable Power Generation*, vol. 13, no. 2, pp. 285–295, 2019.

[119] L. Fan, “Inter-IBR oscillation modes,” *IEEE Trans. Power Syst.*, vol. 37, no. 1, pp. 824–827, 2022.

[120] L. P. Kunjumuhammed, B. C. Pal, C. Oates, and K. J. Dyke, “Electrical oscillations in wind farm systems: Analysis and insight based on detailed modeling,” *IEEE Trans. Sustainable Energy*, vol. 7, no. 1, pp. 51–62, 2016.

[121] H. W. Wenjuan Du, *Analysis of Power System Sub/Super-Synchronous Oscillations Caused by Grid-Connected Wind Power Generation.* Springer Cham, 23 December 2023.

[122] X. Yang *et al.*, “Interpolated DFT-based identification of sub-synchronous oscillation parameters using synchrophasor data,” *IEEE Trans. Smart Grid*, vol. 11, no. 3, pp. 2662–2675, 2020.

[123] T. Rauhala, A. M. Gole, and P. Järventausta, “Detection of subsynchronous torsional oscillation frequencies using phasor measurement,” *IEEE Trans. Power Del.*, vol. 31, no. 1, pp. 11–19, 2016.

[124] F. Zhang, L. Cheng, W. Gao, and R. Huang, “Synchrophasors-based identification for subsynchronous oscillations in power systems,” *IEEE Trans. Smart Grid*, vol. 10, no. 2, 2019.

[125] Z. Feng, R. Pena-Alzola, M. H. Syed, P. J. Norman, and G. M. Burt, “Adaptive Smith predictor for enhanced stability of power hardware-in-the-loop setups,” *IEEE Trans. Ind. Electron.*, vol. 70, no. 10, pp. 10 204–10 214, 2023.

[126] R. L. E. Jacobsen, “An update to the sliding dft,” *IEEE Signal Processing Magazine*, vol. 21, no. 1, pp. 110–111, 2004.

[127] Z. Feng, R. Peña-Alzola, P. Seisopoulos, E. Guillo-Sansano, M. Syed, P. Norman, and G. Burt, “A scheme to improve the stability and accuracy of power hardware-in-the-loop simulation,” in *IECON 2020 The 46th Annual Conference of the IEEE Industrial Electronics Society*, 2020, pp. 5027–5032.

[128] Z. Feng *et al.*, “Interface compensation for more accurate power transfer and signal synchronization within power hardware-in-the-loop simulation,” in

IECON 2021 – 47th Annual Conference of the IEEE Ind. Electron. Society, 2021, pp. 1–8.

[129] A. Chauhan and K. M. Singh, "Recursive sliding dft algorithms: A review," *Digital Signal Processing*, vol. 127, p. 103560, 2022. [Online]. Available: https://www.sciencedirect.com/science/article/pii/S1051200422001774

[130] G. Yu, M. Yu, and C. Xu, "Synchroextracting transform," *IEEE Trans. Ind. Electron.*, vol. 64, no. 10, pp. 8042–8054, 2017.

[131] G. Thakur and H.-T. Wu, "Synchrosqueezing-based recovery of instantaneous frequency from nonuniform samples," *SIAM Journal on Mathematical Analysis*, vol. 43, no. 5, pp. 2078–2095, 2011.

[132] S. Chen, S. Wang, B. An, R. Yan, and X. Chen, "Instantaneous frequency band and synchrosqueezing in time-frequency analysis," *IEEE Trans. Signal Process.*, vol. 71, pp. 539–554, 2023.

[133] R. Behera, S. Meignen, and T. Oberlin, "Theoretical analysis of the second-order synchrosqueezing transform," *Applied and Computational Harmonic Analysis*, vol. 45, no. 2, pp. 379–404, 2018.

[134] Y. Cheng *et al.*, "Real-world subsynchronous oscillation events in power grids with high penetrations of inverter-based resources," *IEEE Trans. Power Syst.*, vol. 38, no. 1, pp. 316–330, 2023.

[135] W. Liu, X. Xie, J. Shair, and X. Li, "A nearly decoupled admittance model for grid-tied VSCs under variable operating conditions," *IEEE Trans. Power Electron.*, vol. 35, no. 9, pp. 9380–9389, 2020.

[136] H. Liu, X. Xie, C. Zhang, Y. Li, H. Liu, and Y. Hu, "Quantitative ssr analysis of series-compensated DFIG-based wind farms using aggregated rlc circuit model," *IEEE Trans. Power Syst.*, vol. 32, no. 1, pp. 474–483, 2017.

[137] W. Liu, X. Xie, J. Shair, H. Liu, and J. He, "Frequency-coupled impedance model-based sub-synchronous interaction analysis for direct-drive wind turbines connected to a weak ac grid," *IET Renewable Power Generation*, vol. 13, no. 16, pp. 2966–2976, 2019. [Online]. Available: https://ietresearch.onlinelibrary.wiley.com/doi/abs/10.1049/iet-rpg.2019.0326

[138] Q. Hao, J. Wang, X. Wang, J. Li, C. Su, and C. Liu, "Localization of sub/super-synchronous oscillation sources in wind power systems based on deep adaptation network," in *2023 4th International Conference on Advanced Electrical and Energy Systems (AEES)*, 2023, pp. 655–659.

[139] X. Xie, W. Liu, H. Liu, Y. Du, and Y. Li, "A system-wide protection against unstable ssci in series-compensated wind power systems," *IEEE Transactions on Power Delivery*, vol. 33, no. 6, pp. 3095–3104, 2018.

[140] F. Salehi, I. B. M. Matsuo, A. Brahman, M. A. Tabrizi, and W.-J. Lee, "Sub-synchronous control interaction detection: A real-time application," *IEEE Transactions on Power Delivery*, vol. 35, no. 1, pp. 106–116, 2020.

[141] M. Beza and M. Bongiorno, "On the risk for subsynchronous control interaction in type 4 based wind farms," *IEEE Transactions on Sustainable Energy*, vol. 10, no. 3, pp. 1410–1418, 2019.

[142] B. Gao, Y. Wang, W. Xu, and G. Yang, "Identifying and ranking sources of SSR based on the concept of subsynchronous power," *IEEE Trans. Power Del.*, vol. 35, no. 1, pp. 258–268, 2020.

[143] Y. Li, L. Fan, and Z. Miao, "Replicating real-world wind farm SSR events," *IEEE Trans. Power Del.*, vol. 35, no. 1, pp. 339–348, 2020.

[144] X. Xie, X. Zhang, H. Liu, H. Liu, Y. Li, and C. Zhang, "Characteristic analysis of subsynchronous resonance in practical wind farms connected to series-compensated transmissions," *IEEE Transactions on Energy Conversion*, vol. 32, no. 3, pp. 1117–1126, 2017.

[145] L. Fan, "Modeling type-4 wind in weak grids," *IEEE Transactions on Sustainable Energy*, vol. 10, no. 2, pp. 853–864, 2019.

[146] J. Adams, V. A. Pappu, and A. Dixit, "Ercot experience screening for subsynchronous control interaction in the vicinity of series capacitor banks," in *2012 IEEE Power and Energy Society General Meeting*, 2012, pp. 1–5.

[147] M. Sahni, B. Badrzadeh, D. Muthumuni, Y. Cheng, H. Yin, S.-H. Huang, and Y. Zhou, "Sub-synchronous interaction in wind power plants- part ii: An ercot case study," in *2012 IEEE Power and Energy Society General Meeting*, 2012, pp. 1–9.

[148] Y. Cheng, M. Sahni, D. Muthumuni, and B. Badrzadeh, "Reactance scan crossover-based approach for investigating ssci concerns for DFIG-based wind turbines," *IEEE Transactions on Power Delivery*, vol. 28, no. 2, pp. 742–751, 2013.

[149] G. D. Irwin, A. K. Jindal, and A. L. Isaacs, "Sub-synchronous control interactions between type 3 wind turbines and series compensated ac transmission systems," in *2011 IEEE Power and Energy Society General Meeting*, 2011, pp. 1–6.

[150] N. Karnik, D. Novosad, H. K. Nia, M. Sahni, M. Ghavami, and H. Yin, "An evaluation of critical impact factors for ssci analysis for wind power plants: A utility perspective," in *2017 IEEE Power Energy Society General Meeting*, 2017, pp. 1–5.

[151] N. Miller, W. Price, and J. Sanchez-Gasca, "Dynamic modeling of ge 1.5 and 3.6 wind turbine-generators," *GE-Power systems energy consulting*, 01 2003.

[152] E. Texas, "New ett 345-kv lines begin delivering power to lrgv," *Electric Transmission Texas*, vol. 2, 2016.

[153] B. Cassell, "250-mw hidalo wind project in texas due for commercial ops on sept 23," *GenerationHub. com*, 2016.

[154] L. Chen, X. Xie, J. He, T. Xu, D. Xu, and N. Ma, "Wideband oscillation monitoring in power systems with high-penetration of renewable energy sources and power electronics: A review," *Renewable and Sustainable Energy Reviews*, vol. 175, p. 113148, 2023. [Online]. Available: https://www.sciencedirect.com/science/article/pii/S1364032123000047

[155] J. Shair, X. Xie, and G. Yan, "Mitigating subsynchronous control interaction in wind power systems: Existing techniques and open

challenges," *Renewable and Sustainable Energy Reviews*, vol. 108, pp. 330–346, 2019. [Online]. Available: https://www.sciencedirect.com/science/article/pii/S1364032119302060

[156] H. A. Mohammadpour, M. M. Islam, E. Santi, and Y.-J. Shin, "Ssr damping in fixed-speed wind farms using series facts controllers," *IEEE Transactions on Power Delivery*, vol. 31, no. 1, pp. 76–86, 2016.

[157] H. A. Mohammadpour and E. Santi, "Modeling and control of gate-controlled series capacitor interfaced with a DFIG-based wind farm," *IEEE Transactions on Industrial Electronics*, vol. 62, no. 2, pp. 1022–1033, 2015.

[158] J. Lyu, X. Cai, M. Amin, and M. Molinas, "Sub-synchronous oscillation mechanism and its suppression in mmc-based hvdc connected wind farms," *IET Generation, Transmission & Distribution*, vol. 12, no. 4, pp. 1021–1029.

[159] J. Shair, X. Xie, L. Wang, W. Liu, J. He, and H. Liu, "Overview of emerging subsynchronous oscillations in practical wind power systems," *Renewable and Sustainable Energy Reviews*, vol. 99, pp. 159–168, 2019. [Online]. Available: https://www.sciencedirect.com/science/article/pii/S1364032118306956

[160] M. Ghafouri, U. Karaagac, J. Mahseredjian, and H. Karimi, "SSCI damping controller design for series-compensated DFIG-based wind parks considering implementation challenges," *IEEE Trans. Power Syst.*, vol. 34, no. 4, pp. 2644–2653, 2019.

[161] M. A. Chowdhury and G. M. Shafiullah, “SSR mitigation of series-compensated DFIG wind farms by a nonlinear damping controller using partial feedback linearization,” *IEEE Trans. Power Syst.*, vol. 33, no. 3, pp. 2528–2538, 2018.

[162] P. Li, L. Xiong, F. Wu, M. Ma, and J. Wang, “Sliding mode controller based on feedback linearization for damping of sub-synchronous control interaction in DFIG-based wind power plants,” *International Journal of Electrical Power Energy Systems*, vol. 107, pp. 239–250, 2019. [Online]. Available: https://www.sciencedirect.com/science/article/pii/S0142061518312973

[163] P. Li, J. Wang, L. Xiong, S. Huang, M. Ma, and Z. Wang, “Energy-shaping controller for DFIG-based wind farm to mitigate subsynchronous control interaction,” *IEEE Transactions on Power Systems*, vol. 36, no. 4, pp. 2975–2991, 2021.

[164] J. Yao, X. Wang, J. Li, R. Liu, and H. Zhang, “Sub-synchronous resonance damping control for series-compensated DFIG-based wind farm with improved particle swarm optimization algorithm,” *IEEE Trans. Energy Convers.*, vol. 34, no. 2, pp. 849–859, 2019.

[165] I. Sami, S. Ullah, N. Ullah, and J.-S. Ro, “Sensorless fractional order composite sliding mode control design for wind generation system,” *ISA Transactions*, vol. 111, pp. 275–289, 2021.

[166] J. Taherahmadi, M. Jafarian, and M.-N. Asefi, “Using adaptive control in DFIG-based wind turbines to improve the subsynchronous oscillations of

nearby synchronous generators," *IET Renewable Power Generation*, vol. 11, no. 2, pp. 362–369.

[167] M. Beza and B. Massimo, "A modified rls algorithm for online estimation of low-frequency oscillations in power systems," *IEEE Trans. Power Syst.*, vol. 31, no. 3, pp. 1703–1714, 2016.

[168] Y. Wang, X. Jiang, X. Xie, X. Yang, and X. Xiao, "Identifying sources of subsynchronous resonance using wide-area phasor measurements," *IEEE Trans. Power Del.*, vol. 36, no. 5, pp. 3242–3254, 2021.

[169] J. Hauer, C. Demeure, and L. Scharf, "Initial results in prony analysis of power system response signals," *IEEE Trans. Power Syst.*, vol. 5, no. 1, pp. 80–89, 1990.

[170] S. J. Zhongsheng Hou, *Model Free Adaptive Control.* Taylor Francis, 2013.

[171] X. Wu, M. Wang, M. Shahidehpour, S. Feng, and X. Chen, "Model-free adaptive control of statcom for sso mitigation in DFIG-based wind farm," *IEEE Transactions on Power Systems*, vol. 36, no. 6, pp. 5282–5293, 2021.

[172] X. Wu, S. Xu, X. Shi, M. Shahidehpour, M. Wang, and Z. Li, "Mitigating subsynchronous oscillation using model-free adaptive control of DFIGs," *IEEE Transactions on Sustainable Energy*, vol. 14, no. 1, pp. 242–253, 2023.

[173] D. Xu, B. Jiang, and F. Liu, "Improved data driven model free adaptive constrained control for a solid oxide fuel cell," *IET Control Theory & Applications*, vol. 10, no. 12, pp. 1412–1419.

[174] O. Bertozzi, H. R. Chamorro, E. O. Gomez-Diaz, M. S. Chong, and S. Ahmed, “Application of data-driven methods in power systems analysis and control,” *IET Energy Systems Integration*, vol. n/a, no. n/a.

[175] X. Wu, S. Feng, P. Jiang, G. Xu, and X. Yang, “An ssr multichannel damping control scheme for tcsc considering multiple operating conditions,” *International Trans. Electr. Energy Syst.*, vol. 26, no. 12, pp. 2759–2773, 2016.

[176] T. Zaman, M. Syed, Z. Feng, and G. Burt, “Mitigation of ssci-driven complex oscillations using dynamic virtual impedance based control,” in *2024 IEEE Power Energy Society General Meeting (PESGM)*, 2024, pp. 1–5.

[177] Y. Song and F. Blaabjerg, “Overview of DFIG-based wind power system resonances under weak networks,” *IEEE Transactions on Power Electronics*, vol. 32, no. 6, pp. 4370–4394, 2017.

[178] L. Wang, X. Xie, Q. Jiang, H. Liu, Y. Li, and H. Liu, “Investigation of ssr in practical DFIG-based wind farms connected to a series-compensated power system,” *IEEE Transactions on Power Systems*, vol. 30, no. 5, pp. 2772–2779, 2015.

[179] X. Xie, X. Zhang, H. Liu, H. Liu, Y. Li, and C. Zhang, “Characteristic analysis of subsynchronous resonance in practical wind farms connected to series-compensated transmissions,” *IEEE Transactions on Energy Conversion*, vol. 32, no. 3, pp. 1117–1126, 2017.

[180] H. Liu, X. Xie, C. Zhang, Y. Li, H. Liu, and Y. Hu, “Quantitative ssr analysis of series-compensated DFIG-based wind farms using aggregated

rlc circuit model," *IEEE Transactions on Power Systems*, vol. 32, no. 1, pp. 474–483, 2017.

[181] A. E. Leon, S. J. Amodeo, and J. M. Mauricio, "Enhanced compensation filter to mitigate subsynchronous oscillations in series-compensated DFIG-based wind farms," *IEEE Trans. Power Del.*, vol. 36, no. 6, pp. 3805–3814, 2021.

[182] C. Huang, Z. Zheng, X. Xiao, and X. Chen, "Enhancing low-voltage ride-through capability of pmsg based on cost-effective fault current limiter and modified wtg control," *Electric Power Systems Research*, vol. 185, p. 106358, 2020. [Online]. Available: https://www.sciencedirect.com/science/article/pii/S0378779620301644

[183] T. Zaman, Z. Feng, S. Mitra, M. Syed, S. Karanki, L. Villa, and G. Burt, "ANN driven fosmc based adaptive droop control for enhanced dc microgrid resilience," *IEEE Trans. Ind. Appl.*, vol. 60, no. 2, pp. 2053–2064, 2024.

[184] T. Zaman, Z. Feng, M. Syed, B. Pilscheur, D. Flynn, and G. Burt, "Multi-mode synchronous resonance detection in converters dominated power system using synchro-waveforms," in *27th International Conference on Electricity Distribution (CIRED 2023)*, 2023, pp. 3620–3624.

[185] T. Zaman, M. Syed, Z. Feng, and G. Burt, "A realigned instantaneous frequency approach for ssci oscillation localization in power networks," *IEEE Transactions on Power Systems*, 2024.

[186] T. Zaman, Z. Feng, and G. Burt, "A finite time dynamic virtual impedance control for ssci mitigation in ibrs dominated network," *IEEE Transactions on Energy Conversion*, 2025, under review.

[187] T. Zaman, Z. Feng, M. Syed, and G. Burt, "Mitigation of ssci-driven complex oscillations using dynamic virtual impedance based control," in *2024 IEEE Power & Energy Society General Meeting (PESGM)*, Seattle, WA, USA, 2024, pp. 1–5.

[188] A. Issah, T. Zaman, M. Syed, H. Yue, G. Burt, and M. S. E. Moursi, "Linear parameter varying model predictive control of a wind energy conversion system," *IEEE Transactions on Sustainable Energy*, 2024.

[189] T. Zaman, Z. Feng, S. Mitra, M. Syed, S. Karanki, L. Villa, and G. M. Burt, "Ann driven fosmc based adaptive droop control for enhanced dc microgrid resilience," *IEEE Transactions on Industry Applications*, vol. 60, no. 2, pp. 2053–2064, March-April 2024.